Probing Dark Matter with Resonant Dynamics of the Galactic Bar

Rimpei Chiba

Supervisor: Prof. Ralph Schönrich

Department of Physics
University of Oxford

A thesis submitted for the degree of
Doctor of Philosophy

Linacre College

October 2022

Probing dark matter with resonant dynamics of the Galactic bar

Rimpei Chiba

Linacre College, University of Oxford

A thesis submitted for the degree of
Doctor of Philosophy

Trinity term 2022

Abstract

This thesis provides a novel dynamical evidence for dark matter by measuring for the first time the deceleration of the Galactic bar. This spin-down of the bar requires the transfer of energy and angular momentum to dark matter by dynamical friction, which not only is in conflict with modified gravity theories, but also imposes constraints on the kinematics and nature of dark matter.

The deceleration of the Galactic bar is quantified using the astrometric and photometric data of the Solar neighbourhood stars recently obtained by the *Gaia* space telescope. When the bar spins down, the resonant phase-space drifts radially outward through the stellar disk while growing in volume, thereby capturing new stars along its path. Since these trapped stars conserve the action of libration, which quantifies the amplitude of motion around the resonance, the resonant phase-space grows just like tree-rings, adding new layers of trapped stars at its surface. Together with the negative metallicity gradient in the disk, this implies a prominent increase in stellar metallicity towards the resonance centre. We detected this tell-tale signal in the bar's corotation resonance, thus quantitatively proving the bar's slowdown. During the course of this research, we also resolved the long-standing issue on the origin of the Hercules stellar stream and provided a precise estimate on the bar's current pattern speed.

Furthermore, in order to constrain the phase-space distribution of dark matter from the measured slowing rate of the bar, we developed a theory of dynamical friction in the non-linear regime in the slow limit of bar evolution. Using the resonant angle-action coordinates, we successfully modelled the long-term oscillation and saturation of dynamical friction as a result of the non-linear phase mixing in the trapped phase-space.

To my wife.

Declaration

I hereby declare that except where specific reference is made to the work of others, the contents of this dissertation are original and have not been submitted in whole or in part for consideration for any other degree or qualification in this, or any other university.

Rimpei Chiba
October 2022

Publications Related to this Thesis

This thesis is based on material presented in the following first-authored papers:

Chapter 2 uses material from Chiba R., Friske J., Schönrich R., 2021, MNRAS, 500, 4710.
Chapter 3 uses material from Chiba R., Schönrich R., 2021, MNRAS, 505, 2412.
Chapter 4 uses material from Chiba R., Schönrich R., 2022, MNRAS, 513, 768.

Acknowledgements

First and foremost, I thank my mentor Ralph Schönrich who has made my D.Phil. study not only possible, but an exciting and hopefully a productive one. He was a generous supervisor, giving me the freedom to pursue whatever I found interesting, yet always steering me in the right direction. I am grateful to his mentorship both in and outside academia.

I would also like to thank my co-supervisor John Magorrian, without whom my study has not successfully ended. He has warmly watched over my progress and has always been available for advice, whether it be about dynamics or important career decisions.

During my studies, I have had the privilege of learning from James Binney. His wit to immediately grasp the essence and to give it a lucid explanation has enlightened me countless times. I thank him for all his insightful advice, which has become my lifelong asset.

I am also grateful to Walter Dehnen who had taught me advanced numerical techniques and gave me invaluable feedbacks on my papers.

Special thanks goes to my friend and officemate Jack Fraser, who has made my time in the office pleasant and intellectually stimulating. Though I could not always digest his elaborate jokes, especially when combined with his rapid utterance, I enjoyed every conversation with him.

I am deeply indebted to my colleague and collaborator Jennifer Friske for her initiative work on the slowing bar without which this thesis has ended up nowhere. I look forward to our lifelong friendship and collaboration.

Many thanks to all the other members of the Oxford Galactic Dynamics group, past and present, including Payel Das, Douglas Bougbert, Chengdon Li, Amery Gration, Dominic Dootson, Tjarda Boekholt, Taras Panamarev, and Bence Kocsis for everyday conversation and stimulating discussions on Monday meetings.

I am also grateful to Jun Lau, Kit George, and Daisuke Kawata at the Mullard Space Science Laboratory for their friendship and creative discussions.

My life in Oxford has been made busy with enjoyable events thanks to the friends I met in Linacre College, in particular the members of the Ursula Hicks House. I miss our potluck dinners and the late-night bull sessions.

This study was not made possible without the financial support from the Takenaka Scholarship Foundation, for which I am truly grateful. I thank the staffs for their hospitality during my visits.

Finally, I thank my family for their unqualified support. In particular, I owe my wife Natsu for her immense effort to move to the UK and for her endless care and encouragement during my studies. She has made my life full of joy and happiness, even in the midst of the pandemic. I look forward to welcoming together the new coming life into this beautiful and mysterious Universe.

Table of contents

CHAPTER 1

Introduction

Numerous astronomical observations point towards the existence of a substantial amount of *dark matter* in the universe. Dark matter is required to gravitationally hold galaxies and galaxy clusters together but has so far eluded direct detection via electromagnetic, strong, or weak interaction. Despite decades of intensive research, the nature of dark matter and even its fundamental kinematic properties remain unknown.

The aim of this thesis is to open a new way to constrain the kinematics and nature of dark matter using the galactic bar as a dynamic probe. By breaking axisymmetry and time symmetry, a rotating galactic bar gravitationally perturbs the surrounding dark matter. This results in a counteraction on the bar known as *dynamical friction*, which makes the bar slow and grow. The spin-down of the bar thus informs us about the existence of dark matter as well as its dynamical nature. We propose a novel method to for the first time quantify the deceleration of the Galactic bar from the fossil records imprinted on the resonant phase space of the outer stellar disk. We apply our method to the latest *Gaia* data and demonstrate that the Galactic bar has indeed been slowing down. This new dynamical evidence for dark matter differs fundamentally from previous evidences in that it measures the *inertial mass* of dark matter rather than its *gravitational mass*, thus precluding the possibility to be accounted for by modifying the laws of gravity.

In this introduction, we first briefly summarize the existing evidence for dark matter. We then describe the general strategy of our new approach. In section 1.3, we introduce galactic bars, featuring their dynamical structure, their formation mechanism, and most importantly, their different evolutionary path in dark matter models and in modified gravity

models. In section 1.4, we discuss how the bar's slowing history can be deciphered from local stellar kinematics. We describe the key points and summarize our main findings. We end this chapter with an overview of the thesis (section 1.5).

1.1 Current evidence for dark matter

One of the first implications for the existence of dark matter was provided by Zwicky (1937). Zwicky argued that determining the mass of galaxy clusters from their luminosity is unreliable and proposed three alternative methods, based respectively on the virial theorem, gravitational lensing, and statistical mechanics. While the latter two did not allow him to get actual numbers, the first was successfully applied to the Coma cluster of galaxies, yielding a mass much larger than that expected from its luminosity. From this result, he concluded that the majority of matter in the Coma cluster is dark (although by 'dark' he only meant cold stars and gases, and not an unknown matter).

Later, dark matter was also found in individual galaxies when astronomers were measuring the galaxies' rotation curve. A rotation curve describes the speed of a circular orbit at the galactic equator as a function of radius. It represents the axisymmetric component of the gravitational potential at the galactic plane and hence provides constraints on the galaxy's mass distribution. The first sign of anomalies in galactic rotation was reported by Babcock (1939) who used a spectrograph to measure the rotation curve of the Andromeda Galaxy and discovered that it tends to become flat at large radii, as opposed to a declining profile expected from the distribution of the luminous matter. Thereafter, rotation curves were measured extensively by several groups, including Rubin & Ford (1970), although most measurements were restricted to the optical region, making the large uncertainty in the mass-to-light ratio difficult to conclude whether dark matter really exists or not. Using the 21 cm line, Roberts & Whitehurst (1975) showed that the flat rotation curve of the M31 extends up to 30 kpc, almost twice the extent of the optical curve. The presence of dark matter became conclusive by the PhD thesis of Bosma (1978) who observed and compiled 21 cm rotation curves for 25 galaxies, all but a few showing

surprisingly flat curves at the outer disk. His results made clear that a substantial mass is present even beyond the optical galaxy.

A similar dynamical evidence has been provided by the X-ray observations of the intracluster medium (ICM), a hot plasma pervading galaxy clusters. If the ICM is in hydrostatic equilibrium, its thermal pressure should balance with gravity. The X-ray measurement of galaxy clusters suggests that the ICM is too hot such that its mass alone, which well surpasses that of the stars, is far less than the mass required to gravitationally hold itself together (e.g. Vikhlinin et al., 2006).

Dark matter has also been mapped directly by gravitational lensing, an idea already considered by Zwicky back in the 1930s. Light emitted from a distant source bends as it passes near a massive dark halo, so the distorted image of a background object informs us about the distribution of the dark matter. This method has the benefit that it does not require dynamical assumptions about the system and can probe the gravitational potential beyond the radius of the visible matter. dell'Antonio & Tyson (1996) analysed the weak lensing effect on a large number of background galaxies and found that the foreground galaxies have on average a mass-to-light ratio of roughly 10, again implying the presence of dark matter.

With the advent of large surveys (e.g. 2-degree Field Galaxy Redshift Survey, Sloan Digital Sky Survey) and large cosmological simulations (e.g. Springel et al., 2005), it became evident that dark matter plays an indispensable role in the formation of the large-scale structure of the universe. Without the gravity of dark matter, ordinary matter would not have coalesced to form galaxies early enough to explain the current distribution of the galaxies. The Lambda cold dark matter (ΛCDM) model, that postulates a cosmological constant Λ and a cold dark matter, successfully describes the observed large-scale structure and has now become the standard model of cosmology.

Last but not least, the anisotropies in the cosmic microwave background (CMB) radiation provide another powerful evidence of dark matter. The angular power spectrum of the CMB shows a series of acoustic peaks that can be precisely fitted by the ΛCDM model. The result predicts that approximately 84% of the total amount of matter in the universe is in the form of dark matter (Planck Collaboration et al., 2020).

1.2 New strategy to probe dark matter

Despite the several implications, dark matter has not yet been detected by any means other than their gravitational effect. For this reason, there have been persistent attempts to account for the observed gravitational anomaly instead by modifying the laws of gravity, thereby removing the need for any additional mass. One of the first and most successful theories is the Milgrom's modified Newtonian dynamics (MOND, Milgrom, 1983), which postulates that the Newton's law of gravity breaks down in the regime of small acceleration. MOND and its relativistic generalization (Bekenstein, 2004) have made partial success in explaining some of the observations, although none has so far explained all observations consistently (Famaey & McGaugh, 2013). Nevertheless, so long as the evidence for dark matter comes only from their gravitational mass, modified gravity will remain a viable alternative.

Therefore, a key step towards identifying dark matter is to find a new type of evidence that (i) cannot be accounted for by modified gravity models and (ii) depends on the nature and kinematic state of dark matter rather than only on their spatial distribution.

The sole such evidence to date is the observation of the Bullet Cluster, a collision between two clusters of galaxies. While the collisional ICM would be slowed by ram pressure, the collisionless stars and dark matter would be less affected and would therefore be spatially separated from the ICM. Clowe et al. (2006) mapped the mass distribution of the two merging clusters using weak gravitational lensing and found concentrations of dark matter that were evidently offset from the ICM. However, this has been opposed by Brownstein & Moffat (2007) who claimed instead that modified gravity is *required* to explain the observations. The discussion is thus yet inconclusive.

In this thesis, we provide a novel dynamical evidence of dark matter that is in strict tension with alternative gravity theories. The principal idea is to detect a transfer of energy and momentum from ordinary matter to dark matter via their gravitational interaction. In particular, any massive stellar object moving or rotating in the dark halo will deposit net energy and momentum to the surrounding dark matter and hence experience a retarding force, a phenomenon generally referred to as dynamical friction (Chandrasekhar, 1943).

Dynamical friction by the dark halo cannot be explained by modified gravity theories, unless they violate conservation of energy and momentum in a peculiar manner.

It is important to note that dynamical friction *per mass* is in fact stronger in MOND since the gravitational interaction is enhanced in the low acceleration regime (Ciotti & Binney, 2004; Nipoti et al., 2008). However, this difference is in most cases overwhelmed by the difference in the total amount of mass required in MOND and in Newtonian systems. Hence, MOND without dark matter generally predicts a significantly reduced dynamical friction (Tiret & Combes, 2007; Combes, 2014).

There are two substructures in galaxies that evolve under the strong influence of dynamical friction: (i) satellite galaxies orbiting around the host galaxy (e.g. Tremaine et al., 1975; White, 1983; Bontekoe & van Albada, 1987) and (ii) galactic bars rotating at the galactic centre (e.g. Weinberg, 1985; Athanassoula, 1996; Debattista & Sellwood, 2000).

In the former case, dynamical friction causes satellite galaxies to spiral in to the centre of the halo, while being tidally stripped of their mass. While many satellite galaxies have been observed and extensively modelled, it has proven difficult to constrain their orbital histories, since they could have followed a wide range of trajectories depending on their initial mass as well as their initial orbital parameters (e.g. Jiang & Binney, 2000; Dierickx & Loeb, 2017). For example, the orbit of the Sagittarius dwarf galaxy, the most well-studied satellite in the Milky Way, can be explained equally well in MOND and in dark matter models (Read & Moore, 2005). Therefore, at the current stage, modelling of satellite galaxies cannot eliminate the possibility of MOND let alone constrain the nature of dark matter.

Galactic bars, on the other hand, directly leave traces of their evolutionary histories in the kinematics and chemistry of the outer stellar disk. Specifically, this thesis will show that the spin-down history of the bar is imprinted inside the phase space of stars resonantly trapped by the bar. Thanks to the recent *Gaia* survey (Gaia Collaboration et al., 2018), which has for the first time measured the phase-space coordinates of a billion stars in our Galaxy, the bar's evolutionary history can now be uncovered.

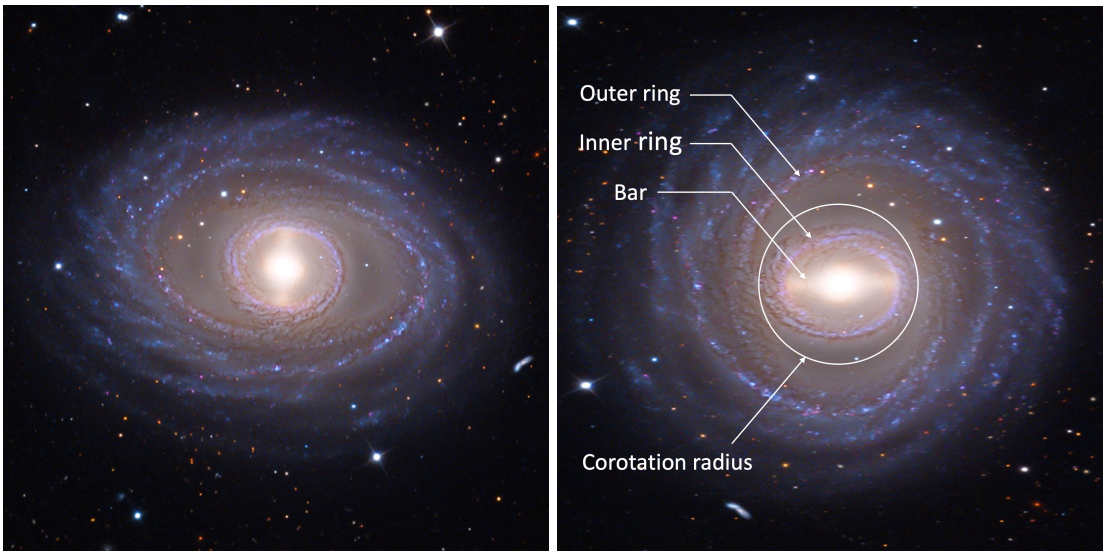

Fig. 1.1 Left panel: Barred spiral galaxy NGC 1398 (Credit: Mount Lemmon Observatory). Right panel: Same image rotated and rescaled to deproject the galaxy. The central bar is surrounded by an inner ring and an outer ring. Between the two rings lies the corotation radius.

1.3 Galactic bars

Galactic bars are linear stellar structures frequently observed at the centres of spiral galaxies. About 40-50% of nearby disk galaxies are barred in the optical (e.g. Sellwood & Wilkinson, 1993; Barazza et al., 2008; Aguerri et al., 2009) and another 10-20% are barred when observed in near-infrared (Eskridge et al., 2000; Marinova & Jogee, 2007; Buta et al., 2015).

We know beyond reasonable doubt that our Milky Way Galaxy is also barred. Evidence comes from (i) the gas kinematics in the inner Galaxy (e.g. de Vaucouleurs, 1964; Binney et al., 1991; Sormani et al., 2015b), (ii) the infrared surface brightness of the bulge region (e.g. Blitz & Spergel, 1991; Weiland et al., 1994; Wegg et al., 2015), and (iii) the longitudinal asymmetries in the distribution of red giants (e.g. Nakada et al., 1991; Weinberg, 1992; Stanek et al., 1994).

Figure 1.1 shows an image of a typical barred spiral galaxy, NGC1398. The bar is the linear structure extending across the centre of the disk. The bar is surrounded by an inner ring elongated parallel to the bar and an outer ring stretched perpendicular to the bar (Buta & Combes, 1996). The two rings are separated by the crescent-shaped regions at the

bar's corotation radius. These rings form naturally in response to the bar's perturbation, although their appearance differs among galaxies: some barred galaxies have a prominent double-ring structure, while in others, rings can be misaligned, broken (pseudo-rings), or indistinguishable from spiral patterns.

1.3.1 Dynamical structure of barred galaxy

Before describing the evolution of bars in different dark matter models and modified gravity theories, we will dip briefly into the basic dynamical structure of a barred galaxy which is best understood in terms of the closed orbits (Contopoulos & Grosbol, 1989). These orbits close in the frame rotating with the bar and, if stable, represent families of non-closed orbits that librate around them[1]. Thus, they are often described as the backbone of the dynamical structure of galaxies. In a realistic axisymmetric potential, the only stable closed orbits are the circular orbits. In a barred potential, these circular orbits are deformed into slightly elongated closed orbits. In addition to these main closed orbits, the broken axial symmetry gives rise to a new family of stable closed orbits that are exactly in resonance with the bar. For orbits confined to the galactic mid-plane (i.e. 2D in-plane orbits), resonances occur when

$$N_R\Omega_R + N_\varphi(\Omega_\varphi - \Omega_\mathrm{p}) = 0, \quad (N_R, N_\varphi) \in \mathbb{Z}^2, \tag{1.1}$$

where Ω_R and Ω_φ are the radial and azimuthal frequencies, while Ω_p is the bar's rotation frequency referred to as the *pattern speed*. These resonant orbits complete N_φ radial oscillations while orbiting around the bar N_R times. Since the potential of the bar is dominated by a quadrupole, resonances with $N_\varphi = 2$ are especially important in barred dynamics. Namely, they are the inner Lindblad resonance (ILR, $N_R = -1$), the corotation resonance (CR, $N_R = 0$), and the outer Lindblad resonance (OLR, $N_R = 1$).

Figure 1.2 shows closed orbits that are stable, prograde, and do not belong to the sequence of high-order resonances ($N_\varphi > 2$). Here, the bar is placed along the x-axis and the radii of the three main resonances are marked with blue circles. Also plotted are

[1] In some literature (e.g. Contopoulos & Grosbol, 1989), the non-closed orbits surrounding the closed orbits are described as 'trapped'. This is not to be confused with the resonantly trapped orbits. In this thesis, 'trapped orbits' always refers to the latter, following the nomenclature of Binney & Tremaine (2008).

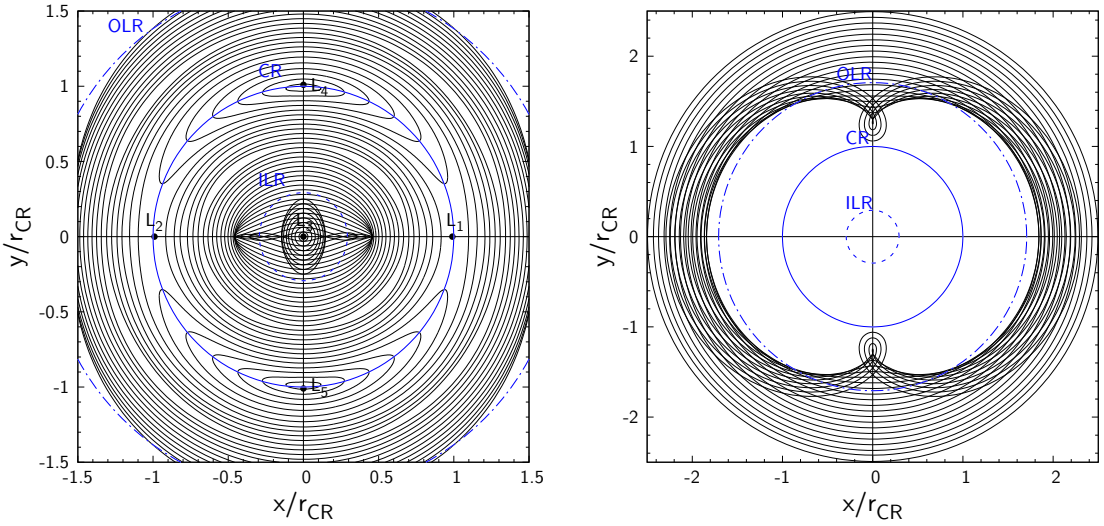

Fig. 1.2 Stable closed orbits in a barred potential where the bar lies along the x-axis. Left panel shows orbits within the OLR (dot-dashed), while right panel shows those beyond it. Sequences of retrograde orbits and high-order resonant orbits ($N_\varphi > 2$) are omitted. The three blue circles show the radius of the ILR (dashed), CR (solid) and OLR (dot-dashed), respectively.

the Lagrange points, which are the stationary points of the galaxy's effective potential $\Phi_{\rm eff}(\boldsymbol{x}) = \Phi(\boldsymbol{x}) - \frac{1}{2}\Omega_{\rm p}^2 R^2$: $L_{1,2}$ are the saddle points, L_3 is the central minimum, and $L_{4,5}$ are the maxima. The Lagrange points $L_{1,2,4,5}$ all exist close to (but not exactly at) the corotation radius.

The main family of orbits building the bar is the so-called x_1 sequence, elongated parallel to the bar within the corotation radius (Contopoulos, 1979). Because orbits spend more time near apocentre than pericentre, these x_1 orbits all contribute to the concentration of mass along the bar's major axis (x-axis). Inside the ILR, there exists the x_2 sequence, which is anti-aligned with the bar and therefore works against the bar's potential. Similarly, beyond the CR, the stable closed orbits become perpendicular to the bar. This implies that self-consistent bars can exist only inside the corotation radius (Contopoulos, 1980).

The shapes of the inner and outer rings naturally follow these stable closed orbits (e.g. Schwarz, 1984): the near circular orbits below the CR trace the inner rings, while orbits outside the CR form the outer rings. There are, however, a series of higher-order resonances piling up towards the CR which may also contribute in shaping the rings (Patsis et al., 2003).

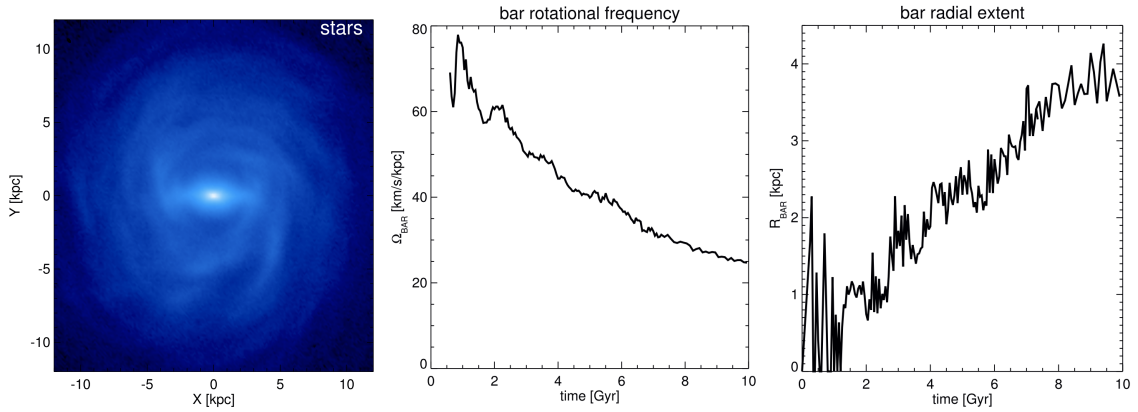

Fig. 1.3 *N*-body+SPH simulation of a barred galaxy evolving inside a live dark matter halo (from Aumer & Schönrich, 2015). Left panel shows the stellar surface density after 7.3 Gyr, while middle and right panels show the bar's pattern speed and length as a function of time. The bar slows down by transferring angular momentum to the dark halo while growing in length by incorporating surrounding stars into the bar region.

The stable closed orbits are also important in gas dynamics since these are the orbits which gas is supposed to follow. Particularly important are the x_1 orbits at the ILR that self-intersect. Since gas flow cannot intersect, gas flowing along these orbits forms dissipative shocks which allow them to sink towards the galactic centre (Athanassoula, 1992; Sormani et al., 2015a). The gas is driven down to the nuclear region, where it moves on the x_2 orbits and forms nuclear rings/disks (Regan & Teuben, 2004a).

The most important structure relevant to this thesis is the two large crescent areas near the corotation radius, which are filled with closed orbits resonantly trapped by the bar. These structures are also clearly visible in the image of NGC 1398 (Figure 1.1). Orbits trapped in the CR do not circulate around the bar, but instead slowly librate about the stable Lagrange points $L_{4,5}$, similarly to the trojan asteroids corotating with Jupiter. The CR is the strongest resonance among all and, as we will see, plays a major role in (i) shaping the kinematics and chemistry of the Solar neighbourhood stars (chapter 2,3) and (ii) exerting dynamical friction on the bar (chapter 4).

1.3.2 Formation of barred galaxy

How do bars form in the first place? From *N*-body simulations, bar formation has been known to be an almost inevitable consequence of disk instability (e.g. Hohl, 1971), but its

theoretical explanation has been rather phenomenological, as it proceeds through several stages which range from linear to highly non-linear regimes. The basic mechanism is understood as follows (Binney & Tremaine, 2008; Sellwood, 2014): In the linear regime, self-gravitating cold disks are globally unstable against non-axisymmetric modes (Kalnajs, 1972), which results in the formation of weak spiral patterns. These spiral waves then grow by successive amplifications at corotation and reflections at the galactic centre (Toomre, 1981). The feedback loop continues until non-linearity kicks in: as the perturbation strengthens, more orbits get trapped into the ILR, where they gain eccentricity and are forced to precess coherently by self-gravity, thereby forming a self-consistent bar (Lynden-Bell, 1979; Earn & Lynden-Bell, 1996). This bar-formation instability sets off spontaneously, although it can also be triggered by tidal perturbation from merging or passing satellites (e.g. Noguchi, 1987).

1.3.3 Evolution of barred galaxy – dark matter vs. modified gravity

The evolution of bars after formation depends critically on the existence and nature of dark matter. If galaxies are embedded in live (responsive) dark matter halos, bars inevitably slow down due to dynamical friction. Figure 1.3 shows an example of the bar's evolution in a self-consistent N-body+hydrodynamic simulation with a live dark halo (Aumer & Schönrich, 2015). Apart from small jitters, the bar spins down steadily (middle panel) while growing in length (right panel). This behaviour is predicted theoretically (e.g. Weinberg, 1985; Little & Carlberg, 1991) and has been confirmed widely in various numerical simulations (e.g. Athanassoula, 1996; Debattista & Sellwood, 2000).

This long-term deceleration of the bar is a characteristic behaviour which we expect only if dark matter exist. This is clarified in the left panel of Figure 1.4 from Tiret & Combes (2007) who compared the evolution of bars in a live dark halo with that in MOND and in an analytical (non-responsive) dark halo: if dark matter does not exist (red) or if they are non-responsive (blue), the bar will not spin down, simply because there is not enough matter to deprive angular momentum from the bar[2]. This conclusion holds also

[2]We note that dynamical friction on bars in MOND can be stronger than that in Newtonian equivalent systems if bars have unrealistically small mass (less than 5% of the total baryonic mass, Ciotti & Binney, 2004; Nipoti et al., 2008).

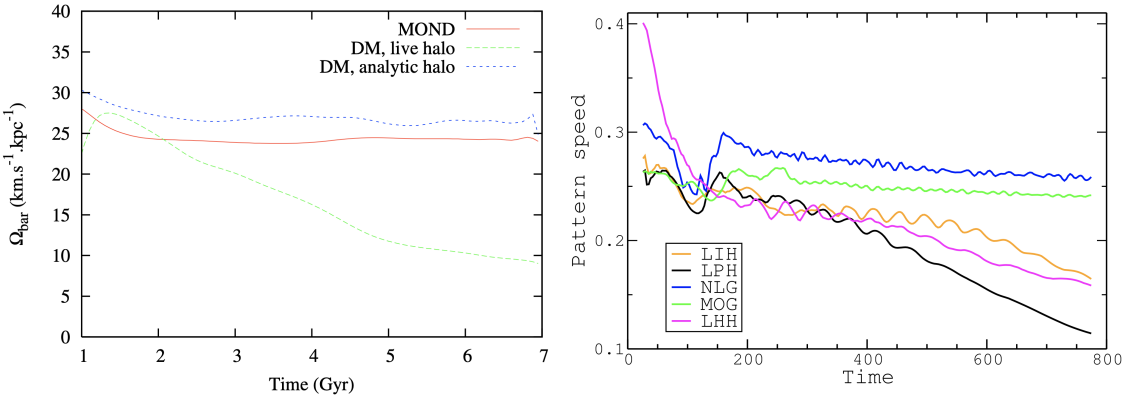

Fig. 1.4 Left panel: Comparison of the evolution of the bar's pattern speed in live or analytic dark halo and in classical MOND (from Tiret & Combes, 2007). Right panel: Comparison of bar evolution in live dark halos with various density profile (LIH, LPH, LHH) and in two modified gravity theories (NLG, MOG) (from Ghafourian et al., 2020). In their model, a unit time amounts to 10 Myr when scaled to the Milky Way. Both studies show that bars only spin down in the presence of a live/responsive dark matter.

for different theories of modified gravity: the right panel of Figure 1.4 from Ghafourian et al. (2020) shows that bars evolving in non-local gravity (blue, NLG, Hehl & Mashhoon, 2009) and scalar-tensor-vector gravity (green, MOG, Moffat, 2006) keep their pattern speed almost constant, while the same bar rotating in a live isothermal (orange, LIH), Plummer (black, LPH) or Hernquist (pink, LHH) halo show considerable deceleration. Bars in modified gravity can still transfer angular momentum to the outer stellar disk and to the stellar halo, but because the mass there is limited, they only slow down by at most 10% within their lifetime. Bars can similarly exchange angular momentum with the gas, although they will more likely to *gain* net angular momentum by driving the gas towards the galactic nuclei (Berentzen et al., 2007; Athanassoula et al., 2013). These studies therefore imply that detecting a substantial drop in the bar's pattern speed will provide strong evidence for the existence of dark matter.

More importantly, measuring the bar's slowing rate will enable us to constrain the large-scale quantum properties of dark matter. For instance, if dark matter forms a Bose-Einstein condensate on a galactic length scale (e.g. repulsive or fuzzy/ultralight dark matter models, Goodman, 2000; Hu et al., 2000), dynamical friction on bars will be significantly reduced because the quantum fluctuation will smooth the density wake

lagging behind the bar (Hui et al., 2017; Lancaster et al., 2020). Similarly, halos made of degenerate fermionic dark matter, which form degenerate cores in the inner galaxy by the Pauli exclusion principle (e.g. Destri et al., 2013), are expected to be less responsive against the bar's perturbation and hence exert weak friction on the bar. Therefore, these dark matter models with different dynamical properties can be tested by computing the bar's slowing rate and challenging it with the observed value.

In the classical CDM paradigm, the bar's slowing rate will place constraints on the kinematics of the dark halo. In particular, the halo's net rotation (angular momentum vector) and velocity anisotropy are important parameters that crucially affect the strength of dynamical friction on the bar (e.g. Saha & Naab, 2013; Long et al., 2014; Sellwood, 2016). The dark halo's kinematics is significant not only to understand its formation history, but also to predict the velocity distribution of dark matter passing through the Earth. The latter is essential to determine the properties of the candidate particles (e.g. mass) from direct-detection experiments (e.g. Marrodán Undagoitia & Rauch, 2016).

1.4 Deciphering bar evolution from local stellar data

In spite of its importance, the deceleration of galactic bars has remained a pure theoretical prediction, lacking any observational proof.

There have been some claims that bars in external disk galaxies have *not* slowed down because the majority are observed to be *fast*, in the sense that their corotation radius lies not far from the end of the bar (e.g. Aguerri et al., 2003; Cuomo et al., 2020). This argument postulates that the ratio between the corotation radius and the bar length ($\mathcal{R} \equiv R_{\rm CR}/R_{\rm b}$) increases as bars slow down. However, in simulations of a single barred galaxy, bars typically grow while slowing down and hence the ratio $\mathcal{R}$ is kept roughly constant (e.g. Debattista & Sellwood, 2000; O'Neill & Dubinski, 2003; Martinez-Valpuesta et al., 2006; Aumer & Schönrich, 2015; Collier et al., 2018). In these simulations, $\mathcal{R}$ increases significantly only after bars reach the outskirts of the disk and cease growing (Villa-Vargas et al., 2009; Athanassoula, 2014a). Therefore, the observational fact that most bars are fast ($\mathcal{R} < 1.4$), and that $\mathcal{R}$ has no statistical correlation with the galaxy's redshift (Pérez

et al., 2012) or Hubble type (Aguerri et al., 2015), can only set upper limits on the slowing rate of the bar (or alternatively on the age of the bar). Debattista & Sellwood (1998, 2000) used this argument to conclude that, for bars to remain in the fast regime, the mass of the inner galaxy must be dominated by the disk (the *maximum disk model*). In cosmological simulations (e.g. IllustrisTNG, EAGLE), however, bars are predicted to have large $\mathcal{R}$ despite them not exceeding the size of the disk (e.g. Roshan et al., 2021). Frankel et al. (2022) showed that the distribution of the bar's pattern speed in IllustrisTNG is consistent with observation while the predicted bar length is systematically shorter than that in real galaxies. Why bars in cosmological simulations fail to grow is still unclear. It may be due to the limited mass resolution, the too-large softening length, or the perturbations by subhalos, which are typically not considered in isolated barred galaxy simulations. In any case, the $\mathcal{R}$ parameter alone cannot provide evidence for the bar's deceleration.

To decipher the bar's evolutionary history from its present state, one needs to know more than just its shape and pattern speed. Fortunately, the bar's spin-down is not traceless: as bars slow, the location of their resonances sweeps outwards through the disk, making irreversible changes to the distribution of stars in phase space. Hence, the current phase-space distribution of the galaxy contains a wealth of information on the bar's past evolutionary history.

The only galaxy for which we can obtain the detailed stellar phase-space distribution is our own. The downside of observing our Galaxy is that its global distribution is difficult to map due to dust extinction. However, because the bar's main resonances (i.e. CR and OLR) lie close to the position of the Sun, the *local* phase-space distribution provides enough information to diagnose the bar's slowing process.

Measuring the precise positions and velocities of nearby stars is an age-old practice, dating back to Hipparchus (190-120 BC), who compiled one of the first comprehensive stellar catalogues. Recently, this field has been revolutionized by the *Gaia* satellite (Gaia Collaboration et al., 2018), which, in its second data release, provided high-precision positions, parallaxes, and proper motions for 1.3 billion stars and line-of-sight velocities for 7.2 million stars, enabling us to analyse the six dimensional phase-space distribution

over an extended spatial coverage. This measurement is already unprecedented both in quantity and quality, but the forthcoming third data release will soon expand this further.

What kinematic signatures would we expect in the local stellar data if the Galactic bar has been slowing down? This is the question we addressed in Chiba et al. (2021). As mentioned earlier, the decline in bar's pattern speed results in a movement of the resonances towards larger radii, where the stellar orbital frequencies are lower. For the untrapped orbits far from resonances, this merely results in a change in the amplitude of the perturbation: the perturbation grows as the resonance approaches and decays as the resonance moves away. However, when the untrapped orbits are swept by the resonance, they have a chance to become trapped. For these resonantly trapped orbits, the impact of the bar's slowdown is drastic – the moving resonances drag the trapped orbits towards the outer disk, while some resonances also enhance their eccentricity. A theoretical account for this *resonant dragging* effect will be given in Chapter 2.

When these resonantly trapped orbits are dragged to the Solar neighbourhood, they are observed as prominent stellar streams: Liouville's theorem ensures that the phase-space density along these dragged orbits is conserved, so the trapped phase-space must have a higher density than its surrounding if they have originated from the dense inner galaxy. As will be shown, this enables the bar's corotation resonance (CR) to produce a prominent peak in the local velocity space, which naturally explains the so-called *Hercules stellar stream*, a group of nearby stars with low angular momentum, heading radially outwards.

The origin of the Hercules stream has been a puzzle for decades where the discussion has centered mainly on the current pattern speed of the bar, which determines the positions of the resonances. Since the seminal work by Dehnen (1999b, 2000), the Hercules stream has been thought to be caused by the OLR of the bar with high pattern speeds $\Omega_\mathrm{p} \simeq 50 - 60\,\mathrm{km\,s^{-1}\,kpc^{-1}}$. This *fast bar model*[3], however, came into tension with the inner gas kinematics (e.g. Rodriguez-Fernandez & Combes, 2008; Sormani et al., 2015b) and modelling of the bar-bulge region (e.g. Long et al., 2013; Portail et al., 2017), which

[3]Confusingly, 'fast' bar in this context refers to a Galactic bar with high pattern speed $\Omega_\mathrm{p} \geq 50\,\mathrm{km\,s^{-1}\,kpc^{-1}}$ (an *absolute* measure), and is unrelated to the aforementioned 'fast' bar with small ratio between the corotation radius and bar length $\mathcal{R} = R_\mathrm{CR}/R_\mathrm{b} < 1.4$ (a *relative* measure). Discussions of fast/slow bar in this thesis will mostly concern the former, while we discuss the latter specifically in section 3.5.4.

preferred a much lower pattern speed $\Omega_{\rm p} \simeq 30-40\,{\rm km\,s^{-1}\,kpc^{-1}}$. Pérez-Villegas et al. (2017) partially resolved the tension by explaining the Hercules stream instead with the CR of a *slow bar model*. However, a slow bar with constant pattern speed had an issue that the phase-space density of the CR has too small contrast with that outside the resonance (e.g. Monari et al., 2017a; Fragkoudi et al., 2019). We show that resonant dragging by a slowing bar naturally solves this problem: if the bar has been slowing, the phase-space density of the CR will be significantly enhanced since the resonance captures stars at the inner disk with high phase-space density and then drags them outwards to the Solar neighbourhood. Combining our result with recent studies of the inner Galaxy, we then arrive at a consistent picture in which the Galactic bar is slow, long, and has been slowing down under the effect of dynamical friction by a typical dark halo.

We note, however, that several authors have proposed alternative models linking the Hercules stream with the high-order resonances of the bar (e.g. Hunt & Bovy, 2018; Asano et al., 2020), the perturbation by spiral arms (e.g. Hunt et al., 2019; Barros et al., 2020), or the impact of merging satellites (e.g. Khanna et al., 2019; Hunt et al., 2021). While these effects are no doubt important in shaping local kinematics, there are several reasons to believe that the Hercules stream is dominantly shaped by the CR of a slowing bar. These are the (i) spatial variation of Hercules, (ii) its chemical composition, and (iii) its internal resonant structure.

The spatial variation of the local stellar streams is one of the most significant structures that *Gaia* has for the first time measured (e.g. Antoja et al., 2018; Kawata et al., 2018). Friske & Schönrich (2019) showed that the angular momentum of each local stellar streams varies uniquely with Galactic azimuth. The Hercules stream shows a narrowing trend in the direction of rotation, i.e. towards the bar's major axis. This trend is consistent only with the CR, where the volume of trapping diminishes towards the unstable Lagrange points $L_{1,2}$ (Fig. 1.2). As we will show, the shape of the Hercules stream in the L_z-φ plane is in quantitative agreement with the CR of a slowing slow bar model.

The chemical composition of Hercules provides us with further evidence for its association with the bar's CR. Stars are not indistinguishable particles, but contain in their spectra rich information regarding their age and origin. In particular, the stellar metallicity implies

their birth place, as our Galaxy has a negative metallicity gradient in radius (Luck, 2018). It has long been known that the Hercules stream is significantly metal rich (Grenon, 1999), while its population is widely spread in age and elemental abundance ratios, suggesting that Hercules is not a dissolving open cluster (Kushniruk et al., 2020). This metal-rich non-coeval feature of Hercules is naturally explained with the slowing slow bar model where the CR has been capturing and dragging stars from the inner disk. In Chiba & Schönrich (2021), we have derived the metallicity of local stars using stellar isochrone models, and shown that the high-metallicity of Hercules can only be achieved by making the bar slow down.

We have further identified a more decisive and quantifiable evidence for a slowing bar in the internal structure of the resonance: when the bar slows down, the resonant phase-space migrates towards the outer galactic disk while simultaneously growing in volume. Liouville's theorem requires that this new volume is occupied by new stars captured along its path. Since these trapped stars adiabatically conserve a dynamical quantity called *libration action* J_ℓ, which characterizes the relative distance to the resonance center, the bar's resonance grows just like tree-rings, adding new layers of trapped stars at its surface. The order of capture is thus preserved inside the resonance: stars captured earlier at the inner disk are confined to the core of the resonance, while stars captured later at the outer disk are nearer to the surface of the resonance. By combining this growth mechanism with the Galactic metallicity gradient, where stars in the inner disk are more metal rich, we expect the bar's resonance to show a prominent metallicity increase towards the resonant center (i.e. small J_ℓ). In Chiba & Schönrich (2021), we have detected this tree-ring structure in the bar's corotation resonance (Hercules stream), thus proving the bar's slowdown.

The metallicity gradient inside the resonance further allows us to quantify the extent of bar slowdown. Since trapped stars must have been diffused by perturbation from giant molecular clouds and transient spiral arms, the current ordering inside the resonance only yields a lower limit on the distance the CR has travelled. With this in mind, we deduced from the observed metallicity gradient in J_ℓ that the bar's pattern speed has dropped at least $24 \pm 6\%$ since its formation. This is already in 2σ tension with modified gravity models, which predict only $\lesssim 10\%$ changes in bar pattern speed (Fig. 1.4). An even more

stringent constraint can be made by properly integrating the effects of stellar diffusion, although this is beyond the scope of the thesis.

As a by-product of the tree-ring analysis, we also obtained a precise measurement on the bar's current pattern speed $\Omega_\mathrm{p} = 35.5 \pm 0.8\,\mathrm{km\,s^{-1}\,kpc^{-1}}$. This is made possible by the uniqueness of the metallicity ordering in J_ℓ to the Hercules stream: the ordering will get lost even by a slight shift of the corotation resonance away from the Hercules. Our estimate is in excellent agreement with local kinematic models, which prefer $\Omega_\mathrm{p} = 35.2 \pm 1\,\mathrm{km\,s^{-1}\,kpc^{-1}}$ (Binney, 2020b), and with the latest made-to-measure models of the bar-bulge region, which predict $\Omega_\mathrm{p} = 33.29 \pm 1.81\,\mathrm{km\,s^{-1}\,kpc^{-1}}$ (Clarke & Gerhard, 2021).

A further investigation into the evolution of the trapped phase-space reveals that the tree-rings are in fact phase spirals that turn into rings when averaged over the libration angle (Chiba & Schönrich, 2022). This raises the possibility of directly inferring the age of the bar from the number of windings in the phase-spiral. These structures may be observed once we have enough data covering a large part of the bar's corotation resonance.

1.5 Thesis outline

The main part of this thesis is composed of three chapters 2-4, each corresponding to the following peer-reviewed papers: Chiba et al. (2021); Chiba & Schönrich (2021, 2022). Apart from minor corrections in texts, figures and equations, the content and conclusion are unchanged.

In Chapter 2, we start by introducing the *Gaia*'s observations, together with a short summary on the problem of modelling the data with a constantly rotating bar and how it can be resolved using a slowing bar. We then specify our model of the Galactic disk and bar, which we employ both to formulate the orbital response using classical Hamiltonian perturbation theory and to perform test-particle simulations. After reviewing the disk response against a constantly rotating bar, we demonstrate that a slowing bar resonantly drags the trapped orbits both in angular momentum and radial action as predicted analytically. We show that this results in a drastic change in the stellar kinematics throughout the disk. We also show that the degree of impact depends in large measure on

the slowing rate of the bar. Finally, by fitting our models to the *Gaia* data, we provide the first measurement of the bar's slowing rate. In the future, this measurement must be reassessed using an improved model, taking into account the 3D structure of the disk as well as the perturbations by spiral arms and merging satellites.

Chapter 3 studies the mechanism by which the trapped phase-space gets populated. We first show that, unless the bar weakens rapidly, the trapped phase-space always grows in volume as it migrates towards large angular momentum. This ensures that more orbits are captured than damped. We then demonstrate that, due to the conservation of the libration action, the trapped phase-space forms a layered structure, where metal-rich stars trapped earlier at the inner region of the galaxy are confined to the core of the resonance. To test our theory, we first derive the metallicity of local stars by fitting their colours and magnitudes with stellar isochrones. We calibrate our scheme with spectroscopic measurements of open clusters and find good qualitative agreement. By subtracting the age-dispersion and age-metallicity relations, which is reflected in the dependence of metallicity on radial action, we find that the bar's corotation resonance shows a prominent metallicity increase towards small libration action. We explore an extended range of bar parameters and show that this trend is unique to the Hercules stream, thus corroborating the slowing slow-bar model. We end by providing estimates on the bar's slowdown extent as well as its current pattern speed.

Having quantified the bar's slowdown in the previous chapters, Chapter 4 looks towards using the measurement to constrain the phase-space distribution of the dark matter halo. To this end, we have developed a theory of dynamical friction in the *slow limit* of bar evolution. Conventional theories of dynamical friction are formulated based on the linear approximation, which are only valid for a few dynamical periods or in the so-called *fast limit* (i.e. for rapidly slowing bars) where nonlinear effects are evaded by limiting the time for resonant interaction. Given the observational implication for resonant trapping by the Galactic bar, this theory needs to be extended to the slow/nonlinear regime in order to be applicable for realistic barred galaxy evolution. Chapter 4 begins with specifying the issue of conventional linear theories, and then formulates the torque in the slow limit (i.e. constant bar pattern speed) using the resonant angle-action coordinates. We calculate

the nonlinear response of the halo's distribution function near resonances and find theory and simulation in good agreement. The resulting dynamical friction is also well modelled. We also discuss the accuracy of our formalism when resonances overlap, resulting in the onset of chaos. Finally, we numerically study the phase-space response in the general slow regime.

In Chapter 5, we give our concluding remarks and summarize the area for improvement. We discuss our findings in a broader context and indicate future directions.

CHAPTER 2

Resonance sweeping by a decelerating Galactic bar

2.1 Abstract

In this chapter, we provide the first quantitative evidence for the deceleration of the Galactic bar from local stellar kinematics in agreement with dynamical friction by a typical dark matter halo. The kinematic response of the stellar disk to a decelerating bar is studied using secular perturbation theory and test-particle simulations. We show that the velocity distribution at any point in the disk affected by a naturally slowing bar is qualitatively different from that perturbed by a steadily rotating bar with the same current pattern speed Ω_p and amplitude. When the bar slows down, its resonances sweep through phase space, trapping and dragging along a portion of previously free orbits. This enhances occupation on resonances, but also changes the distribution of stars within the resonance. The decelerating bar model reproduces with its corotation resonance the offset and strength of the Hercules stream in the local velocity space (radial v_R vs. azimuthal v_φ) and the double-peaked structure of mean radial velocity $\bar{v}_R$ plotted over the angular momentum L_z and Galactic azimuth φ. At resonances other than the corotation, resonant dragging in angular momentum is accompanied with an increase in radial action, leading to multiple resonance ridges in the action plane as identified in the *Gaia* data. This work shows models using a constant bar pattern speed likely lead to qualitatively wrong conclusions. Most importantly we provide a quantitative estimate of the current slowing rate of the bar

$\dot{\Omega}_{\rm p} = (-4.5 \pm 1.4)\,{\rm km\,s^{-1}\,kpc^{-1}\,Gyr^{-1}}$ with additional systematic uncertainty arising from unmodelled impacts of e.g. spiral arms.

2.2 Introduction

2.2.1 Slowing bar as probe for dark halo kinematics

As discussed in Chapter 1, galactic bars spinning inside dark matter halos experience angular momentum loss due to dynamical friction and hence slow down. This implies that any observational evidence for the slowdown of the bar will serve as an evidence for the existence of a live (responsive) dark matter. Furthermore, while the density distribution of the dark halo can be mapped from its gravitational potential (e.g. Iocco et al., 2011; Cole & Binney, 2017), its kinematic state is only accessible by dynamical modelling, making (if measured) the slowing rate of the bar $\dot{\Omega}_{\rm p}$ an important constraint for the nature of dark matter.

Our best bet to trace the bar's slowdown is the stellar kinematics in the Solar neighbourhood with full 6D phase space information. Motions of local stars are known to be strongly affected by the bar's gravitational perturbation, especially near resonances, i.e. when stellar orbital frequencies are in commensurable relation with the bar's pattern speed. As the bar decelerates, the resonance regions sweep through the stellar phase-space, trapping and dragging a number of orbits, leaving noticeable changes in the stellar distribution. Therefore the current local kinematics can be used as archaeological evidence to probe the evolutionary history of the bar (Weinberg, 1994). However, most past studies attempting to fit the stellar streams in the Solar neighbourhood use a static bar with constant $\Omega_{\rm p}$ (e.g. Dehnen, 2000). One exception is a notion of a suddenly formed, very young bar (albeit still with a constant $\Omega_{\rm p}$), which would leave some transient effects lingering in stellar kinematics (Minchev et al., 2010). However, such a young age appears not fully in line with the low relative star-formation rates in the Milky Way's nuclear disk. Fux (2001) attributed little importance to the effects of a slowing bar, claiming that it mainly introduces a delayed response.

In contrast, we will show that the bar's slowdown has a profound impact on the kinematics of the Solar neighbourhood stars. In the next subsection, we summarize the local kinematic substructures observed by *Gaia*, which has been used in the past to judge the pattern speed and strength of the Galactic bar. We will also provide a first glimpse of how much a slowing bar model differs from the predictions of a constant Ω_p model with otherwise identical parameters. We will list the main observable features explained by the slowing bar model, which in turn provide us with the leverage to estimate the current $\dot{\Omega}_\mathrm{p}$. At the end of Section 2.2.2, we give an outline of this chapter.

2.2.2 Kinematic structure of the Solar neighbourhood

The top row of Fig. 2.1 shows the kinematic substructure revealed by *Gaia* DR2 (Gaia Collaboration et al., 2018) with parallax offset and distance derivation from Schönrich et al. (2019). We identify the 2D in-plane structure in three different statistics:

1. Left-hand panel: Velocity distribution $f(v_R, v_\varphi)$ of local stars showing substructures which have long been suspected to be caused by resonances with non-axisymmetric components of the Galaxy (e.g. Kalnajs, 1991). In particular, the large sub-population seen at low v_φ and positive v_R, known as the Hercules stream, has been extensively modelled with bar resonances (e.g. Dehnen, 2000).

2. Middle panel: Distribution in the action plane $f(J_\varphi, J_R)$ estimated in an axisymmetric logarithmic potential, which was first identified by Sellwood (2010) (using data from the Geneva Copenhagen survey) to show structures along the resonant lines and more recently been used by works on *Gaia* DR2 (e.g. Trick et al., 2021).

3. Right-hand panel: Mean radial velocity $\bar{v}_R$ plotted over the angular momentum L_z and Galactic azimuth φ. *Gaia*'s large-scale coverage permitted the first probe into the spatial dependence of the kinematic structure. Each stripe shows a different azimuthal dependence, indicating a distinct origin (Friske & Schönrich, 2019).

With this phase space information, one should in principle be able to identify the positions of resonances with the bar and thus predict the bar's pattern speed. Yet this

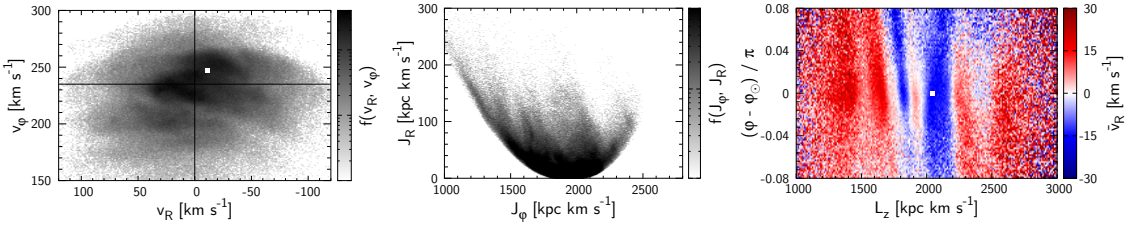

(a) Local kinematics observed by *Gaia* DR2.

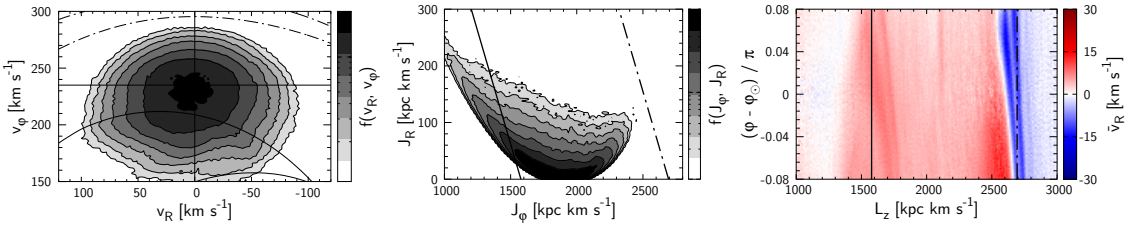

(b) Test-particle simulation with a steadily rotating bar.

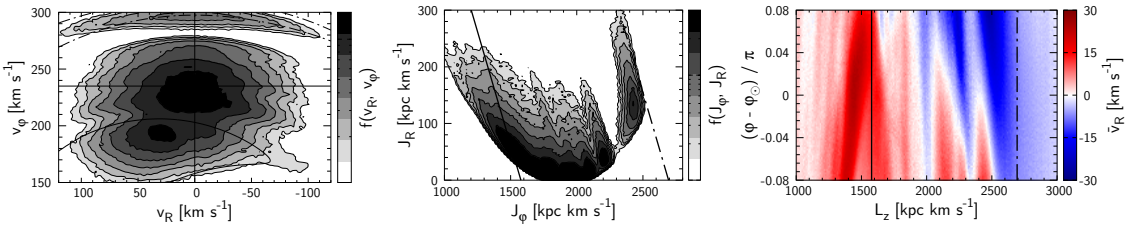

(c) Test-particle simulation with a slowing bar.

Fig. 2.1 Top panel: Kinematic data from *Gaia* DR2 with quality cut on parallax of $p/\sigma_p > 5$. For the distribution in velocity space (left) and action space (middle), we restrict the samples to heliocentric distance $s < 0.3\,\mathrm{kpc}$. The small white square indicates the coordinate of the Sun (Section 2.3.1). Middle row: Test particle simulation of a constantly rotating quadrupole bar with pattern speed $\Omega_p = 35\,\mathrm{km\,s^{-1}\,kpc^{-1}}$. Solid lines mark the corotation resonance, dashed lines the outer Lindblad resonance. Bottom row: Test particle simulation of a *rapidly* slowing bar presented in 2.5.2. Snapshot taken at $\Omega_p = 35\,\mathrm{km\,s^{-1}\,kpc^{-1}}$. Apart from the deceleration, the bar parameters are identical to the constant pattern speed model.

task is plagued by degeneracies. There are currently many possible models which can reproduce the observed features with different resonances. This has led to a major debate between proponents of a fast/short bar ($\Omega_p \gtrsim 50\,\mathrm{km\,s^{-1}\,kpc^{-1}}$) and a slow/long bar ($\Omega_p \lesssim 40\,\mathrm{km\,s^{-1}\,kpc^{-1}}$), where the debate has mainly concentrated on the cause of the Hercules stream: Fast bar proponents (e.g. Dehnen, 2000; Antoja et al., 2014; Fragkoudi et al., 2019) interpreted the Hercules stream as stars near the outer Lindblad resonance (OLR), which well matches the strength of the feature and the offset in v_R, though the required high pattern speed contradicts with the modelling of the bar/bulge using red clump stars (Portail et al., 2017) and studies on the inner gas dynamics (Sormani et al.,

2015b). Slow bar proponents (Pérez-Villegas et al., 2017; Binney, 2018; Monari et al., 2019a; D'Onghia & L. Aguerri, 2020) interpreted the Hercules stream as due to orbits trapped in the corotation resonance (CR). However, models with constant slow pattern speeds tend to underpredict the strength of the observed feature (or vice versa require a too strong bar).

In the middle row of Fig. 2.1, we present a test particle simulation for such a slow bar rotating with a constant $\Omega_\mathrm{p} = 35\,\mathrm{km\,s^{-1}\,kpc^{-1}}$ and reasonable strength fitted to the model of Sormani et al. (2015b) (see 2.3.2 for details). We mark the CR and the OLR in solid and dot-dashed lines. As mentioned above, the Hercules stream is underpredicted. The bottom row displays our slowing/elongating bar model with otherwise identical parameters. The deceleration of the bar increases the strength of the Hercules stream, as well as offsetting it towards larger v_R, in better agreement with the data. This difference is also indicated in N-body studies: With a steadily rotating bar, Fragkoudi et al. (2019) reported that the CR do not create a prominent feature in the Solar neighbourhood, while with a self-consistently slowing bar, D'Onghia & L. Aguerri (2020) confirmed a clear asymmetry in v_R at the CR akin to the Hercules stream. Our slowing bar model also produces strong resonance features of high order resonances in between the CR and the OLR as confirmed in the action plane (middle). We can also see in the $\bar{v}_R(L_z, \varphi)$ plane (right) that the CR appear as a spear-head structure which is identifiable in the *Gaia* data near $L_z \sim 1500\,\mathrm{kpc\,km\,s^{-1}}$.

We note, however, that perturbation by yet unconstrained spiral arms offers additional freedom in reproducing the data. Hunt et al. (2018) showed that repeated perturbation by transient spiral arms can reproduce the Hercules stream either with or without the presence of a bar, and Sellwood et al. (2019) showed how some of the structures in action-angle space can be linked with spiral arms. We also note that our work employs the simplest possible model for a slowing bar; we did not include higher-order modes of the bar which will enhance the signature of minor resonances (Monari et al., 2019a). Therefore, we do not aim at a model that accounts for all observed features, but rather to show the significant impact of the bar's deceleration.

The chapter is organized as follows. In Section 2.3, we introduce our slowing bar model and discuss resonant dragging effects using secular perturbation theory. Section 2.4

describes the method of our test-particle simulation. In Section 2.5, we start our discussion with a constantly rotating bar and subsequently explore the kinematic consequence of a slowing bar. Section 2.6 concludes.

2.3 Theory

2.3.1 Coordinate frame

Throughout the thesis, we take the position of an observer at the Galactic South Pole, thus using positive pattern speed. In our frame the radial velocity v_R points outwards, in contrast to the heliocentric radial velocity U. We use Galactic circular speed $v_c = 235\,\mathrm{km\,s^{-1}}$ (Reid et al., 2019), Solar Galactocentric radius $R_0 = 8.2\,\mathrm{kpc}$ (Gravity Collaboration et al., 2019), $\varphi_b - \varphi_\odot = 30°$ for the Sun's azimuthal angle with respect to the bar major axis φ_b (Wegg et al., 2015), and Solar velocity $(v_{R\odot}, v_{\varphi\odot} - v_c) = (-11.1, 12.24)\,\mathrm{km\,s^{-1}}$ in concordance with previous findings (Joshi, 2007; Schönrich et al., 2010; Schönrich, 2012; McMillan, 2017a). To make explicit the time dependence of $\Omega_p(t)$, we work in an inertial frame.

2.3.2 Model

We study orbits perturbed purely by a slowing bar. We thus neglect self-gravitational effects in our model and assume a logarithmic background potential corresponding to a constant circular speed v_c. We further simplify the discussion by restricting the model to 2D in-plane motion, and by modelling the bar as a $m = 2$ quadrupole, rotating like a rigid body (i.e. no flexing or winding up):

$$\Phi(R, \varphi, t) = \Phi_0(R) + \Phi_b(R, \varphi, t) = v_c^2 \ln(R) + \Phi_m(R, t) \cos m \left[\varphi - \int_0^t \mathrm{d}t'\ \Omega_p(t') \right], \qquad (2.1)$$

where $\Omega_p(t)$ denotes the time-dependent pattern speed and $\varphi_b = \int_0^t \mathrm{d}t' \Omega_p(t')$ expresses the current azimuth of the bar major axis (we choose $\Phi_m < 0$). In this thesis, m always refers to 2, although we retain the expression m to keep our discussion general and to avoid confusion with other factors of 2. Studies from N-body simulations (e.g. Aumer & Schönrich, 2015) imply that the bar's slowing rate $-\dot{\Omega}_p$ decreases with time, i.e. $\ddot{\Omega}_p > 0$. A reasonable model for the pattern speed is thus $\Omega_p(t) \propto t^n$, where $n < 0$. In approximation

to Aumer & Schönrich (2015), we choose $n = -1$, which corresponds to a linear increase in corotation radius R_{CR}. Therefore

$$\Omega_{\mathrm{p}}(t) = \frac{v_{\mathrm{c}}}{R_{\mathrm{CR}}(t)} = \frac{v_{\mathrm{c}}}{R_{\mathrm{CR}}(0) + v_{\mathrm{CR}} t}, \tag{2.2}$$

where v_{CR} is the velocity of the corotation radius. The bar's slowing rate is best described with the following dimensionless parameter:

$$\eta \equiv -\frac{\dot{\Omega}_{\mathrm{p}}}{\Omega_{\mathrm{p}}^2} = \text{const.} \tag{2.3}$$

Since we only consider the case where the bar is slowing down ($\dot{\Omega}_{\mathrm{p}} < 0$), η is defined to be positive. In our model with a flat rotation curve, η is $v_{\mathrm{CR}}/v_{\mathrm{c}}$, the dimensionless representation of v_{CR}.

A finite size of the bar implies that the amplitude of the quadrupole bar $\Phi_m(R, t)$ decays at large radii as R^{-3}. At small radii the bar's quadrupole must vanish as fast as R^2 to ensure the perturbed surface density to be azimuthally smooth at the origin. Thus we model the radial dependence of the bar as

$$\Phi_m(R, t) \propto \frac{R^2}{[R_{\mathrm{b}}(t) + R]^5}, \tag{2.4}$$

where $R_{\mathrm{b}}(t)$ is a scale length of the bar modelled to increase as the bar slows down. In concordance with Athanassoula (1992), we model $R_{\mathrm{b}}(t)$ such as to keep the ratio against the corotation radius constant:

$$b \equiv \frac{R_{\mathrm{b}}(t)}{R_{\mathrm{CR}}(t)} = \text{const.} \tag{2.5}$$

The strength of the perturbation is parametrized by the ratio of the maximum azimuthal force due to the bar and the radial force due to the unperturbed potential at the corotation radius R_{CR}:

$$A \equiv \frac{\left| \frac{1}{R} \frac{\mathrm{d}\Phi_{\mathrm{b}}}{\mathrm{d}\varphi} \right|_{R_{\mathrm{CR}}}}{\left| \frac{\mathrm{d}\Phi_0}{\mathrm{d}R} \right|_{R_{\mathrm{CR}}}}. \tag{2.6}$$

The amplitude of the bar potential then takes the following form:

$$\Phi_m(R, t) = -\frac{A v_{\mathrm{c}}^2}{m} \left[\frac{R}{R_{\mathrm{CR}}(t)} \right]^2 \left[\frac{b+1}{b + R/R_{\mathrm{CR}}(t)} \right]^5. \tag{2.7}$$

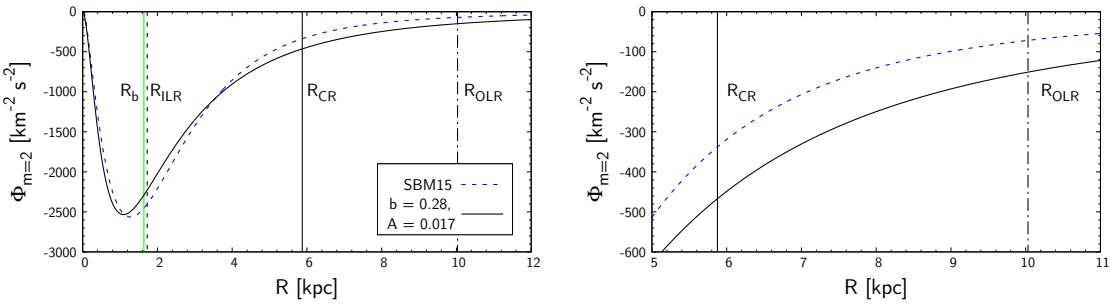

Fig. 2.2 Left panel: Amplitude of the quadrupole bar as a function of the Galactocentric radius R. Blue dashed curve is the most successful model reported in SBM15 and the black curve is our fitted model. Right panel zooms into the region near the CR and the OLR.

The choice of negative sign ensures alignment of $\varphi = \varphi_b$ with the bar's major axis (the potential minimum). Fig. 2.2 shows Φ_m where we fit our model to that of Sormani et al. (2015b, hereafter SBM15), which was constrained to reproduce the central Milky Way's gas flow pattern. In accordance with SBM15, we set $\Omega_p = 40\,\mathrm{km\,s^{-1}\,kpc^{-1}}$ corresponding to $R_{CR} = 5.875\,\mathrm{kpc}$ and fit the model via b and A. We note that our bar potential is significantly stronger near the OLR, and needs to be adapted when a quantitative fit of the resonance is required. The fitted value $b = 0.28$[1] is used for all simulations presented in this thesis. For the strength of the bar, we run simulations with a variety of values in the range $A \in [0.01, 0.03]$. In our slowing bar model, both b and A are kept constant while the bar slows down.

2.3.3 Review of linear perturbation theory

Orbits free of resonant trapping are well described by linear perturbation theory where any deviation from circular orbit is assumed to be small at the order of $\epsilon \sim \Phi_b/\Phi_0$ (see Binney & Tremaine 2008, pp.189-191 where the equation below is derived). Clearly, this assumption breaks down near resonances. Specifically, when the change in Ω_p per bar rotation period is sufficiently small, we obtain the following solution for the radius of an

[1]This value should not be identified with $\mathcal{R}$ (section 1.4), the ratio between R_{CR} and the length of the bar semimajor axis as reported in Athanassoula (1992).

orbit perturbed by the bar:

$$R(t) = R_\mathrm{g} + R_\mathrm{a}\cos\left(\kappa t + \theta_{R0}\right) - \left[\frac{2\Omega\Phi_m}{R\left(\Omega - \Omega_\mathrm{p}\right)} + \frac{\partial\Phi_m}{\partial R}\right]_{R_\mathrm{g}} \frac{\cos m\left(\Omega - \Omega_\mathrm{p}\right)t}{\kappa^2 - m^2\left(\Omega - \Omega_\mathrm{p}\right)^2}, \tag{2.8}$$

where R_g is the guiding radius and Ω is the rotation frequency of a circular orbit at R_g. The second term describes the epicycle motion with amplitude R_a, frequency κ and initial phase θ_{R0}. The third term oscillates with a beat frequency $m(\Omega - \Omega_\mathrm{p})$ between the orbit and the perturbation implying that in the absence of epicycle motion, the orbit closes in the corotating frame of the bar after a beat period. These orbits with $R_\mathrm{a} = 0$ are termed the parent orbit of a class of orbits with identical parameters but $R_\mathrm{a} > 0$. Akin to a driven harmonic oscillator, the assumption of small excursion breaks down near resonances: the third term in equation (2.8) indicates a divergence of radius at the corotation resonance (CR, $\Omega = \Omega_\mathrm{p}$), the outer Lindblad resonance (OLR, $\Omega - \Omega_\mathrm{p} = -\kappa/m$), and the inner Lindblad resonance (ILR, $\Omega - \Omega_\mathrm{p} = \kappa/m$). Each divergence is accompanied by a sign change in the third term: typically the first term in the square bracket dominates, so that at each major resonance, the orientation of the parent orbits switch between alignment (x_1 orbits) and anti-alignment (x_2) with the bar major axis. Thus when the pattern speed changes, orbits passed by the major resonances switch their alignment (if not caught).

Linearizing the equation of motion has swept away the possibility of finding excitations of other high-order resonances with the bar. In principle, an unlimited number of resonances occur, when commensurability is satisfied between the radial frequency Ω_R (κ in the limit of epicycle approximation) and the azimuthal frequency Ω_φ (Ω for circular orbits) with respect to the bar pattern speed:

$$N_R\Omega_R + N_\varphi(\Omega_\varphi - \Omega_\mathrm{p}) = 0, \qquad \boldsymbol{N} = (N_R, N_\varphi) \in \mathbb{Z}^2. \tag{2.9}$$

With no loss of generality, we define $N_\varphi \geq 1$ since resonance at $(N_R, -N_\varphi)$ is a repetition of $(-N_R, N_\varphi)$. This resonance condition depends on the bar pattern speed but not on the wave number m of the bar: even with a quadrupole bar ($m = 2$), resonances with $N_\varphi \neq m$ occur, but adding e.g. an octopole ($m = 4$) affects their relative strength (Monari et al., 2019a). Orbits that exactly satisfy the resonant condition are closed in the co-rotating frame of

the bar. Their stability — the capability of becoming a parent orbit — was analysed in detail, e.g. by Contopoulos & Grosbol (1989).

2.3.4 Angle-action variables

The dynamics near resonances is best described by secular perturbation theory using angle-action variables (Lichtenberg & Lieberman, 1992). Actions $\boldsymbol{J}$ are integrals of motions, fulfilling the role of generalized momenta, and the conjugate angles $\boldsymbol{\theta}$ evolve linearly in time with orbital frequencies $\boldsymbol{\Omega}$. Geometrically, actions define a torus, while angles parametrize the position on the surface of the torus. The important property of actions is their invariance under adiabatic changes: if the galaxy slowly gains mass, or the bar slowly decelerates, actions of most orbits will be conserved, with the exception of orbits with a resonant condition, or a too long orbital period.

For orbits in a two-dimensional axisymmetric potential, the two actions commonly used are the angular momentum J_φ and the radial action J_R, which quantifies the radial oscillations around the guiding orbit. One can canonically map from $(\boldsymbol{q}, \boldsymbol{p})$ to $(\boldsymbol{\theta}, \boldsymbol{J})$ by solving the following equations (e.g. Lynden-Bell & Kalnajs, 1972):

$$J_\varphi \equiv \frac{1}{2\pi}\oint \mathrm{d}\varphi\; p_\varphi = p_\varphi, \qquad J_R \equiv \frac{1}{2\pi}\oint \mathrm{d}R\; p_R = \frac{1}{\pi}\int_{R_-}^{R_+} \mathrm{d}R\; p_R, \tag{2.10}$$

$$\Omega_\varphi = \frac{\Delta\varphi}{T_R} = \frac{2J_\varphi}{T_R}\int_{R_-}^{R_+} \mathrm{d}R\; \frac{1}{p_R R^2}, \qquad \Omega_R = \frac{2\pi}{T_R}, \qquad T_R = 2\int_{R_-}^{R_+} \frac{\mathrm{d}R}{p_R}, \tag{2.11}$$

$$\theta_\varphi = \varphi + \int_C \frac{\mathrm{d}R}{p_R}\left(\Omega_\varphi - \frac{J_\varphi}{R^2}\right), \qquad \theta_R = \Omega_R \int_C \frac{\mathrm{d}R}{p_R}, \tag{2.12}$$

where

$$p_R(R) = \sqrt{2\left[E - \Phi_0(R)\right] - J_\varphi^2/R^2}, \tag{2.13}$$

T_R is the period of radial motion, and $\Delta\varphi$ is the change of azimuthal angle after one radial oscillation. The integrals in equations (2.10) and (2.11) run from pericentre R_- to apocentre R_+, which are the roots of

$$E = \Phi_0(R_\pm) + \frac{J_\varphi^2}{2R_\pm^2}. \tag{2.14}$$

The integration curves C in equations (2.12) run from the pericentre R_- to the current radius R. Since the integrals in equations (2.10-2.12) include poles at the bounds, we employ

the Tanh-Sinh quadrature scheme to obtain accurate results. The following calculations also require the inverse map from $(\boldsymbol{\theta}, \boldsymbol{J})$ to $(\boldsymbol{q}, \boldsymbol{p})$. This is not straightforward since we must first find the energy given the actions. To achieve this, we precalculate the energy on a fine grid in action space and interpolate linearly.

2.3.5 Resonant dragging

We here set out to study orbits trapped and dragged by a slowing bar. Some of the results presented in this section are found in Tremaine & Weinberg (1984) who quantified the dynamical friction exerted on the bar by a spherical halo. Here, we focus on the behaviour of the perturbed orbits rather than their feedback on the bar.

We consider a Hamiltonian of the form

$$H(\boldsymbol{\theta}, \boldsymbol{J}, t) = H_0(\boldsymbol{J}) + H_1(\boldsymbol{\theta}, \boldsymbol{J}, t) \tag{2.15}$$

where H_0 is the Hamiltonian of the unperturbed axisymmetric system, for which we have angle-action coordinates, and H_1 describes the bar's perturbation. Near a resonance, the standard linear perturbation theory yields a solution that features a small denominator (section 2.3.3). This divergence at resonance can be removed by performing a canonical transformation to a frame of reference that rotates with the resonant frequency (Lichtenberg & Lieberman, 1992, pp.109-117). Near but slightly off the resonance, the resonant frequency

$$\Omega_s \equiv N_R \Omega_R + N_\varphi (\Omega_\varphi - \Omega_\mathrm{p}) \tag{2.16}$$

becomes very small and thus its time integral, the so called slow angle variable,

$$\theta_\mathrm{s} \equiv N_R \theta_R + N_\varphi \left[\theta_\varphi - \int_0^t \mathrm{d}t' \; \Omega_\mathrm{p}(t') \right] \tag{2.17}$$

evolves slowly around the resonance compared to, for example, θ_R. The time-scale disparity between θ_s and θ_R enables us to separate the dynamics into slow and fast components. Thus we make a canonical transformation to a new set of angle-action variable $(\boldsymbol{\theta}', \boldsymbol{J}')$ by choosing θ_R to be the other new angle which we rename as the fast angle variable:

$$\theta_f \equiv \theta_R. \tag{2.18}$$

To obtain the new actions $\boldsymbol{J}' = (J_\mathrm{f}, J_\mathrm{s})$, we perform a canonical transformation via a generating function of form $W(\boldsymbol{\theta}, \boldsymbol{J}', t)$. Recall from classical mechanics that

$$\boldsymbol{\theta}' = \frac{\partial W}{\partial \boldsymbol{J}'}, \qquad \boldsymbol{J} = \frac{\partial W}{\partial \boldsymbol{\theta}}, \quad \text{and} \quad H'(\boldsymbol{\theta}', \boldsymbol{J}', t) = H(\boldsymbol{\theta}, \boldsymbol{J}, t) + \frac{\partial W}{\partial t}, \tag{2.19}$$

where $H'(\boldsymbol{\theta}', \boldsymbol{J}', t)$ is the new Hamiltonian. The first equality instructs us how to construct the simplest W:

$$W(\boldsymbol{\theta}, \boldsymbol{J}', t) = \left\{ N_R \theta_R + N_\varphi \left[\theta_\varphi - \int_0^t \mathrm{d}t' \; \Omega_\mathrm{p}(t') \right] \right\} J_\mathrm{s} + \theta_R J_\mathrm{f}. \tag{2.20}$$

The second equation gives

$$J_\varphi = N_\varphi J_\mathrm{s}, \qquad J_R = N_R J_\mathrm{s} + J_\mathrm{f}, \tag{2.21}$$

and thus

$$J_\mathrm{s} = \frac{J_\varphi}{N_\varphi}, \qquad J_\mathrm{f} = J_R - \frac{N_R}{N_\varphi} J_\varphi. \tag{2.22}$$

The last of the three equations in (2.19) provides

$$H'(\boldsymbol{\theta}', \boldsymbol{J}', t) = H_0(\boldsymbol{J}') + \sum_{\boldsymbol{k}} \Psi_{\boldsymbol{k}}(\boldsymbol{J}', t) \; \mathrm{e}^{i\boldsymbol{k}\cdot\boldsymbol{\theta}'} - N_\varphi \Omega_\mathrm{p}(t) J_\mathrm{s}, \tag{2.23}$$

where the perturbing potential is developed into a Fourier series on the set of indices $\boldsymbol{k} = (k_\mathrm{f}, k_\mathrm{s})$. The Fourier coefficients $\Psi_{\boldsymbol{k}}(\boldsymbol{J}', t)$ are

$$\Psi_{\boldsymbol{k}}(\boldsymbol{J}', t) = \int_0^{2\pi} \frac{\mathrm{d}^2\boldsymbol{\theta}'}{(2\pi)^2} \Phi_\mathrm{b}(R, \varphi, t) \mathrm{e}^{-i\boldsymbol{k}\cdot\boldsymbol{\theta}'} = \sum_m \int_0^{2\pi} \frac{\mathrm{d}^2\boldsymbol{\theta}'}{(2\pi)^2} \hat{\Phi}_m(R, t) \mathrm{e}^{im(\varphi - \varphi_\mathrm{b})} \mathrm{e}^{-i\boldsymbol{k}\cdot\boldsymbol{\theta}'}, \tag{2.24}$$

where we have also expanded the bar potential in φ. For our quadrupole bar, only terms with $m = \pm 2$ are non-zero and their coefficients are $\hat{\Phi}_{\pm 2}(R, t) = \Phi_m(R, t)/2$, where $\Phi_m(R, t)$ is given in equation (2.7). We split $\varphi - \varphi_\mathrm{b}$ into $\theta_\varphi - \varphi_\mathrm{b}$ (the azimuthal angle of the guiding centre with respect to the bar) and $\varphi - \theta_\varphi$ (the deviation from the guiding centre which is only a function of θ_R), and use equation (3.1)-(2.18) to convert between $\boldsymbol{\theta}$ and $\boldsymbol{\theta}'$:

$$\begin{aligned}
\Psi_{\boldsymbol{k}}(\boldsymbol{J}', t) &= \sum_m \int_0^{2\pi} \frac{\mathrm{d}^2\boldsymbol{\theta}'}{(2\pi)^2} \hat{\Phi}_m(R, t) \mathrm{e}^{im\left(\theta_\varphi - \int_0^t \mathrm{d}t' \Omega_\mathrm{p} + \varphi - \theta_\varphi\right)} \mathrm{e}^{-i\boldsymbol{k}\cdot\boldsymbol{\theta}'} \\
&= \sum_m \int_0^{2\pi} \frac{\mathrm{d}\theta_\mathrm{s}}{2\pi} \; \mathrm{e}^{i\left(\frac{m}{N_\varphi} - k_\mathrm{s}\right)\theta_\mathrm{s}} \int_0^{2\pi} \frac{\mathrm{d}\theta_\mathrm{f}}{2\pi} \; \hat{\Phi}_m(R, t) \mathrm{e}^{i\left[m(\varphi - \theta_\varphi) - \left(m\frac{N_R}{N_\varphi} + k_\mathrm{f}\right)\theta_\mathrm{f}\right]} \\
&= \sum_m \delta_{m, N_\varphi k_\mathrm{s}} \int_0^{\pi} \frac{\mathrm{d}\theta_R}{\pi} \hat{\Phi}_m(R, t) \cos\left[m(\varphi - \theta_\varphi) - \left(m\frac{N_R}{N_\varphi} + k_\mathrm{f} \right) \theta_R \right],
\end{aligned}$$

where the last line is valid only for $N_\varphi \leq m$. δ is the Kronecker delta.

During the rapid cycles in θ_f, θ_s can be assumed constant. Hence, one can extract the slow dynamics of θ_s by averaging the Hamiltonian (2.23) over θ_f:

$$\bar{H}'(\theta_\mathrm{s}, \boldsymbol{J}', t) = H_0(\boldsymbol{J}') + \sum_{k_\mathrm{s}\neq 0} \Psi_{k_\mathrm{s}}(\boldsymbol{J}', t)\ \mathrm{e}^{ik_\mathrm{s}\theta_\mathrm{s}} - N_\varphi \Omega_\mathrm{p}(t) J_\mathrm{s}, \tag{2.25}$$

where $\Psi_{k_\mathrm{s}} \equiv \Psi_{(0,k_\mathrm{s})}$. For the major resonances with $N_\varphi = m$, Ψ_{k_s} is non-zero only at $k_\mathrm{s} = \pm 1$. Since the Hamiltonian must be real ($\Psi_{-k_\mathrm{s}} = \Psi^*_{k_\mathrm{s}}$), we have

$$\bar{H}'(\theta_\mathrm{s}, \boldsymbol{J}', t) = H_0(\boldsymbol{J}') + 2|\Psi_1(\boldsymbol{J}', t)| \cos(\theta_\mathrm{s} + \psi_1) - N_\varphi \Omega_\mathrm{p}(t) J_\mathrm{s}, \tag{2.26}$$

where ψ_1 is the phase of the complex Fourier coefficients Ψ_1, and

$$|\Psi_1(\boldsymbol{J}', t)| = \frac{\delta_{mN_\varphi}}{\pi} \left| \int_0^\pi \mathrm{d}\theta_R \hat{\Phi}_m(R, t) \cos\left[m(\varphi - \theta_\varphi) - N_R \theta_R \right] \right|. \tag{2.27}$$

The sum over m is now removed since δ_{mN_φ} only allows positive m (we have defined $N_\varphi > 0$ without loss of generality, section 2.3.3). In the limit $J_R \to 0$ at the CR ($N_R = 0$), $\Psi_1 = |\hat{\Phi}_m|$. For the purpose of brevity, we henceforth use the following auxiliary variables:

$$\Psi \equiv 2|\Psi_1(\boldsymbol{J}', t)|, \qquad \theta \equiv \theta_\mathrm{s} + \psi_1. \tag{2.28}$$

The equations of motion are then

$$\dot{J}_\mathrm{s} = -\frac{\partial \bar{H}'}{\partial \theta_\mathrm{s}} = \Psi \sin\theta, \tag{2.29}$$

$$\dot{\theta} = \frac{\partial \bar{H}'}{\partial J_\mathrm{s}} = \frac{\partial H_0}{\partial J_\mathrm{s}} + \frac{\partial \Psi}{\partial J_\mathrm{s}} \cos\theta - N_\varphi \Omega_\mathrm{p}(t). \tag{2.30}$$

By differentiating equation (2.30) with respect to time, ignoring terms small to second order in Ψ and also $\dot{\theta}_\mathrm{s} (= \Omega_s)$ as it vanishes at the resonance, and substituting equation (2.29), we obtain

$$\ddot{\theta} - G\Psi \sin\theta - \frac{\partial \dot{\Psi}}{\partial J_\mathrm{s}} \cos\theta + N_\varphi \dot{\Omega}_\mathrm{p}(t) = 0 \tag{2.31}$$

where

$$G \equiv \frac{\partial^2 H_0}{\partial J_\mathrm{s}^2} = \frac{\partial}{\partial J_\mathrm{s}} (\boldsymbol{N} \cdot \boldsymbol{\Omega}) = \boldsymbol{N} \cdot \frac{\partial}{\partial \boldsymbol{J}} (\boldsymbol{N} \cdot \boldsymbol{\Omega}) = \sum_{i,j} N_j N_i \frac{\partial \Omega_i}{\partial J_j}. \tag{2.32}$$

is the *nonlinearity parameter* (Lichtenberg & Lieberman, 1992). The indices i, j are summed over $\{R, \varphi\}$. In practice, we compute the partial derivatives of $\boldsymbol{\Omega}$ by finite differences with $\Delta J = 1\,\mathrm{kpc\,km\,s^{-1}}$. For near circular orbits ($J_R < \Delta J$), we estimate G by epicycle

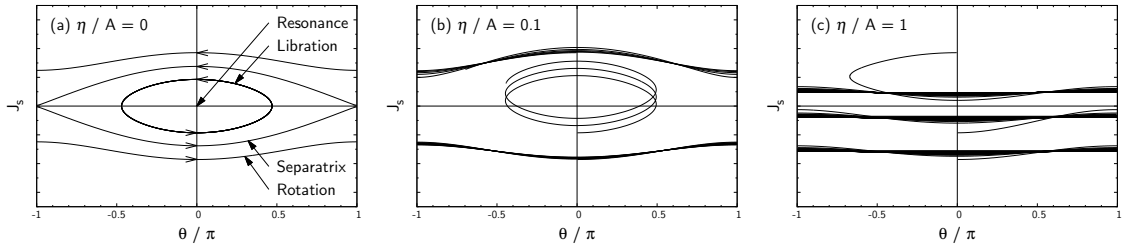

Fig. 2.3 Understanding the motion near resonance in terms of pendulum dynamics. The plots are drawn by numerically integrating equation (2.37). (a) In a constantly rotating bar ($\eta/A = 0$), θ of trapped orbits librates around the resonance while that of non-trapped orbits circulates above or below the separatrix (Lichtenberg & Lieberman, 1992). (b) When the bar slows down slowly such that $0 < \eta/A < 1$, trapped orbits can be resonantly dragged towards higher J_s. (c) Orbits cannot stay in resonance when the resonance sweeps too fast ($\eta/A \geq 1$).

approximation. In a logarithmic background potential, the orbital frequencies are

$$\mathbf{\Omega} = (\Omega_R, \Omega_\varphi) \simeq \left(\kappa, \Omega + \frac{\mathrm{d}\kappa}{\mathrm{d}J_\varphi} J_R\right) = \left(\sqrt{2}\,, 1 - \sqrt{2}\frac{J_R}{J_\varphi}\right)\Omega \tag{2.33}$$

and therefore G is

$$G = -\frac{\left(1 + 2\sqrt{2}N_R/N_\varphi - 2\sqrt{2}J_R/J_\varphi\right)}{\left(1 + \sqrt{2}N_R/N_\varphi - \sqrt{2}J_R/J_\varphi\right)^2}\frac{N_\varphi^2}{R_\mathrm{CR}^2}. \tag{2.34}$$

At the OLR and the CR, J_R is typically an order smaller than J_φ so G is almost always negative. At the ILR, however, G is positive.

We recognize equation (2.31) as a classical pendulum equation (Chirikov, 1979) with additional terms incorporating the growth of the bar (third term) and the change in pattern speed (fourth term). In our model, the order of the third term compared to the fourth term is as small as

$$-\frac{\partial\dot{\Psi}}{\partial J_\mathrm{s}}\frac{1}{N_\varphi\dot{\Omega}_\mathrm{p}} \sim \frac{-\dot{\Psi}}{J_\varphi\dot{\Omega}_\mathrm{p}} \sim \frac{-Av_\mathrm{c}^2}{m}\frac{v_\mathrm{CR}}{R}\frac{1}{Rv_\mathrm{c}\dot{\Omega}_\mathrm{p}} = \frac{A}{m}, \tag{2.35}$$

so as first order approximation we will neglect the third term. The third term will become non-negligible when the strength of the bar is modelled to grow rapidly (in our current model we assumed A = const, so $\dot{\Psi}$ is due only to the stretching of the bar). We leave exploration of a slowing + strengthening bar to a later study.

We now look at the impact of the dragging/slowing term on the modified pendulum equation (2.31). The order of the slowing term $N_\varphi \dot{\Omega}_\mathrm{p}(t)$ is

$$\frac{N_\varphi \dot{\Omega}_\mathrm{p}}{G\Psi} \sim \frac{N_\varphi \dot{\Omega}_\mathrm{p}}{\left(-\dfrac{N_\varphi^2}{R_\mathrm{CR}^2}\right)\left(\delta_{mN_\varphi}\dfrac{Av_\mathrm{c}^2}{m}\right)} = \frac{\eta}{A} \tag{2.36}$$

where we assumed $G < 0$ and invoked the parameter $\eta = -\dot{\Omega}_\mathrm{p}/\Omega_\mathrm{p}^2$ defined in equation (2.3). In the limit $J_R \to 0$, the approximation made above is exact at the CR but underestimates by a factor of ~ 0.83 at the OLR. Using equation (2.36), we may rewrite equation (2.31) as

$$\ddot{\theta} - G\Psi\left(\sin\theta - \frac{\eta}{A}\right) = 0. \tag{2.37}$$

Note that the sign of the slowing term η/A reverses at the ILR where G becomes positive. In the following, we approximate G and Ψ with their values at the resonance $J_\mathrm{s} = J_\mathrm{s,res}$ at the time of capture $t = t_\mathrm{res}$ on the assumption that their time evolution is slow compared to that of θ. The corresponding J_f is determined by the resonance condition $\Omega_s(J_\mathrm{s,res}, J_\mathrm{f}) = 0$. We numerically integrate equation (2.37) together with (2.29) and follow the motion of orbit in the (θ, J_s) plane. Fig. 2.3 (a) shows the phase plane of a pendulum with $\eta/A = 0$. As described in the figure, trapped orbits librate around the resonance at $(\theta, J_\mathrm{s}) = (0, J_\mathrm{s,res})$. This region is bounded by the separatrix, which has maximal/infinite libration period. Outside the separatrix, non-trapped orbits freely circulate, with less amplitude in J_s the further they are from the resonance. Figures 2.3 (b) and (c) show the same plot when the bar slows down moderately ($0 < \eta/A \ll 1$) and extremely rapidly ($\eta/A = 1$). As in Fig. 2.3 (a) the amplitude of oscillations in non-trapped orbits depends on the proximity to the resonant region, so fluctuations of orbits circulating above the separatrix amplifies as the resonance approach while that below the separatrix attenuates as the resonance pass away. On the other hand, in the librating regime, the additional term η/A causes a drift in J_s. To see how this works, let us employ the small-angle approximation $\theta \ll 1$. We then obtain

$$\theta = \hat{\theta}\cos(\omega t + \phi) + \mathrm{sgn}(-G)\frac{\eta}{A}, \quad \text{where} \quad \omega \equiv \sqrt{|G|\Psi}. \tag{2.38}$$

$\hat{\theta}$ and ϕ are the amplitude and initial phase of the oscillation. To justify the small-angle approximation, we require η/A to be small which is satisfied when the bar is either strong

Table 2.1 Summary of the direction of resonant dragging due to decrease in bar pattern speed. The sign of $\dot{J}_\varphi$ is determined by the sign of the non-linearity parameter G, and $\dot{J}_R$ is related to $\dot{J}_\varphi$ by equation (2.40).

	ILR	CR	OLR
$\dot{J}_\varphi$	−	+	+
$\dot{J}_R$	+	0	+

or slowing down slowly. We insert this solution into equation (2.29) and integrate:

$$J_\mathrm{s} = \Psi\Bigg\{\cos\left[\mathrm{sgn}(-G)\frac{\eta}{A}\right]\int \mathrm{d}t\ \ \sin\left[\hat{\theta}\cos\left(\omega t+\phi\right)\right] + \sin\left[\mathrm{sgn}(-G)\frac{\eta}{A}\right]\int \mathrm{d}t\ \ \cos\left[\hat{\theta}\cos\left(\omega t+\phi\right)\right]\Bigg\}. \tag{2.39}$$

Clearly, this describes an oscillation (first term) plus a small drift (second term) of the orbit in J_s along with the resonance. When $\eta = 0$ ($\dot{\Omega}_\mathrm{p} = 0$), the drift term vanishes. When $\eta > 0$ ($\dot{\Omega}_\mathrm{p} < 0$) we find that, at the OLR and the CR ($G < 0$), it leads to a positive drift in J_s and thus in J_φ; trapped orbits at the OLR and the CR are dragged radially outwards by the slowing bar. In contrast, at the ILR ($G > 0$), resonant orbits are dragged towards lower J_φ. Fig. 2.3 (c) shows that if the bar is too weak and/or the resonant sweeping is too fast, the third term of equation (2.37) dominates the dynamics and will force θ to circulate. In such case, orbits cannot stay trapped at resonance and thus dragging will not occur.

On averaging the Hamiltonian over the fast angle, we have implicitly concluded that the fast action is effectively conserved ($\dot{J}_\mathrm{f} = 0$). Therefore any change in angular momentum will be accompanied by a change in the radial action:

$$\dot{J}_R = \frac{N_R}{N_\varphi}\dot{J}_\varphi. \tag{2.40}$$

This is still the well-known result known to most readers in the context of radial migration (Sellwood & Binney, 2002): as a response to the positive dragging in J_φ, the radial action of trapped orbits is conserved at CR ($N_R/N_\varphi = 0$) whereas it increases at OLR ($N_R/N_\varphi > 0$). On the other hand, a negative dragging in J_φ at ILR ($N_R/N_\varphi < 0$) will be compensated by an increase in radial action. This explains why Weinberg (1994) observed a large increase

in velocity dispersion near the OLR. We summarize the direction of resonant dragging in table 2.1. These behaviours are confirmed numerically in Fig. 2.15.

We can also understand the effect of the slowing term from the viewpoint of an effective potential. Multiplying the modified pendulum equation (2.37) by $\dot{\theta}$ and integrating over time, we obtain the following energy integral:

$$E_{\rm p} \equiv \frac{1}{2}\dot{\theta}^2 + V(\theta), \quad \text{where} \quad V(\theta) \equiv \omega^2 \left(-\cos\theta - \frac{\eta}{A}\theta\right). \tag{2.41}$$

As in the analogous case of a harmonic oscillator, $E_{\rm p}$ is not conserved under adiabatic/slow changes in ω. The associated adiabatic invariant is the action of libration which quantifies the amplitude of motion in the slow angle-action plane:

$$J_\ell \equiv \frac{1}{2\pi}\oint \mathrm{d}\theta J_{\rm s}(\theta) = \frac{1}{\pi}\int_C \mathrm{d}\theta \sqrt{\frac{2}{|G|}\left[E_{\rm p} - V(\theta)\right]}, \tag{2.42}$$

where the integral C runs from $-\pi$ to π wherever the integrand is real. J_ℓ is approximately conserved if the libration period T_ℓ is sufficiently shorter than the migration time-scale of the resonance $T_{\rm res}$. Apart from the vicinity of the separatrix, T_ℓ is of order

$$T_\ell \sim \frac{2\pi}{\omega} \sim \frac{1}{\sqrt{A}\Omega_{\rm p}}, \tag{2.43}$$

while the time for a resonance to move by its width (eq. 2.49) is

$$T_{\rm res} = \frac{\Delta J_{\rm s,max}}{\dot{J}_{\rm s}} \sim \frac{\sqrt{A}}{\eta\Omega_{\rm p}}. \tag{2.44}$$

Thus J_ℓ is conserved for most orbits when $T_\ell/T_{\rm res} \sim \eta/A$ is small.

Figure 2.4 shows the configuration of the effective potential $V(\theta)$ which is inclined due to the η/A term in equation (2.41). The resonance centre $\theta_{\rm res}$ and the angle of the local maximum $\theta_{\rm sep}$ reached by stars orbiting along the separatrix are

$$\theta_{\rm res} = \sin^{-1}\left(\frac{\eta}{A}\right), \quad 0 \le \theta_{\rm res} \le \frac{\pi}{2}, \tag{2.45}$$

$$\theta_{\rm sep} = \sin^{-1}\left(\frac{\eta}{A}\right), \quad \frac{\pi}{2} \le \theta_{\rm sep} \le \pi. \tag{2.46}$$

This positive shift of $\theta_{\rm res}$ is barely noticeable in Fig. 2.3 (b), but prominently tilts the equilibrium angle in Fig. 2.15. Further, the maximum $E_{\rm p}$ and J_ℓ at the separatrix are

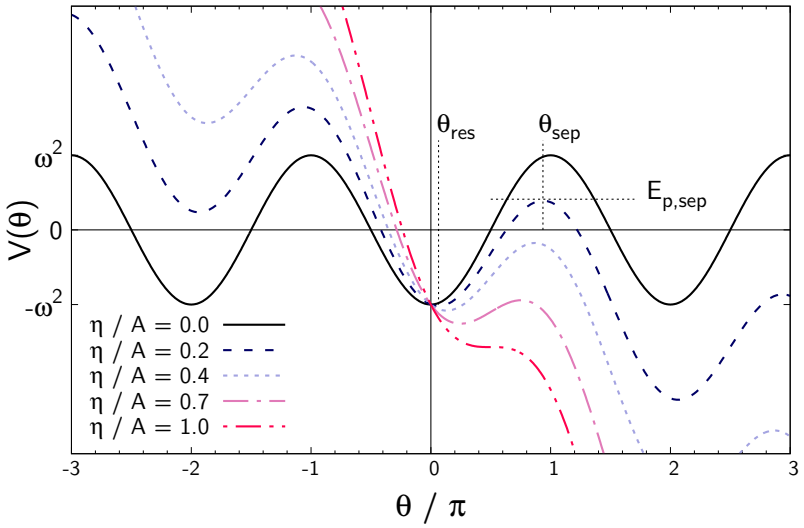

Fig. 2.4 Potential of the modified pendulum. Orbits trapped by the resonance are confined within the potential well. A decreasing pattern speed results in a tilt in the potential and thus the minimum E_p necessary to escape the resonance becomes smaller than that with constant Ω_p.

reduced by the η/A term:

$$E_{\mathrm{p,sep}} \equiv \omega^2 \left(-\cos\theta_{\mathrm{sep}} - \frac{\eta}{A}\theta_{\mathrm{sep}} \right), \tag{2.47}$$

$$J_{\ell,\mathrm{sep}} \equiv \sqrt{\frac{2\Psi}{|G|}} \int_C \frac{\mathrm{d}\theta}{\pi} \sqrt{\left[\cos\theta - \cos\theta_{\mathrm{sep}} + \frac{\eta}{A}\left(\theta - \theta_{\mathrm{sep}}\right) \right]}. \tag{2.48}$$

If $E_\mathrm{p} < E_{\mathrm{p,sep}}$ orbits are trapped and dragged, otherwise they will escape the resonance from θ_{sep} and enter the lower circulating regime. The potential barrier of trapped orbits decreases as the bar slows down more rapidly. Beyond the critical value $\eta/A = 1$ where $\theta_{\mathrm{res}} = \theta_{\mathrm{sep}} = \pi/2$, the potential does not form a local extremum and thus orbits can no longer stay trapped in resonance.

A decrease in $E_{\mathrm{p,sep}}$ implies that the phase space volume of the resonance shrinks when the bar slows down. Fig. 2.5 shows this in action space. The thick white lines are the resonance lines, and the solid green lines mark the maximum excursion of trapped orbits from the exact resonance $\Delta J_{\mathrm{s,max}} \equiv (J_\mathrm{s} - J_{\mathrm{s,res}})_{\mathrm{max}}$, which happens at $E_\mathrm{p} = E_{\mathrm{p,sep}}$ and $\theta = \theta_{\mathrm{res}}$:

$$\Delta J_{\mathrm{s,max}} = \sqrt{\frac{2\Psi}{|G|}} \left[\cos\theta_{\mathrm{res}} - \cos\theta_{\mathrm{sep}} + \frac{\eta}{A}\left(\theta_{\mathrm{res}} - \theta_{\mathrm{sep}}\right) \right]. \tag{2.49}$$

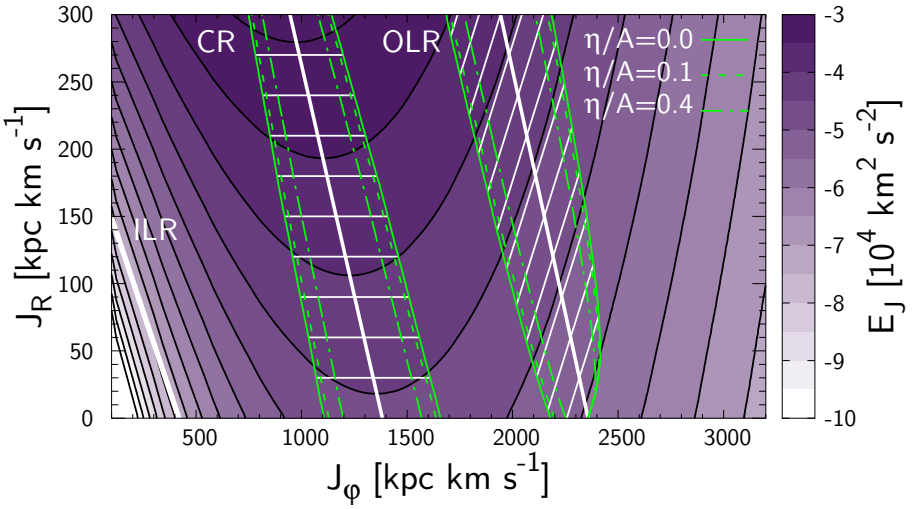

Fig. 2.5 Thick white lines mark the location where the resonance condition is exactly satisfied and green lines indicate the maximum excursion of trapped orbits for different η/A. The color map shows the Jacobi integral E_J. At the resonances, the lines of constant J_f (thin white lines) are tangent to the contours of E_J. The parameters used are $A = 0.02$ and $\Omega_\mathrm{p} = 40\,\mathrm{km\,s^{-1}\,kpc^{-1}}$.

The resonant volumes shrink with increasing η/A, and vanish when η/A reaches unity. Note that not all orbits within the green boundary are trapped, as the trapping also depends on the angles $\boldsymbol{\theta}$.

The white thin lines crossing the resonance represent the line of constant J_f which the librating orbits are assumed to follow in our resonance theory. In fact, conservation of J_f is truly satisfied only at the resonance line ($\boldsymbol{J} = \boldsymbol{J}_\mathrm{res}$) and is otherwise an approximation to the precise conservation of the Jacobi integral E_J which is mapped by the colour scale in Fig. 2.5 as in Binney (2018), where he computed the actions in a 3D axisymmetric potential using torus mapping. The lines of constant J_f and E_J match precisely at the resonance line but deviate for large libration amplitude which is most notable at the CR. Mathematically, conservation of $E_\mathrm{J} = E - \Omega_\mathrm{p} J_\varphi$ requires

$$\Delta E_\mathrm{J} = \frac{\partial E}{\partial J_R}\Delta J_R + \frac{\partial E}{\partial J_\varphi}\Delta J_\varphi - \Omega_\mathrm{p}\Delta J_\varphi = \Omega_R \Delta J_R + (\Omega_\varphi - \Omega_\mathrm{p})\Delta J_\varphi = 0 \tag{2.50}$$

which becomes equivalent to $\Delta J_\mathrm{f} = \Delta J_R - N_R/N_\varphi \Delta J_\varphi = 0$ only when the frequencies $\boldsymbol{\Omega}(\boldsymbol{J})$ are approximated by their values at $\boldsymbol{J}_\mathrm{res}$.

2.4 Test-particle simulation

To ensure full control over the model parameters, we use a test-particle simulation in the analytical potential presented in Section 2.3.2. Our simulation technique is similar to Mühlbauer & Dehnen (2003), who examined the kinematics around a steadily rotating bar. We integrate in each simulation 10^8 particles forward in time using a 4th order symplectic integrator (Yoshida, 1993), with a time step of 0.1 Myr. Parameters of our model are summarized in Table 2.2.

2.4.1 Initial distribution function

The initial distribution function is given by (Dehnen, 1999a):

$$f(E, L_z) \propto \frac{\Sigma(R_E)}{\sigma_R^2(R_E)} \exp\left[-\frac{\Omega(R_E)\,[L_c(E) - L_z]}{\sigma_R^2(R_E)}\right], \tag{2.51}$$

where R_E, $\Omega(R_E)$, $L_c(E)$ is the radius, circular frequency, and angular momentum of a circular orbit with energy E. We assume an exponential profile with scale lengths R_Σ and R_σ for both the surface density $\Sigma(R)$ and the radial velocity dispersion $\sigma_R(R)$ of the disk:

$$\Sigma(R) = \Sigma_\odot \exp\left[-(R - R_0)/R_\Sigma\right], \quad \sigma_R(R) = \sigma_\odot \exp\left[-(R - R_0)/R_\sigma\right], \tag{2.52}$$

where R_0 is the Galactocentric distance of the Sun and $\sigma_\odot$ is the local stellar velocity dispersion. Throughout our work, we adopt $R_\Sigma = 2.5$ kpc, $R_\sigma = R_0 = 8.2$ kpc, and $\sigma_\odot \equiv \sigma_R(R_0) = 40\,\mathrm{km\,s^{-1}}$.

Once E and L_z are determined from equation (2.51), we compute the initial radius R by integrating equation (2.12) up to a random value of $\theta_R \in [0, 2\pi)$. The corresponding initial velocities are then determined $v_\varphi = L_z/R$, $v_R^2 = 2[E - \Phi(R)] - L_z^2/R^2$. The initial azimuthal angle is sampled randomly from $\varphi \in [0, 2\pi)$.

2.4.2 Adiabatic growth of the bar

A sudden onset of the bar will permanently change the actions. As in the past literature, we avoid such an unnecessary distortion from a more realistic case by growing the bar slowly, i.e. we ramp up its strength A from 0 to its final value A_f during the time interval

$0 < t < t_1$ using the polynomial law from (Dehnen, 2000):

$$A(t) = A_\mathrm{f}\left(\frac{3}{16}\xi^5 - \frac{5}{8}\xi^3 + \frac{15}{16}\xi + \frac{1}{2}\right), \quad \xi = \frac{2t}{t_1} - 1. \tag{2.53}$$

Choosing $t_1 = 2\,\mathrm{Gyr}$, this ramp is adiabatic for most orbits, apart from those near the surface/separatrix of the resonance where the libration period diverges.

2.4.3 Pattern speed

As described in section 2.3.2, we model the pattern speed to decrease inversely proportional to time which amounts to a linear increase in corotation radius R_CR. To separate effects, we keep R_CR constant during the ramp-up of the bar amplitude ($0 < t < t_1$), and then smoothly start the slowing within ($t_1 < t < t_2$):

$$R_\mathrm{CR}(t) = \begin{cases} R_\mathrm{CR0} & (0 < t < t_1) \\ R_\mathrm{CR0} + \frac{1}{2} v_\mathrm{CR} \frac{(t-t_1)^2}{t_2 - t_1} & (t_1 < t < t_2) \\ R_\mathrm{CR0} + \frac{1}{2} v_\mathrm{CR}(t_2 - t_1) + v_\mathrm{CR}(t - t_2) & (t_2 < t) \end{cases} \tag{2.54}$$

where R_CR0 is the initial corotation radius and v_CR is the velocity of the corotation radius (here typically of the order of $0.1 - 1\,\mathrm{km\,s^{-1}}$). We remind the reader that, in line with the decrease in the pattern speed, the bar grows such that $R_\mathrm{b} = bR_\mathrm{CR}$. The time variation of the bar's properties are drawn in Fig. 2.6.

2.4.4 Selection function

When we compare our model with observational data, we apply to our simulation the distance-dependent selection function of the *Gaia* data with quality cut in parallax of $p/\sigma_\mathrm{p} > 5$ (Schönrich et al., 2019). The adopted selection function is shown in Fig. 2.7. Two things are to be noted here:

1. As a somewhat trivial point, the function here is similar but not identical to the function provided in equation (6) of Schönrich et al. (2019), as we have to figure in the additional effect of the parallax cut, which must not be applied to the distance estimation.

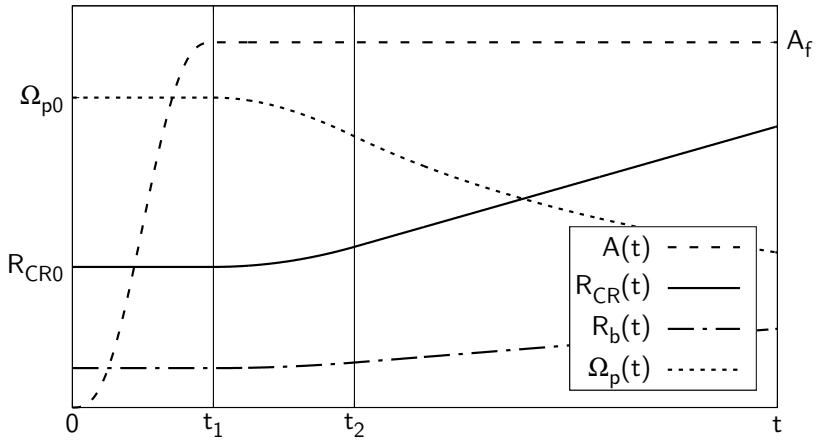

Fig. 2.6 Schematic diagram of the strength of the bar $A(t)$, the corotation radius $R_{\rm CR}(t)$, the bar length $R_{\rm b}(t)$, and the pattern speed $\Omega_{\rm p} = v_{\rm c}/R_{\rm CR}(t)$. The bar is adiabatically grown while keeping the pattern speed constant, and subsequently slowed down with its strength unchanged. The length of the bar is elongated proportional to the corotation radius as $R_{\rm b}(t) = bR_{\rm CR}(t)$ where $b = 0.28$ is determined by fitting our model to SBM15.

2. More importantly, this is only an indicative bias. In truth, the sample selection is based on a photometric selection, which will result in strong biases along age and metallicity, which are much too complex for coverage in this exploratory study. These effects will also be distance dependent, as the near field ($s < 1\,$kpc) is dominated by dwarf/subgiant stars, which have a very different age-metallicity selection function from the giant branches dominating the far field.

2.5 Results and Discussions

2.5.1 Constantly rotating bar

Before we turn to the main topic of this chapter, i.e. the effects of bar deceleration, we discuss the simpler case of a constantly rotating bar. Here we choose amplitude $A = 0.02$ and pattern speed $\Omega_{\rm p} = 40\,{\rm km\,s^{-1}\,kpc^{-1}}$ according to SBM15.

Fig. 2.8 shows examples of different classes of orbits seen in the frame corotating with the bar, where the bar's major axis is represented by a thick black line along the x axis. Note the different scale of each panel. The black circles mark the radii of ILR (dotted), CR (solid) and OLR (dot-dashed). We show non-resonant orbits in the left panel. The

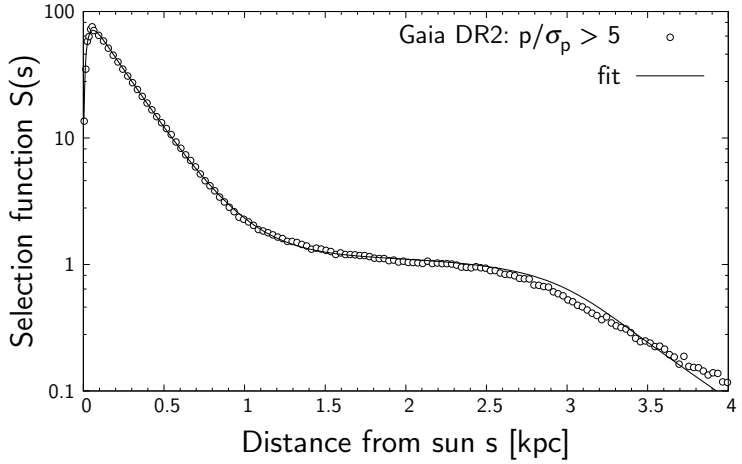

Fig. 2.7 Distance selection function of *Gaia* DR2. We apply this to our simulation to assess the impact of the selection effects.

Table 2.2 Summary of parameters used in our slowing bar model. Parameters to be varied are A, η, and $\Omega_{\rm p0}$.

Parameter	Symbol	Value
Parameters for the slowing bar		
Bar wave number	m	2
Bar angle w.r.t. the Sun	$\varphi_{\rm b} - \varphi_\odot$	30°
Bar strength	A	0.01 - 0.03
Bar scale length ratio	$b \equiv R_{\rm b}/R_{\rm CR}$	0.28
Bar slowing rate	$\eta = -\dot{\Omega}_{\rm p}/\Omega_{\rm p}^2$	0.001 - 0.0055
Bar initial pattern speed	$\Omega_{\rm p0}$	60 - 100 $\mathrm{km\,s^{-1}\,kpc^{-1}}$
Bar growth time	t_1	2 Gyr
Transition time from constant to linear increase in $R_{\rm CR}$	$t_2 - t_1$	1 Gyr
Parameters for the Galactic disk		
Circular velocity	$v_{\rm c}$	$235\,\mathrm{km\,s^{-1}}$
Disc scale length	R_Σ	2.5 kpc
Local velocity dispersion	$\sigma_R(R_0)$	$40\,\mathrm{km\,s^{-1}}$
σ_R scale length	R_σ	R_0

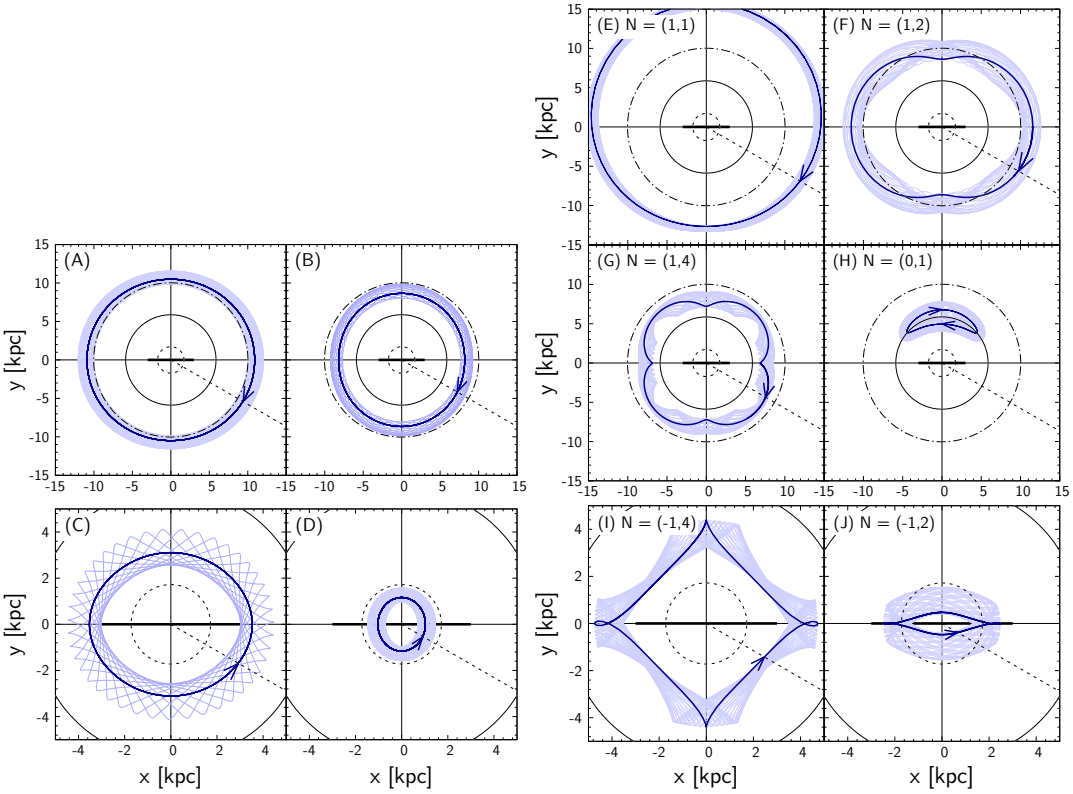

(a) Non-resonant orbits. (b) Resonantly trapped orbits.

Fig. 2.8 Typical orbits in a co-moving frame of a $m = 2$ bar rotating anti-clockwise with a steady pattern speed $\Omega_p = 40\,\mathrm{km\,s^{-1}\,kpc^{-1}}$. The left figures show orbits free from resonance while the right figures show orbits trapped at some of the major resonances. Non-closed orbits (light blue) are parented by stable closed orbits (dark blue). The black dotted, solid, and dot-dashed circles are the ILR, CR, and OLR radii respectively. The black horizontal line is the bar's long axis and the black dotted line indicates the Solar azimuth at $\varphi_b - \varphi_\odot = 30°$.

non-closed orbits (light blue) with non-zero J_R surround their parent/closed orbits with the same L_z (dark blue). As discussed in Section 2.3.3, the orbit orientation changes at each major resonance: orbits are elongated parallel to the bar (A) outside OLR, and (C) between CR and ILR, while they are elongated perpendicular to the bar (B) between CR and OLR, and (D) inside ILR. The right panel of Fig. 2.8 shows examples of orbits trapped at the main resonances: (E) the outer 1:1 resonance, (F) the outer Lindblad resonance, (G) the outer ultra-harmonic resonance, (H) the corotation resonance, (I) the inner ultra-harmonic resonance, (J) and the inner Lindblad resonance. The corresponding resonant closed parent orbits, again depicted in dark blue, are far from circular and are beyond the description of equation (2.8).

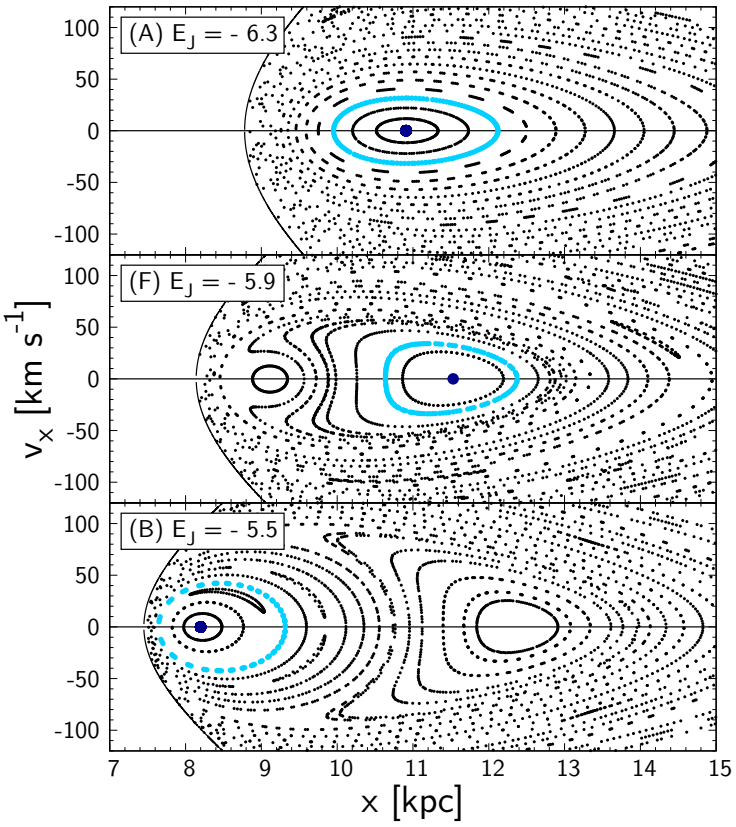

Fig. 2.9 Figures of section near OLR for $E_{\rm J}$ = -6.3, -5.9, and -5.5 km^{2}s^{-2} respectively. The coloured invariant curves correspond to orbits presented in Fig. 2.8 (A), (F), and (B). Non-closed orbits (light blue) encircle their corresponding closed parent orbits (dark blue). The phase space is restricted to the right of the thick limiting curve defined by the equation $(v_y - \Omega_{\rm p} x)^2 = -v_x^2 + \Omega_{\rm p}^2 x^2 + 2[E_{\rm J} - \Phi(x)] = 0$.

The orbits' family relations at resonance are better understood using surfaces of section. In Fig. 2.9, we show surfaces of section in the reduced phase-space (x, v_x) at $y = 0$ and $v_y < 0$ near the OLR. Each panel shows a set of orbits with the same Jacobi integral, $E_{\rm J} = E - \Omega_{\rm p} L_z$, indicated in the top left corner. Each non-closed orbit forms consequents, which appear as ring-like features in these plots (though subsequent passages are not adjacent to each other). Each colored invariant corresponds to an orbit shown in Fig. 2.8 (A), (B), and (F). Near the OLR, increasing $E_{\rm J}$ from top to bottom generally moves the mapped phase space towards lower L_z and higher J_R as can be recognized in Fig. 2.5. The orbits in the top plot have too small $E_{\rm J}$ to reach the OLR, so they all belong to the same x_1 non-resonant parent orbit. The larger $E_{\rm J}$ in the middle panel allows the contour of $E_{\rm J}$ in action space (Fig. 2.5) to cross the OLR line. Consequently, we now see three

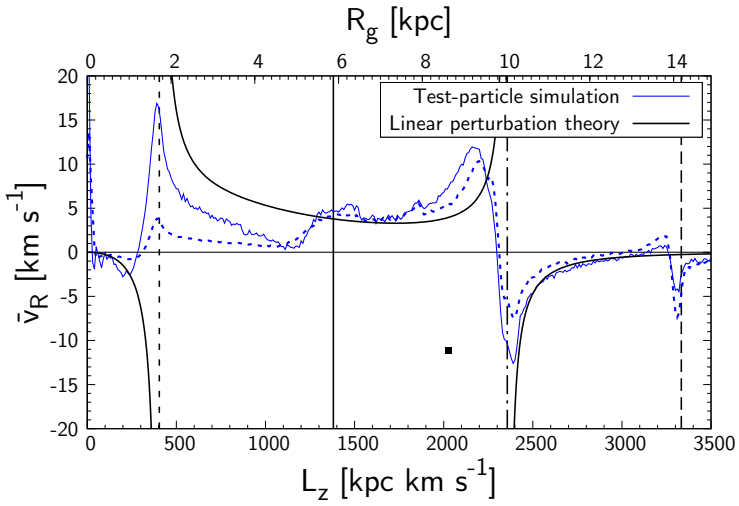

Fig. 2.10 Mean radial velocity $\bar{v}_R$ vs. L_z at Solar azimuth. Linear perturbation theory (solid black curve, eq.2.55) is compared to test particle simulations without (solid blue) and with (dashed blue) the *Gaia* selection function applied. Black vertical lines represent, from left to right, ILR, CR, OLR, and O11R respectively. Black square marks the coordinates of the Sun. Since the majority of orbits are non-resonant and near circular, linear theory qualitatively captures the main features of the simulations.

different types of orbits: non-resonant x_2 orbits below the lower separatrix with small J_R circulating near $x \sim 9.2\,\mathrm{kpc}$, resonant orbits inside the separatrix around $x \sim 11.2\,\mathrm{kpc}$, and non-resonant x_1 orbits above the upper separatrix with large J_R surrounding the other two groups. In the bottom panel the region of x_2 orbits around $x \sim 8.3\,\mathrm{kpc}$ has expanded, and the resonant domain at $x \sim 12.5\,\mathrm{kpc}$ starts shrinking. Also, there are minor resonances occupying much smaller regions of phase space, e.g. the small crescent shape belonging to the 2:3 resonance.

Now we look into the velocity distribution of an ensemble of these test particles. Fig. 2.10 shows the mean radial velocity $\bar{v}_R$ as a function of L_z at the Solar azimuth ($\varphi_\mathrm{b} - \varphi_\odot = 30°$). The velocity is sampled from particles within a narrow slice ($|\Delta\varphi| < 0.5°$) centred on the Sun. The general relationship between $\bar{v}_R$ and L_z can be understood from the orientation (aligned or anti-aligned with the bar) and the rotating direction (prograde or retrograde with respect to the bar) of the closed parent orbits: e.g. orbits outside the OLR are aligned with the bar and are retrograde so at the Solar azimuth the closed orbit points inwards (i.e. $v_R < 0$). Within the epicycle approximation, the mean radial velocity at Solar azimuth is

obtained by differentiating and averaging equation (2.8) with respect to time:

$$\bar{v}_R = \left[\frac{2\Omega\Phi_m}{R} + \left(\Omega - \Omega_\mathrm{p}\right) \frac{\partial \Phi_m}{\partial R} \right]_{R_\mathrm{g}} \frac{m \sin m \left(\varphi_\odot - \varphi_\mathrm{b}\right)}{\kappa^2 - m^2 \left(\Omega - \Omega_\mathrm{p}\right)^2}, \tag{2.55}$$

where $R_\mathrm{g} = L_z / v_\mathrm{c}$, $\Omega = v_\mathrm{c}/R_\mathrm{g}$, and $\kappa = \sqrt{2}\Omega$. The above equation delivers the black line in Fig. 2.10, which qualitatively explains the numerical results. The positive peak just behind the OLR line was the original interpretation for the Hyades stream by Kalnajs (1991) and the Hercules stream by Dehnen (2000). The small positive peak at CR is due to the resonantly trapped orbits reaching the Solar azimuth as they rotate around the Lagrange point $\mathrm{L}_{4,5}$. Pérez-Villegas et al. (2017) attributed the Hercules stream to this peak, and supported the idea of a slow/long bar. The dotted blue curve in Fig. 2.10 shows the result after imposing the *Gaia* selection function, which deviates from the non-biased result mostly at small L_z.

One of the central benefits from *Gaia* is that we can now observe stars over a wide range in Galactic azimuth, and this dependence was quantified by Friske & Schönrich (2019) and is also shown in Fig. 2.1 (b). Analogously, we show in Fig. 2.11 the φ-L_z dependence of the mean radial velocity $\bar{v}_R$. The vertical black lines show, from left to right, the ILR (dotted), CR (solid), OLR (dot-dashed) and 1:1 resonance (dashed) at $J_R = 0$. The findings agree with previous studies: the sign of v_R flips when we pass through the bar's major/minor axes (vertically), and through ILR/OLR (horizontally). We also see a weak eye-like shape of orbits trapped in the CR rotating around the Lagrange points at $\varphi - \varphi_\mathrm{b} = \pm\pi/2$. The bottom panel zooms into the *Gaia* DR2 area (marked by a black box) and applies the spatial selection to compare with Fig. 2.1 (b). We see a pair of positive and negative stripes at the OLR and a broad stripe at the CR that narrows towards the bar major axis. This somewhat resembles the *Gaia* data but is far from qualitatively matching the full pattern.

Fig. 2.12 shows the changes in the density distribution in action space after the bar has fully developed. Orbits near the resonances become trapped and librate back and forth across the resonance along constant J_f (thin black rungs), but not further than the purple boundary (eq. 2.49). At the CR, J_R is conserved, so the exponential disk profile in J_φ implies a mild redistribution from small to large J_φ. The other resonances redistribute

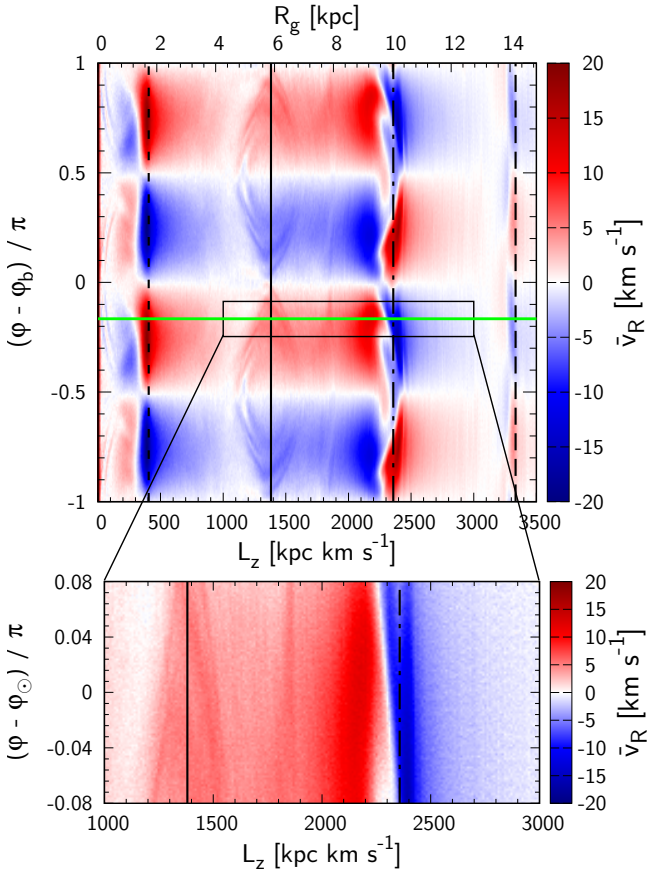

Fig. 2.11 Azimuthal dependance of $\bar{v}_R$ vs. L_z. Black lines show the L_z of ILR (dotted), CR (solid), OLR (dot-dashed), and O11R (dashed) at $J_R = 0$, respectively. Green line indicates the azimuth of the Sun and the rectangle window indicates the range of *Gaia* DR2. Bottom panel magnifies the *Gaia* region and applies the spatial selection bias.

towards larger J_R, with extreme effect at the ILR, where the resonance line almost coincides with constant J_f.

Finally, Fig. 2.13 shows the velocity distribution $f(v_R, v_\varphi)$ in the Solar neighbourhood ($s < 0.3\,\mathrm{kpc}$) drawn from test particle simulations with three different bar strength (row) and two different pattern speeds (columns) both identified as a slow bar. A wider range of pattern speeds, including the traditional fast bar, will be shown with their corresponding slowing bar models in the next section. The black solid and dot-dashed curves mark the separatrices enclosing the resonant regions of the CR and the OLR as done in Monari et al. (2017b). At $\Omega_\mathrm{p} = 40\,\mathrm{km\,s^{-1}\,kpc^{-1}}$, orbits trapped by the OLR appear distinctively as an arch at $v_\varphi \sim 280\,\mathrm{km\,s^{-1}}$, whereas the velocity distribution of orbits trapped by the CR shows little contrast to the surrounding non-resonant region. For this reason, past studies

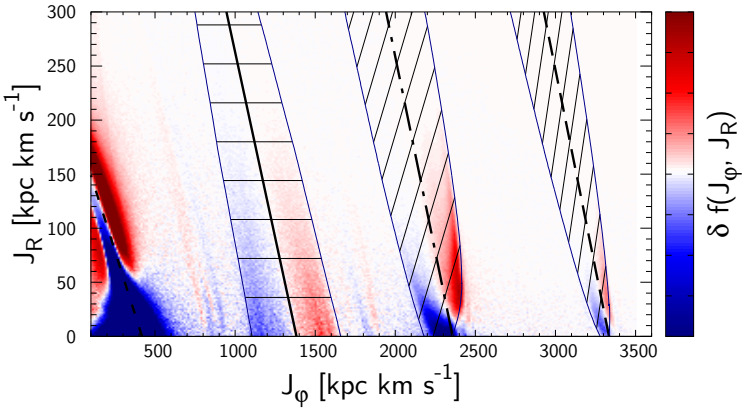

Fig. 2.12 Changes in the density distribution in action space $\delta f(J_\varphi, J_R)$ from the initial unperturbed state. Densities change when trapped orbits librate between regions of different initial phase-space density around the resonance lines (thick black lines) along contours of constant J_f (thin black lines). Purple curves mark the maximum libration range.

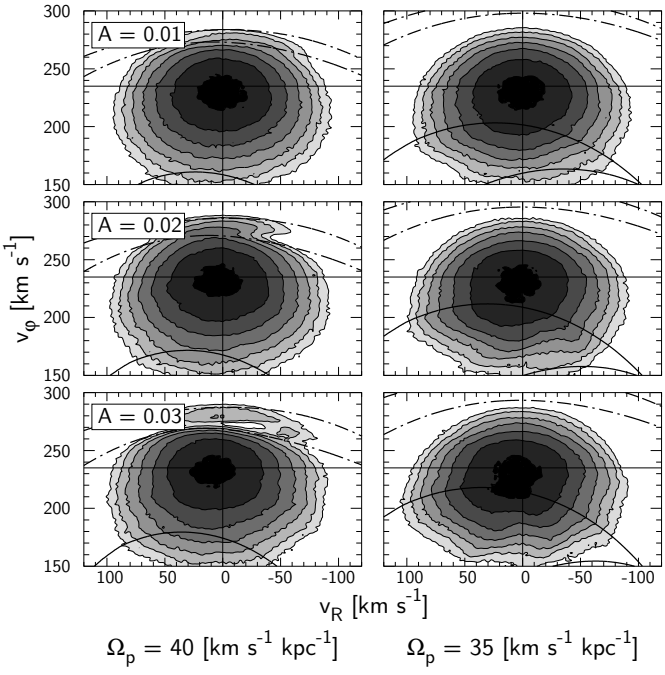

Fig. 2.13 Velocity distribution $f(v_R, v_\varphi)$ in the Solar neighbourhood (distance from Sun $s < 0.3\,\mathrm{kpc}$) perturbed by a steadily rotating bar. The solid and dashed curves mark the separatrices ($E_\mathrm{p} = E_\mathrm{p,sep}$) of the CR and the OLR. The contours are logarithmic with a 0.44 dex spacing.

disfavoured linking the Hercules stream with the CR (Dehnen, 2000; Monari et al., 2017a; Fragkoudi et al., 2019). In the next section, we will show that this problem is naturally resolved by a decelerating bar where the CR captures more stars and on a different action distribution as it forms further inside and then sweeps outwards.

However we mention here again that studies by Pérez-Villegas et al. (2017); Monari et al. (2019a) report better success in reproducing the Hercules stream with a constantly rotating bar which suggests that higher-order modes of the bar can be important for shaping the distinct outline of the Hercules stream. We further note that the Hercules stream can also be reproduced by transient spirals alone or in combination with the bar (Hunt et al., 2018). Since none of these effects are ignorable, it will be important in the future to combine these models and distinguish their role, once the kinematic consequence of individual perturbations are well understood.

2.5.2 Slowing bar

We now consider the effect of a slowing bar. Two new processes arise from resonance sweeping: dragging of resonantly trapped orbits along with the moving resonance and trapping of non-resonant orbits when the resonance crosses over their domain. At the current stage, capture and loss from resonances require numerical treatment. Nevertheless the analytic approach predicts that the resonance volume shrinks with decreasing amplitude A and increasing slow-down rate η of the bar, so we have a naive, but firm expectation that the capture and retention rates will also decrease with increasing η/A.

In Fig. 2.14 (a) we show the probability of being successfully dragged by the moving OLR as a function of bar strength A and slowing rate η. The orbits are initially trapped in the OLR at $\Omega_\mathrm{p} = 60\,\mathrm{km\,s^{-1}\,kpc^{-1}}$ and the bar is subsequently slowed down to $\Omega_\mathrm{p} = 30\,\mathrm{km\,s^{-1}\,kpc^{-1}}$. The plot shows the fraction of successfully dragged stars defined as those originally in the OLR that then experience a relative increase $\delta L_z/L_{z0} > 0.2$. The threshold is chosen to safely exceed the maximum libration amplitude in L_z. For each parameter set (A, η), we use 100 particles with the same initial actions $(J_R, J_\varphi) = (19.4, 1524.5)\,\mathrm{kpc\,km\,s^{-1}}$ but with random angular phase. The initial actions are placed exactly on the resonance line to ensure trapping independent of angular phase. The result confirms the analytical

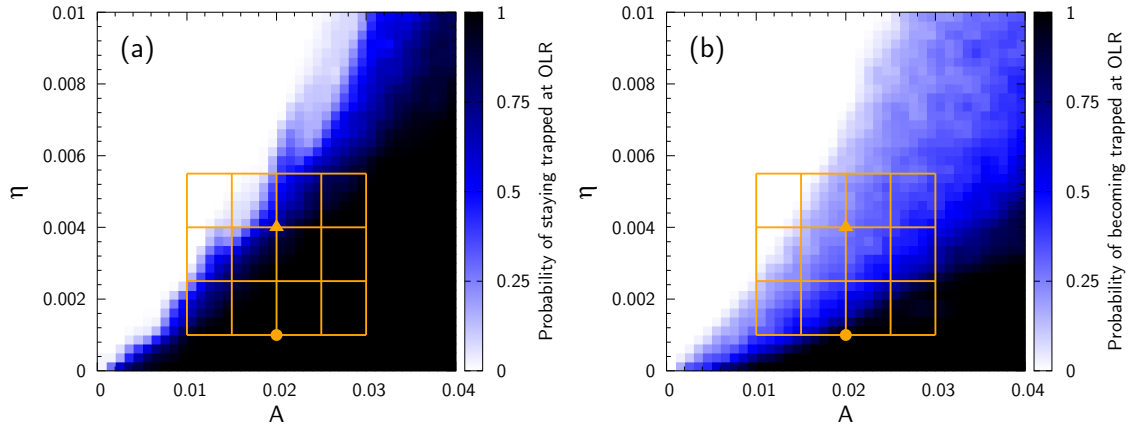

Fig. 2.14 Left (a): Fraction of orbits initially trapped at OLR being dragged by the slowing bar as a function of bar strength A and slowing rate η. The orange circle and triangle mark the parameters of our standard slowly and rapidly decelerating bar. Results using the full grid are shown in Fig. 2.20. Right (b): Fraction of orbits *becoming* trapped by the OLR. The blue transition zone is broad since resonant capturing depends on the initial angles.

expectation that the retention probability increases with A and decreases with η. The critical boundary is fairly linear which backs our idea that η/A satisfactorily describes the dragging efficiency. Similarly, Fig. 2.14 (b) shows the capturing rate by the moving OLR. Here we set the initial actions $(J_R, J_\varphi) = (19.4, 1921.1)\,\mathrm{kpc\,km\,s^{-1}}$ which is outside the resonance. The blue transition region roughly matches that of Fig. 2.14 (a), but is wider, indicating a strong dependence of resonant capturing on angular phase.

Figure 2.14 implies three parameter regimes in which the dynamical consequence of a slowing bar differs qualitatively. In the white regime, the resonance sweeping is too fast or the bar is too weak for resonant trapping to occur. The extreme opposite is the black regime where most orbits are captured and dragged by the resonance resulting in a great migration of orbits. In the blue intermediate regime, most resonant orbits are dragged but not all non-resonant orbits are captured. This discussion neglects that orbits can also be kicked out of and into resonances by gravitational fluctuations due to satellite galaxies, transient spiral arms, and giant molecular clouds, a discussion which we defer to a later study. The CR shows similar behaviour to the OLR, but the situation is more complicated due to the series of small higher-order resonances piling up towards the CR, leading to chaotic behaviour. We therefore prefer the parameter map at OLR to qualify the slowing

regime, while using the CR as a corroborating source of evidence. In the following, we discuss results from the full orange parameter grid, which covers all three regimes, first starting with an in-depth analysis of the slowly (orange circle) and the rapidly (triangle) decelerating bar.

Slowly decelerating bar

Fig. 2.15 analyses typical orbits in a slowly decelerating bar ($\eta = 0.001$, $A = 0.02$, and thus $\eta/A = 0.05$), where Ω_p decreases from 80 to 45 $\mathrm{km\,s^{-1}\,kpc^{-1}}$ in 9 Gyr (with a transition period of $t_2 - t_1 = 1\,\mathrm{Gyr}$). As in Fig. 2.8, we show more eccentric orbits (light blue, second column) and their closed parents (dark blue, first column). Grey and black circles indicate the initial and final resonance radii for ILR (dotted), CR (solid), and OLR (dot-dashed). The orbits have initial guiding radii of (a) 7.1, (b) 5.2, (c) 4.0, (d) 3.0, (e) 1.7, and (f) 1.0 kpc. The other columns provide the evolution of the actions.

The rows (a)-(d) show orbits trapped and dragged outwards by O11R, OLR, OUHR, and CR. In the rotating frame of the bar, frame deceleration causes an Euler force $\dot{\boldsymbol{\Omega}}_\mathrm{p} \times \boldsymbol{R}$ responsible for the slight anti-clockwise turn of the orbits' configuration. The orbit in row (e) remains non-resonant and thus roughly maintains its orbital configuration. The orbit (f) is dragged by the ILR until it turns chaotic. The qualitative behaviour of the actions agrees with the secular perturbation theory (Section 2.3.5): at the outer resonances (a)-(c), both L_z and J_R continuously increase, whereas at the CR (d), only L_z enhances while J_R is kept fixed; actions of non-resonant orbits (e) are unchanged; at the ILR (f), L_z declines while J_R rises.

Fig. 2.16 follows the evolution of the phase-space distribution perturbed by a slowly decelerating bar. The rows from top to bottom show the distribution every 2 Gyr, denoting the pattern speed Ω_p on the right in $\mathrm{km\,s^{-1}\,kpc^{-1}}$. We provide the velocity distribution and action distribution near the Sun ($s < 0.3\,\mathrm{kpc}$), as well as the mean radial velocity $\bar{v}_R$ in the L_z-φ plane in a narrow slice around the Solar azimuth applying our approximated *Gaia* selection function. For each panel we provide to its right the comparison case of a constantly rotating bar with identical amplitude and current Ω_p.

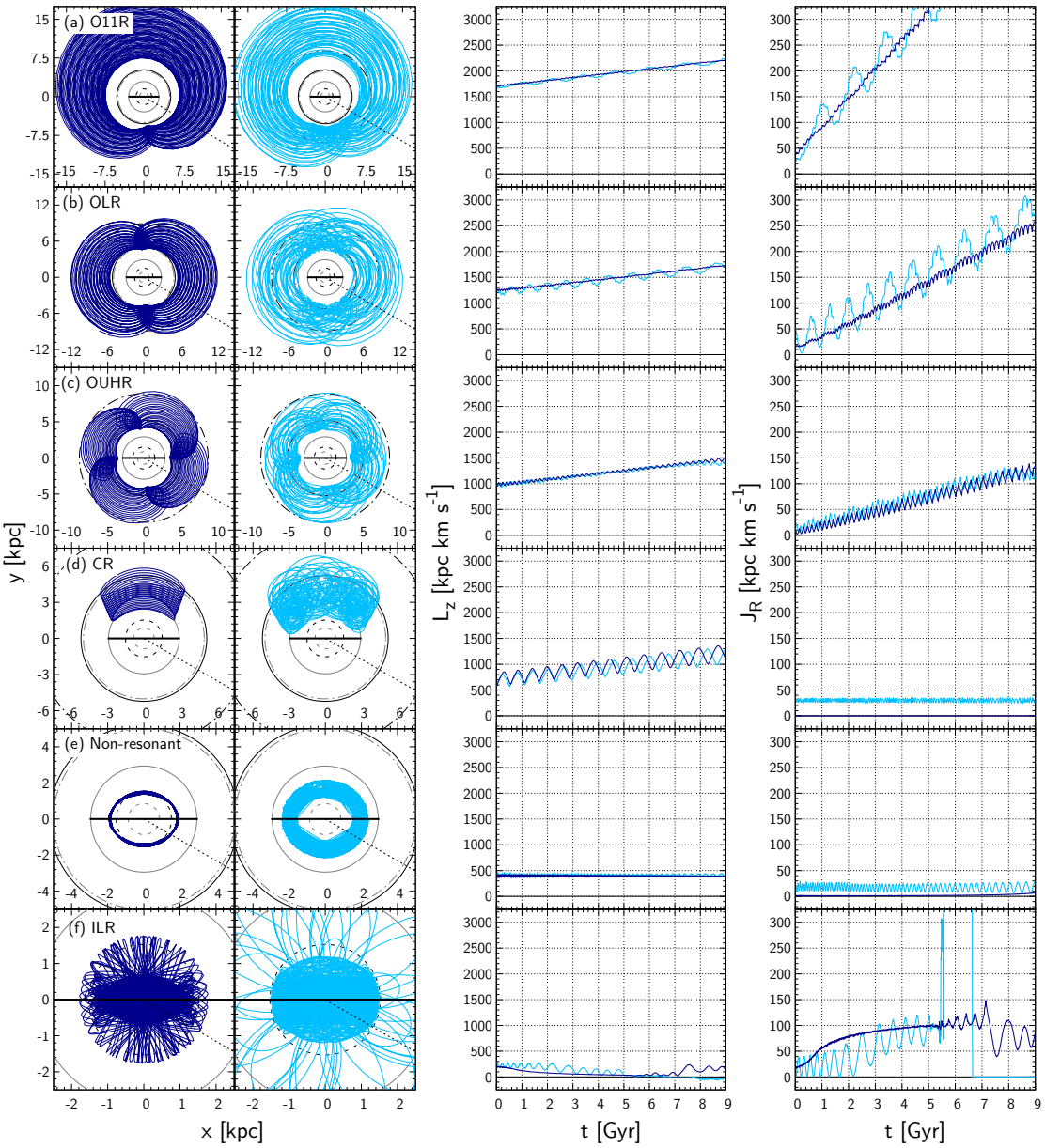

Fig. 2.15 Orbits swept by the resonance of a slowing bar decreasing its pattern speed from $\Omega_p = 80$ to 45 $\mathrm{km\,s^{-1}\,kpc^{-1}}$ in 9 Gyr ($\eta = 0.001$). Each row displays the trajectory of a single star gradually changing its orbit. Dark blue orbits (left column) are initially closed while light blue orbits (2nd column) are initially non-closed. The grey and black circles are the initial and final radii of ILR (dashed), CR (solid), and OLR (dot-dashed). Drift in angular momentum (3rd column) is only seen for resonantly trapped orbits. The radial action (right column) increases when dragged at all resonances except at the CR.

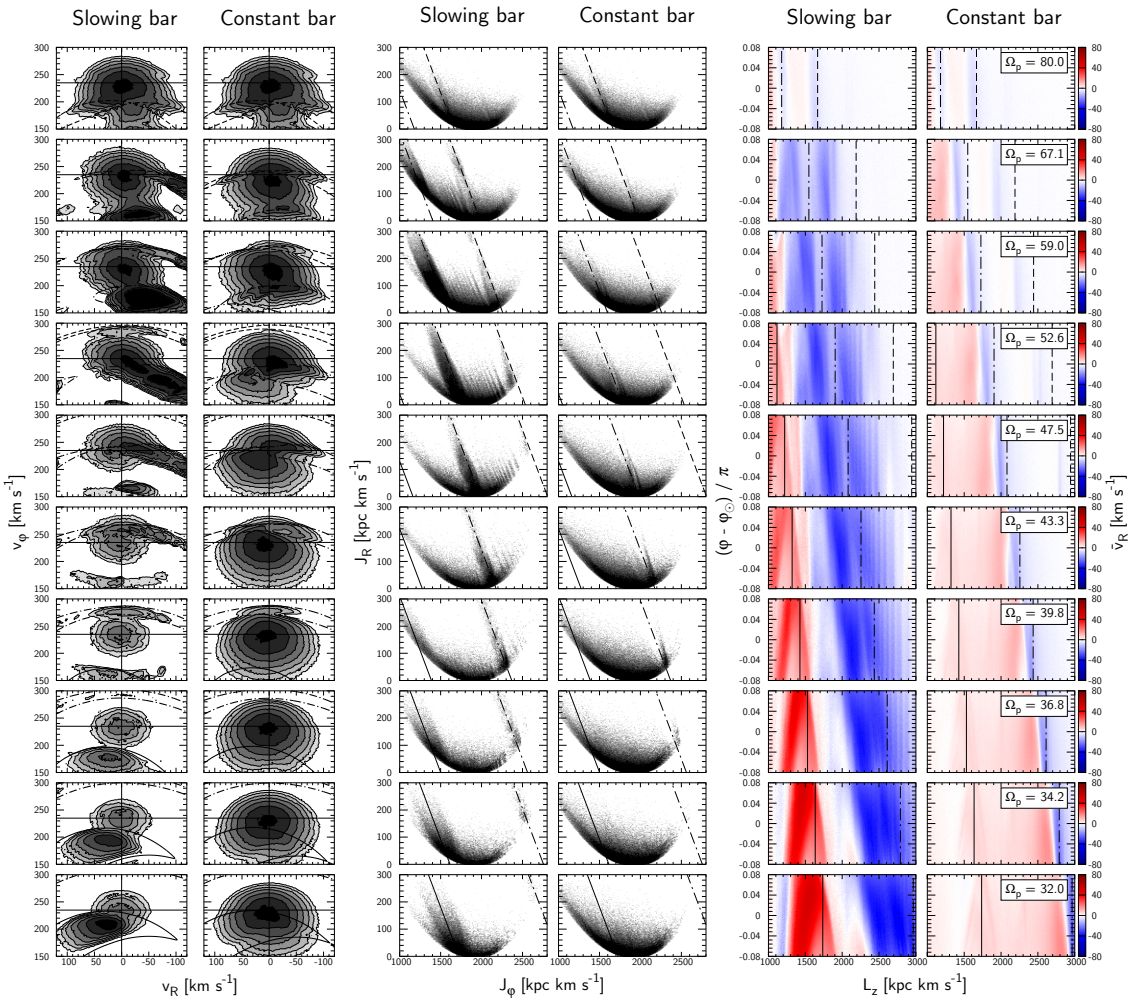

Fig. 2.16 Simulated phase space when the bar decelerates slowly from $\Omega_\mathrm{p} = 80$ to 45 $\mathrm{km\,s^{-1}\,kpc^{-1}}$ in 9 Gyr. Time-interval between the rows is 2 Gyr (last three snapshots extends beyond the age of the Galaxy). Each pair of columns compare the decelerating bar vs. a constantly rotating bar at the same Ω_p indicated by white panels in the right-hand column. Black solid, dot-dashed, and dashed lines represent CR, OLR, and O11R respectively. In the velocity plane we mark the separatrix of the resonances, while in the action plane we draw the exact resonance line, and in the (L_z, φ) plane we indicate the loci of resonances at $J_R = 0$. The OLR and CR capture and retain the majority of orbits along their way resulting in an unrealistically intense stellar stream.

The local velocity plane (left-hand columns) is dominated by the main resonances. First, the OLR captures and carries away the majority of non-resonant orbits leaving behind a significantly depleted phase space, until the CR brings along the next swath of stars. At around $\Omega_\mathrm{p} = 43.3\,\mathrm{km\,s^{-1}\,kpc^{-1}}$ (before the CR arrives), an arc-shaped distribution develops at $v_\varphi \sim 160\,\mathrm{km\,s^{-1}}$. Orbits below this arc have sufficient kinetic energy to cross over the crest of the effective potential $\Phi - \frac{1}{2}\Omega_\mathrm{p}^2 R^2$ in the rotating frame and can wander in and out of the bar regime. Fux (2001) proposed that the Hercules stream may be associated with these orbits. However, this slowly decelerating bar will always have a radically too strong resonance occupation to match the *Gaia* data.

The action plane (middle columns) shows similarly the capture and drag by the main resonances. In between the OLR and the O11R, we see multiple narrow lines. We confirm that they are due to orbits trapped and dragged by minor resonances (e.g. 2:3 resonance). The occupation on minor resonances depends on their stability under the deceleration but also on depletion by anteceding resonances — minor resonances behind the OLR are less prominent since the OLR sweeps away most of the non-resonant orbits in advance.

In the right columns of Fig. 2.16, the amplitude of $\bar{v}_R(L_z, \varphi)$ near resonances continues to increase as they keep collecting stars. The red spear-like stripe at the CR increases in strength at the edge indicating accumulation of orbits near the separatrix. The blue stripe associated with the OLR widens to the left over time since trapped orbits increase J_R while dragged and thus satisfy the resonance condition at a relatively lower L_z compared to those with small J_R.

Rapidly decelerating bar

N-body studies indicate that bars slow down more rapidly than we have assumed in Section 2.5.2. In accordance with Aumer & Schönrich (2015) we choose the slowing rate $\eta = 0.004$ as indicated by the orange triangle in Fig.2.14. The pattern speed decreases from $\Omega_\mathrm{p} = 80$ to $30\,\mathrm{km\,s^{-1}\,kpc^{-1}}$ in 5.6 Gyr. The strength of the bar is unchanged ($A = 0.02$), so $\eta/A = 0.2$. Fig. 2.17 shows from left to right the velocity distribution, the action distribution, and the mean v_R in the L_z-φ plane, along with the results of a constantly rotating bar on the right of each column.

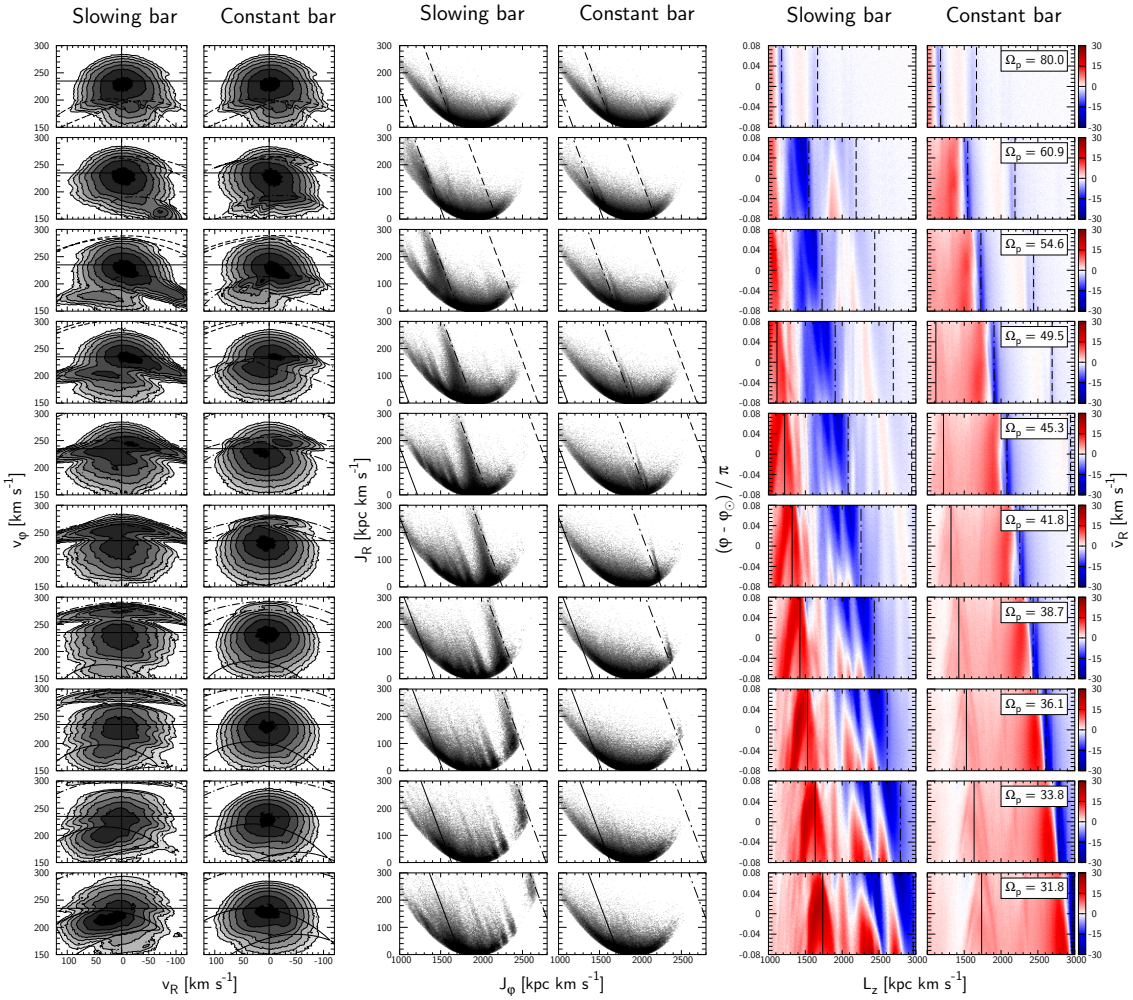

Fig. 2.17 Simulated phase space as in Fig. 2.16 plotted every 0.56 Gyr when the bar decelerates rapidly from $\Omega_p = 80$ to $30\,\mathrm{km\,s^{-1}\,kpc^{-1}}$ in 5.6 Gyr. Unlike the case of a slowly slowing bar, the effect of resonance sweeping is moderate, yet enhances the resonance features compared to a constantly rotating bar (right of each column). The CR reproduces well the Hercules stream in the velocity plane and the spear-like double peak in $\bar{v}_R(L_z, \varphi)$ seen in the *Gaia* data (Fig. 2.1).

In the velocity plane, the resonances are much smaller in volume than those of the constantly rotating bar, but appear more distinctively. At around $\Omega_\mathrm{p} = 36.1\,\mathrm{km\,s^{-1}\,kpc^{-1}}$, the orbits trapped at the CR form a peak that resembles the observed Hercules stream much better both in strength (by sweeping up more stars) and in location (due to the shrinkage of the resonance region towards high v_R). The Hercules stream modelled by a constantly rotating bar (see also Pérez-Villegas et al., 2017) is far too symmetric in v_R, while the decelerating bar provides the strong asymmetry which previously could only be achieved by the OLR (e.g. Dehnen, 2000).

In the action plane, multiple inclined ridges appear between the CR and the OLR — a smaller capture rate at the OLR leaves opportunity for orbits to be captured into the minor resonances passing later. Obviously the signatures of minor resonances will be enhanced if we add higher order modes of the bar. These inclined ridges are also seen in the *Gaia* data (Fig. 2.1 (a)). However, the ILR of spiral arms also lies in the vicinity (Sellwood et al., 2019) making the exact identification of individual ridges difficult.

The right columns in Fig. 2.17 show that the amplitude in the $\bar{v}_R$ increases much less than for the slowly decelerating bar due to the smaller capturing rates (note the different colour scales). Again at the CR, the newly captured orbits accumulate near the resonance boundary and form a spear-like (an eye-like, if we saw the full φ range; Fig. 2.18) structure which closely resembles the double positive peak in the *Gaia* data. In between the CR and the OLR line, we observe roughly two pairs of positive and negative stripes.

To better understand the origin of the multiple stripes in $\bar{v}_R(L_z, \varphi)$, we show in Fig. 2.18 the relative change of number density with respect to the initial distribution ($\delta f/f_0 = f/f_0 - 1$), and the $\bar{v}_R$ over the full φ range without imposing the selection bias (indicating the Solar azimuth $\varphi_\mathrm{b} - \varphi_\odot = 30°$ with a green line). The left panel shows that, at the CR, trapped stars follow the resonance line plotted for $J_R = 0$, whereas at the OLR, orbits lag increasingly behind the $J_R = 0$ resonant line since their J_R increases (resonance line is negatively inclined in J_R vs. L_z as in Fig. 2.5). Blue/Underpopulated areas are left behind the travelling OLR and CR, as these resonances sweep part of stars along their path. An even more intense depopulation is caused by the ILR where trapped stars drift towards lower L_z and larger J_R. Note that the initial distribution in L_z declines exponentially so

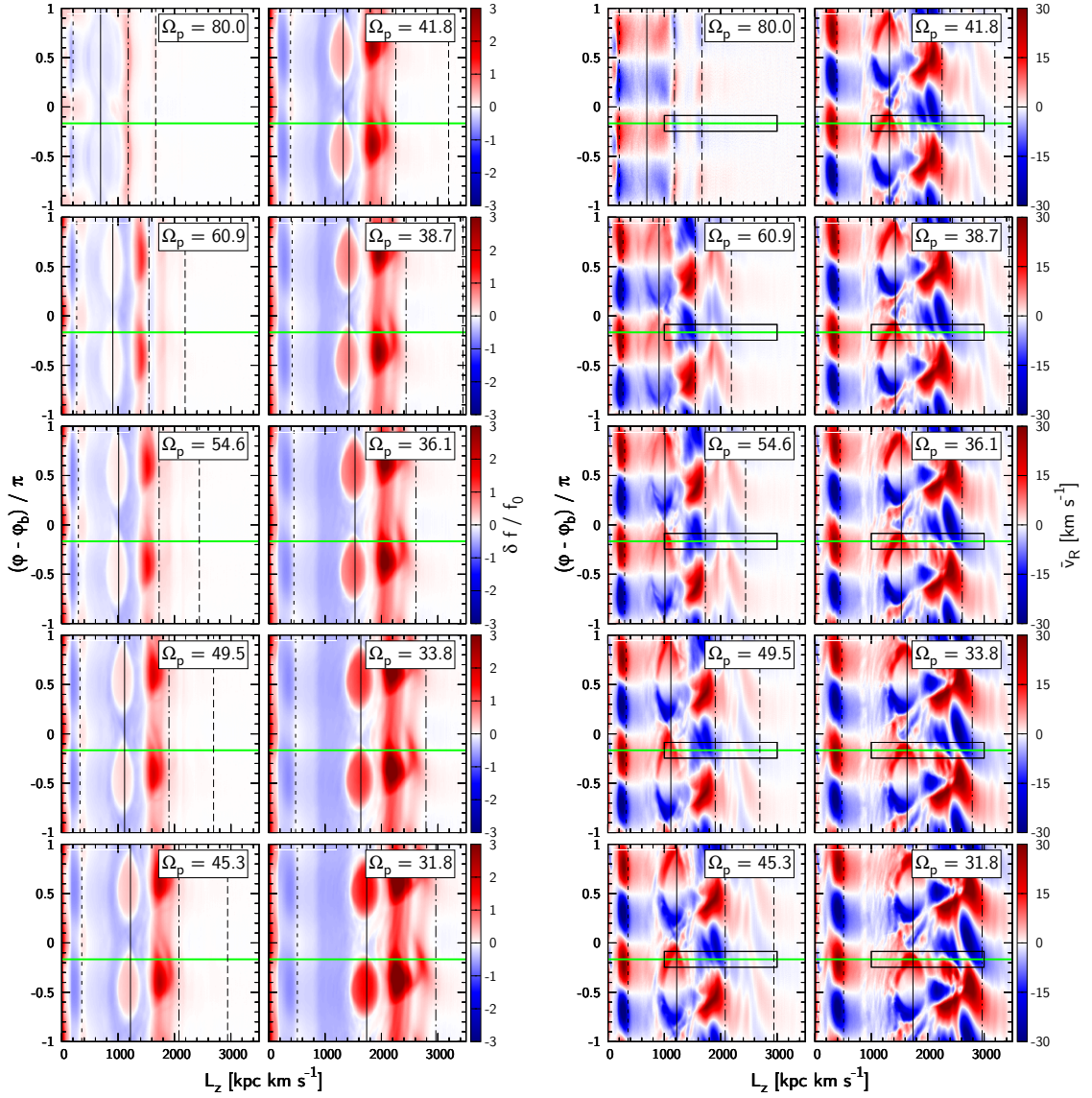

Fig. 2.18 Left panel: Evolution of the distribution $\delta f(L_z, \varphi)$ from the unperturbed state f_0 when the bar slows rapidly from $\Omega_\mathrm{p} = 80$ to $30\,\mathrm{km\,s^{-1}\,kpc^{-1}}$ in 5.6 Gyr. By definition, $\delta f/f_0 > -1$. The black lines represent, from left to right, ILR, CR, OLR, and O11R at $J_R = 0$. Stars captured at the CR comove with the resonant line, while stars resonating at the OLR fall behind in L_z due to their increase in J_R. Right panel: The corresponding mean radial velocity distribution $\bar{v}_R(L_z, \varphi)$. The black narrow rectangles represent the range of *Gaia* data. Behind the OLR line (dot-dashed), two negative (blue) peaks are formed near Solar azimuth indicated by the green horizontal line. Comparison with the left panel implies that the inner peaks are formed by the resonant orbits dragged and heated by the OLR.

a group of orbits moving toward high L_z with constant number density show apparent enhancement in δf. The mean radial velocity is strongly distorted and much more complex than the constantly rotating bar case shown in Fig. 2.11, particularly between CR and OLR. Nevertheless we can identify two pairs of blue and red peaks behind the OLR near the Solar azimuth ($L_z \sim 2400$ and 2800 $\mathrm{kpc\,km\,s^{-1}}$ in the last frame). These structures appear as multiple stripes when seen in the *Gaia* range indicated by the narrow rectangle. By comparing the left panel (the location of the orbits dragged by the OLR) and the right panel (the location of the stripes) we conclude that the pair of $\bar{v}_R$ stripes just inside the OLR are due to the orbits freshly trapped by the OLR while the stripes that appear further inside the OLR line are due to the superposition of orbits dragged and heated by the OLR and orbits trapped in the minor resonances. The weakly negative v_R outside the OLR are associated with non-resonant x_1 orbits swept but not captured by the O11R.

The location and inclination of these multiple stripes at large L_z do not match perfectly with the *Gaia* data (Fig. 2.1 (a)). The neglected transient spiral arms can play at least two important roles here: i) Spiral patterns can independently form these stripes by leaving scars in the action distribution near resonances and also by perturbing the angular distribution, which develops multiple fine stripes in $\bar{v}_R$ as they phase mix over time (Hunt et al., 2019). ii) Scattering by transient spiral arms would reduce the resonant occupation, particularly of the OLR, since it trades stars with the much less densely occupied surrounding phase space at high J_R. This would significantly weaken the contribution of the OLR to structures at large L_z. The relative position of the resonances will also vary with the inclination of the circular speed curve: negative/positive inclination leads to smaller/larger separation of the resonances.

Dependence on initial pattern speed

We have so far discussed the impact of the slowing rate while keeping the initial pattern speed fixed at $\Omega_{\mathrm{p0}} = 80\,\mathrm{km\,s^{-1}\,kpc^{-1}}$. We now take a look at the impact of Ω_{p0}. Fig. 2.19 plots $\bar{v}_R(L_z, \varphi)$ and $f(v_R, v_\varphi)$ for three different choices of Ω_{p0} increasing from top to bottom. The faster the bar is originally, the further inside the disk the original locations of the resonances will be, and thus the larger the volume of phase space swept by the resonance.

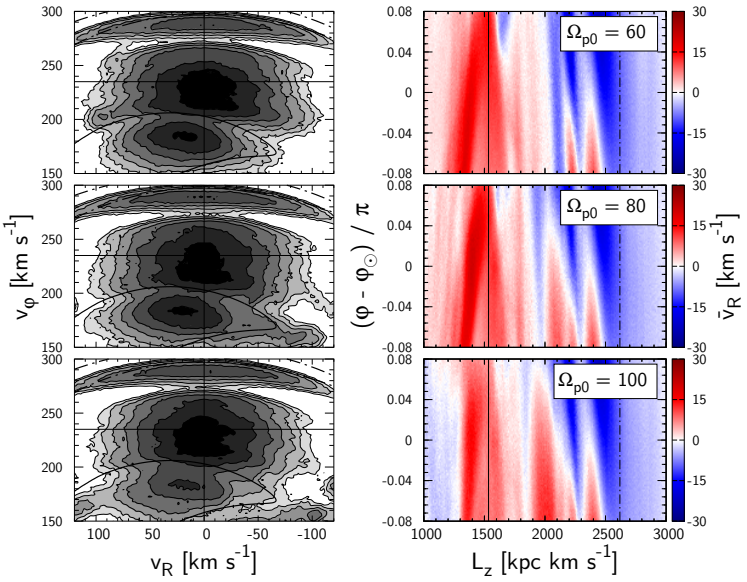

Fig. 2.19 Dependence on initial pattern speed: from top row, $\Omega_{p0} = 60$, 80, and 100 $\mathrm{km\,s^{-1}\,kpc^{-1}}$. The bar is rapidly decelerating ($A = 0.02, \eta = 0.004$) and the pattern speed now is $\Omega_p = 36$ $\mathrm{km\,s^{-1}\,kpc^{-1}}$.

However, the variation of the initial pattern speed do not result in a big difference here because the capturing rate is relatively low for a rapidly decelerating bar.

Determining the slowing rate of the bar

Beyond constraining the current pattern speed, modelling local kinematics perturbed by a decelerating bar yields measurement of the bar's slowing rate $\dot{\Omega}_p$. Fig. 2.20 shows the local velocity distribution of stars $f(\boldsymbol{v})$ for various values of bar amplitude A (columns) and slowing parameter η (rows) corresponding to the orange grid nodes in Fig. 2.14. The present pattern speed $\Omega_p = 35\,\mathrm{km\,s^{-1}\,kpc^{-1}}$ is determined by matching the location of the CR with the Hercules stream. The fraction of orbits trapped in the CR increases with increasing A and decreasing η in concordance with changes in retention/capture rates (see Fig. 2.14). We now need quantifiable statistics linked to this resonance occupation. A reasonable quantity is the *asymmetricity* of Hercules in the radial velocity v_R defined as the difference of fraction of stars with positive vs. negative v_R:

$$B \equiv \int_{v_{\varphi,\min}}^{v_{\varphi,\max}} \mathrm{d}v_\varphi \left[\frac{\int_0^\infty \mathrm{d}v_R f(\boldsymbol{v}) - \int_{-\infty}^0 \mathrm{d}v_R f(\boldsymbol{v})}{\int_{-\infty}^\infty \mathrm{d}v_R f(\boldsymbol{v})} \right]. \tag{2.56}$$

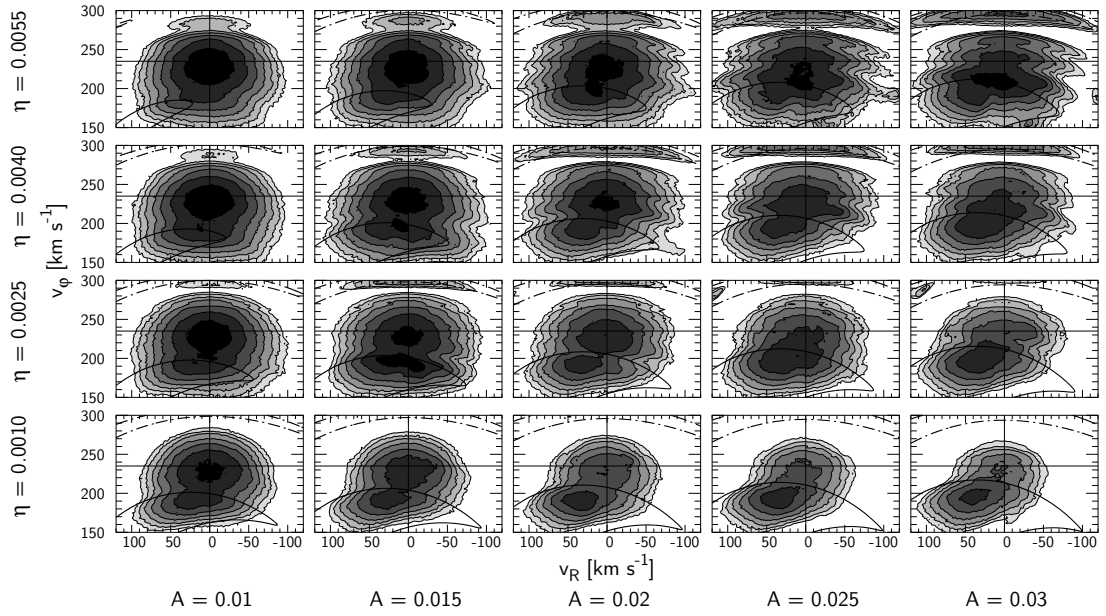

Fig. 2.20 Simulated distributions in local velocity space for the grid of bar strength A and slowing rate η shown in Fig. 2.14.

We choose $v_{\varphi,\min} = 100\,\mathrm{km\,s^{-1}}$ and $v_{\varphi,\max} = 210\,\mathrm{km\,s^{-1}}$ to approximately cover the CR. Fig. 2.21 shows the asymmetricity B evaluated on the parameter space (A, η). The white contours of B are gained from spline interpolation and the black contour marks the observed value ($B = 0.225$) from *Gaia* DR2 (Fig. 2.1 (a)). B increases towards large A and small η, and closely follows η/A marked by the green lines.

To estimate the posterior distribution of η and η/A by comparing B between simulations and observations, we need an appropriate prior on A. SBM15 compared their gas dynamic models to the inner Milky Way photometry and constrained the possible range of their bar amplitude parameter $A_\mathrm{s} \in [0.4, 0.8]$. To translate their A_s to our A, we must correct for the disparity between the models at large radius evident in Fig. 2.2. Since we need consistent perturbation strength near the CR, and not in the the inner bar region, we fit our model at radii beyond half of R_CR which yields $A \in [0.013, 0.026]$. To ensure a smooth prior obeying Cromwell's rule, we prescribe a normal distribution $P(A)$ with mean $\mu_A = 0.0195$ and standard deviation $\sigma_A = 0.0065$ within the allowed region, and a smooth

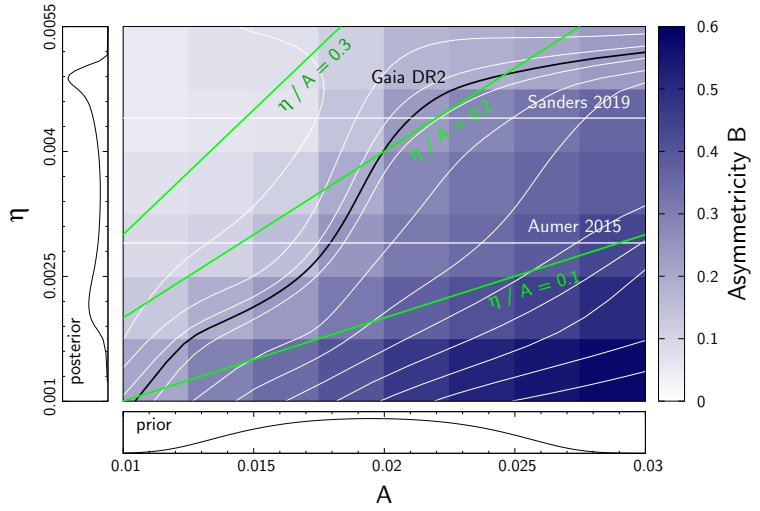

Fig. 2.21 Asymmetricity B in v_R in the Hercules region (see equation 2.56), plotted over bar strength A and slowing rate η. The colours map the simulated values, with the white contours gained from spline interpolation. The black contour marks the value obtained from *Gaia* DR2. We show the resulting posterior probability distributions for η on the left panel when using a prior distribution on A (bottom panel) inferred from SBM15.

cutoff at $A = \mu_A \pm \sigma_A$:

$$P(A) \propto \frac{\exp\left(-x^2/2\right)}{\frac{1}{2}\left(\exp|x^k| + 1\right)}, \quad x \equiv \frac{A - \mu_A}{\sigma_A} \tag{2.57}$$

where k controls the steepness of the cutoff. We choose $k = 4$. The prior $P(A)$ is shown at the bottom panel of Fig. 2.21. The posterior $P(\eta)$ is the product of the prior $P(A)$ and the slope of the observational curve $A(\eta)$ (the black curve in Fig. 2.21):

$$P(\eta) = P(A(\eta)) \, \frac{\mathrm{d}A}{\mathrm{d}\eta}. \tag{2.58}$$

The posterior $P(\eta)$, shown in the left panel of Fig. 2.21, has expectation value $\langle\eta\rangle = 0.0036$, median $\tilde{\eta} = 0.0039$, and standard deviation $\sigma_\eta = 0.0011$. The estimators are robust, i.e. they vary by less than 10% when extending the upper limits of the v_φ sampling range from $v_{\varphi,\max} = 170\,\mathrm{km\,s^{-1}}$ to $220\,\mathrm{km\,s^{-1}}$. Decrease in the steepness of the prior from $k = 4$ to $k = 2$ increases the standard deviation by 2.3% although merely changes the mean value of η (variation less than 0.2%). The estimated bar slowing rate η roughly agrees with values encountered in N-body simulations (horizontal white lines in Fig. 2.21): $\eta = 0.0029$ from Fig. 2 of Aumer & Schönrich (2015), and $\eta = 0.0044$ from Fig. 7 of Sanders et al. (2019). Using a current pattern speed $\Omega_\mathrm{p} = 35\,\mathrm{km\,s^{-1}\,kpc^{-1}}$, our η estimate translates to:

$\dot{\Omega}_\mathrm{p} = -\eta\Omega_\mathrm{p}^2 = (-4.5 \pm 1.4)\,\mathrm{km\,s^{-1}\,kpc^{-1}\,Gyr^{-1}}$. The posterior expectation value for the ratio $\eta/A = 0.18 \pm 0.03$ is more tightly constrained as expected. These estimates agree with the visual inspection/comparison of the velocity plane.

We caution however that this analysis is based on a pure $m = 2$ slowing bar model. There will be modifications due to e.g. the spiral arms which impact local kinematics on top of the bar (e.g. Sellwood et al., 2019). The successive emergence of transient spiral arms may change the resonant orbit population, and some models consider it shaping the Hercules stream (Hunt et al., 2018). This analysis is hence only a first step towards a more comprehensive model. Allowing for the additional impacts will greatly increase the number of free parameters, and estimating the bar slowing rate will necessitate making use of all available statistics, e.g. the spatial variation of the kinematic structures. Other missing factors that may affect the estimation of the bar slowing rate are (i) the neglected bar modes with $m > 2$, which will strengthen the minor resonances that sweeps the Solar neighbourhood before the CR, (ii) changes in bar amplitude, affecting the time dependence of the resonant capturing rate, and (ii) the choice of current bar pattern speed $\Omega_\mathrm{p} = 35\,\mathrm{km\,s^{-1}\,kpc^{-1}}$. We note that some studies advocate a somewhat higher Ω_p: Sanders et al. (2019) and Bovy et al. (2019) both derived $\Omega_\mathrm{p} = 41 \pm 3\,\mathrm{km\,s^{-1}\,kpc^{-1}}$ by applying the continuity equation to stars in the bulge, while Portail et al. (2017) deduced $\Omega_\mathrm{p} = 39 \pm 3.5\,\mathrm{km\,s^{-1}\,kpc^{-1}}$ with the made-to-measure models in the bar region, and Clarke et al. (2019) further fit that model to the proper motion data and derived $\Omega_\mathrm{p} = 37.5\,\mathrm{km\,s^{-1}\,kpc^{-1}}$ in closer agreement with our assumed pattern speed. A higher pattern speed $\Omega_\mathrm{p} = 38\,\mathrm{km\,s^{-1}\,kpc^{-1}}$ would lower our slowing rate estimate to $\eta = 0.0031 \pm 0.0008$ (using $v_{\varphi,\mathrm{max}} = 190\,\mathrm{km\,s^{-1}}$ to account for the shift of the CR). We note that several factors disfavour models with a higher Ω_p. Above $\Omega_\mathrm{p} \sim 37$, the upper separatrix of the CR would cut right through the Hercules stream. The alternative argument would be that the separatrix of the bar's CR corresponds to one of the interior structures of Hercules, e.g. separating the weak peak at $v_\varphi \simeq 180\,\mathrm{km\,s^{-1}}$ below the main clump at $v_\varphi \simeq 200\,\mathrm{km\,s^{-1}}$. However such models are inconsistent with the larger-scale structure observed, in particular with the azimuthal variation of stellar kinematics (Monari et al., 2019b) and with the arrow-shaped structure in the L_z-ϕ plane, which currently has no other explanation than the CR. Moreover, Binney (2020b) applied the Jeans' theorem

to trapped orbits in local velocity space and showed that the violation of Jean's theorem is minimized at a bar pattern speed $\Omega_\mathrm{p} = 36 \pm 1\,\mathrm{Gyr}^{-1} = 35.2 \pm 1\,\mathrm{km\,s}^{-1}\,\mathrm{kpc}^{-1}$.

2.6 Conclusions

While there have been extensive discussions in the literature interpreting the local velocity plane in Hipparcos and *Gaia* datasets with different values of the current pattern speed Ω_p of the bar, we find that the slowing rate $\dot{\Omega}_\mathrm{p}$ of the bar profoundly affects the observed substructure. Due to the highly significant and drastic impact of resonant sweeping found in this thesis, we argue that any results based on a constantly rotating bar pattern speed ought to be re-examined for their robustness against this process and how their parameters have been biased by the neglect of the deceleration.

The deceleration $\dot{\Omega}_\mathrm{p}$ of a Galactic bar is a theoretical requirement resulting from the angular momentum balance of the bar: the angular momentum gain from forcing gas onto the Galactic nuclear disk is (in a standard dark matter simulation) more than offset by the dynamical friction with the dark halo (and to a minor part the surrounding disk), which implies $\dot{\Omega}_\mathrm{p} < 0$ and thus the long-term deceleration/growth of the Galactic bar. While this has been theoretically known, we are not aware of any study that would have provided a pathway to observationally estimate the long term evolution of Ω_p. However, by neglecting perturbations other than the bar and by investigating the effect on resonance occupation using a simple slowing bar model where the pattern speed is modelled to decline inversely proportional to time, we now provide an estimate of the current slowing rate of the bar to be $\dot{\Omega}_\mathrm{p} = (-4.5 \pm 1.4)\,\mathrm{km\,s}^{-1}\,\mathrm{kpc}^{-1}\,\mathrm{Gyr}^{-1}$ at current pattern speed $\Omega_\mathrm{p} = 35\,\mathrm{km\,s}^{-1}\,\mathrm{kpc}^{-1}$.

The deceleration of the bar also resolves three major issues with the appearance of the Hercules stream/corotation resonance: i) The observed Hercules stream is highly asymmetric in radial velocity v_R, featuring a strong outward motion. This asymmetry is underpredicted by models with a constantly rotating bar. ii) Resonant capturing by the sweeping resonance allows for larger occupation numbers than in a steadily rotating bar model, thus fitting the observed density with a reasonable bar strength. iii) The stars captured near the surface of the resonance allow for a much stronger eye-shaped (or

spear-shaped for the observable Solar neighbourhood) feature in the mean radial velocity $\bar{v}_R$ of the L_z-φ plane, which in the observed Solar neighbourhood data explains the two strong positive $\bar{v}_R$ features near $L_z \sim 1400$ and $\sim 1600\,\mathrm{kpc\,km\,s^{-1}}$ together with their inclination against azimuth. To facilitate point (ii), we have examined how resonant capturing and retention/dragging vary with the deceleration parameter $\eta = -\dot{\Omega}_\mathrm{p}/\Omega_\mathrm{p}^2$ and the amplitude A of the bar. We find that η/A can be used as a good indicator for retention and capture and that expectations for this parameter from the observationally estimated strength A and the expected slowing rate η from N-body simulations in a typical dark matter halo place the parameter in the region, where the v_R asymmetricity of the simulated local velocity plane matches that of the *Gaia* data.

We stress that this work is largely of an exploratory and qualitative nature. We have not attempted to go beyond the simplest possible $m = 2$ model and we have restricted ourselves to a 2D in-plane analysis. High order modes and vertical motions would bring additional resonances and more complications, which we found would have reduced the clarity of this work. We remark though that our first exploratory simulations were performed in full 3D and confirmed the same qualitative answers as presented here in 2D. Further, for the sake of simplicity, we omitted several processes that we consider to be important: spiral structure will overlay the suggested pattern, and by its transience should knock stars in and out of resonances, changing the occupation of resonant orbits. A similar role is taken by giant molecular clouds, galaxy mergers, subhalo passages, and not least, the possible jitter of the bar pattern speed itself.

In the next chapter, we will dig into the detailed phase-space structure of resonances and explore its relation with stellar properties.

CHAPTER 3

Tree-ring structure of Galactic bar resonance

3.1 Abstract

In this chapter, we present an evidence for the bar's slowdown from the chemical distribution of stars within the trapped phase-space. When the bar slows down, its resonance sweeps radially outwards through the galactic disk while growing in volume, thereby sequentially capturing new stars at its surface (separatrix). Since trapped stars conserve their action of libration, which measures the relative distance to the resonance centre, the order of capturing is preserved: the surface of the resonance is dominated by stars captured recently at large Galactocentric radius, while the core of the resonance is occupied by stars trapped early at small radius. The slow-down of the bar thus results in a rising mean metallicity of trapped stars from the surface towards the centre of the resonance as the Galaxy's metallicity declines towards large radii. This argument, when applied to Solar neighbourhood stars, allows a novel precision measurement of the bar's current pattern speed $\Omega_\mathrm{p} = 35.5 \pm 0.8\,\mathrm{km\,s^{-1}\,kpc^{-1}}$, placing the corotation radius at $R_\mathrm{CR} = 6.6 \pm 0.2\,\mathrm{kpc}$. With this pattern speed, the corotation resonance precisely fits the Hercules stream in agreement with kinematics. Beyond corroborating the slow bar theory, this measurement implies a deceleration of the bar of more than 24% since its formation and thus the angular momentum transfer to the dark halo by dynamical friction. The measurement therefore

supports the existence of a standard dark-matter halo rather than alternative models of gravity.

3.2 Introduction

In the previous chapter, we have shown that local stellar kinematics favors a slowing bar, which naturally explains the strength, asymmetry, and azimuthal variation of the Hercules stream with its corotation resonance that has been migrating from further inside the Galaxy. However, kinematics only does not make the slowdown of the bar an absolutely necessary (even though a sufficient) condition to reproduce the Hercules stream, as one may achieve a similar phase space configuration from perturbation by spiral arms (e.g. Hunt et al., 2018) and merging satellites (e.g. Minchev et al., 2009). In this chapter, we therefore investigate the metallicity distribution in local phase-space to find a chemo-dynamical structure that is unique to the bar's slowdown. For this, we must first understand how stars get populated into the bar's resonances.

Orbits resonantly trapped by the bar occupy a distinct volume of phase space bounded by the separatrix. When the bar decelerates, these resonant islands sweep radially outwards through the stellar phase-space. As resonances migrate outwards, their phase-space volume generally grows, so surrounding stars are sequentially captured into the resonance from the separatrix. Once in resonance, these trapped stars are dragged along with the resonance while approximately conserving their action of libration, which quantifies the amplitude of motion around the resonance. As a result, stars trapped at the early epoch of bar formation remain confined to the core of the trapped phase-space, while newly trapped stars fill in the phase space opened up by the expanding separatrix — the bar's resonance evolves analogously to the rings of a growing tree where new layers of cells form at the bark and continuously record the climate condition of that time. Since stars trapped later originate from larger radii with typically lower metallicity, the deceleration history of the bar will be imprinted on the metallicity distribution inside the resonance.

The tree-ring structure of the bar resonance has a bi-directional application: Once the current pattern speed of the bar and thus the location of the resonance is known, we can

read out the history of bar evolution by looking at the variation of stellar metallicity with distance to the resonance centre. Conversely, we can pin down the current bar pattern speed by demanding the metallicity inside the resonance to rise from the surface towards the core as expected from the deceleration of the bar.

In this thesis, we take both approaches. We first posit the recently favored slow bar model [1] and analyse the tree-ring structure inside the corotation resonance (Hercules stream). Using stellar metallicity derived from the colors and magnitudes of the *Gaia* sample, we show that the Hercules stream exhibits a monotonic increase in metallicity towards the resonance centre as predicted by our slowing bar model. We then constrain the current bar pattern speed from the metallicity ordering inside the resonance. We show that demanding a monotonic trend in metallicity inside the corotation resonance of the bar narrowly constrains the current pattern speed to $\Omega_\mathrm{p} = 35.5 \pm 0.8\,\mathrm{km\,s^{-1}\,kpc^{-1}}$ where the corotation resonance perfectly fits the Hercules stream in excellent agreement with kinematic models (e.g. Pérez-Villegas et al., 2017; Monari et al., 2019a; D'Onghia & L. Aguerri, 2020; Binney, 2020b; Chiba et al., 2021) as well as the the latest bar/bulge model (Clarke et al., 2019; Clarke & Gerhard, 2021).

In the following section, we provide a brief description on resonant dynamics which underlies our analysis. In section 3.4, the method of estimating metallicity from *Gaia* photometry is described and tested with open clusters for which the metallicity is measured independently from spectroscopy. In section 3.5, we present the mean metallicity map in the local velocity and action plane, and subsequently constrain the bar pattern speed by evaluating the likelihood of monotonic increase towards the resonance centre. Systematic errors due to sample selection and uncertainties in model parameters are reported. Section 3.6 sums up.

[1] Here 'slow' vs. 'fast' does not refer to the ratio between corotation radius and bar length as in studies of external galaxies, but exclusively describes slow pattern speed $\Omega_\mathrm{p} \lesssim 40\,\mathrm{km\,s^{-1}\,kpc^{-1}}$ instead of the formerly favoured fast models with $\Omega_\mathrm{p} \gtrsim 50\,\mathrm{km\,s^{-1}\,kpc^{-1}}$. See section 3.5.4 for a discussion.

3.3 Theoretical background

3.3.1 Adiabatic invariants of resonantly trapped orbits

As explained in section 2.3, orbits near resonance exhibit slow motion around the resonance which can be modelled by averaging the Hamiltonian over the fast motions. The averaged Hamiltonian takes a form similar to that of a pendulum and the slow dynamics of trapped orbits is described in the slow angle-action plane $(\theta_\mathrm{s}, J_\mathrm{s})$ with one degree of freedom, where

$$\theta_\mathrm{s} \equiv N_R\theta_R + N_\varphi\left(\theta_\varphi - \int dt\ \Omega_\mathrm{p}\right) \quad \text{and} \quad J_\mathrm{s} \equiv \frac{J_\varphi}{N_\varphi}. \tag{3.1}$$

The phase-space in $(\theta_\mathrm{s}, J_\mathrm{s})$ is split by the separatrix into regimes of libration (trapped orbits), and circulation (non-trapped orbits). Trapped orbits have two approximate constants of motions: the fast action $J_\mathrm{f} \equiv J_R - (N_R/N_\varphi)J_\varphi$ (J_R in the case of corotation resonance), and the action of libration

$$J_\ell \equiv \frac{1}{2\pi}\oint d\theta_\mathrm{s}\ J_\mathrm{s}(\theta_\mathrm{s}), \tag{3.2}$$

which characterizes the amplitude of motion around the resonance and takes maximal value at the separatrix. The conservation of J_ℓ is subject to the adiabaticity condition that the libration period, which diverges to infinity at the separatrix, is significantly smaller than the migration timescale of the resonance. J_ℓ is thus not conserved near the separatrix, which allows orbits to enter or leave the resonance there.

3.3.2 Increase in phase-space volume of resonance

The phase-space volume occupied by each resonance is represented by the libration action evaluated at the separatrix $J_{\ell,\mathrm{sep}}$ (equation 2.48). Figure 3.1 shows $J_{\ell,\mathrm{sep}}$ of the CR at $J_\mathrm{f} = 50\,\mathrm{kpc\,km\,s^{-1}}$ as a function of the decreasing pattern speed. We present various bar models (section 2.3.2) with their strength varying according to

$$A(t) = A_1\left[\frac{\Omega_\mathrm{p}(t)}{\Omega_\mathrm{p1}}\right]^{-\gamma}, \tag{3.3}$$

such that it takes the current amplitude $A_1 = 0.02$ at the current pattern speed $\Omega_\mathrm{p1} = 35\,\mathrm{km\,s^{-1}\,kpc^{-1}}$. The functional form of $\Omega_\mathrm{p}(t)$ is irrelevant here but, for instance, with $\Omega_\mathrm{p}(t) \propto t^{-1}$ as assumed in our simulations, the bar strength scales as $A(t) \propto t^\gamma$. We show

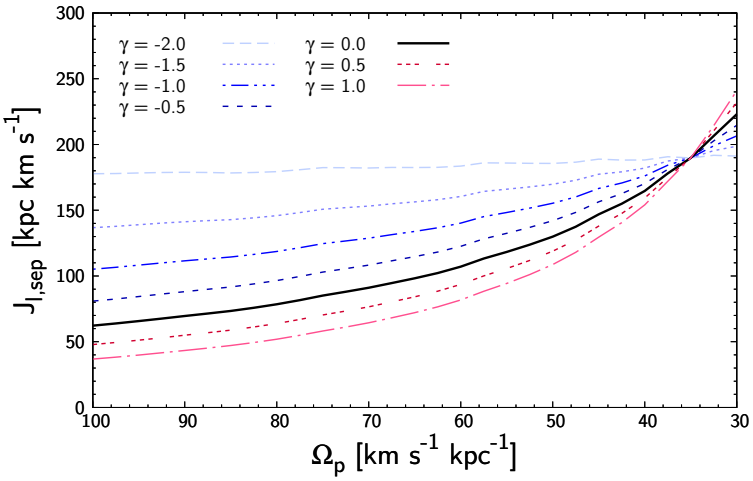

Fig. 3.1 Phase-space volume of the bar's corotation resonance characterized by the libration action at the separatrix as a function of the decreasing pattern speed. The fast action is fixed to $J_\mathrm{f} = 50\,\mathrm{kpc\,km\,s^{-1}}$. Models with different bar growth/decay rate γ are plotted. All models take the same current bar amplitude $A = 0.02$ at the current pattern speed $\Omega_\mathrm{p} = 35\,\mathrm{km\,s^{-1}\,kpc^{-1}}$. The resonance volume generally grows unless the bar amplitude decay rapidly ($\gamma \lesssim -2$).

all cases where A is constant ($\gamma = 0$, black), decreases ($\gamma < 0$, blue), or increases ($\gamma > 0$, red). The phase-space volume of the resonance $J_{\ell,\mathrm{sep}}$ increases monotonically unless the bar weakens significantly ($\gamma \lesssim -2$) while slowing down. N-body simulations show that deceleration of the bar is typically accompanied by an increase in bar amplitude (e.g Debattista & Sellwood, 2000; Martinez-Valpuesta et al., 2006; Ghafourian et al., 2020) except at the early buckling phase, so we expect the resonance to grow and thus continuously sweep up stars as it moves outwards.

The reason behind the increase in trapped volume, despite the constant or even decreasing bar amplitude, is the drop in the quantity $G = \partial\Omega_s/\partial J_\mathrm{s}$ (equation 4.22) towards the outer galaxy. This is evident in equation (2.48) which reads $J_{\ell,\mathrm{sep}} \sim |G|^{-1/2}$. G quantifies the gradient of orbital frequencies with respect to actions. In the inner galaxy, $|G|$ is large, i.e. a small change in actions results in a large change in orbital frequencies, which means that trapped orbits with frequencies close to the resonance condition are confined to a narrow region of action space. In contrast, in the outer galaxy, the orbital frequencies are less sensitive to changes in actions (small $|G|$), which allows a larger region of action space

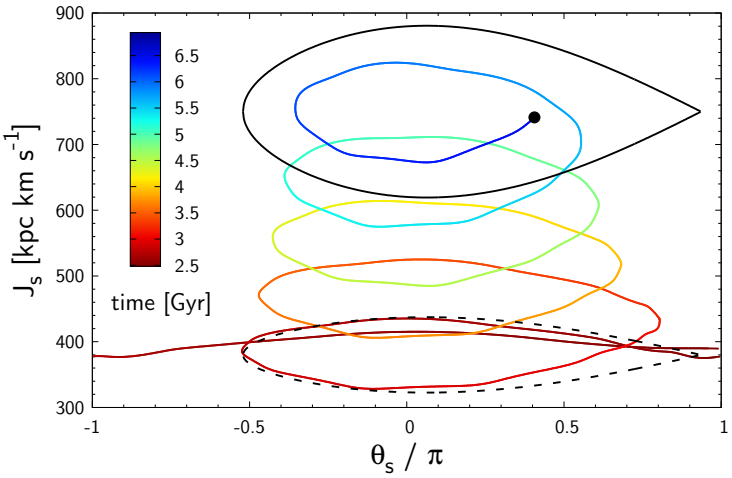

Fig. 3.2 Trajectory of a test particle trapped and dragged by the corotation resonance of a decelerating bar where the colour indicates time. The black curves represents the separatrix at the time of capture (dashed) and at the end of the simulation (solid). The star streams along the separatrix at the moment of capture but is then detached from the separatrix as the volume of resonance grows.

to be trapped in resonance. It can be trivially shown that $J_{\ell,\mathrm{sep}}$ scales as $\sqrt{A}v_c^2/\Omega_\mathrm{p}$ in the epicycle limit which explains why $J_{\ell,\mathrm{sep}}$ is approximately constant when $\gamma = -2$.

3.3.3 Tree-ring structure of resonance

When a resonance grows in volume, a fraction of stars outside the resonance that are passed by the separatrix may be captured into the resonance depending on their angular phase (see Appendix 3.A for the angle-averaged capture probability). Figure 3.2 shows a typical stellar trajectory captured into the sweeping resonance. The star initially circulates at $J_\mathrm{s} \sim 400\,\mathrm{kpc\,km\,s^{-1}}$ above the resonance, while the separatrix approaches from below. The star then passes the separatrix, becomes trapped in the resonant region and gets dragged towards larger J_s (and thus towards larger angular momentum J_φ) while keeping its J_ℓ and J_R approximately constant. The black curves depict the separatrix (equation 2.48) at the time of trapping (dashed) and at the final time (solid).

The conservation of the libration action J_ℓ has an interesting consequence. Since the phase space volume of the resonance grows as the bar slows down, which is directly visible in Fig. 3.2 as the increase in volume occupied by the separatrix, the gap between the separatrix and the trapped orbits grows. Due to Liouville's theorem, this interspace must

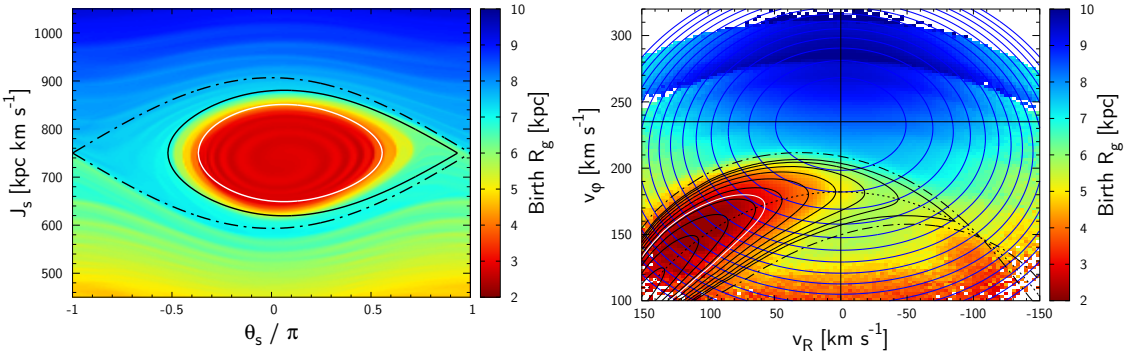

Fig. 3.3 Test-particle simulation of the Galactic disk perturbed by a decelerating bar. Left panel: Mean birth guiding radius in the slow angle-action plane at $J_R = 10\,\mathrm{kpc\,km\,s^{-1}}$. The white line marks the contour of constant libration action with a value equivalent to that at the separatrix of the initial bar, while the black solid and dot-dashed curves mark the current separatrix of the moving and resting resonance, respectively. Right panel: Mean birth guiding radius in local velocity space. The blue and black curves are contours of constant J_R and $\hat{J}_\ell$.

be filled with newly trapped stars. Hence the resonance builds up layers of trapped stars like a tree grows rings at its bark.

As demonstrated with our test particle simulation in the left panel of Fig. 3.3, this separates the final resonance into two regimes: the core and the growth region. The initial core, marked by the white curve mapping the original separatrix onto the current volume, contains a relatively homogeneous population trapped initially from further inside the disk at the formation of the bar. Measuring the core can inform us about the initial size and location of the resonance. Between the core and the current separatrix (solid black) lies the growth region where the birth radius monotonically increases towards the separatrix as the fresh layers accreted at later times and thus at larger angular momentum.

Note that the initial formation of the bar introduce a slight phase-space spiral inside the resonance. Since the period at the separatrix is infinite, the number of wrappings reflects the number of libration periods at the core of the resonance since bar formation. The shape of the phase-space spiral could be used to constrain the change in libration period, which is determined by the shape of the effective potential of the resonance, and ultimately give an estimate on the age of the bar. However, at the current level of *Gaia* data this pattern is not yet detectable.

The black dot-dashed curve shows the separatrix calculated at fixed pattern speed, while the black solid curve takes into account the contraction of the separatrix due to the deceleration (section 2.3.5). Only stars within the latter are bound to the resonance, while stars in between are either in transit between the circulating zones or are becoming caught by the resonance.

To test this on observational data, we need to overcome two observational challenges: (i) the Sun is far from the Lagrange points and the available sample from *Gaia* only touches the outskirts of the corotation resonance so currently we can only see stars of relatively large J_ℓ or J_R that travel far enough from the Lagrange point to reach the Solar neighbourhood. The right panel of Fig. 3.3 shows how resonances can be identified in the velocity plane of radial vs. azimuthal velocity at the Solar neighbourhood, again coloured by the original guiding centre radii of stars. To guide the eye, we superposed contours of constant J_R in blue equally spaced by $30\,\mathrm{kpc\,km\,s^{-1}}$, and J_ℓ normalized by the value at the separatrix ($\hat{J}_\ell \equiv J_\ell/J_{\ell,\mathrm{sep}}$) in black with 0.1 spacing. The outermost black curve corresponds to the separatrix (as in the upper panel, dot-dashed for a *resting* resonance and solid for a *moving* resonance). The dotted black arch represents the location where the resonance condition is exactly satisfied. Although the centre of the resonance cannot be observed, we can see the mean birth radius decreasing towards the initial core of the resonance marked by the white curve. (ii) In practice, we cannot measure the stellar position at trapping, so we employ the metallicity gradient of the Galactic disk. The metallicity of stars increases towards the Galactic centre, so metallicity is a proxy for radius at trapping with one caveat: older stars tend to be more metal poor and have larger radial action (more eccentric), so we need to filter this out when investigating the metallicity trends in J_ℓ.

3.4 Method of metallicity estimation

The metallicity of main sequence stars can be inferred from the position across the main sequence in the colour-magnitude diagram. In general, stars in the main sequence with higher metallicity appear redder. The reason of reddening is two-fold: (i) Metals enhance the internal opacity of the star which impedes radiative transport and hence forces the star

to swell up with a lower surface temperature. (ii) Metals have most of their absorption lines in the UV-blue region. We restrict our analysis to stars sufficiently low on the main sequence (i.e. large absolute magnitude) so that their colours and magnitudes do not vary significantly with stellar age. In this region, the colour-magnitude position directly encodes the metallicity of a star, with some contamination from binaries and extinction (the extinction vector runs almost parallel to the main sequence, limiting the impact of reddening uncertainties on metallicity estimates).

3.4.1 Sample selection

We use stellar samples in the Solar neighbourhood (distance from Sun $s < 0.3\,\mathrm{kpc}$) taken from the *Gaia* DR2 RV catalogue (Gaia Collaboration et al., 2018; Cropper et al., 2018; Sartoretti et al., 2018; Katz et al., 2019) with parallax offset and distance estimation from Schönrich et al. (2019). We adopt the Solar Galactocentric radius $R_0 = 8.2\,\mathrm{kpc}$ (Gravity Collaboration et al., 2019), Solar Galactocentric azimuth with respect to the bar major axis 30° (Wegg et al., 2015), Solar distance from the disk plane $\mathrm{z}_\odot = 0.02\,\mathrm{kpc}$ (Joshi, 2007), and Solar velocity $(v_{R\odot}, v_{\varphi\odot} - v_\mathrm{c}, v_{\mathrm{z}\odot}) = (-11.1, 12.24, 7.25)\,\mathrm{km\,s^{-1}}$ (Schönrich et al., 2010). We apply quality cuts on parallax $p/\sigma_\mathrm{p} > 10$ and restrict samples to those with Galactic latitude $b > 10°$ to minimize the reddening effect by interstellar extinction. As the resonance lines are expected (and measured, see Friske & Schönrich 2019) to exert a mild drift with vertical energy, we exclude stars having $E_z > 200\,\mathrm{km^2\,s^{-2}}$ corresponding to a maximum vertical velocity of $v_z = 20\,\mathrm{km\,s^{-1}}$ and a maximum vertical excursion from the Galactic plane of $z \sim 0.3\,\mathrm{kpc}$. The vertical potential is evaluated using the Milky Way model of McMillan (2017b).

3.4.2 Colour-magnitude diagram

Figure 3.4 shows the colour-magnitude diagram of the selected samples with stellar isochrones at (a) fixed age (4 Gyr, blue) and (b) fixed metallicity ([M/H] = 0, red) superimposed. The isochrones are constructed using PARSEC version 1.2S (Bressan et al., 2012). The *Gaia* passbands are taken from Weiler (2018). As discussed at the beginning of this section, an increase in metallicity shifts the isochrones redwards, while age dependence

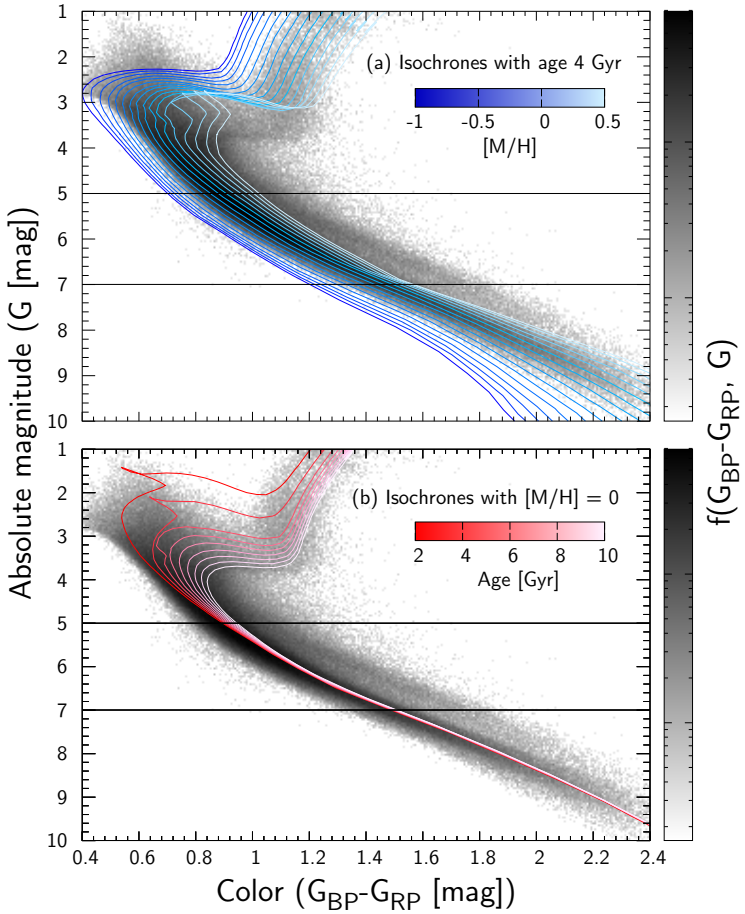

Fig. 3.4 Colour-magnitude diagram of the selected stellar samples in the Solar Neighbourhood. The upper panel overlays isochrones with different metallicities at fixed age 4 Gyr, while the lower panel plots isochrones with different age at fixed metallicity [M/H] = 0. The binary sequence is visibly detached above the [M/H] = 0.5 isochrone, where we apply the upper metallicity cut. The two black horizontal lines show our upper/lower limit in magnitude G.

only has an effect near the turn-off region, i.e. at the blue-bright end. To estimate the metallicity of individual stars, we generate isochrones with fixed age (4 Gyr by default) for metallicities [M/H] between −1.0 and 0.5 dex in 0.05 dex increments, and linearly interpolate them in magnitude G. When evaluating the mean metallicity, we cut samples near the main-sequence turnoff point ($G > 5$). We also apply an upper limit in magnitude ($G < 7$) since the selection function in distance becomes more skewed with increasing magnitude. Finally, we discard samples with metallicity beyond [M/H] = 0.5 since they are most likely to be binary or double stars mistaken for a bright single star.

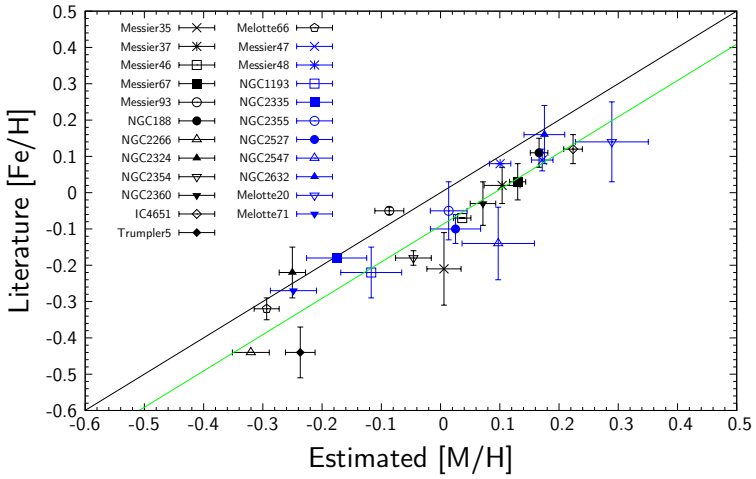

Fig. 3.5 Metallicity of open clusters measured by our method compared with literature values (Netopil et al., 2016). Data points without vertical error bars are those lacking uncertainty reports in the reference. Open clusters with more than 100 stellar samples are shown in black while those with less than 100 but more than 10 sample stars are shown in blue. The green line, linearly fitted to the data, quantifies the offset 0.091 ± 0.017 dex of our metallicity estimation due to contamination from binary/double stars.

3.4.3 Calibration of photometric metallicity

Due to the contamination by binary/double stars, the metallicity estimated from photometry is generally biased towards high metallicity. To quantify this bias, and to validate our method, we applied our technique to open clusters with metallicities known from spectroscopic measurement. Fig. 3.5 compares our estimated metallicity [M/H] with the literature values of [Fe/H] taken from Netopil et al. (2016). We select *Gaia* samples within 20 mas from the cluster core and apply narrow cuts in proper motions around the peak ($\Delta\mu \sim 1\,\mathrm{mas\,yr^{-1}}$) to extract members of the clusters. The black data show metallicity inferred from stellar cluster with more than 100 sample stars, while the blue data show those with less than 100 but more than 10 samples. The metallicity estimated from *Gaia* photometry agrees well with that from spectroscopic surveys over a wide range of metallicity up to a constant offset[2] (0.091 ± 0.017 dex) shown in green line (linear fit). The result validates our method and demonstrates that we could compare our results quantitatively with spectroscopic metallicity [Fe/H] by subtracting the constant offset. We caution however that the literature values contain uncertainties beyond the shown

[2]Some of the bias may originate from variations in α enhancement (Casagrande et al., 2011).

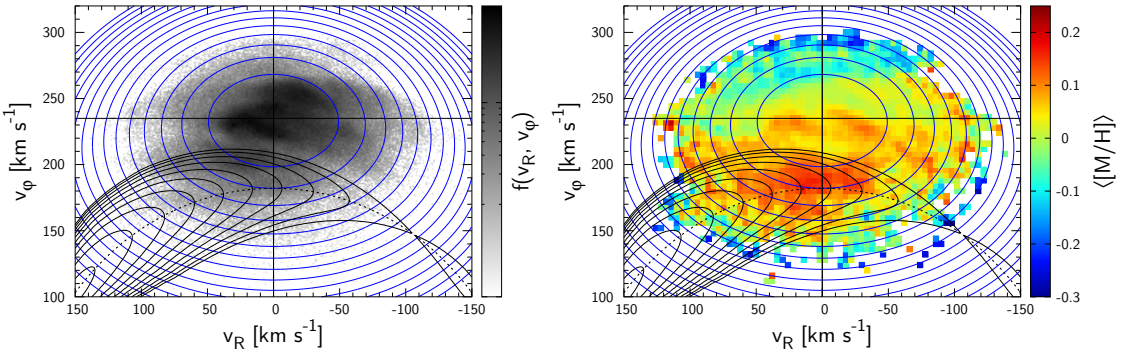

Fig. 3.6 Density (left panel) and mean metallicity (right panel) of Solar neighbourhood stars in local velocity plane. Superposed are the uniformly spaced contours of constant J_R in blue and $\hat{J}_\ell \equiv J_\ell / J_{\ell,\mathrm{sep}}$ in black. The dotted black curve marks the location where the resonance condition is exactly satisfied. The mean metallicity is calculated by fitting stellar isochrones to samples in each velocity cell of width $4\,\mathrm{km\,s^{-1}}$. The Hercules moving group is relatively metal rich indicating an origin at small radii. As we go around the blue contours of constant J_R (in particular the three innermost ellipses), the metallicity rises as we cross the black curves towards small $\hat{J}_\ell$ in agreement with expectation from a decelerating bar model. Note that the colour palette is chosen so that metal-rich/poor stars appear with similar colour as small/large birth R_g in Fig. 3.3.

error bars as evidenced by the scatter between different catalogues: e.g. Messier 67 has a metallicity of 0.03 ± 0.05 dex according to Netopil et al. (2016) but Carrera et al. (2019) reports 0.07 ± 0.03 dex while Leaman (2012) reports -0.19 ± 0.042 dex.

3.5 Results

3.5.1 Mean metallicity map in local velocity/action space

The left-hand panel of Fig. 3.6 shows the density of stars in the local velocity plane. As in Fig. 3.3, we overlay contours of constant J_R (blue) and $\hat{J}_\ell$ (black) at $\Omega_\mathrm{p} = 35\,\mathrm{km\,s^{-1}\,kpc^{-1}}$. The stellar group concentrated around $(v_R, v_\varphi) \sim (30, 190)\,\mathrm{km\,s^{-1}}$ is the 'Hercules stream'. Since the studies by Dehnen (1999b, 2000), the origin of the Hercules stream was suspected to be the non-resonant x_2 orbits circulating below the outer Lindblad resonance (OLR) of a fast bar ($\Omega_\mathrm{p} \gtrsim 50\,\mathrm{km\,s^{-1}\,kpc^{-1}}$) (e.g. Antoja et al., 2014; Fragkoudi et al., 2019). However studies in the past few years have increasingly favoured a slow bar ($\Omega_\mathrm{p} \lesssim 40\,\mathrm{km\,s^{-1}\,kpc^{-1}}$) in agreement with dynamical models fitted to the kinematics of inner gas (Sormani et al., 2015b) and red clump stars in the bar/bulge region (e.g. Portail et al., 2017; Clarke et al.,

2019). In a slow bar model, the Hercules stream consists of orbits trapped in the corotation resonance (CR) of the bar (e.g. Pérez-Villegas et al., 2017; Monari et al., 2019a; D'Onghia & L. Aguerri, 2020; Binney, 2020b). This model has the problems that the deformation in the velocity distribution predicted by a constantly rotating bar is not strong enough and less asymmetric in v_R compared to observations. However these problems are resolved by a slowing bar where the CR contracts towards positive v_R and brings stars at high phase-space density from the inner disk (Chiba et al., 2021). There are also models linking the Hercules with the 1:4 resonance of the bar (e.g. Hunt & Bovy, 2018; Asano et al., 2020) or with transient spiral arms (e.g. Hunt et al., 2018), making the debate indecisive with kinematics only. We will show however that the decelerating slow bar model is singled out by the metallicity trend of Hercules stars. For an extensive kinematics comparison between different bar models, see Trick et al. (2021).

Figure 3.6 right-hand panel colours the local velocity plane in mean metallicity. A similar plot is given by Antoja et al. (2017) based on spectroscopic metallicity obtained from the RAVE survey and the Geneva-Copenhagen survey. The overall distribution displays the anticipated trends: the decline of metallicity towards larger v_φ (or respectively $J_\varphi = v_\varphi R_0$, where R_0 is the Solar Galactocentric radius), reflecting the negative metallicity gradient in Galactocentric radius, and the lower metallicities at larger J_R, resulting from the age-metallicity and age-dispersion relationships. However, the most conspicuous feature is the high metallicity clump directly at the position of the Hercules stream. This has already been reported as early as Grenon (1972) from the Geneva photometry and Grenon (1999) using the Hipparcos catalogues. Since Hercules is an in-plane stellar stream and is not a dissolved cluster (Bovy & Hogg, 2010) nor an accreted population (Kushniruk et al., 2020), the only natural explanation for its high metallicity is that it originates from the inner Galaxy. This is expected in a decelerating slow bar model since stars trapped in the CR have been dragged from small radii as the bar decelerates (Halle et al., 2018; Chiba et al., 2021). In contrast, this observation is unexplainable with a fast bar model where Hercules stars are identified as non-resonant orbits that cannot have been dragged while the resonance swept. The metal-rich nature of Hercules is thus a strong indication that it is composed of resonantly trapped orbits rather than non-trapped orbits. Antoja

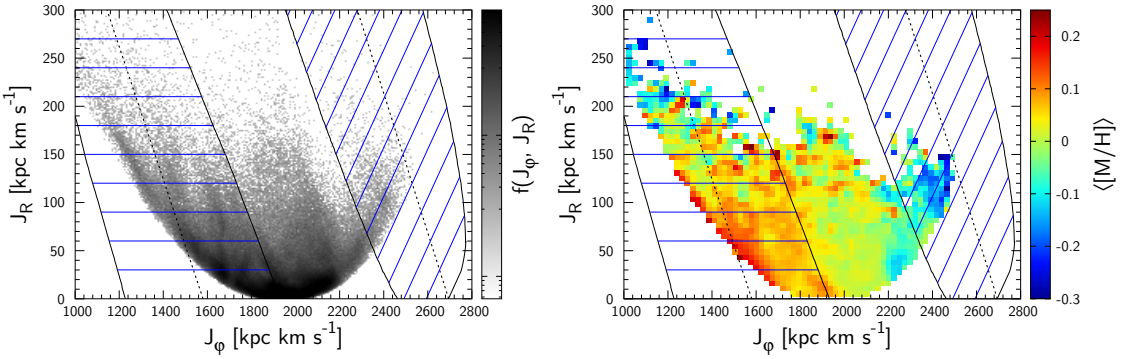

Fig. 3.7 Density (left panel) and mean metallicity (right panel) of local stars in action space. The metal poor population appears at high J_φ (stars visiting the sun from the outer disk) and at high J_R (old stars). The dotted black lines are the CR (left) and the OLR (right) and the solid black lines mark the maximum excursion achieved by trapped orbits librating along contours of constant J_f (blue lines).

et al. (2017) proposed that, in the context of a non-decelerating fast bar model, the high metallicity of Hercules may be explained by the non-resonant x_2 orbits which have a slightly smaller mean radius than orbits trapped in the OLR. However, as we show in Appendix 3.C using a simple age-metallicity-dispersion relation, a fast bar model is incapable of reproducing the observed high metallicity at the position of the Hercules as the difference in birth radii between trapped and non-trapped orbits is too small (see Fig. 3.15). An analogous argument applies to a non-decelerating slow bar model. Only the decelerating slow bar model can bring the metal rich stars from far inside the disk sufficiently to achieve a metallicity above 0.2 dex as in the data.

Figure 3.7 shows the density and mean metallicity in local action space where the general trend is best observed: the metallicity decreases towards large angular momentum due to the increase in birth radius but also towards large radial action due to the increase in age. There is clearly additional substructure, which can, however, be explained by resonances. Particularly, the metal-rich Hercules stream on the left side of the plot is fitted well with the corotation resonance where the black boundaries mark the the maximum excursion of trapped orbits librating along constant $J_\mathrm{f} = J_R$ (blue lines). At the predicted location of OLR, there is a clear over density (left panel) comprised of metal poor stars (right panel). The distance by which the stars at the OLR can be dragged is limited by the observed radial action; conservation of $J_\mathrm{f} = J_R - J_\varphi/2$ implies that the stars acquire a

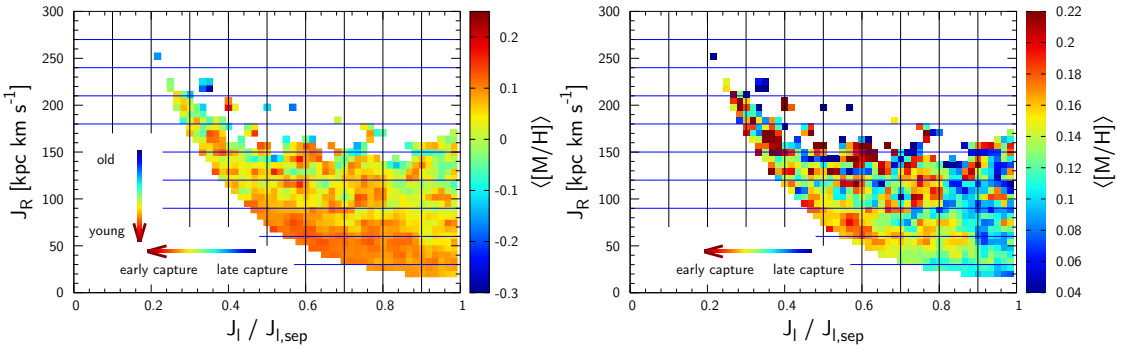

Fig. 3.8 Mean metallicity of local stars trapped at the bar's corotation resonance as a function of the resonant actions. Bar pattern speed set to $\Omega_\mathrm{p} = 35\,\mathrm{km\,s^{-1}\,kpc^{-1}}$. Left panel: Metallicity map on resonant actions $\hat{J}_\ell$ and J_R. The rectilinear grid corresponds to the contours of constant $\hat{J}_\ell$ and J_R drawn in the local velocity plane (Fig. 3.6). Metallicity is predicted to increase in the directions indicated by the multi-coloured arrows. Right panel: Same plot after removing the metallicity trend in J_R ($\mathrm{d[M/H]}/\mathrm{d}J_R = -0.00078\,\mathrm{dex\,kpc^{-1}\,km^{-1}\,s}$) to highlight the metallicity trend in $\hat{J}_\ell$.

fixed amount of radial action per angular momentum gained, and so the stars observed at e.g. $J_R = 100\,\mathrm{kpc\,km\,s^{-1}}$ have been dragged in J_φ by no more than $\Delta J_\varphi = 200\,\mathrm{kpc\,km\,s^{-1}}$ and thus we do not expect high metallicity. In fact, the orientation of resonant dragging in (J_R, J_φ) space, which is determined by the resonant vector (N_R, N_φ)[3], casts strong limitation on the origin of the Hercules: since any outer resonances with $N_R > 0$ will inevitably pump stars up towards larger J_R while dragging them towards the outer disk, they cannot explain the metal-rich Hercules stars which we observe even at low J_R. The only resonance that can carry stars with high metallicity from the inner disk without increasing their eccentricity is the corotation resonance ($N_R = 0$). Therefore the slow bar is the only model that can explain the metal-rich nature of Hercules using resonantly trapped orbits.

We now map the metallicity onto the resonant actions of the CR to conduct the tree-ring analysis. For this, we have to set parameters for the bar which determine the mapping from $(\boldsymbol{x}, \boldsymbol{v})$ to $(\hat{J}_\ell, J_R)$ for each star within the region of the corotation resonance. The resulting mean metallicity in the $(\hat{J}_\ell, J_R)$ plane is shown in Fig. 3.8. The uncertainty of $\hat{J}_\ell$ propagated from the uncertainties in the *Gaia* data is at the percentage level (Appendix 3.B), so it would not qualitatively affect the signal. The contours of constant $\hat{J}_\ell$ and J_R

[3]The direction of resonant dragging also depends on the sign of $G \equiv \partial^2 H_0 / \partial J_\mathrm{s}^2$ which is identical for resonances at $N_R \geq 0$ (Chiba et al., 2021).

now form a rectilinear grid. The x-axis ranges between 0 (the resonance centre) and 1 (the separatrix), meaning that only stars considered to be inside the resonance enter this plot. The parabola-like boundary on the left represents the minimum J_R required for trapped orbits to reach the Solar neighbourhood; since orbits with smaller $\hat{J}_\ell$ are confined closer to the Lagrange point, a larger minimum J_R is required to visit us. In the velocity plane, this boundary corresponds to points where the contours of $\hat{J}_\ell$ and J_R are tangential to each other. The mean metallicity increases towards small $\hat{J}_\ell$ (stars captured early at the inner disk) and small J_R (young stars), as indicated by the multi-coloured arrows. To further clarify the metallicity trend in $\hat{J}_\ell$, we show in the right panel the metallicity after subtracting the gradient in J_R obtained by fitting Fig. 3.7 right panel with a plane which yields $\mathrm{d[M/H]}/\mathrm{d}J_R = -0.00078\,\mathrm{dex\,kpc^{-1}\,km^{-1}\,s}$. We clearly see a monotonic increase towards the resonance centre as predicted for a growing/sweeping resonance, thus implying the slow-down of the bar.

To get a quantitative grip on the observed [M/H] feature, we project the 2D distribution onto 1D statistics in J_ℓ. Since the sample distribution over (J_ℓ, J_R) is non-uniform and the [M/H] depends on J_R, a naive averaging over J_R would cause a fatal bias. Therefore, we instead calculate the gradient of [M/H] with respect to J_ℓ at each fixed J_R and then average the gradient over J_R

$$\frac{\mathrm{d}\langle[\mathrm{M/H}]\rangle}{\mathrm{d}\hat{J}_\ell} = \frac{\sum_i^{N_{J_R}} w_i \left(\langle[\mathrm{M/H}]\rangle_i^+ - \langle[\mathrm{M/H}]\rangle_i^-\right)}{\Delta\hat{J}_\ell \sum_i^{N_{J_R}} w_i}, \quad w_i = \frac{n_i^+ n_i^-}{n_i^+ + n_i^-}, \tag{3.4}$$

where the superscript $(\pm)$ denotes quantities associated with stars in the bins $\hat{J}_\ell \in [\hat{J}_\ell, \hat{J}_\ell + \Delta\hat{J}_\ell]$ and $\hat{J}_\ell \in [\hat{J}_\ell - \Delta\hat{J}_\ell, \hat{J}_\ell]$. $n_i^\pm$ and $\langle[\mathrm{M/H}]\rangle_i^\pm$ are the number of stars and the mean metallicity in the ith J_R bin, respectively. The weights w_i are necessary since each J_R bin contains a different number of stars. Once the metallicity gradient with respect to $\hat{J}_\ell$ is obtained, we reconstruct the metallicity as a function solely of $\hat{J}_\ell$ by integrating the gradient starting from the separatrix. We accumulate the uncertainty of the reconstructed metallicity while taking into account the correlated errors between the metallicity gradients evaluated at adjacent points where they use the same $\hat{J}_\ell$ bin in between. Here we set the bin widths to $\Delta\hat{J}_\ell = 0.05$ and $\Delta J_R = 10\,\mathrm{kpc\,km\,s^{-1}}$ below which the results do not change significantly.

The result for this is shown in Fig. 3.9. The left panel shows the change of mean metallicity with $\hat{J}_\ell$ for a range of bar amplitudes A at fixed pattern speed $\Omega_\mathrm{p} = 35\,\mathrm{km\,s^{-1}\,kpc^{-1}}$. The signal only weakly depends on the bar strength, i.e. over the whole range of reasonable bar amplitude, we see the same monotonic increase of metallicity towards the resonance centre. As explicitly demonstrated in Appendix 3.C using pseudo-data generated from test-particle simulations, this uptrend in metallicity is only expected when the bar is slowing down (Fig. 3.16). From the total increase in metallicity inside the resonance, we can quantify a lower limit for how much the bar has decelerated (this should turn into a full estimate once *Gaia* can penetrate the core of the resonance). In doing so, we must bear in mind that stars in the disk can be randomly scattered by fluctuations in the gravitational field due to external perturbations (e.g. mergers or satellite interactions) and intrinsic noises (e.g. transient spiral arms or giant molecular clouds), which will tend to weaken the observed metallicity gradient. With this caveat, and given the metallicity gradient of the Galactic disk $-0.05\,\mathrm{dex/kpc}$ (Luck, 2018), the maximum increase in the mean metallicity ($\sim 0.08\,\mathrm{dex}$) implies that the corotation radius has moved at least $\sim 1.6\,\mathrm{kpc}$ outward and thus the pattern speed has declined in excess of $\sim 24\%$ since the formation of the bar.

The right-hand panel of Fig. 3.9 shows the metallicity trend inside the resonance for various bar pattern speeds at fixed bar strength $A = 0.02$. In contrast to the variation in bar amplitude, the pattern speed sensitively affects the metallicity structure. As we decrease the pattern speed, the resonance in the velocity plane shifts towards large v_φ so the metal rich Hercules stars are placed nearer to the lower separatrix of the resonance. Consequently, the metal rich stars become more concentrated at large J_ℓ and the metallicity wrongly drops towards the inner region of the mis-placed resonance. Similarly, for larger pattern speeds, the upper separatrix of the resonance approaches the metal rich zone and hence the relative increase of metallicity from the separatrix becomes small. A monotonic rise in metallicity towards the core of the resonance is only observed with pattern speed $\Omega_\mathrm{p} = 35\,\mathrm{km\,s^{-1}\,kpc^{-1}}$ where the CR fits the Hercules stream. This result demonstrates that the slow bar theory is consistent with and strongly favoured by predictions from a decelerating bar.

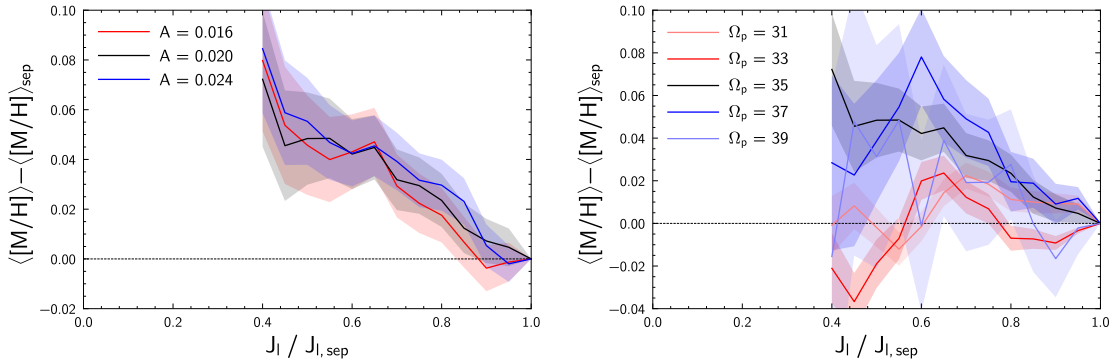

Fig. 3.9 Variation of mean metallicity with $\hat{J}_\ell$ derived by integrating the metallicity gradient in $\hat{J}_\ell$. Left panel: Dependence on bar amplitude A at fixed pattern speed $\Omega_\mathrm{p} = 35\,\mathrm{km\,s^{-1}\,kpc^{-1}}$. At all bar strength, the metallicity decreases monotonically from the centre of the resonance, indicating sequential occupation of the resonance from the core by stars from ever larger radii and thus at lower metallicities. This is the signature of outward migration of the resonance and thus the slow-down of the bar. The coloured bands represent the uncertainties propagated from the 1σ uncertainties of the mean metallicity gradient in $\hat{J}_\ell$. Right panel: Dependence on bar pattern speed Ω_p (units given in $\mathrm{km\,s^{-1}\,kpc^{-1}}$) at fixed bar strength $A = 0.02$. A monotonic trend is only seen with $\Omega_\mathrm{p} = 35\,\mathrm{km\,s^{-1}\,kpc^{-1}}$ where the location of bar corotation resonance matches the Hercules stream.

3.5.2 Estimation of bar pattern speed

In the last section we have established the detailed metallicity pattern. We now use its strong Ω_p dependence to measure the bar pattern speed at high precision: The positioning of the resonant actions is only correct with the true pattern speed, and thus the reconstructed metallicity profile will come out of order if we get Ω_p wrong. Since we do not expect the metallicity to undulate against libration action, here we demand a monotonic increase of metallicity towards lower libration action which we quantify by the likelihood of the metallicity to increase at each point in $\hat{J}_\ell$ starting from the separatrix down to $\hat{J}_{\ell,\mathrm{min}}$. We consider the metallicity change at each point from the previous value

$$z_i \equiv \langle[\mathrm{M/H}]\rangle_i - \langle[\mathrm{M/H}]\rangle_{i-1} \tag{3.5}$$

as a random variable distributed normally with its mean μ_{z_i} and uncertainty σ_{z_i} measured. The cumulative distribution function

$$F_i(x) = \frac{1}{2}\left[1 + \mathrm{erf}\left(\frac{x - \mu_{z_i}}{\sqrt{2}\sigma_{z_i}}\right)\right] \tag{3.6}$$

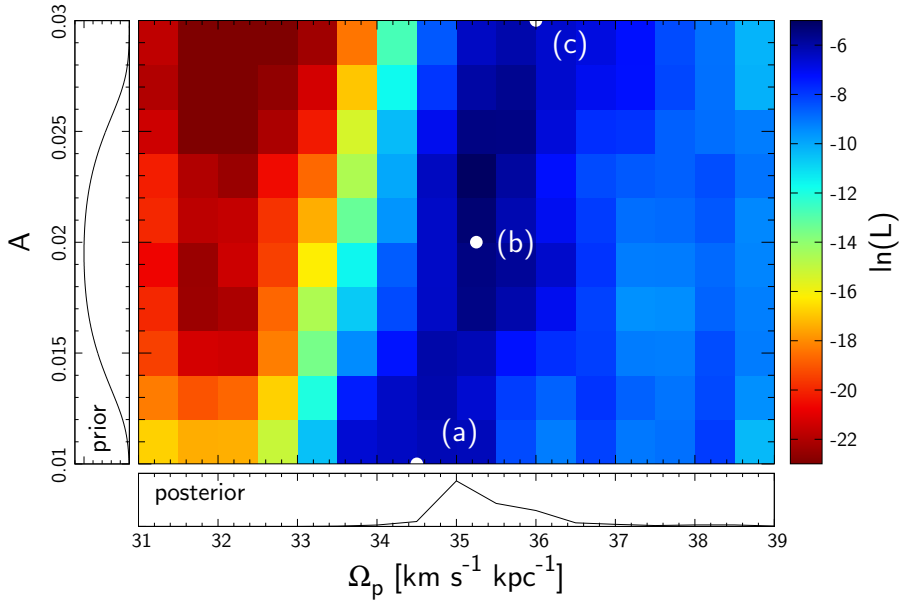

Fig. 3.10 Likelihood (equation 3.8) of increase in mean metallicity towards the centre of the bar's corotation resonance plotted over bar pattern speed Ω_p and bar strength A. From the prior distribution in A (left panel) inferred from SBM15, we calculate the posterior distribution in Ω_p (bottom panel) which shows a peak at around $\Omega_p = 35-36\,\mathrm{km\,s^{-1}\,kpc^{-1}}$.

describes the probability of z_i being smaller than x, so the likelihood of z_i being larger than zero is

$$\mathcal{L}_i(A, \Omega_p | \mu_{z_i}, \sigma_{z_i}) = 1 - F_i(0) = \frac{1}{2}\left[1 - \mathrm{erf}\left(\frac{-\mu_{z_i}}{\sqrt{2}\sigma_{z_i}}\right)\right]. \tag{3.7}$$

The total likelihood of the metallicity to increase towards the resonance centre is then

$$\mathcal{L}(A, \Omega_p | \boldsymbol{\mu}_z, \boldsymbol{\sigma}_z) = \prod_i^N \mathcal{L}_i(A, \Omega_p | \mu_{z_i}, \sigma_{z_i}), \tag{3.8}$$

where $N \equiv (1 - \hat{J}_{\ell,\mathrm{min}})/\Delta\hat{J}_\ell$ is the number of evaluation points in $\hat{J}_\ell$. Since the number of samples drops towards small libration action, the lower limit $\hat{J}_{\ell,\mathrm{min}}$ is fixed to 0.4 such that, for all bar parameters, each bin in $\hat{J}_\ell$ has more than 30 samples. We have confirmed that the likelihood estimation of equation (3.8) is robust against the choice of $\Delta\hat{J}_\ell$ smaller than 0.1.

Figure 3.10 shows the log-likelihood function of the monotonic increase. We observe an inclined peak which means that the faster the rotation of the bar (and thus the lower the location of the resonance in the velocity plane), the more strength (larger resonance size) is required for the metallicity to increase towards the core of the resonance. To have an

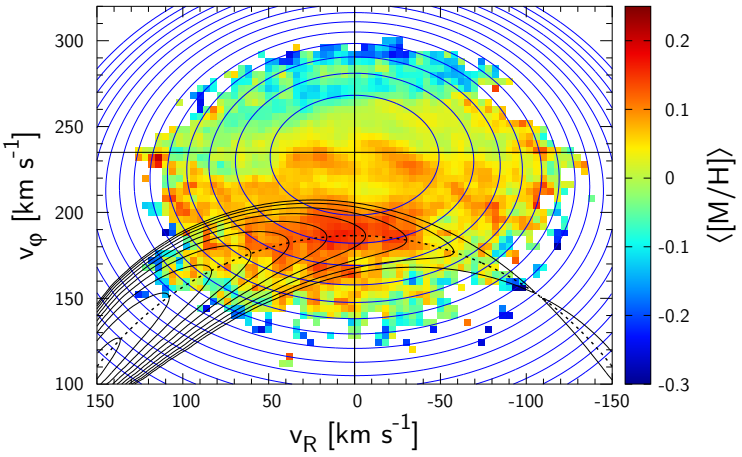

(a) $\Omega_\mathrm{p} = 34.50\,\mathrm{km\,s^{-1}\,kpc^{-1}}$, $A = 0.01$.

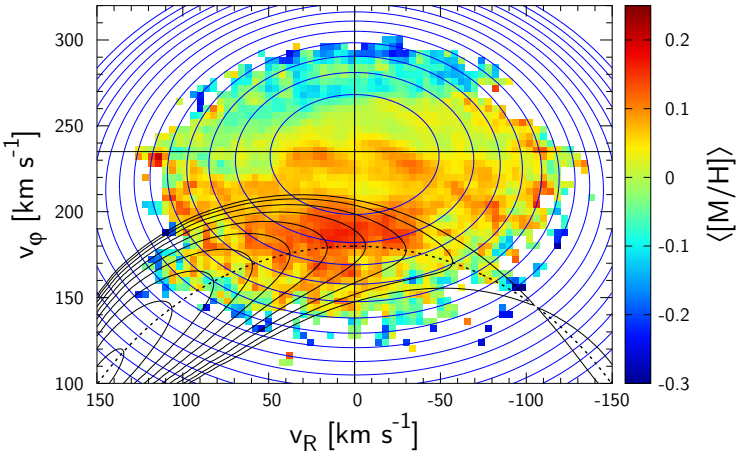

(b) $\Omega_\mathrm{p} = 35.25\,\mathrm{km\,s^{-1}\,kpc^{-1}}$, $A = 0.02$.

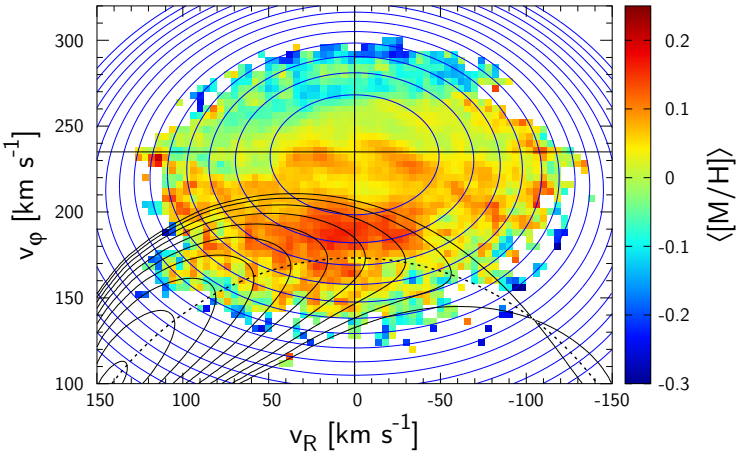

(c) $\Omega_\mathrm{p} = 36.00\,\mathrm{km\,s^{-1}\,kpc^{-1}}$, $A = 0.03$.

Fig. 3.11 Mean metallicity in local velocity space superposed by contours of constant J_R (blue) and $\hat{J}_\ell \equiv J_\ell / J_{\ell,\mathrm{sep}}$ (black) for orbits trapped in the corotation resonance of the bar. All three figures (a)-(c) assume bar parameters (marked on Fig. 3.10 in white) which yield monotonic increase of metallicity towards small $\hat{J}_\ell$ demanded from the slow-down of the bar.

intuitive understanding of why bar parameters along this inclination are favored in our analysis, we show in Fig. 3.11 the configuration of the resonance in local velocity space for three bar parameters along the peak shown as white circles (a)-(c) in Fig. 3.10. From top to bottom, both Ω_p and A increase, i.e. the resonance shifts down but also inflates. Under such a change, the position of the upper separatrix of the CR is kept fixed just above the metal rich zone. As a consequence, for all three figures, the metallicity along constant J_R approximately peaks at points where $\hat{J}_\ell$ is the smallest, i.e. points where contours of J_R and $\hat{J}_\ell$ are tangent to one another, hence resulting in an overall monotonic increase of metallicity towards small $\hat{J}_\ell$. The results simply suggest that bar models with the upper boundary of the CR placed just above the Hercules stream is favoured, in agreement with prediction from kinematics.

From Fig. 3.10, we may constrain the bar pattern speed given the priors for the bar amplitude. As in Chiba et al. (2021), we infer the priors from the study of SBM15. The hydrodynamic simulation by SBM15 suggests that the observed longitude-velocity diagrams of CO and $\mathrm{H_I}$ are well reproduced with bar strengths in the range $A_\mathrm{s} \in [0.4, 0.8]$ in their notation which translates to $A \in [0.013, 0.026]$ in our model if we fit our analytical bar model to their bar potential beyond half of the corotation radius where the local kinematics are affected by the bar. We assume a normal prior distribution in A with mean $\mu_A = 0.0195$, standard deviation $\sigma_A = 0.0065$, and a smooth cutoff given at $\mu_A \pm \sigma_A$;

$$P(A) \propto \frac{\exp\left(-x^2/2\right)}{\frac{1}{2}\left(\exp|x^k| + 1\right)}, \quad x \equiv \frac{A - \mu_A}{\sigma_A} \tag{3.9}$$

where k is the cutoff rate set to $k = 4$ as default. $P(A)$ is shown in the left panel of Fig. 3.10. The posterior distribution in Ω_p is calculated by integrating $P(A)$ and $\mathcal{L}(A, \Omega_\mathrm{p})$ over A;

$$P(\Omega_\mathrm{p}) = \int_{A_\mathrm{min}}^{A_\mathrm{max}} dA\ P(A)\mathcal{L}(A, \Omega_\mathrm{p}). \tag{3.10}$$

Figure 3.10 bottom panel shows $P(\Omega_\mathrm{p})$ which takes mean $\langle\Omega_\mathrm{p}\rangle = 35.5\,\mathrm{km\,s^{-1}\,kpc^{-1}}$, median $\tilde{\Omega}_\mathrm{p} = 35.0\,\mathrm{km\,s^{-1}\,kpc^{-1}}$, and standard deviation $\sigma_{\Omega_\mathrm{p}} = 0.8\,\mathrm{km\,s^{-1}\,kpc^{-1}}$. This is in good agreement with Binney (2020b) who derived $\Omega_\mathrm{p} = 36 \pm 1\,\mathrm{Gyr^{-1}} = 35.2 \pm 1.0\,\mathrm{km\,s^{-1}\,kpc^{-1}}$ by applying Jean's theorem to trapped orbits visiting the Sun. Since both studies reached the same conclusion using independent statistics, $\Omega_\mathrm{p} = 35 - 36\,\mathrm{km\,s^{-1}\,kpc^{-1}}$ is reliably the

optimal pattern speed for the Hercules stream to be composed of orbits trapped in the bar's corotation resonance.

The pattern speed estimated in this work is slightly lower than recent estimations from stellar kinematics in the bar: both Sanders et al. (2019) and Bovy et al. (2019) estimated $\Omega_\mathrm{p} = 41 \pm 3\,\mathrm{km\,s^{-1}\,kpc^{-1}}$ using the continuity equation. With these intermediate pattern speeds, the upper separatrix of the CR cuts or passes under the metal rich population in the local velocity plane and thus an alternative explanation must be given to the metal rich population outside the bar's corotation resonance. Portail et al. (2017) derived $\Omega_\mathrm{p} = 39 \pm 3.5\,\mathrm{km\,s^{-1}\,kpc^{-1}}$ by fitting their dynamical models of the bar region to the density and kinematics of red clump giants using the made-to-measure method, and their models were further used by Clarke et al. (2019) to reproduce the integrated on-sky maps of the longitudinal proper motion which was best achieved at $\Omega_\mathrm{p} = 37.5\,\mathrm{km\,s^{-1}\,kpc^{-1}}$ in close agreement with our estimation. We conjecture that the small discrepancy is partly due to the uncertainty in the bar strength but more dominantly caused by the difference in the underlying axisymmetric potential.

3.5.3 Quantifying systematic uncertainties

In the following, we discuss the systematic errors of our estimation. Including faint stars by extending the upper limit in *Gaia* magnitude from $G = 7$ to $G = 8$ has a negligible effect, not changing the optimal bar pattern speed within the reported precision. Changing the age of the isochrone (default 4 Gyr) has a marginal impact: with age 6 Gyr we obtain $\Omega_\mathrm{p} = 35.5 \pm 0.9\,\mathrm{km\,s^{-1}\,kpc^{-1}}$, while with age 2 Gyr we have $\Omega_\mathrm{p} = 35.4 \pm 0.7\,\mathrm{km\,s^{-1}\,kpc^{-1}}$. Throughout our analysis, we have assumed the angle of bar major axis φ_b to be 30° ahead from the sun (Wegg et al., 2015). By varying the bar angle φ_b, we vary the distance from the sun to the centre of the bar's corotation resonance, i.e. the stable Lagrange point. Therefore, varying the bar angle has an effect on local kinematics similar to varying the bar amplitude. With bar angle of $\varphi_\mathrm{b} = 35°$, the optimal pattern speeds rises to $\Omega_\mathrm{p} = 35.8 \pm 0.9\,\mathrm{km\,s^{-1}\,kpc^{-1}}$. Conversely, decreasing the bar angle to $\varphi_\mathrm{b} = 25°$ lowers the best pattern speed down to $\Omega_\mathrm{p} = 35.2 \pm 0.9\,\mathrm{km\,s^{-1}\,kpc^{-1}}$. We have also analysed the data using resonant actions evaluated in a slowing bar with slowing rate $\eta = 0.0036$

as constrained by Chiba et al. (2021). This yields $\Omega_\mathrm{p} = 35.5 \pm 1.1\,\mathrm{km\,s^{-1}\,kpc^{-1}}$. The mean is unaffected since the deceleration does not change the location of the resonance, but the uncertainty increases since the resonance contracts reducing the effective sample size. Variation in the axisymmetric potential from a flat circular speed to a slightly inclined one $v_\mathrm{c}(R) \equiv (R/R_0)^{\,\beta} v_\mathrm{c}(R_0)$ has the largest impact changing the pattern speed to $\Omega_\mathrm{p} = 34.5 \pm 1.1\,\mathrm{km\,s^{-1}\,kpc^{-1}}$ with $\beta = 0.1$ and $\Omega_\mathrm{p} = 36.8 \pm 0.8\,\mathrm{km\,s^{-1}\,kpc^{-1}}$ with $\beta = -0.1$.

Finally, uncertainties in R_0 and v_c cannot be treated separately as our measurement to first order depends on the local angular frequency $\Omega_0 \equiv v_\mathrm{c}/R_0$ which is constrained by the proper motion of Sagittarius A*, $\mu_{\ell,\mathrm{A}^*} = (-6.411 \pm 0.008)\,\mathrm{mas\,yr^{-1}} = (30.391 \pm 0.038)\,\mathrm{km\,s^{-1}\,kpc^{-1}}$ (Reid & Brunthaler, 2020) through the relation $v_{\varphi,\odot} = \mu_{\ell,\mathrm{A}^*} R_0 = v_\mathrm{c} + V_\odot$ and thus

$$\Omega_0 = \mu_{\ell,\mathrm{A}^*} - V_\odot/R_0 = 28.90 \pm 0.10\,\mathrm{km\,s^{-1}\,kpc^{-1}}, \tag{3.11}$$

where we take $R_0 = 8.18 \pm 0.02\,\mathrm{kpc}$ (Gravity Collaboration et al., 2019) and $V_\odot = 12.24 \pm 0.47\,\mathrm{km\,s^{-1}}$ (Schönrich et al., 2010). There is a systematic uncertainty from wobbles of the black hole against the Galactic centre (Batcheldor et al., 2010) and wobbles of the nuclear region against the large scale disk. These uncertainties amount to a few $\mathrm{km\,s^{-1}}$ peculiar motion of Sagittarius A* or vice versa a couple per cent in μ_{ℓ,A^*}. In this thesis, we have assumed $\Omega_0 = v_\mathrm{c}/R_0 = 235\,\mathrm{km\,s^{-1}}/8.2\,\mathrm{kpc} = 28.66\,\mathrm{km\,s^{-1}\,kpc^{-1}}$, so we may be underestimating the pattern speed by a factor of 0.992 which shifts our fiducial estimation up to $\Omega_\mathrm{p} = 35.8 \pm 0.8\,\mathrm{km\,s^{-1}\,kpc^{-1}}$.

3.5.4 The relative pattern speed

Throughout the chapter we have referred to the Galactic bar as 'slow' in the sense that its pattern speed is $\Omega_\mathrm{p} \lesssim 40\,\mathrm{km\,s^{-1}\,kpc^{-1}}$ as opposed to a 'fast' bar with $\Omega_\mathrm{p} \gtrsim 50\,\mathrm{km\,s^{-1}\,kpc^{-1}}$. This slow/fast dichotomy based on the absolute pattern speed is not to be confused with the slow/fast classification based on the dimensionless ratio $\mathcal{R} \equiv R_\mathrm{CR}/a_\mathrm{b}$, where R_CR is the corotation radius and a_b is the apparent length of a bar in stellar density. When $1 < \mathcal{R} < 1.4$, the bar is classified as 'fast' (Athanassoula, 1992; Debattista & Sellwood, 2000; Athanassoula, 2014b). Most barred galaxies are found to possess a fast bar (Aguerri

et al., 2015). Whether our Galactic bar is fast or slow in the latter sense depends on the measurement of the bar length. Wegg et al. (2015) fitted the observed red clump stars in the bar region with a parametrized density model and derived $a_\mathrm{b} = 5.0 \pm 0.2\,\mathrm{kpc}$. Adopting their upward revision of the bar length together with our estimation $R_\mathrm{CR} = 6.2 \pm 0.2$ yields $\mathcal{R} = 1.3 \pm 0.1$ and thus makes our 'slow' pattern speed bar model a typical 'fast bar' in this classification.

3.6 Conclusions

We have shown that the resonances of a slowing bar develop like the rings on a growing tree: the distance of trapped orbits to the core of the resonance is adiabatically invariant (i.e. the libration action J_ℓ) and indicates the order of trapping. Since the volume of bar resonance is shown to grow while it sweeps outwards through the disk, newly trapped stars sequentially occupy the phase space near the expanding separatrix. Due to the Galaxy's negative radial metallicity gradient, this pattern is directly observable as a monotonic increase of mean stellar metallicity from the surface towards the core of the resonance.

Using photometric metallicities and stellar kinematics from *Gaia* data, we have shown that the Hercules stream in the Solar Neighbourhood carries this signature. The data displays a highly significant and clean metallicity ordering within the Hercules stream, which we can only explain by identifying Hercules with the bar's corotation resonance.

The metallicity ordering is only preserved with the correct current bar pattern speed Ω_p. The mapping from phase space to the libration action depends critically on Ω_p, and so the metallicity ordering in J_ℓ gets lost at even small changes of Ω_p. We showed that this tightly constrains the current pattern speed to $\Omega_\mathrm{p} = 35.5 \pm 0.8\,\mathrm{km\,s^{-1}\,kpc^{-1}}$ and thus $R_\mathrm{CR} = 6.6 \pm 0.2\,\mathrm{kpc}$, providing another key evidence for the slow bar theory. We stress that a fast bar which associates Hercules with the non-resonant orbits below the outer Lindblad resonance is incompatible with the data since there are no viable mechanism that makes non-trapped orbits significantly metal rich. We further stress that any outer resonances with $N_R > 0$ cannot explain the metal-rich nature of Hercules since resonant dragging in angular momentum will be accompanied by an increase in radial action while the high

metallicity stars of Hercules is observed even at low J_R. The significant metallicity rise also demands a long sweep in radius, which seems not feasible with a short-lived spiral pattern.

The overall increase in metallicity inside the resonance implies that the corotation radius of the bar must have moved more than 1.6 kpc outwards which corresponds to a decrease of pattern speed by at least 24% since its formation. A more quantitative understanding on the evolutionary history of the Galactic bar can be gained in the future by fitting the full resonance structure with detailed chemo-dynamical models. Owing to the Sun's position far from the stable Lagrange points, we currently see only the outer region of the resonance. By performing the analysis at a spatial coordinate closer to the Lagrange points, we could probe deeper into the inner region of the resonance, where we may find traces of events that happened in the early epoch of bar formation (e.g. vertical buckling), and also determine the size of the initial core of the resonance which stems from the formation of the bar. This will be possible in the future with extended data covering the full range of resonance and a proper chemo-dynamical model predicting the age-dependent effects, e.g. the flattening of the radial metallicity gradient towards higher ages by inside-out formation (e.g. Spagna et al., 2010; Schönrich & McMillan, 2017). We identify further caveats pertaining to diffusion processes. We have not yet evaluated how precisely the structure of a bar-driven resonance will be modified by diffusion processes in phase space due to a variety of perturbations: spiral arms, giant molecular clouds, dwarf galaxy impacts, etc. A naive expectation is that this weakens the metallicity gradient along J_ℓ.

Adding to our previous arguments for a slowing Galactic bar purely based on kinematics, this work provides further evidence using photometry. Hence, our works support the existence of a standard dark-matter halo that has taken up angular momentum from the slowing bar. Alternative theories of gravity are disfavored since they cannot explain the missing angular momentum (Tiret & Combes, 2007; Ghafourian et al., 2020). Exotic dark matter in the form of degenerate quantum condensates (e.g. Goodman, 2000; Hu et al., 2000), recently favored by virtue of preventing the formation of density cusps, must be tested for their degree of angular momentum exchange with the baryonic bar. Thus, the discovery of the deceleration of the bar provides a new testbed through which any

successful dark matter model must pass. The bar slow-down also paves the path to a new class of constraints on the dark halo: The dynamical friction on the bar depends on both the dark halo's density and kinematics, and thus in combination with standard maps of the gravitational potential, gives us access to measuring the dynamical properties of the dark halo (e.g. net rotation, velocity anisotropy).

Appendix

3.A Capture probability

Here we report on the capture rate of our slowing bar. Figure 3.12 depicts the evolution of the contracted resonance with time (from left to right). As the resonance advances in J_s, the area of resonance grows (section 3.3.2), so a fraction of stars above the resonance (region I) that encounter the separatrix may either be captured into the resonance (region II) or transfer to the lower side (region III) depending on their incident phase. If we assume that trapped orbits always remain trapped as the resonance moves and grows (i.e. if the area enclosed by the dotted curve in Fig. 3.12 (b) is comprised of stars that occupied region II in Fig. 3.12 (a)), the capture probability $P_{\mathrm{I}\to\mathrm{II}}$ averaged over the phase can be calculated from the rate of change in the phase-space area of each region (Henrard, 1982; Collett et al., 1997; Binney & Tremaine, 2008, problem 3.43):

$$P_{\mathrm{I}\to\mathrm{II}} = \frac{\dfrac{\mathrm{d}S_\mathrm{II}}{\mathrm{d}t}}{-\dfrac{\mathrm{d}S_\mathrm{I}}{\mathrm{d}t}}, \qquad P_{\mathrm{I}\to\mathrm{III}} = \frac{\dfrac{\mathrm{d}S_\mathrm{III}}{\mathrm{d}t}}{-\dfrac{\mathrm{d}S_\mathrm{I}}{\mathrm{d}t}}, \qquad P_{\mathrm{I}\to\mathrm{II}} + P_{\mathrm{I}\to\mathrm{III}} = 1, \tag{3.12}$$

where $S_{\mathrm{I,II,III}}$ are the phase-space area of region I, II and III respectively which change according to

$$\frac{\mathrm{d}S_\mathrm{I}}{\mathrm{d}t} = -\frac{1}{2}\frac{\mathrm{d}S_\mathrm{II}}{\mathrm{d}t} - 2\pi\frac{\mathrm{d}J_{\mathrm{s,res}}}{\mathrm{d}t}, \qquad \frac{\mathrm{d}S_\mathrm{II}}{\mathrm{d}t} = 2\pi\frac{\mathrm{d}J_{\ell,\mathrm{sep}}}{\mathrm{d}t}, \qquad \frac{\mathrm{d}S_\mathrm{III}}{\mathrm{d}t} = -\frac{1}{2}\frac{\mathrm{d}S_\mathrm{II}}{\mathrm{d}t} + 2\pi\frac{\mathrm{d}J_{\mathrm{s,res}}}{\mathrm{d}t}, \tag{3.13}$$

and are conserved in total

$$\frac{\mathrm{d}S_\mathrm{I}}{\mathrm{d}t} + \frac{\mathrm{d}S_\mathrm{II}}{\mathrm{d}t} + \frac{\mathrm{d}S_\mathrm{III}}{\mathrm{d}t} = 0. \tag{3.14}$$

The capture probability is determined by two factors: how fast the resonance sweeps $\mathrm{d}J_{\mathrm{s,res}}/\mathrm{d}t$ and how fast it grows in volume $\mathrm{d}J_{\ell,\mathrm{sep}}/\mathrm{d}t$. Figure 3.13 top panel shows the

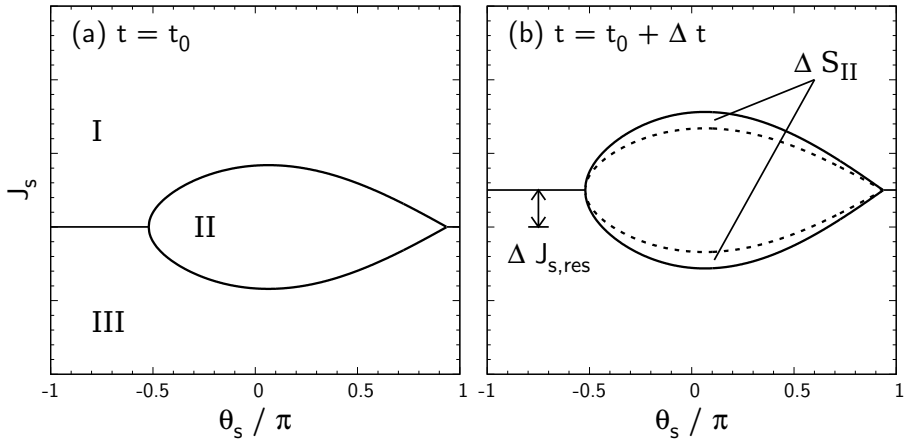

Fig. 3.12 Schematic drawing of the evolution of a resonance. The phase space is split into three regime: the upper circulation regime (I), the libration regime (II), and the lower circulation regime (III). As time Δt passes (from left panel to right panel), the resonance moves up by $\Delta J_{\mathrm{s,res}}$ and grows by $\Delta S_{\mathrm{II}} = 2\pi\Delta J_{\ell,\mathrm{sep}}$. The time variation of the phase-space area of the respective regions determines the capture rate (equation 3.12).

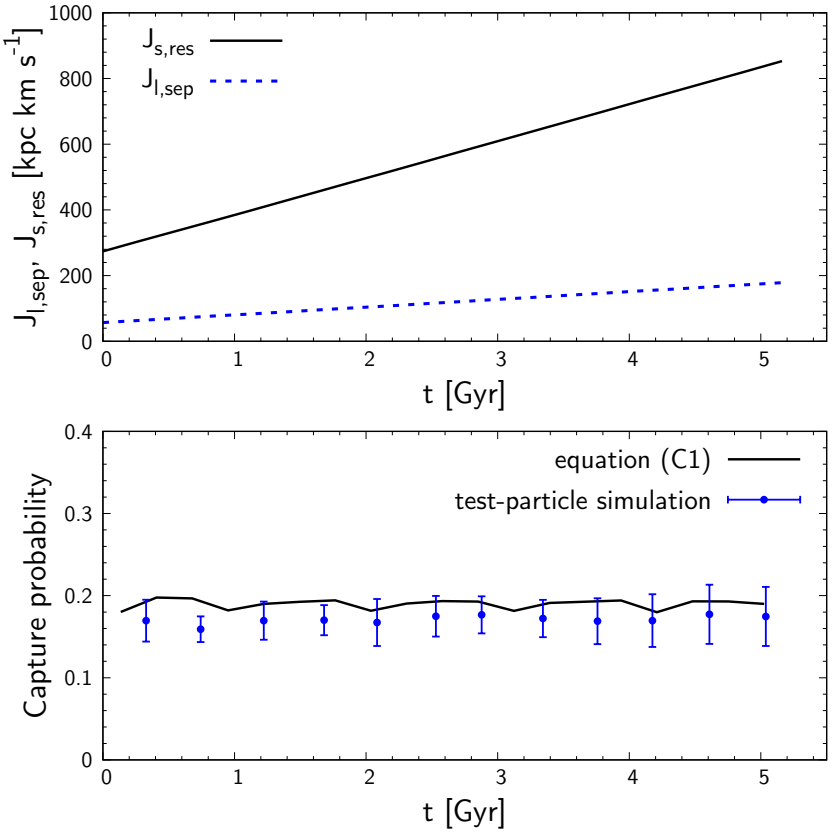

Fig. 3.13 Upper panel: The time evolution of the CR's location $J_{\mathrm{s,res}}$ and its volume $J_{\ell,\mathrm{sep}}$. Lower panel: The angle-averaged capture probability calculated analytically (black) and numerically (blue).

time evolution of $J_{\rm s,res}$ and $J_{\ell,\rm sep}$ at the CR of our slowing/elongating bar model. As in the simulation shown in Fig. 3.3, the bar amplitude A is kept constant and the fast action is $J_{\rm f} = 10\,{\rm kpc\,km\,s^{-1}}$. Since the corotation radius $R_{\rm CR}$ of our bar is modeled to expand linearly with time, both $J_{\rm s,res}$ and $J_{\ell,\rm sep}$ are linear as they scale according to $J_{\rm s,res} \sim v_{\rm c} R_{\rm CR},\ J_{\ell,\rm sep} \sim \sqrt{\Psi/|G|} \sim \sqrt{A} v_{\rm c} R_{\rm CR}$. Consequently, the capture probability, shown in the bottom panel of Fig. 3.13 (black curve), is roughly constant around 0.2. We also calculated the capture rate using test-particle simulation where we place 10^4 stars with identical initial actions just above the resonance ($J_{\rm s0} = \zeta J_{\rm s,res},\ \zeta > 1$) but with random angles, and judge capture if $J_{\rm s}$ increase by a factor of more than 1.2 from the initial value (see section 2.5.2 for detail). It is self-evident that our measurement is affected by the higher-order resonances which pass the stars before the CR. These resonances have a small phase-space volume, yet are still able to temporarily capture and sweep some stars, and also alter the angle distribution of the stars interacting with the CR. We ascertained that the capture probability to the CR indeed depends at the 20% level on the chosen initial position parametrized by ζ. Thus, we conduct the measurement with $\zeta = 1.15, 1.20, 1.25, 1.30$ and take the mean value. The numerical result (blue), which is plotted at the time when the resonance passes $J_{\rm s0}$, is slightly lower than the analytical estimation (black) but confirms the qualitative behaviour. The overestimation of our analytical approach is most likely due to the assumption that all trapped stars remain trapped as the resonance moves/grows which is invalid at the separatrix where the libration period diverges and thus allows orbits to escape from the moving resonance despite the growth in volume.

3.B Uncertainty in libration action.

It is important to check that the uncertainty of the libration action $\hat{J}_\ell \equiv J_\ell / J_{\ell,\rm sep}$ arising from the uncertainties in the *Gaia* data is sufficiently smaller than the scale of $\hat{J}_\ell$ at which we are looking. To quantify the uncertainty in $\hat{J}_\ell$, we prescribe a Gaussian distribution for *Gaia* parallax p, proper motions μ_l, μ_b, and line-of-sight velocity $v_{\rm los}$ using the reported errors, and estimate the uncertainty by Monte Carlo method with 1000 realization for each star. Figure 3.14 upper panel plots the mean uncertainty of $\hat{J}_\ell$ over the velocity space.

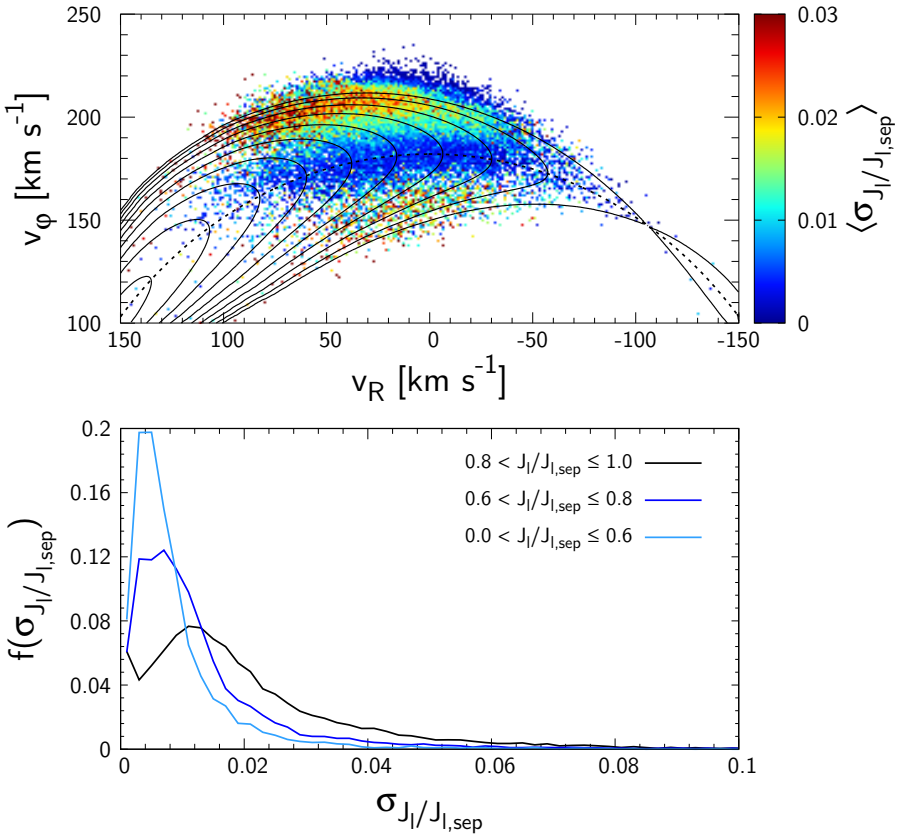

Fig. 3.14 Upper panel: Mean uncertainty of $\hat{J}_\ell$ measurement due to *Gaia* errors. The uncertainty follows the gradient of $\hat{J}_\ell$. Lower panel: The distribution of uncertainty in $\hat{J}_\ell$. For the majority of stars, the uncertainty is of order 0.01 which is sufficiently smaller than the range of $\hat{J}_\ell$ over which we measure the metallicity trend.

Gaia's observational errors enter velocity space almost linearly, so the uncertainty in $\hat{J}_\ell$ is largest where the gradient of $\hat{J}_\ell$ in velocity space is steepest. Since the contours of $\hat{J}_\ell$ are calculated using the position of the Sun, some local stars relatively far from the Sun (at most 0.3 kpc) appear beyond the separatrix. Figure 3.14 lower panel shows the distribution of the uncertainty for three regions of the resonance: the inner region ($0 < \hat{J}_\ell < 0.6$, light blue), the intermediate region ($0.6 < \hat{J}_\ell < 0.8$, blue), and near the separatrix ($0.8 < \hat{J}_\ell < 1$, black). The uncertainty becomes larger towards the separatrix, although for the vast majority of stars it is only a few per cent, so more than an order of magnitude smaller than the range in $\hat{J}_\ell$ across which we have shown the monotonic increase in metallicity.

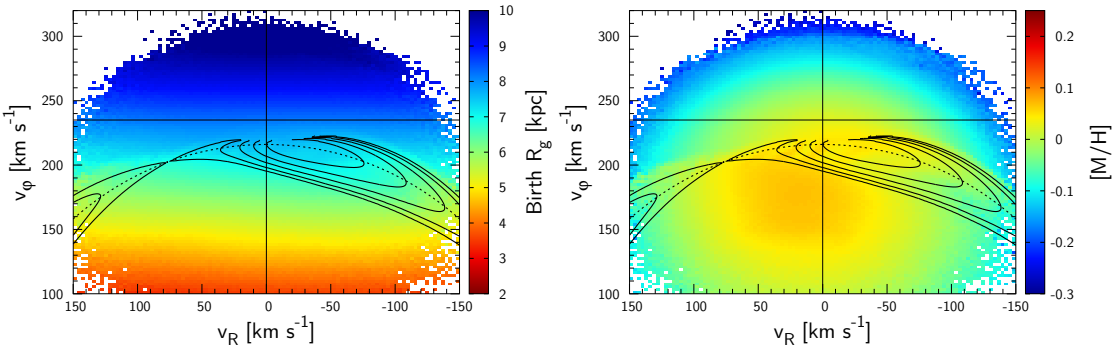

(a) Constant fast bar ($\eta = 0$, $\Omega_\mathrm{p} = 53\,\mathrm{km\,s^{-1}\,kpc^{-1}} = 1.85\Omega_0$).

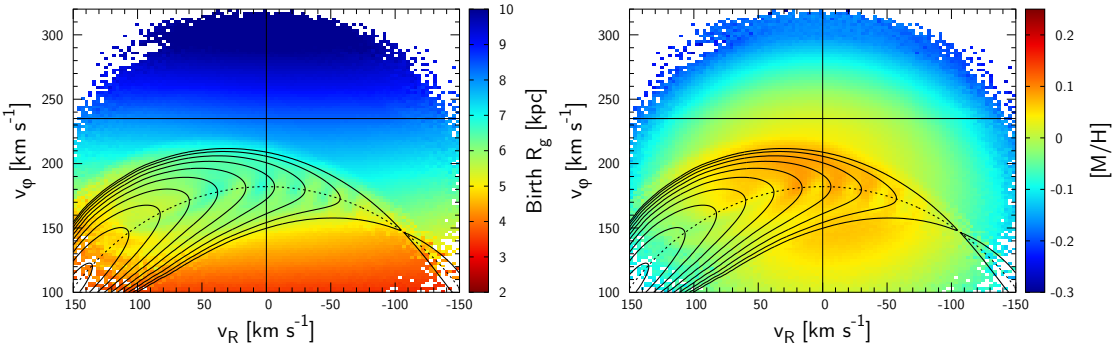

(b) Constant slow bar ($\eta = 0$, $\Omega_\mathrm{p} = 35\,\mathrm{km\,s^{-1}\,kpc^{-1}} = 1.22\Omega_0$).

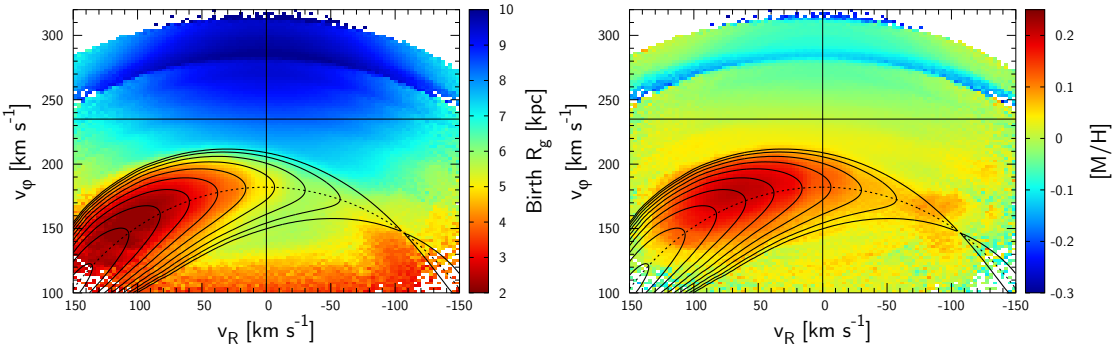

(c) Decelerating slow bar ($\eta = 0.004$, $\Omega_\mathrm{p} = 35\,\mathrm{km\,s^{-1}\,kpc^{-1}} = 1.22\Omega_0$).

Fig. 3.15 The birth guiding radius (left column) and the estimated local metallicity (right column) for three bar models. Top panels: a constant fast bar ($\Omega_\mathrm{p} = 53\,\mathrm{km\,s^{-1}\,kpc^{-1}} = 1.85\Omega_0$). Middle panels: a constant slow bar ($\Omega_\mathrm{p} = 35\,\mathrm{km\,s^{-1}\,kpc^{-1}} = 1.22\Omega_0$). Bottom panels: a decelerating slow bar.

3.C Model of local metallicity.

Modelling the local metallicity distribution is an involved task requiring a chemo-dynamical model that deals with the age-dispersion relation, the variation of the radial metallicity gradient with age, and radial mixing of stars, all of which are non-trivial and is thus beyond the scope of this thesis. Here we just provide a rough guidance on how the different bar models would translate into an observable metallicity distribution.

As evident from the data, both the age-metallicity and the age-velocity dispersion relationships combine into a negative metallicity gradient towards larger radial action which is superimposed onto the J_φ dependence resulting from the radial metallicity gradient. We fit this metallicity-J_R relationship linearly to roughly cover this effect: $\mathrm{d[M/H]/d}J_R = -0.00078\,\mathrm{dex\,kpc^{-1}\,km^{-1}\,s}$. This relation is then applied to the original J_R of the test particles together with the radial metallicity gradient $-0.05\,\mathrm{dex/kpc}$ (Luck, 2018) applied to the birth R_g (i.e. original L_z).

Fig. 3.15 displays the birth guiding radius (left column) and the corresponding metallicity (right column) of three different bar models. The top panels show the previously favored fast bar model with pattern speed $\Omega_\mathrm{p} = 53\,\mathrm{km\,s^{-1}\,kpc^{-1}}$ (Dehnen, 1999b). The OLR is located above the Hercules stream and the non-resonant x_2 orbits below the OLR constitute the Hercules. The contours of $\hat{J}_\ell$ are broken at small J_R due to the failure of the pendulum formalism at the Lindblad resonances where trapped stars are modeled to librate down to negative J_R, although this problem could be resolved by appropriate coordinate transformation (Binney, 2020a). As demonstrated by Antoja et al. (2017), the left panel shows that the non-trapped stars at the position of Hercules originate from smaller radii than the OLR stars with similar v_φ. Note that Antoja et al. (2017) plotted the current mean radius of the stars whereas our plot depicts the original guiding radius which is the relevant quantity for assessing the metallicity gradient. As can be seen from our plots, the difference in the original R_g is too small such that, when the simple metallicity-age-dispersion relation is applied, the metallicity at Hercules is only 0.05 dex larger than that at the LSR while the data shows a difference of more than $\Delta\mathrm{[M/H]} > 0.2\,\mathrm{dex}$ (Fig. 3.6).

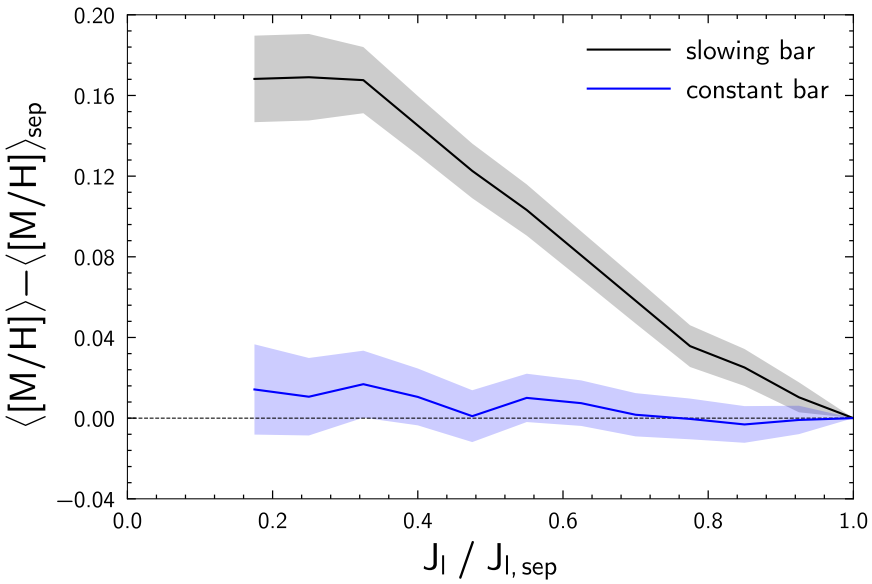

Fig. 3.16 Prediction of mean metallicity [M/H] inside the resonance using mock data generated from test-particle simulation. Increase in [M/H] towards small $\hat{J}_\ell$ exclusively happens in the slowing bar model, while there is no appreciable rise in the corresponding model with a constant bar pattern speed.

The middle panels show the slow bar model with constant pattern speed. The Hercules is now associated with orbits trapped in the CR which have a larger range of radial oscillation compared to non-trapped orbits, resulting in a slightly higher metallicity than the fast bar model. However, the predicted metallicity remains below the level of the data. Note the stripes along the contours of libration action arising from the incomplete phase mixing inside the resonance (even though we have run the simulation for 12 Gyr).

The bottom panels show the decelerating slow bar model which we have elaborated on in the main text (section 3.3.3). The slow down of the bar brings trapped stars from far inside the disk (~ 3 kpc) that could potentially have metallicity as high as 0.2 dex in agreement with data. The metallicity-$\hat{J}_\ell$ relation of our models is shown in Fig. 3.16. The slowing bar (black) exhibits a profound linear increase in metallicity towards the resonance center up to the initial core ($\hat{J}_\ell \lesssim 0.3$) within which the metallicity is flat as expected. The steady bar (blue) shows no significant rise in metallicity. The result thus corroborates our argument that the observed uptrend in metallicity manifests the deceleration of the bar. We stress though that this is a mere order of magnitude estimation and that many

important galactic evolution processes have been ignored, in particular the change in the radial metallicity gradient with time and position as a result of inside-out formation (e.g. Spagna et al., 2010; Schönrich & McMillan, 2017). Naively, this inside-out signature should flatten or even invert the J_φ-metallicity relationship for old stars (large J_R) and thus reduce the metallicity contrast between the CR and the surrounding non-resonant stars at very large J_R. A quantitative prediction must await a proper chemo-dynamical model that fully considers these effects.

CHAPTER 4

Oscillating dynamical friction on galactic bars by trapped dark matter

4.1 Abstract

In this chapter, we develop a method to predict dynamical friction on galactic bars by resonantly trapped dark matter. Traditional approximations to dynamical friction are formulated using the linearized collisionless Boltzmann equation and have been shown to be valid in the *fast limit*, i.e. for rapidly slowing bars. However, the linear assumption breaks down within a few dynamical periods for typical slowly evolving bars, which trap a significant amount of disk stars and dark matter in resonances. Recent observations of the Galactic bar imply this *slow regime* at the main bar resonances. We formulate the time-dependent dynamical friction in the *slow limit* and explore its mechanism in the general slow regime with test-particle simulations. Here, angular momentum exchange is dominated by resonantly trapped orbits which slowly librate around the resonances. In typical equilibrium haloes, the initial phase-space density within the trapped zone is higher at lower angular momentum. Since the libration frequency falls towards the separatrix, this density contrast winds up into a phase-space spiral, resulting in a dynamical friction that oscillates with ~Gyr periods and damps over secular timescales. We quantify the long-term behaviour of this torque with secular perturbation theory, and predict two observable consequences: i) The phase-space spirals may be detectable in the stellar disk where the

number of windings encodes the age of the bar. ii) The torque causes weak oscillations in the bar's pattern speed, overlaid on the overall slowdown – while not discussed, this feature is visible in previous simulations.

4.2 Introduction

In the previous two Chapters, we have provided quantitative evidence for the bar's slowdown consistent with the standard ΛCDM model. We now set out to constrain the phase space distribution of the dark matter from the measured slowing rate of the bar. This, however, requires quantitative understanding of the angular momentum exchange between the bar and all the other mass components (i.e. dark matter, stars, gas) which is beyond the reach of this thesis. Here, we only study the dynamical friction by the dark matter halo, which is the dominant driver for the bar's deceleration.

While a wide range of numerical simulations have addressed the angular momentum transfer from bars to haloes (e.g. Hernquist & Weinberg, 1992; Debattista & Sellwood, 2000; Athanassoula, 2003), the theoretical understanding is still incomplete. Tremaine & Weinberg (1984, hereafter TW84) derived a formula of dynamical friction in an inhomogeneous spherical system using linear perturbation theory. Their formula generalises the earlier torque formula by Lynden-Bell & Kalnajs (1972, hereafter LBK72), which describes the angular momentum transport in two-dimensional disk galaxies. Unlike the dynamical friction in a homogeneous system (Chandrasekhar, 1943), the LBK formula shows that in an inhomogeneous system, where orbits are quasi-periodic, the dominant angular momentum transfer arises from discrete resonances. TW84 also investigated the non-linear motion of orbits near resonances and showed that the LBK formula is only valid in what they call the *fast limit*. Here, 'fast' means that the resonances sweep across the phase space of the halo rapidly enough to preclude the growth of non-linear responses, in particular resonant trapping. This allows the system to remain in the linear regime. Weinberg (1985) showed that the LBK torque formula predicts a strong friction on the bar, extracting most of its angular momentum in a few rotation periods. This problem was revisited by Weinberg (2004, hereafter W04), where he pointed out that the assumption of the perturbation being

turned on adiabatically in the distant past (the time-asymptotic limit) is problematic since the evolution timescale of the bar is only several times the characteristic dynamical period. Relaxing this assumption enabled W04 to model the transient effect and reduce the overall torque. Yet, the linear treatment by W04 remains restricted to the fast regime and cannot be applied to the *slow regime* where resonant trapping comes into play.

This slow regime (resonant trapping by the Galactic bar) is, however, implied by the stellar kinematics of the Solar neighbourhood observed by the *Gaia* satellite (e.g. Katz et al., 2019; Hunt et al., 2019; Monari et al., 2019a; Binney, 2020b; Trick et al., 2021). The resonantly trapped stars manifest as stellar streams which occupy a sizeable fraction of the local phase-space volume. Modelling particularly the Hercules stream, we inferred that the bar is decelerating at a moderate rate, keeping a good portion of local stars trapped (Chapter 2, Chiba et al., 2021). Furthermore, signatures of trapping is found in the metallicity distribution of local stars: the corotation resonance of the slow/long bar exhibits a monotonic increase in metallicity towards the core of the resonance, indicating a tree-ring like growth as predicted by a naturally slowing bar that sequentially captured stars from small Galactocentric radii (Chapter 3, Chiba & Schönrich, 2021).

Resonant trapping by the bar are also commonly seen in self-consistent N-body simulations: spectral analysis of orbits in barred galaxies shows significant clustering near resonances (e.g. Ceverino & Klypin, 2007). Simulations by Halle et al. (2018) show that these trapped stars adhere to the resonance as the bar slows down. Some works have also discussed direct trapping of dark matter into a 'shadow bar' (Athanassoula, 2007; Petersen et al., 2016; Collier & Madigan, 2021).

Thus, both observations and simulations indicate that the main resonances of typical bars evolve in the slow regime. Generally, bar evolution involves both fast and slow regimes depending on the evolutionary phase, the type of resonance, and the position along each resonance, since fast or slow is decided by the measure of the bar's slowing rate against the local libration frequency. While the dynamical friction in the fast limit has been modelled successfully by linear theory (W04), the slow regime has been little explored. The sole exception is TW84 who formulated the net change in angular momentum of orbits swept past by a resonance by analytically integrating the torque from $t = -\infty$ to ∞. Their formula,

however, does not describe the dynamical friction due to the transient response against the passage of the resonance (e.g. phase mixing). Similarly to the point raised by W04 in the fast limit, we show that the transient effects are significant and even more so in the slow regime due to the long mixing time of trapped orbits. Therefore, beyond the work of TW84, modelling bar evolution requires a time-dependent theory of dynamical friction in the slow regime. This thesis takes the first step towards this problem by working in the *slow limit* of bar evolution (i.e. no slowdown). Taking the slow limit enables us to analytically model dynamical friction by both trapped and untrapped orbits in a fully time-dependent manner while setting aside the more complicated process of resonant capture and escape (e.g. Henrard, 1982; Sridhar & Touma, 1996). We will, however, show numerically that the qualitative mechanism of dynamical friction identified in the slow limit applies generally to the slow regime.

The dynamics of resonant trapping is best viewed in the slow angle-action plane which exhibits a phase flow akin to that of a simple pendulum: trapped orbits librate around the resonance centre (and their slow angle oscillates around the resonance midpoint), while untrapped orbits circulate above and below the separatrix (i.e. their slow angle moves freely across the whole 2π range). Before bar formation, the phase-space density typically declines towards large slow action (i.e. the z-angular momentum). When the bar forms, the trapped region grows and captures orbits from both above and below the resonance, reconnecting phase space across regions of different densities. The newly trapped orbits are thus inevitably non-uniform in the libration angle. As these trapped orbits librate around the resonance along contours of constant libration actions, their innate angle imbalance results in a periodic dynamical friction on the bar. However, due to the monotonic decrease of libration frequency towards the separatrix, the density inside the trapped zone gradually winds up into a phase-space spiral, and the net torque from trapped orbits slowly attenuates. The phase mixing timescale is set by the libration period (typically $> 1\,\mathrm{Gyr}$), which prevents complete mixing in a Hubble time. This leads us to predict that bars are subject to pattern speed oscillations on the timescale of the libration, which is an order of magnitude longer than the short-period fluctuations due to bar-spiral interactions (Wu et al., 2016; Hilmi et al., 2020).

In this thesis, we study this behaviour both analytically and in test particle simulations. The analytical approach uses the resonant angle-action coordinates for each resonance obtained by the method of averaging (e.g. Lichtenberg & Lieberman, 1992). These local coordinates allow us to model the resonant dynamics trivially. We also discuss the accuracy of the averaging method when chaos emerges due to the overlap of multiple resonances.

This chapter is organized as follows. In section 4.3, we specify our model of the halo and the bar. Section 4.4 reviews the torque formula in the fast limit and discusses its problems when applied to systems in the slow regime. In section 4.5, we lay out the standard method to treat the non-linear dynamics near resonance and formulate the dynamical friction in the slow limit which we verify against test-particle simulations. We will discuss the consequences of an evolving bar in section 4.6 and sum up in section 4.7.

4.3 Model

4.3.1 Model of dark halo

We model the dark halo with an isotropic Hernquist (1990) model:

$$\rho_0(r) = \frac{M}{2\pi}\frac{r_\mathrm{s}}{r(r_\mathrm{s}+r)^3}, \qquad \Phi_0(r) = -\frac{GM}{r_\mathrm{s}+r}, \tag{4.1}$$

where G is the gravitational constant, M is the total halo mass, and r_s the halo scale radius. By default, we set $M = 1.5\times10^{12}\,\mathrm{M}_\odot$ and $r_\mathrm{s} = 20\,\mathrm{kpc}$. The corresponding distribution function and setup of the test-particle simulations are described in Appendix 4.A.

4.3.2 Model of Galactic bar

We use the same quadrupole bar model as in Chapters 2 and 3, but extend it to three dimension. As a reasonable model, we adopt the real part of the spherical harmonics Y_{22}

$$\Phi_\mathrm{b}(r,\vartheta,\varphi,t) = \Phi_\mathrm{b}(r)\sin^2\vartheta\cos 2\left(\varphi-\Omega_\mathrm{p}t\right), \tag{4.2}$$

where (r,ϑ,φ) are the usual spherical coordinates. The radial dependence of the bar potential is given by equation (2.7). By default, we set $\Omega_\mathrm{p} = 35\,\mathrm{km\,s^{-1}\,kpc^{-1}} \simeq 35.8\,\mathrm{Gyr^{-1}}$ (Binney, 2020b; Chiba & Schönrich, 2021; Clarke & Gerhard, 2021).

4.3.3 Angle-action variables in spherical potential

The description of orbits in an integrable system is greatly simplified with the use of angle-action variables $(\boldsymbol{\theta}, \boldsymbol{J})$ (e.g. Binney & Tremaine, 2008). By construction, the Hamiltonian $H_0(\boldsymbol{J})$ does not depend on the angles, so the equations of motion are trivial in these coordinates:

$$\dot{\boldsymbol{J}} = -\frac{\partial H_0}{\partial \boldsymbol{\theta}} = \boldsymbol{0}, \qquad \dot{\boldsymbol{\theta}} = \frac{\partial H_0}{\partial \boldsymbol{J}} \equiv \boldsymbol{\Omega}(\boldsymbol{J}), \tag{4.3}$$

i.e., the actions are conserved and the conjugate angles increase linearly with time at constant rate $\boldsymbol{\Omega}(\boldsymbol{J})$.

In a spherically symmetric potential, a convenient set of actions are $\boldsymbol{J} = (J_r, L, L_z)$ where J_r is the radial action, L is the magnitude of the angular momentum vector $\boldsymbol{L}$, and L_z is the z-component of $\boldsymbol{L}$. The ratio between L and L_z defines the orbital inclination $\beta \equiv \cos^{-1}(L_z/L)$. The conjugate angle variables $\boldsymbol{\theta} = (\theta_r, \theta_\psi, \theta_\varphi)$ describe, respectively, the radial phase, the azimuthal phase in the orbital plane, and the (fixed) longitude of the ascending node, i.e. the intersection of the orbital plane and the galactic equatorial plane.

4.4 Torque in the fast limit

To compare our approach (section 4.5) with the conventional approximations, we here briefly review the torque formula in the fast limit developed by TW84 and W04. Following W04, we solve for the second-order torque using the linear solution to the collisionless Boltzmann equation. We will demonstrate the breakdown of the formula in the slow regime and discuss the cause of the problem. Throughout the thesis, we ignore the halo's self-gravitational perturbation.

We assume that the halo is in a steady state prior to bar formation. The unperturbed distribution is then a function of the actions alone $f_0(\boldsymbol{J})$ (Jeans' theorem). When the bar forms, the perturbing potential changes the halo's distribution by $f_1(\boldsymbol{\theta}, \boldsymbol{J}, t)$. We can then write the Hamiltonian H and the distribution function f as

$$H(\boldsymbol{\theta}, \boldsymbol{J}, t) = H_0(\boldsymbol{J}) + \Phi_1(\boldsymbol{\theta}, \boldsymbol{J}, t), \qquad f(\boldsymbol{\theta}, \boldsymbol{J}, t) = f_0(\boldsymbol{J}) + f_1(\boldsymbol{\theta}, \boldsymbol{J}, t), \tag{4.4}$$

where Φ_1 consists of the bar potential (4.2) and the self-gravitational perturbation induced by the response of the halo f_1, although here we ignore the latter. The angle variables are, by construction, 2π periodic, so one can expand the perturbations into a Fourier series:

$$\Phi_1(\boldsymbol{\theta}, \boldsymbol{J}, t) = \sum_{\mathbf{n}} \hat{\Phi}_{\mathbf{n}}(\boldsymbol{J}, t) \mathrm{e}^{i\mathbf{n}\cdot\boldsymbol{\theta}}, \qquad f_1(\boldsymbol{\theta}, \boldsymbol{J}, t) = \sum_{\mathbf{n}} \hat{f}_{\mathbf{n}}(\boldsymbol{J}, t) \mathrm{e}^{i\mathbf{n}\cdot\boldsymbol{\theta}}, \tag{4.5}$$

where $\mathbf{n} = (\mathrm{n}_r, \mathrm{n}_\psi, \mathrm{n}_\varphi)$ is a vector of integers. $\hat{\Phi}_{\mathbf{n}}(\boldsymbol{J}, t)$ is given in Appendix 4.B. The torque exerted on a single orbit is then

$$\frac{\mathrm{d}L_z}{\mathrm{d}t} = -\frac{\partial H}{\partial \theta_\varphi} = -i \sum_{\mathbf{n}} \mathrm{n}_\varphi \hat{\Phi}_{\mathbf{n}}(\boldsymbol{J}, t) \mathrm{e}^{i\mathbf{n}\cdot\boldsymbol{\theta}}, \tag{4.6}$$

and the total torque integrated over the full distribution is

$$\begin{aligned} \left\langle \frac{\mathrm{d}L_z}{\mathrm{d}t} \right\rangle &= \int \mathrm{d}^3\boldsymbol{J} \mathrm{d}^3\boldsymbol{\theta} f(\boldsymbol{\theta}, \boldsymbol{J}, t) \frac{\mathrm{d}L_z}{\mathrm{d}t} \\ &= \int \mathrm{d}^3\boldsymbol{J} \mathrm{d}^3\boldsymbol{\theta} \left[f_0(\boldsymbol{J}) + \sum_{\mathbf{n}} \hat{f}_{\mathbf{n}}(\boldsymbol{J}, t) \mathrm{e}^{i\mathbf{n}\cdot\boldsymbol{\theta}} \right] \left[-i \sum_{\mathbf{n}'} \mathrm{n}'_\varphi \hat{\Phi}_{\mathbf{n}'}(\boldsymbol{J}, t) \mathrm{e}^{i\mathbf{n}'\cdot\boldsymbol{\theta}} \right]. \end{aligned} \tag{4.7}$$

The first term vanishes upon integration over $\boldsymbol{\theta}$ and the second term is non-zero only when $\mathbf{n}' = -\mathbf{n}$, so

$$\left\langle \frac{\mathrm{d}L_z}{\mathrm{d}t} \right\rangle = i\,(2\pi)^3 \sum_{\mathbf{n}} \mathrm{n}_\varphi \int \mathrm{d}^3\boldsymbol{J}\, \hat{f}_{\mathbf{n}}(\boldsymbol{J}, t) \hat{\Phi}^*_{\mathbf{n}}(\boldsymbol{J}, t), \tag{4.8}$$

where we used $\hat{\Phi}_{-\mathbf{n}} = \hat{\Phi}^*_{\mathbf{n}}$ as required by $\mathrm{Im}[\Phi_1] = 0$. We see from the above equation that the torque is second order in the perturbation. To proceed, we need to develop the response $\hat{f}_{\mathbf{n}}(\boldsymbol{J}, t)$ as a function of the potential perturbation $\hat{\Phi}_{\mathbf{n}}(\boldsymbol{J}, t)$. This is described by the collisionless Boltzmann equation (CBE):

$$\frac{\mathrm{d}f}{\mathrm{d}t} = \frac{\partial f}{\partial t} + \frac{\partial f}{\partial \boldsymbol{\theta}} \cdot \frac{\partial H}{\partial \boldsymbol{J}} - \frac{\partial f}{\partial \boldsymbol{J}} \cdot \frac{\partial H}{\partial \boldsymbol{\theta}} = 0. \tag{4.9}$$

Using the Fourier decomposition (4.5), we have, for each $\mathbf{n}$,

$$\frac{\partial \hat{f}_{\mathbf{n}}}{\partial t} + i\mathbf{n}\cdot\boldsymbol{\Omega}\hat{f}_{\mathbf{n}} - i\mathbf{n}\cdot\frac{\partial f_0}{\partial \boldsymbol{J}}\hat{\Phi}_{\mathbf{n}} + \sum_{\mathbf{n}'} \left[i(\mathbf{n}-\mathbf{n}')\cdot\frac{\partial \hat{\Phi}_{\mathbf{n}'}}{\partial \boldsymbol{J}} \hat{f}_{\mathbf{n}-\mathbf{n}'} - i\mathbf{n}'\cdot\frac{\partial \hat{f}_{\mathbf{n}-\mathbf{n}'}}{\partial \boldsymbol{J}} \hat{\Phi}_{\mathbf{n}'} \right] = 0. \tag{4.10}$$

The standard prescription to solve this for $\hat{f}_{\mathbf{n}}$ is to ignore the non-linear terms inside the square bracket assuming that both $|f_1/f_0|$ and $|\Phi_1/H_0|$ are sufficiently small. This yields the linearized CBE, which has the following solution for an external perturbation imposed

after $t = 0$:

$$\hat{f}_{\mathbf{n}}(\boldsymbol{J}, t) = i\mathbf{n} \cdot \frac{\partial f_0}{\partial \boldsymbol{J}} \int_0^t \mathrm{d}t' \mathrm{e}^{-i\mathbf{n}\cdot\boldsymbol{\Omega}(t-t')} \hat{\Phi}_{\mathbf{n}}(\boldsymbol{J}, t'). \tag{4.11}$$

Substituting equation (4.11) to (4.8) yields the general torque formula

$$\left\langle \frac{\mathrm{d}L_z}{\mathrm{d}t} \right\rangle = -(2\pi)^3 \sum_{\mathbf{n}} \mathrm{n}_\varphi \int \mathrm{d}^3\boldsymbol{J}\mathbf{n} \cdot \frac{\partial f_0}{\partial \boldsymbol{J}} \left[\int_0^t \mathrm{d}t' \mathrm{e}^{-i\mathbf{n}\cdot\boldsymbol{\Omega}(t-t')} \hat{\Phi}_{\mathbf{n}}(\boldsymbol{J}, t') \right] \hat{\Phi}^*_{\mathbf{n}}(\boldsymbol{J}, t). \tag{4.12}$$

For a perturbation with constant amplitude and pattern speed $\boldsymbol{\Omega}_\mathrm{p}$, the time dependence separates as $\hat{\Phi}_{\mathbf{n}}(\boldsymbol{J}, t) = \hat{\Phi}_{\mathbf{n}}(\boldsymbol{J}) \mathrm{e}^{-i\mathrm{n}_\varphi \Omega_\mathrm{p} t}$, and we have (W04)

$$\left\langle \frac{\mathrm{d}L_z}{\mathrm{d}t} \right\rangle = -(2\pi)^3 \sum_{\mathbf{n}} \mathrm{n}_\varphi \int \mathrm{d}^3\boldsymbol{J}\mathbf{n} \cdot \frac{\partial f_0}{\partial \boldsymbol{J}} |\hat{\Phi}_{\mathbf{n}}(\boldsymbol{J})|^2 \frac{\sin\left[\left(\mathbf{n}\cdot\boldsymbol{\Omega} - \mathrm{n}_\varphi\Omega_\mathrm{p}\right) t\right]}{\mathbf{n}\cdot\boldsymbol{\Omega} - \mathrm{n}_\varphi\Omega_\mathrm{p}}, \tag{4.13}$$

which, in the time-asymptotic limit $t \to \infty$, reduces to the LBK formula (TW84; LBK72)

$$\left\langle \frac{\mathrm{d}L_z}{\mathrm{d}t} \right\rangle = -(2\pi)^3 \sum_{\mathbf{n}} \mathrm{n}_\varphi \int \mathrm{d}^3\boldsymbol{J}\mathbf{n} \cdot \frac{\partial f_0}{\partial \boldsymbol{J}} |\hat{\Phi}_{\mathbf{n}}(\boldsymbol{J})|^2 \pi\delta\left(\mathbf{n}\cdot\boldsymbol{\Omega} - \mathrm{n}_\varphi\Omega_\mathrm{p}\right). \tag{4.14}$$

W04 (and more recently Banik & van den Bosch, 2021) emphasized the problem of taking the time-asymptotic limit as the evolution time for galaxies is not well separated from the relevant dynamical time.

It is obvious from equations (4.13) and (4.14) that the torque is dominated by contributions from phase space near resonances, i.e. $\mathbf{n}\cdot\boldsymbol{\Omega} - \mathrm{n}_\varphi\Omega_\mathrm{p} \approx 0$. However, the vicinity of resonances is precisely where the linearized CBE becomes invalid: if resonances do not move, the linear response (4.11) grows indefinitely at resonances (Appendix 4.C), and this will soon violate the assumption that the non-linear terms of the CBE (4.10) are negligible, which is the basis of this formalism. A correct physical description must respect that the orbits near resonances become trapped, a non-linear secular behaviour that cannot be described by linear theory.

To illustrate the problem, we show in Fig. 4.1 the torque exerted on the halo by a constantly rotating bar. We compare the torque measured from a test particle simulation (black) with linear theory (equation 4.13, blue) and the LBK formula (equation 4.14, dashed green). For the two approximations, we restrict the summation to indices with $\mathrm{n}_r \in [-10, 10]$, $\mathrm{n}_\psi \in -2, 0, 2$, and $\mathrm{n}_\varphi = 2$. Since both the halo density and the perturbing potential decrease towards large radii, the contributions are largely limited to the main resonances with small r, the strongest being the corotation resonance $\mathbf{n} = (0, 2, 2)$. The top

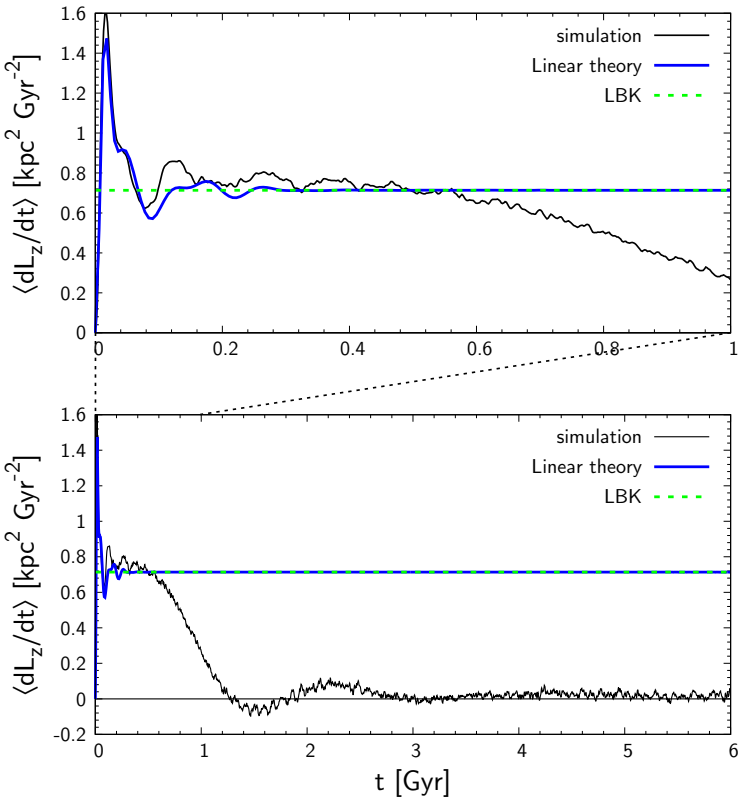

Fig. 4.1 Total torque on the halo (divided by the total halo mass) perturbed by a bar with constant pattern speed and amplitude switched on at $t = 0$. Linear theory (blue, equation 4.13) agrees with the torque of the test-particle simulation (black) for a few dynamical period (top panel) but fails to predict the long-term evolution (bottom panel). The LBK formula (green, equation 4.14) gives the time-asymptotic value of linear theory.

panel shows the evolution for the first 1 Gyr which we see a fair agreement between the simulation (black) and the time-dependent linear theory (blue) up to ~ 500 Myr. However, the linear theory qualitatively fails to predict the subsequent long-term evolution shown in the bottom panel: while the torque of linear theory rapidly converges to a non-zero constant value predicted by the LBK formula, the numerical torque fluctuates over a much longer timescale, gradually settling down to zero[1]. This relaxation is driven by phase mixing (a collisionless relaxation), as we describe in the next section.

In this experiment, we have kept the bar's pattern speed constant. If the bar decelerates sufficiently fast that the resonances pass over the orbits before they can respond non-linearly, resonant trapping will not occur and linear theory will properly predict the torque for an

[1]We note that this limit depends on the time-dependence of the perturbation. Here the approach to a steady state (zero torque) is the result of the assumed constant bar pattern speed and amplitude.

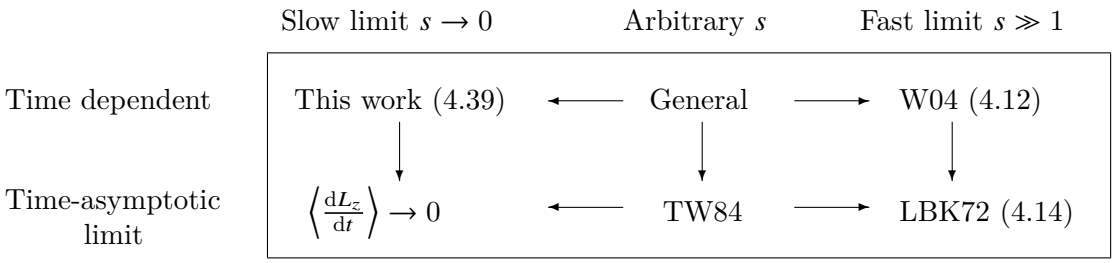

Fig. 4.2 Domain of applicability. The numbers in brackets numerate the equations within our thesis. TW84 formulated the torque for arbitrary s in the time-asymptotic limit, and demonstrated the recovery of the LBK72 formula (4.14) in the fast limit ($s \gg 1$). The time-dependent formula (4.12) derived by W04 is valid in the fast limit and reduces to LBK in the time-asymptotic limit. We formulate the time-dependent torque in the slow limit ($s \to 0$) which, in the time-asymptotic limit, predicts zero torque in agreement with TW84.

extended period of time as demonstrated in W04. For this reason, the linear formalism is said to be valid in the *fast limit* (TW84). The validity is characterized by the speed parameter[2](TW84):

$$s \equiv \left| \frac{\mathrm{n}_\varphi \dot{\Omega}_\mathrm{p}}{\omega_0^2} \right|, \tag{4.15}$$

where $\dot{\Omega}_\mathrm{p}$ measures the long-term evolution of the pattern speed (i.e. not the short-term fluctuations as discussed in Wu et al., 2016) and ω_0 is the libration frequency of trapped orbits at the core of the resonance (equation 4.23). In the fast limit $s \gg 1$, orbits cannot stay trapped in resonance because the resonant potential no longer features a local minimum (TW84, Chiba et al., 2021, see also Appendix 4.E).

If the perturbation vanishes before any non-linear effect develops, the formulae will be valid regardless of s. This could be the case for e.g. transient spiral arms. Hence, the traditional torque formulas (4.12)-(4.14) are appropriate to study the evolution of perturbations that either decelerate rapidly or decay rapidly. Since neither applies to long-lived galactic bars, we must fully model the non-linear response of the halo, i.e. trapping at resonances.

[2]In the limit of epicycle approximation, the speed parameter reduces to $s \sim \eta/A$ where $\eta \equiv -\dot{\Omega}_\mathrm{p}/\Omega_\mathrm{p}^2$ is the bar's dimensionless slowing rate and A the dimensionless bar strength (Chiba et al., 2021, equation 27).

4.5 Torque in the slow limit

4.5.1 Approach by Tremaine & Weinberg (1984)

The torque in the slow regime has been discussed in TW84, who derived a general formula of dynamical friction valid for arbitrary speed parameter s by Taylor expansion around each sweeping resonance (equation 86 in TW84). By retaining the first two terms of the Taylor series, they demonstrate that the LBK72 formula (4.14) is recovered in the fast limit ($s \gg 1$). In the slow non-linear regime ($s < 1$), by retaining the leading order term, TW84 approximates the total dynamical friction by the torque on resonant orbits averaged over their initial phase and integrated from $t = -\infty$ to $t = \infty$. The resulting equation[3] describes the net change in angular momentum of orbits that have jumped over a moving resonance. This slow formula, however, does not describe the temporal fluctuations in the torque caused by the transient responses to the passage of a resonance. As we show in section 4.6, the sweeping resonance leaves behind a striated perturbation in phase space that requires several orbital periods to phase mix and reach a steady state. The slow formula of TW84 is thus equivalent in essence to the prediction in the time-asymptotic limit, i.e. the net torque after any phase imbalance is smoothed away by phase mixing. In the slow limit ($s \to 0$ and thus $\dot{\Omega}_\mathrm{p} \to 0$), the TW84 formula predicts zero torque (since their torque depends linearly on $\dot{\Omega}_\mathrm{p}$) which is consistent with the limiting behaviour of the damped oscillation shown in Fig. 4.1. We summarize the relations among the existing theories in Fig. 4.2. The formulae are classified based on slow vs. fast limit and time-dependent vs. time-asymptotic limit. In this map, our equation (4.39) derived in the following fills the top-left corner: a time-dependent formula valid in the slow limit ($s \to 0$). By our notation $s \to 0$, we imply the strict limit, where the bar rotates constantly, and not a bar slowing in the limit of small s. The time-dependent dynamical friction in the general slow regime ($0 < s < 1$) will be discussed numerically in section 4.6.

[3] A summarized formula is given in equation (39) of Weinberg (1985).

4.5.2 Angle-action variables near resonances

The alternative to Taylor expansion or to solving the non-linear terms in the CBE (4.10) is simply to change the coordinates. The majority of orbits near each resonance $\boldsymbol{N} = (N_r, N_\psi, N_\varphi)$ behave quasi-periodically regardless of trapping and thus there exists a new set of angle-action coordinates for them (e.g. TW84; Kaasalainen, 1994; Sridhar & Touma, 1996; Binney, 2016, 2018; Monari et al., 2017b). In these resonant angle-action coordinates, the time evolution of the distribution function can be solved trivially using the non-linearized CBE (section 4.5.3). In this section, we first lay out the known coordinate transformations, and from there develop our equations for the torque on both trapped and untrapped orbits.

We start with a canonical transformation to the so-called slow-fast angle-action variables $(\boldsymbol{\theta}', \boldsymbol{J}') = (\theta_{\mathrm{f}_1}, \theta_{\mathrm{f}_2}, \theta_\mathrm{s}, J_{\mathrm{f}_1}, J_{\mathrm{f}_2}, J_\mathrm{s})$ (e.g. TW84):

$$\theta_{\mathrm{f}_1} = \theta_r, \qquad \theta_{\mathrm{f}_2} = \theta_\psi, \qquad \theta_\mathrm{s} = \boldsymbol{N}\cdot\boldsymbol{\theta} - N_\varphi \Omega_\mathrm{p} t, \tag{4.16}$$

$$J_{\mathrm{f}_1} = J_r - \frac{N_r}{N_\varphi} L_z, \quad J_{\mathrm{f}_2} = L - \frac{N_\psi}{N_\varphi} L_z, \quad J_\mathrm{s} = \frac{L_z}{N_\varphi}, \tag{4.17}$$

using the generating function

$$W(\boldsymbol{\theta}, \boldsymbol{J}', t) = \theta_r J_{\mathrm{f}_1} + \theta_\psi J_{\mathrm{f}_2} + \left(\boldsymbol{N}\cdot\boldsymbol{\theta} - N_\varphi \Omega_\mathrm{p} t\right) J_\mathrm{s}. \tag{4.18}$$

The Hamiltonian (4.4) transforms to

$$H(\boldsymbol{\theta}', \boldsymbol{J}') = H_0(\boldsymbol{J}') - N_\varphi \Omega_\mathrm{p} J_\mathrm{s} + \sum_{\boldsymbol{k}} \hat{\Psi}_{\boldsymbol{k}}(\boldsymbol{J}')\, \mathrm{e}^{i\boldsymbol{k}\cdot\boldsymbol{\theta}'}, \tag{4.19}$$

where we have expanded the perturbation H_1 into a Fourier series (Appendix 4.B) with indices $\boldsymbol{k} = (k_{\mathrm{f}_1}, k_{\mathrm{f}_2}, k_\mathrm{s})$. The purpose of transforming to the slow-fast variables is to separate the motion into slow and fast components: near the resonance, the slow angle θ_s evolves much slower than the fast angles $\boldsymbol{\theta}_\mathrm{f} = (\theta_{\mathrm{f}_1}, \theta_{\mathrm{f}_2})$. This allows one to average the Hamiltonian over $\boldsymbol{\theta}_\mathrm{f}$ while holding θ_s fixed which removes all perturbation terms in (4.19) with $\boldsymbol{k}_\mathrm{f} = (k_{\mathrm{f}_1}, k_{\mathrm{f}_2}) \neq \boldsymbol{0}$. Since only terms with $k_\mathrm{s} = \pm 1$ are non-zero for resonances with $N_\varphi = 2$ (Appendix 4.B), we may write

$$\bar{H}(\theta_\mathrm{s}, \boldsymbol{J}') = H_0(\boldsymbol{J}') - N_\varphi \Omega_\mathrm{p} J_\mathrm{s} + \Psi(\boldsymbol{J}') \cos\left(\theta_\mathrm{s} - \theta_{\mathrm{s,res}}\right), \tag{4.20}$$

where $\Psi \equiv 2|\hat{\Psi}_{(0,0,1)}|$. In this averaged system, the two fast actions $\boldsymbol{J}_\mathrm{f} = (J_{\mathrm{f}_1}, J_{\mathrm{f}_2})$ are conserved, i.e. $\dot{\boldsymbol{J}}_\mathrm{f} = -\frac{\partial \bar{H}}{\partial \boldsymbol{\theta}_\mathrm{f}} = \mathbf{0}$. Thus this Hamiltonian is integrable: it has three isolating integrals, the two fast actions and the Hamiltonian itself, meaning that angle-action coordinates for $\bar{H}$ exist.

A convenient analytical transformation to the angle-action coordinates of $\bar{H}$ is available if we Taylor expand $\bar{H}$ around the resonance $J_\mathrm{s,res}$ up to second order and ignore terms smaller than $|\Psi/H_0|$:

$$\bar{H}(\theta_\mathrm{s}, \boldsymbol{J}') \simeq \frac{1}{2} G\left(\boldsymbol{J}_\mathrm{f}, J_\mathrm{s,res}\right)\left(J_\mathrm{s} - J_\mathrm{s,res}\right)^2 + \Psi\left(\boldsymbol{J}_\mathrm{f}, J_\mathrm{s,res}\right)\cos\left(\theta_\mathrm{s} - \theta_\mathrm{s,res}\right), \tag{4.21}$$

where

$$G(\boldsymbol{J}') \equiv \frac{\partial^2 H_0}{\partial J_\mathrm{s}^2} = \frac{\partial \Omega_s}{\partial J_\mathrm{s}}. \tag{4.22}$$

The first order derivative of $H_0(\boldsymbol{J}') - N_\varphi \Omega_\mathrm{p} J_\mathrm{s}$ vanishes at the resonance and we have dropped the constant terms. The approximated Hamiltonian takes the form of a classical pendulum Hamiltonian apart from a different sign. In galactic dynamics, G (equation 4.22) is in many cases negative (TW84, Figure 5), so in what follows we will assume $G < 0$ although cases with $G > 0$ can be treated similarly by adjusting $\theta_\mathrm{s,res}$ as appropriate. For subsequent use, we define

$$\omega_0^2 \equiv -G\Psi, \quad J_0^2 \equiv -\frac{\Psi}{G}, \quad \varepsilon \equiv \sqrt{\frac{1}{2}\left(1 - \frac{\bar{H}}{\Psi}\right)}. \tag{4.23}$$

Depending on the value of $\bar{H}$, parametrized by the dimensionless energy of the pendulum ε, there are two types of qualitatively different motions as depicted in Fig. 4.3: orbits librate when $0 \leq \varepsilon < 1$ (trapped) and circulate above or below the resonance when $\varepsilon > 1$ (untrapped). $\varepsilon = 1$ defines the separatrix.

In the following, we summarize the canonical transformation from the slow angle-action variables $(\theta_\mathrm{s}, J_\mathrm{s})$ to the angle-action coordinates of libration/circulation (Brizard, 2013), and formulate the secular torque on trapped/untrapped orbits.

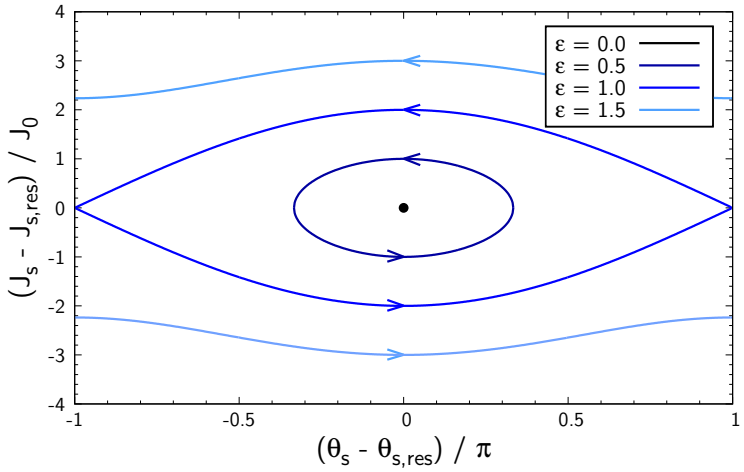

Fig. 4.3 Phase flow for the approximate $\bar{H}$ (4.21). Level curves of $\bar{H}$ parametrized by ε are plotted. For $0 \leq \varepsilon < 1$, the motion of orbits in θ_s is bounded (libration) whereas for $\varepsilon > 1$, θ_s is unbounded (circulation).

Trapped orbits $(0 \leq \varepsilon < 1)$

The angle-action coordinates of libration are

$$\theta_\ell = \theta_{\ell 0} + \Omega_\ell t, \quad \Omega_\ell = \frac{\pi}{2K(\varepsilon)}\omega_0, \tag{4.24}$$

$$J_\ell = \frac{1}{2\pi}\oint \mathrm{d}\theta_s J_s = \frac{8J_0}{\pi}\left[E(\varepsilon) - \left(1-\varepsilon^2\right)K(\varepsilon)\right], \tag{4.25}$$

where $K(\varepsilon)$ and $E(\varepsilon)$ are the complete elliptic integral of the first and second kinds (Appendix 4.D). ω_0 and J_0 are defined in equation (4.23). The inverse transformation is

$$\theta_s - \theta_{s,\mathrm{res}} = 2\arcsin\left[\varepsilon \mathrm{sn}\left(\frac{2K(\varepsilon)}{\pi}\theta_\ell \middle| \varepsilon\right)\right], \tag{4.26}$$

$$J_s - J_{s,\mathrm{res}} = 2J_0\varepsilon \mathrm{cn}\left(\frac{2K(\varepsilon)}{\pi}\theta_\ell \middle| \varepsilon\right), \tag{4.27}$$

where sn, cn and dn are the Jacobi elliptic functions (Appendix 4.D). The torque exerted on trapped orbits is then

$$\frac{\mathrm{d}L_z}{\mathrm{d}t} = N_\varphi \Omega_\ell \frac{\mathrm{d}J_s}{\mathrm{d}\theta_\ell} = 2N_\varphi \varepsilon \Psi \mathrm{sn}\left(\frac{2K(\varepsilon)}{\pi}\theta_\ell \middle| \varepsilon\right)\mathrm{dn}\left(\frac{2K(\varepsilon)}{\pi}\theta_\ell \middle| \varepsilon\right), \tag{4.28}$$

which becomes harmonic near the centre of the resonance:

$$\frac{\mathrm{d}L_z}{\mathrm{d}t} \simeq 2N_\varphi \varepsilon \Psi \sin\theta_\ell \quad \text{for} \quad \varepsilon \ll 1. \tag{4.29}$$

Non-trapped orbits ($\varepsilon > 1$)

The angle-action coordinates of circulation are

$$\theta_\mathrm{c} = \theta_{\mathrm{c}0} + \Omega_\mathrm{c} t, \quad \Omega_\mathrm{c} = \frac{\pi\varepsilon}{K(\varepsilon^{-1})}\omega_0, \tag{4.30}$$

$$J_\mathrm{c} = \frac{1}{2\pi}\oint \mathrm{d}\theta_\mathrm{s} J_\mathrm{s} = J_{\mathrm{s,res}} \pm \frac{4J_0\varepsilon}{\pi}E(\varepsilon^{-1}), \tag{4.31}$$

where the ± signs correspond to the upper and lower circulating regimes, respectively. Note that the subscript 'c' denotes 'circulating' (untrapped) orbits and not 'circular' orbits. The inverse transformation is

$$\theta_\mathrm{s} - \theta_{\mathrm{s,res}} = \pm 2 \arcsin\left[\mathrm{sn}\left(\frac{K(\varepsilon^{-1})}{\pi}\theta_\mathrm{c}\middle|\varepsilon^{-1}\right)\right], \tag{4.32}$$

$$J_\mathrm{s} - J_{\mathrm{s,res}} = \pm 2J_0\varepsilon\,\mathrm{dn}\left(\frac{K(\varepsilon^{-1})}{\pi}\theta_\mathrm{c}\middle|\varepsilon^{-1}\right). \tag{4.33}$$

In the limit $\varepsilon \to \infty$, the slow action is conserved and the slow angle θ_s asymptotically approaches the angle of circulation θ_c. The torque exerted on untrapped orbits is

$$\frac{\mathrm{d}L_z}{\mathrm{d}t} = \pm 2N_\varphi\Psi\,\mathrm{sn}\left(\frac{K(\varepsilon^{-1})}{\pi}\theta_\mathrm{c}\middle|\varepsilon^{-1}\right)\mathrm{cn}\left(\frac{K(\varepsilon^{-1})}{\pi}\theta_\mathrm{c}\middle|\varepsilon^{-1}\right). \tag{4.34}$$

Far from the resonance, the torque again becomes harmonic:

$$\frac{\mathrm{d}L_z}{\mathrm{d}t} \simeq \pm N_\varphi\Psi\sin\theta_\mathrm{c} \quad \text{for} \quad \varepsilon \gg 1. \tag{4.35}$$

The behaviour of the torque is plotted in Fig. 4.4. As seen in (4.29) and (4.35), the torque fluctuates sinusoidally near the core ($\varepsilon \ll 1$) of the resonance, as well as far from it ($\varepsilon \gg 1$). The torque on trapped orbits diminishes towards $\varepsilon = 0$ where it vanishes. Near the separatrix ($\varepsilon \approx 1$), the torque forms a dip at $\theta_\ell = \pi/2, 3\pi/2$ since orbits stagnate near the unstable singular points $(\theta_\mathrm{s} - \theta_{\mathrm{s,res}}, J_\mathrm{s} - J_{\mathrm{s,res}}) = (\pm\pi, 0)$, which, for the corotation resonance, correspond to the unstable Lagrange points $L_{1,2}$ on the bar's major axis. As the orbit approaches the separatrix, the dip deepens and eventually the torque becomes zero over the entire phase except at $\theta_\ell = 0$ and π. This situation is analogous to a real pendulum in transition from oscillation to circulation that spends most of its time/phase stagnating at the top of the pivot with hardly any change in momentum.

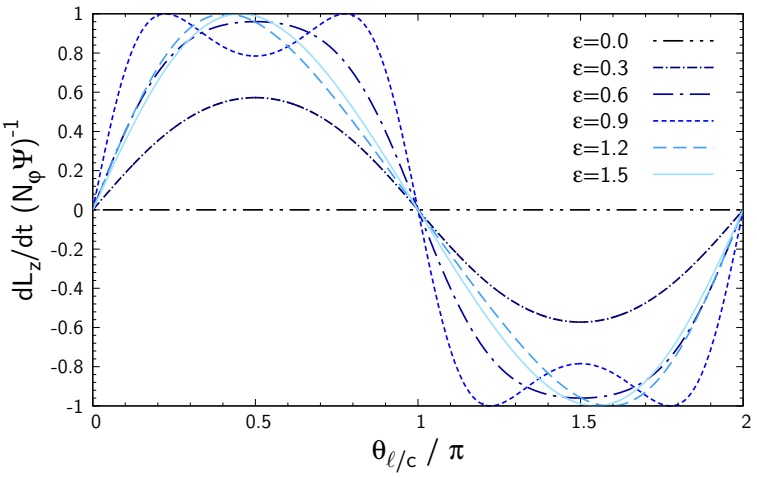

Fig. 4.4 Torque applied to trapped ($\varepsilon < 1$) and untrapped ($\varepsilon > 1$) orbits as a function of the libration/circulation angle $\theta_{\ell/\mathrm{c}}$. The behaviour deviates from a sinusoidal wave near the separatrix $\varepsilon = 1$.

4.5.3 Evolution of the distribution function

The averaged Hamiltonian $\bar{H}$ (4.21) now only depends on the new actions $\boldsymbol{J}'' = (J_{\mathrm{f}_1}, J_{\mathrm{f}_2}, J_{\ell/\mathrm{c}})$ that are conjugate to the new angles $\boldsymbol{\theta}'' = (\theta_{\mathrm{f}_1}, \theta_{\mathrm{f}_2}, \theta_{\ell/\mathrm{c}})$ where the subscript 'ℓ/c' indicates libration or circulation depending on ε. The collisionless Boltzmann equation (4.9) for the averaged system is then

$$\frac{\partial f}{\partial t} + \boldsymbol{\Omega}'' \cdot \frac{\partial f}{\partial \boldsymbol{\theta}''} = 0, \quad \text{where} \quad \boldsymbol{\Omega}''(\boldsymbol{J}'') \equiv \frac{\partial \bar{H}}{\partial \boldsymbol{J}''}. \tag{4.36}$$

This equation has the trivial solution

$$f(\boldsymbol{\theta}'', \boldsymbol{J}'', t) = f(\boldsymbol{\theta}'' - \boldsymbol{\Omega}'' t, \boldsymbol{J}'', 0). \tag{4.37}$$

One can thus readily obtain the phase space density at any time $t = \tau$ from the original distribution at $t = 0$ by simply winding the angles backward by $\boldsymbol{\Omega}''\tau$. Since the initial unperturbed distribution of the halo (4.41) is uniform in the fast angle $(\theta_{\mathrm{f}_1}, \theta_{\mathrm{f}_2})$ but *not* in the libration/circulation angle $\theta_{\ell/\mathrm{c}}$, the system is out of equilibrium after the emergence of the bar and starts phase mixing in $\theta_{\ell/\mathrm{c}}$.

Figure 4.5 shows the evolution of the phase-space density near the corotation resonance (CR) at $(J_{\mathrm{f}_1}, J_{\mathrm{f}_2}) = (10, 0)\,\mathrm{kpc}^2\,\mathrm{Gyr}^{-1}$ plotted every 1 Gyr from top to bottom. The bar is instantaneously switched on at $t = 0$. The left-hand column shows the distribution of the

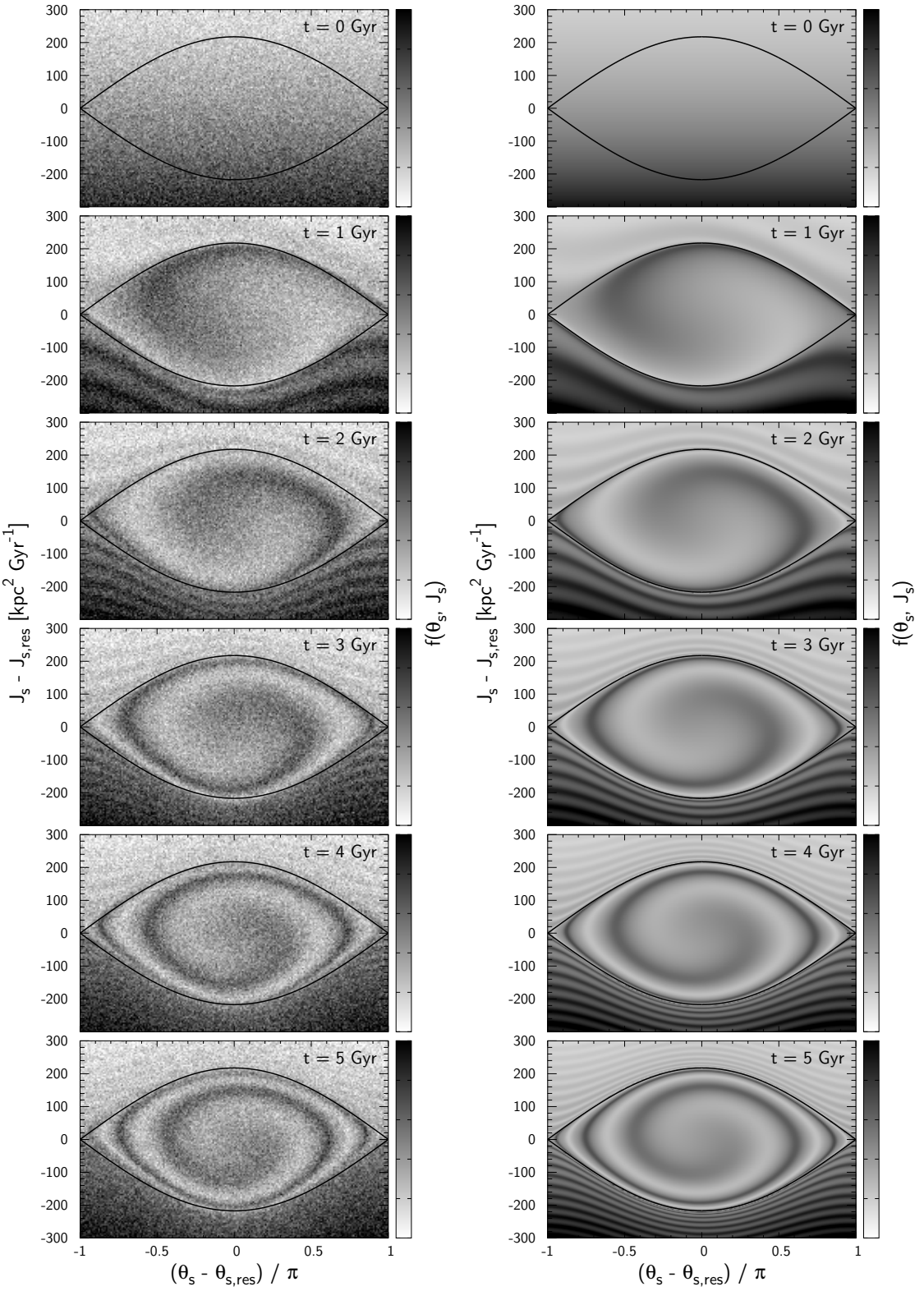

Fig. 4.5 Time evolution of the phase-space density $f(\theta_\mathrm{s}, J_\mathrm{s})$ near the corotation resonance $\boldsymbol{N} = (0, 2, 2)$ at $(J_{\mathrm{f}_1}, J_{\mathrm{f}_2}) = (10, 0)\,\mathrm{kpc}^2\,\mathrm{Gyr}^{-1}$ plotted every 1 Gyr. Left column: test particle simulation. Right column: analytical (equation 4.37). Black curves mark the separatrix.

test-particle simulation which is well reproduced by the analytical distribution shown on the right. Inside the separatrix (black curves), the density, initially uniform in the slow angle, phase mixes in the libration angle. Since the libration period increases towards the separatrix, the phase space differentially rotates, resulting in a phase-space spiral. Similarly, the phase space outside the separatrix winds into stripes since the circulation period is also maximal (infinite) at the separatrix and drops away from there.

The general mechanics of this phase spiral is rather similar to the vertical phase spiral found in *Gaia* (Antoja et al., 2018). In the case of the Gaia phase-spiral, a non-uniform distribution in the vertical angle is created, e.g., by the impact of a dwarf galaxy (Binney & Schönrich, 2018; Bland-Hawthorn & Tepper-García, 2021). In our case, the non-uniformity in the libration/circulation angles is inherited from the phase-space configuration prior to bar formation. We also remark that the phase mixing of trapped orbits and its resulting decay in dynamical friction is equivalent in mechanism to the non-linear Landau damping observed in plasma systems (O'Neil, 1965; Malmberg & Wharton, 1967).

The development of a phase-space spiral inside the resonance does not hinge on the instantaneous emergence of the bar. It also happens in a slowly growing bar, as shown in Fig. 4.6, which displays the same phenomenon for a bar that slowly grows over 4 Gyr following a polynomial prescription (Dehnen, 2000, equation 4). Here, we resort to test-particle simulations only because our current analytical treatment (4.37) assumes conservation of $J_{\ell/\mathrm{c}}$, which is violated at the separatrix when the bar grows, leading to resonant capture. Far outside the separatrix, the change is generally adiabatic since the circulation periods are small compared to the timescale on which the potential changes. There, the circulation action J_c is conserved and so the distribution in the circulation angle is kept uniform as it was at $t = 0$, thus showing no stripes. The evolution in the trapped region is, however, qualitatively different. The separatrix simultaneously engulfs the high-density region from below and the low-density region from above, thus rendering the distribution in the libration angle inevitably nonuniform (almost like a rectangular wave distribution). Due to this abrupt transition between maximum and minimum density, the phase-space spiral in a growing bar has a hard boundary compared to the non-growing case (Fig. 4.5) which shows a smoother transition between peaks and troughs.

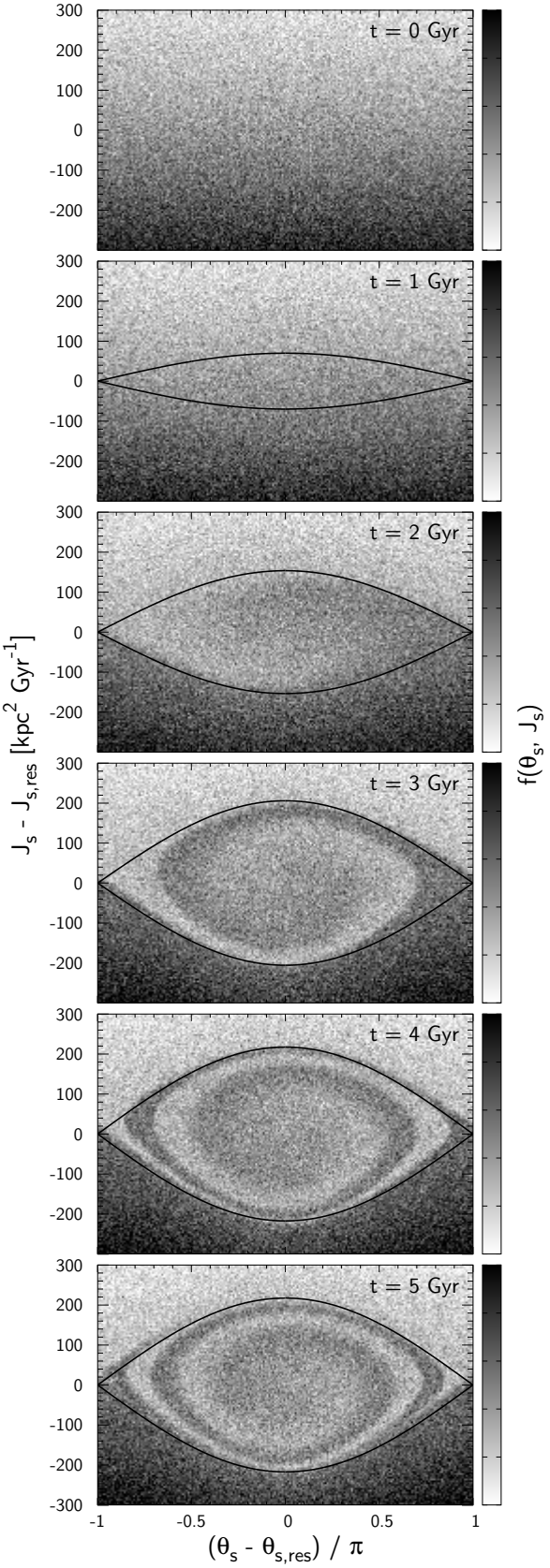

Fig. 4.6 Phase-space density of the halo perturbed by a bar growing slowly in 4 Gyr. The distribution outside the resonance is smooth due to the adiabatic emergence of the bar, while that inside the resonance displays a winding spiral since the expanding separatrix simultaneously captures orbits from above (low density) and below (high density).

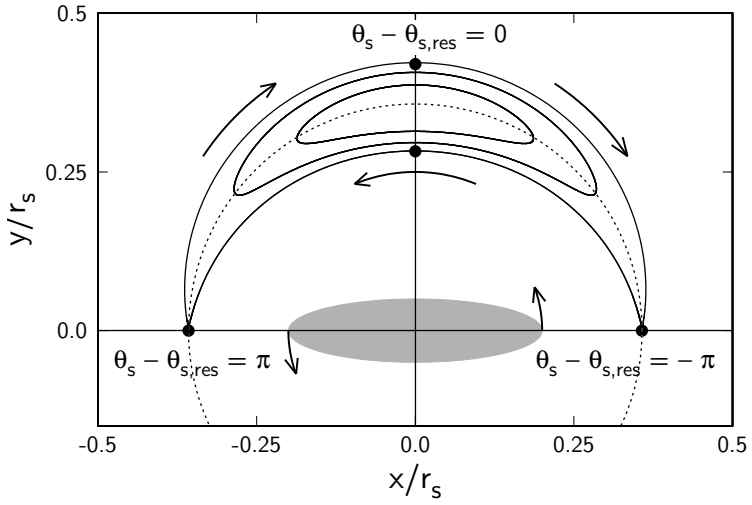

Fig. 4.7 Guiding orbits of particles in the galactic plane ($\beta = 0$) trapped in the CR of the bar (gray ellipse). Resonantly trapped orbits at $\theta_\mathrm{s} - \theta_\mathrm{s,res} > 0$ ($x < 0$) are pulled forward by the bar (gain angular momentum), while those at $\theta_\mathrm{s} - \theta_\mathrm{s,res} < 0$ ($x > 0$) are pulled back by the bar (lose angular momentum). The net torque on the bar is determined by the phase distribution of these trapped dark matter. As they slowly phase mix, the net torque attenuates.

It is instructive to relate the behaviour in the slow angle-action plane to the Chandrasekhar's classical picture of dynamical friction, i.e. as an over-density lagging behind the moving object (bar). At the CR, the slow angle (4.16) is $\theta_\mathrm{s} = 2[\theta_\psi - (\varphi_\mathrm{b} - \theta_\varphi)]$ where θ_ψ is the azimuthal angle of the guiding orbit in its orbital plane, and $\varphi_\mathrm{b} - \theta_\varphi$ is the azimuthal angle of the bar in the galactic plane measured from the ascending node. The centre of oscillation of the CR is at the bar's minor axis $\theta_\psi - (\varphi_\mathrm{b} - \theta_\varphi) = \pi/2$, so $\theta_\mathrm{s,res} = \pi$, and thus the range $\theta_\mathrm{s} - \theta_\mathrm{s,res} \in [-\pi, \pi]$ corresponds to $\theta_\psi - (\varphi_\mathrm{b} - \theta_\varphi) \in [0, \pi]$. Figure 4.7 shows typical in-plane ($\beta = 0$) orbits in the bar's corotating frame. For $\theta_\mathrm{s} - \theta_\mathrm{s,res} > 0$, the trapped orbits are lagging behind the bar, so they exert a negative torque on the bar, while for $\theta_\mathrm{s} - \theta_\mathrm{s,res} < 0$, they are ahead of the bar, exerting a positive torque on the bar. The net torque is then determined by the distribution in θ_s: In the beginning, the overdensity at small z-angular momentum (or J_s) librates towards $\theta_\mathrm{s} - \theta_\mathrm{s,res} > 0$ thus giving rise to a net negative torque on the bar. Subsequently, this overdensity librates back and forth between $\theta_\mathrm{s} - \theta_\mathrm{s,res} > 0$ and $\theta_\mathrm{s} - \theta_\mathrm{s,res} < 0$, providing a systematic oscillation of dynamical friction, which will fade with phase mixing. Eventually, the distribution in θ_s approaches

equilibrium and the net torque on a constantly rotating bar converges to zero as we saw in Fig. 4.1.

If the perturbation is transient (e.g. short-lived spiral arms), once it fades away, the halo will resume phase mixing in the slow angle θ_s, which recovered its role as an angle variable. However, since the libration angle θ_ℓ at which the orbits were captured and released are generally different, the final DF near resonances will be flatter than the original distribution. This 'scar' in the DF will affect the evolution of the renewed spiral arms (Sellwood & Carlberg, 2014; Sridhar, 2019), and can cause self-gravitational instabilities, exciting further spiral modes (Sellwood & Carlberg, 2019).

4.5.4 Onset of chaos by overlap of resonances

By averaging over the fast motions, we have approximated the Hamiltonian near a resonance with an integrable Hamiltonian $\bar{H}$ (4.21). We now ask whether the system remains integrable when the neglected terms of the full Hamiltonian $\delta H = H - \bar{H}$ are added back in. To consider the effect of δH, we Fourier expand it in the new angles

$$\delta H(\boldsymbol{\theta}'', \boldsymbol{J}'') = \sum_{\mathbf{m}} \hat{\Psi}_{\mathbf{m}}(\boldsymbol{J}'') \mathrm{e}^{i\mathbf{m}\cdot\boldsymbol{\theta}''}. \tag{4.38}$$

The Kolmogorov-Arnold-Moser (KAM) theorem (Arnol'd, 1963) implies that these terms will only slightly perturb the motion and the system will stay integrable so long as they are small and sufficiently far from satisfying a resonance condition $\mathbf{m}\cdot\boldsymbol{\Omega}'' = 0$ where $\boldsymbol{\Omega}'' = (\Omega_{\mathrm{f}_1}, \Omega_{\mathrm{f}_2}, \Omega_{\ell/\mathrm{c}})$. However, if δH contains a resonant term, it may render the system non-integrable. These *secondary resonances* form new resonant islands (either inside or outside the original separatrix) and can in principle be modelled in much the same way as we have dealt with the original resonance of the unperturbed system H_0 (e.g. Lichtenberg & Lieberman, 1992; Malhotra, 1998; Wisdom, 2004). However, when the separatrices of the secondary resonances come sufficiently close to the separatrix of the original resonances, orbits may behave stochastically, moving from one domain of resonance to another (Chirikov, 1979). A significant secondary resonance is expected when two resonances of the unperturbed Hamiltonian H_0 reside close to each other. The resonances in a bar-halo system indeed partially overlap, and some orbits there turn chaotic.

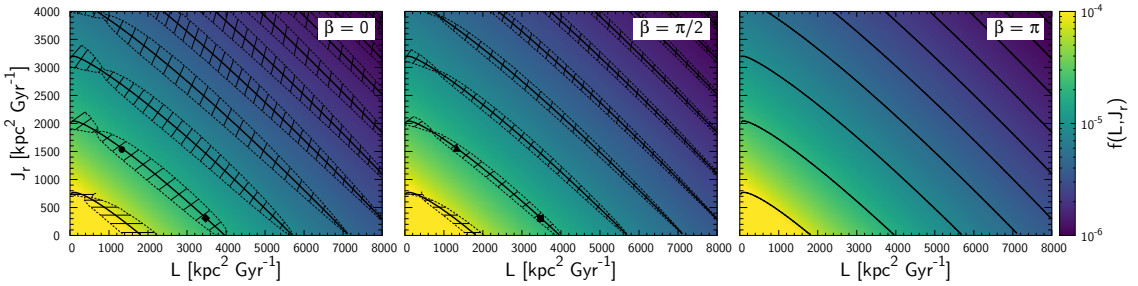

(a) Resonances with $N_\psi = 2, N_\varphi = 2$. N_r spans from 0 (left bottom) to 9 (top right).

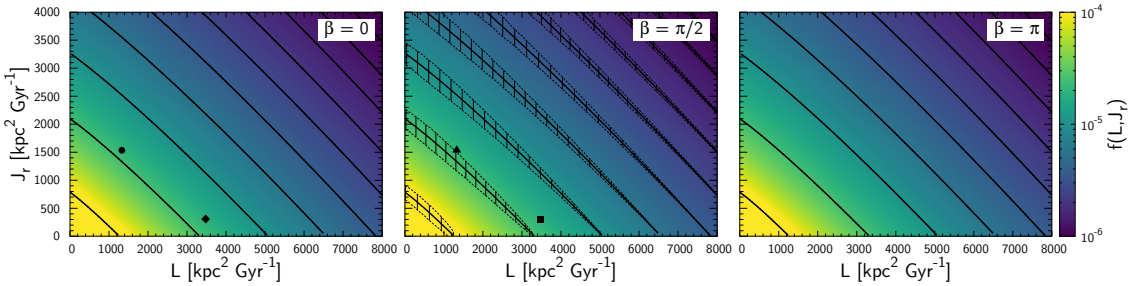

(b) Resonances with $N_\psi = 0, N_\varphi = 2$. N_r spans from 1 (left bottom) to 10 (top right).

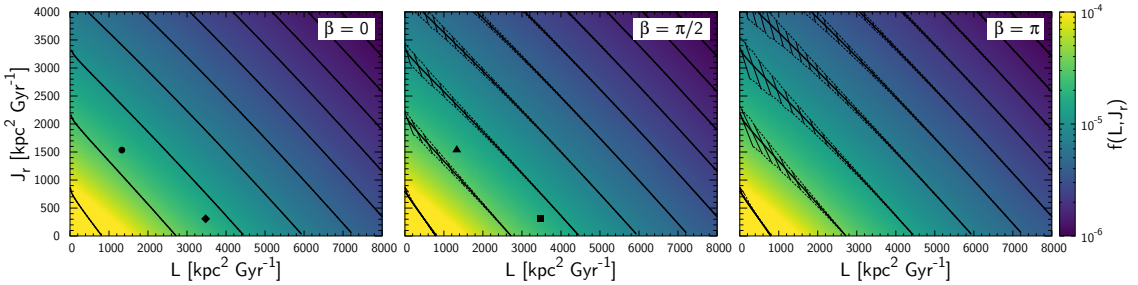

(c) Resonances with $N_\psi = -2, N_\varphi = 2$. N_r spans from 2 (left bottom) to 11 (top right).

Fig. 4.8 Bar-halo resonances $\boldsymbol{N} = (N_r, N_\psi, N_\varphi)$ at three different orbital planes $\beta = \cos^{-1}(L_z/L) = 0, \pi/2, \pi$ from left to right. The thick black curves mark the location of resonances, the dotted curves mark the maximum extent of the separatrix, and the thin black lines mark the direction of libration. The colours show the phase-space density in log scale. Top panel: Resonances with $N_\psi = 2$. Resonantly trapped volume is largest at $\beta = 0$ and vanishes at $\beta = \pi$. The black symbols, placed on the outer Lindblad resonance $\boldsymbol{N} = (1, 2, 2)$, mark the initial actions of orbits shown in Fig. 4.9. Middle panel: Resonances with $N_\psi = 0$. Trapped volume is largest at $\beta = \pi/2$ and decays towards $\beta = 0, \pi$. Bottom panel: Resonances with $N_\psi = -2$. Trapped volume increases towards $\beta = \pi$.

To illustrate the overlapping of resonances, we show in Fig. 4.8 the configuration of bar resonances with $N_\varphi = 2$ and $N_\psi = 2, 0, -2$ from top to bottom. In a spherical system, the resonant condition only depends on L and J_r. However, the volume of the trapped zone depends in addition on the orbital inclination $\beta \equiv \cos^{-1}(L_z/L)$. We thus show three plots from left to right with $\beta = 0$ (prograde), $\beta = \pi/2$ (perpendicular), and $\beta = \pi$ (retrograde). Following Binney (2018), we draw the furthest excursions of trapped orbits with dotted

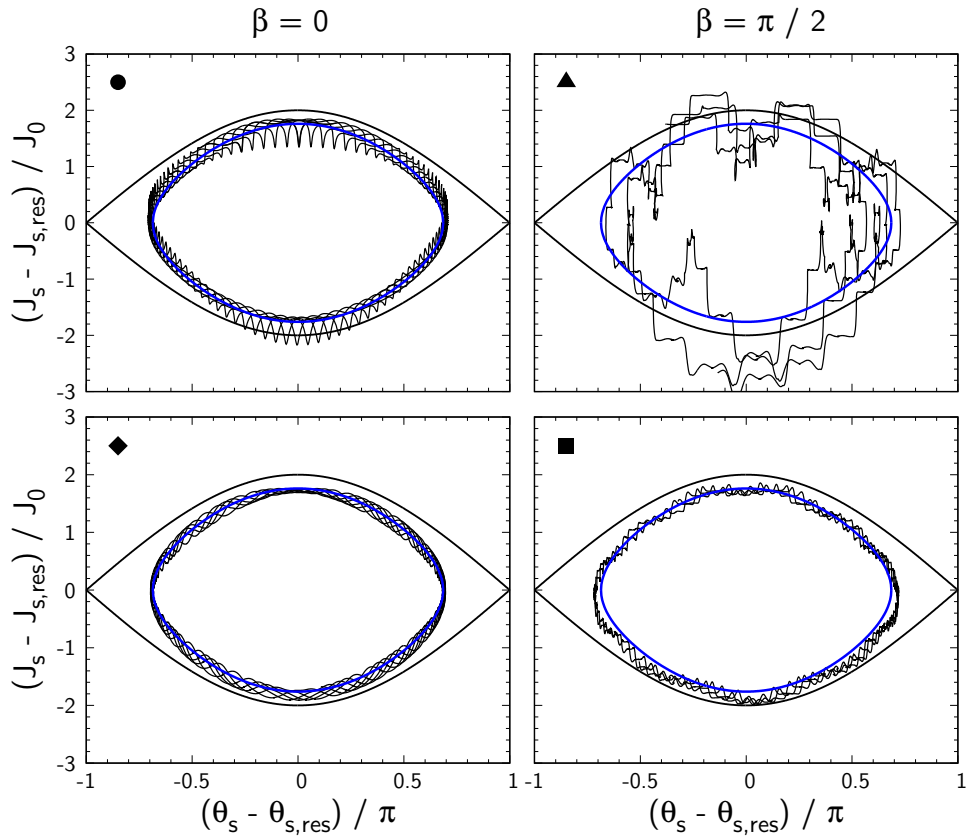

Fig. 4.9 Motion of orbits trapped at the OLR. The symbols on the left top corner represent the position of the initial actions marked in Fig. 4.8. The black orbits are integrated numerically using the full Hamiltonian and the blue orbits are obtained analytically from the averaged Hamiltonian. The orbit in the top-right panel exhibits chaotic oscillations as it is overlapped by the $\boldsymbol{N} = (2, 0, 2)$ resonance. All orbits have similar values of $\varepsilon \sim 0.9$.

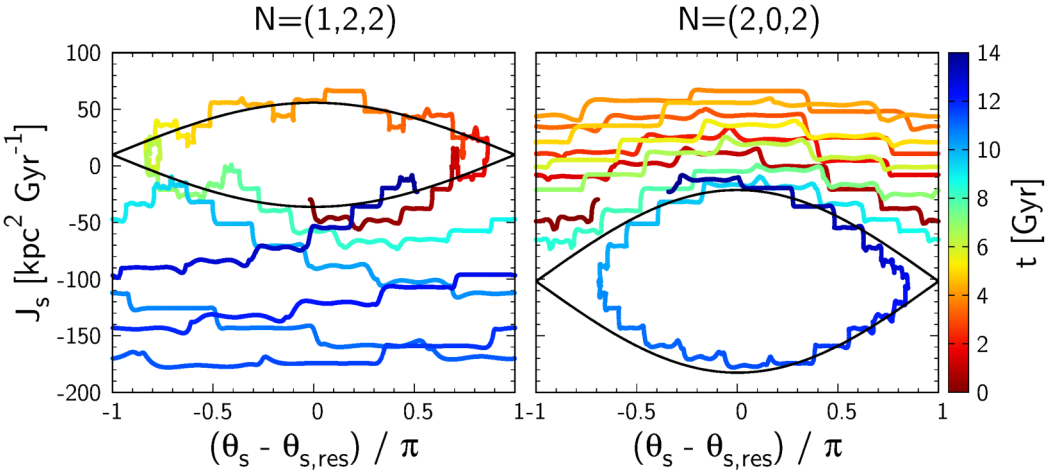

Fig. 4.10 Both panels show the same orbit in the angle-action plane of the $\boldsymbol{N} = (1, 2, 2)$ (OLR, left-hand) and the $\boldsymbol{N} = (2, 0, 2)$ resonance (right-hand). Colours encode the time. The orbit is initially on the OLR and then passes to the $\boldsymbol{N} = (2, 0, 2)$ resonance.

curves and mark the direction of libration with thin black lines. The colours show the phase-space density of the unperturbed distribution function (4.41).

The top panels of Fig. 4.8 show resonances with $N_\psi = 2$ which are familiar in disk dynamics: the resonance at the bottom-left corner is the corotation resonance (CR, $N_r = 0$) and the neighbouring one is the outer Lindblad resonance (OLR, $N_r = 1$). The trapped volume is largest at $\beta = 0$ (left, in-plane prograde), and decreases towards $\beta = \pi$ (right, in-plane retrograde) where it vanishes. The panels in the middle row present resonances with $N_\psi = 0$. Orbits trapped in these resonances complete N_φ radial oscillations in N_r bar periods regardless of their azimuthal phase with respect to the bar. Weinberg & Katz (2007) called these resonances the 'direct radial resonances' (DRRs). The strength/size of DRRs peaks at $\beta = \pi/2$. The lowest panels show resonances with $N_\psi = -2$ which are strongest at $\beta = \pi$.

Comparing the different sets of resonances, we can see from Fig. 4.8 that the resonances partly overlap, especially near $\beta \approx \pi/2$, where all resonances occupy a finite phase-space volume. To see the impact of resonance overlap, we plot in Fig. 4.9 four orbits trapped in the OLR $\boldsymbol{N} = (1, 2, 2)$ with different initial actions marked by black points in Fig. 4.8. As expected, the two orbits at $\beta = 0$ (circle and rhombus, left column in Fig. 4.9) are well modelled by the averaged Hamiltonian (blue), since only resonances with $N_\psi = 2$ have a non-zero volume. The right-hand column of Fig. 4.9 (triangle and square) shows two contrasting examples for $\beta = \pi/2$: the bottom right orbit (square) is mildly distorted as it is near, but still outside the second resonance, while the top right orbit (triangle) shows marked excursions as it is within the region of the $\boldsymbol{N} = (2, 0, 2)$ resonance. We note that we ascribe only the large-scale distortions to the presence of the second resonance, e.g. the irregular dip near $\theta_\mathrm{s} - \theta_\mathrm{res} \approx 0$. The step-like behaviour comes instead from the high eccentricity of the orbit, i.e. its J_s changes abruptly whenever the orbit rapidly passes near the bar at its pericentre.

When the domains of two resonances overlap, orbits may also pass from one resonance to another. Figure 4.10 shows an example of such an orbit moving between the OLR and the $(2, 0, 2)$ resonance. When viewed in the slow plane of the OLR (left panel), the orbit is initially trapped and then escapes the resonance after roughly one cycle of libration. In

contrast, from the viewpoint of the $(2, 0, 2)$ resonance (right panel), the orbit is at first outside the resonance but then becomes trapped soon after it leaves the OLR at around 9 Gyr.

The question here is how much does the overlap of resonances affect the calculation of the net torque based on the averaged Hamiltonian? The first thing to note is that the three sets of resonances with $N_\psi \in 2, 0, -2$ have their main territories at $\beta = 0, \pi/2, \pi$ respectively, so the majority of resonant phase-space is well isolated. Secondly, the chaotic orbits found at the overlapped regions still librate quasi-periodically around one of the two resonances over a finite time interval. Thirdly, these oscillations on top of the libration behave mostly stochastically without any apparent law, so they should not leave a systematic bias when averaged over the whole set of orbits. Hence, we do not expect a significant loss of accuracy in estimating the torque using the averaged Hamiltonian. We will demonstrate this below.

4.5.5 Total torque on the halo

After these preliminary considerations, we can now achieve our goal to estimate the torque between the bar and the dark halo. Using equation (4.28), (4.34), and (4.37), we obtain the total torque by summation over all resonances $\boldsymbol{N}$:

$$\begin{aligned}\left\langle \frac{\mathrm{d}L_z}{\mathrm{d}t} \right\rangle =& \sum_{\boldsymbol{N}} \int \mathrm{d}^3\boldsymbol{J}''\mathrm{d}^3\boldsymbol{\theta}''\ f(\boldsymbol{\theta}'', \boldsymbol{J}'', t)\frac{\mathrm{d}L_z}{\mathrm{d}t} \\ =& 8(2\pi)^2 \sum_{\boldsymbol{N}} N_\varphi \int \mathrm{d}^2\boldsymbol{J}_\mathrm{f}\Psi J_0 \\ & \times \left[\int_0^1 \mathrm{d}\varepsilon\varepsilon^2\hat{K} \int_0^{2\pi} \mathrm{d}\theta_\ell f(\theta_\ell - \Omega_\ell t, \boldsymbol{J}'', 0)\ \mathrm{sn}\left(\hat{K}\theta_\ell \middle| \varepsilon\right) \mathrm{dn}\left(\hat{K}\theta_\ell \middle| \varepsilon\right) \right. \\ & \left. \pm \int_1^{\varepsilon_\mathrm{cut}} \mathrm{d}\varepsilon\tilde{K} \int_0^{2\pi} \mathrm{d}\theta_\mathrm{c} f(\theta_\mathrm{c} - \Omega_\mathrm{c} t, \boldsymbol{J}'', 0)\ \mathrm{sn}\left(\tilde{K}\theta_\mathrm{c} \middle| \varepsilon^{-1}\right) \mathrm{cn}\left(\tilde{K}\theta_\mathrm{c} \middle| \varepsilon^{-1}\right) \right], \end{aligned} \tag{4.39}$$

where f is the distribution function (4.37) dependent on the libration/circulation angle $\theta_{\ell/\mathrm{c}}$ and the resonant actions $\boldsymbol{J}'' = (J_{\mathrm{f}_1}, J_{\mathrm{f}_2}, J_{\ell/\mathrm{c}})$, Ψ is the bar perturbation (4.53), J_0 measures the width of the resonance (4.23), and ε parametrizes the value of the Hamiltonian $\bar{H}$ (4.23). sn, cn and dn are the Jacobi's elliptic functions (4.61) and we have defined $\hat{K} \equiv 2K(\varepsilon)/\pi$ and $\tilde{K} \equiv K(\varepsilon^{-1})/\pi$ where K is the complete elliptic integral of the first kind (4.59). The first term in the square bracket describes the torque applied on the trapped phase-space, while the second term describes the torque on the untrapped phase-space which we cut at

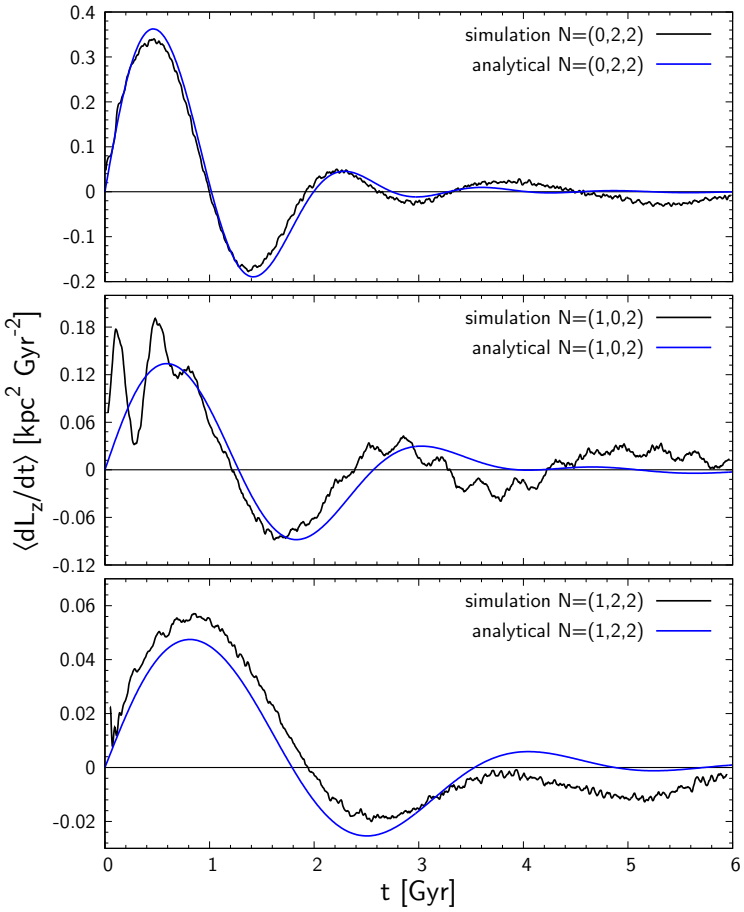

Fig. 4.11 Total torque on orbits trapped in each resonance divided by the total halo mass. From top to bottom, the three strongest resonances are shown (note the different y-axis scale in each figure). The analytical curves (blue) agree well with that of the simulation (black).

$\varepsilon_{\rm cut}(>1)$ to avoid duplicately integrating the phase space between neighbouring resonances. However duplication cannot be fully avoided where resonances overlap. As described above and demonstrated below, we expect the effects of overlap to be minor and defer detailed modelling for the overlap regions to future study. Here, we cut the integration universally at $\varepsilon_{\rm cut} = 2-3$ which is roughly the ratio of the width and interval between the neighbouring resonances (Fig. 4.8). The $\pm$ sign in (4.39) denotes integration over the upper and the lower circulating regions for which the mapping from $(\theta_{\rm c}, \boldsymbol{J}'')$ to $\boldsymbol{J} = (J_r, L, L_z)$ is different.

Figure 4.11 compares the total torque on trapped orbits calculated with the analytical approach to a test-particle simulation. From top to bottom, we show the torques on the three strongest resonances: $(N_r, N_\psi, N_\varphi) = (0,2,2)$, $(1,0,2)$, and $(1,2,2)$. We select the

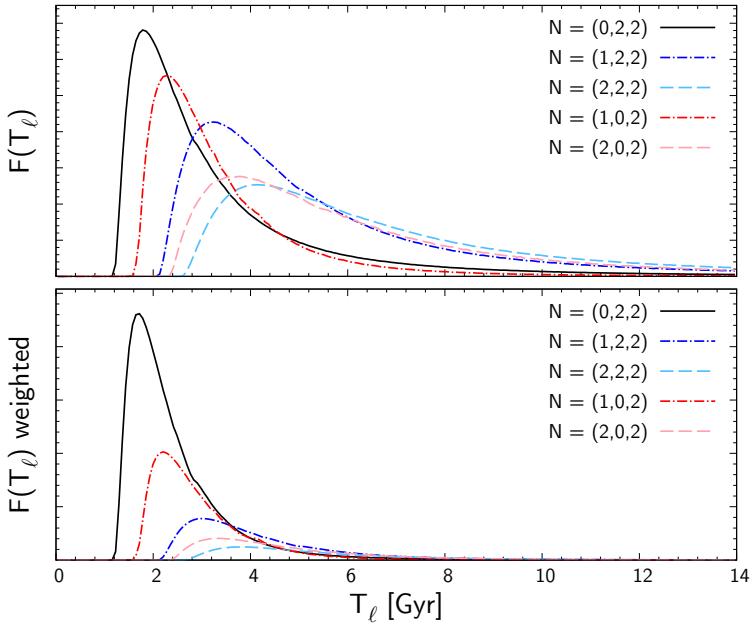

Fig. 4.12 Top panel: Distribution of trapped orbits in libration period. Bottom panel: Distribution weighted by the amplitude of the torque which provides the actual spectrum of the total torques shown in Fig. 4.11.

trapped orbits in the simulation by demanding that they never pass $\theta_s - \theta_{s,res} = \pm\pi$. We then place the particles back to their initial coordinates, re-run the simulation exclusively for these particles, and sum up their torque. For all three resonances, the analytical torque (blue) captures the principal features of the simulation (black), i.e. the torque fluctuates and damps as phase mixing progresses inside each resonance.

To better quantify the time dependence of the torque, we plot the spectra of libration periods calculated analytically in the top panel of Fig. 4.12. The distribution of each resonance peaks at a period which matches the main oscillating period of the total torque shown in Fig. 4.11. Since the majority of orbits with long libration periods are those trapped at small Ψ (rather than those near the separatrix) and thus have little impact on the total torque, we plot on the lower panel of Fig. 4.12 the distribution when weighted by the amplitude of the torque on each orbit. Note though that this is not a Fourier analysis of Fig. 4.11 since the torque on individual orbits becomes increasingly non-sinusoidal when approaching the separatrix (Fig. 4.4). The weighted distribution clarifies that the dominant contribution to the torque comes from the corotation resonance and in particular from those with libration periods $\sim 2\,\mathrm{Gyr}$.

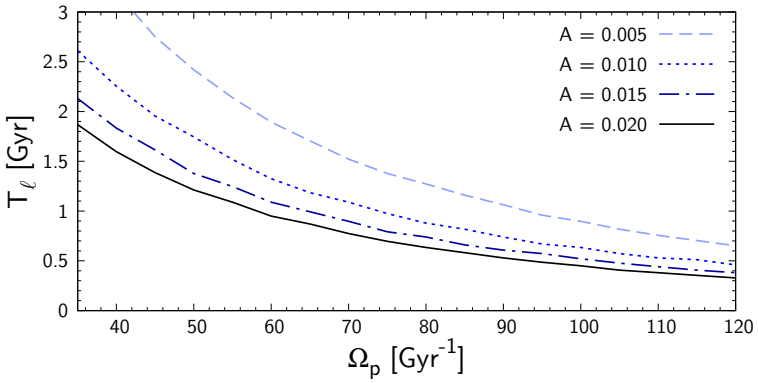

Fig. 4.13 The libration period of the CR at the peak of its distribution $F(T_\ell)$ vs. bar pattern speed Ω_p and bar strength A.

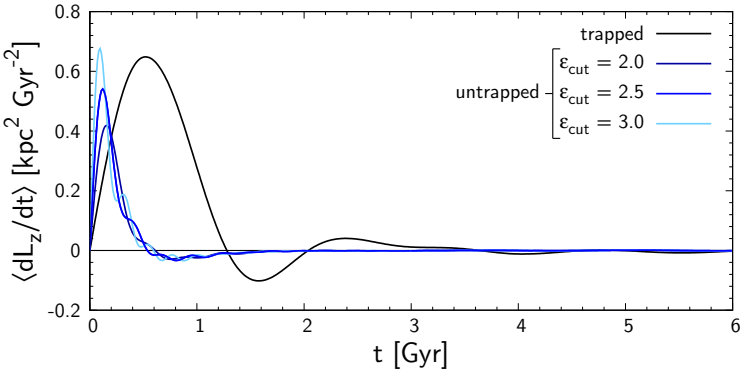

Fig. 4.14 Comparison between the total torque exerted on resonantly trapped (black) and untrapped (blue) orbits in the dark halo calculated analytically using equation (4.39). We cut the integration over the untrapped phase space at ε_cut to avoid duplication by neighbouring resonances. Dynamical friction by trapped and untrapped orbits rises and decays over different timescales.

The libration period depends on both the bar pattern speed and the bar strength which vary over time. A simple scaling suggests $T_\ell \sim \omega_0^{-1} = |G\Psi|^{-1/2} \sim \Omega_\mathrm{p}^{-1} A^{-1/2}$. Figure 4.13 shows the mode of the distribution of libration period for a given pattern speed Ω_p and bar strength A. As expected, the libration period is shorter for higher pattern speeds and for stronger bars. Since the bar directly after formation is expected to be faster but weaker than at present, the initial torque in an expected parameter range typical for the Milky Way should have fluctuated with roughly a Gyr period.

Figure 4.14 compares the contribution to the total torque from trapped and untrapped phase space with three cutoff $\varepsilon_\mathrm{cut} = \{2, 2.5, 3\}$. As before, we summed over the resonances with $N_r \in [-10, 10]$, $N_\psi \in -2, 0, 2$, and $N_\varphi = 2$. The torques on trapped and untrapped

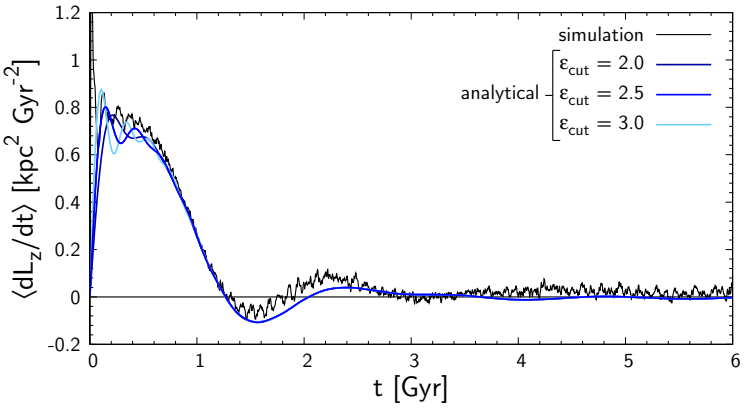

Fig. 4.15 Total torque on the dark halo. The analytical curves (blue, equation 4.39) quantitatively explain the behaviour of the simulation (black).

orbits rise and decay on different timescales which simply reflects the difference in their orbital periods, i.e. the period of circulation is generally shorter than that of libration. As we increase the upper limit of integration $\varepsilon_{\rm cut}$, the total torque on untrapped orbits gets larger and slightly shifts towards early time because contributions from orbits with short circulation periods far away from the resonances are added into the calculation.

Figure 4.15 shows the sum of trapped and untrapped components (blue) which quantitatively reproduces the total torque of the simulation (black). The result assures us that the trapped orbits comprise the majority of the torque at late times. In the very early times $< 0.1\,$Gyr, the torque of the simulation rises sharply as high as $1.6\,{\rm kpc}^2\,{\rm Gyr}^{-2}$ (see Fig. 4.1 for the full range) but our model fails to predict this rapid response for several reasons: (i) we have neglected the fast non-resonant terms of the perturbation by averaging over the fast angles, (ii) the second order Taylor approximation makes our model inaccurate in the region of rapid circulation far from the resonances, (iii) there is a substantial volume of untrapped phase-space that were not integrated due to the cutoff at $\varepsilon_{\rm cut}$.

4.5.6 Density wake in the halo

Figure 4.16 shows the spatial density response of the dark halo at the galactic mid-plane. The bar lies along the x-axis and rotates anticlockwise. The solid and dot-dashed circles represent the radii of CR and OLR respectively. The top row of Fig. 4.16 restricts orbits to those that are confined to the galactic mid-plane ($L = L_z$) and initially circular ($J_r = 0$).

Their behaviour in the x-y plane can be directly compared with the slow angle-action plane (Fig. 4.5) since, for near circular orbits at the CR, the slow angle-actions are simply $(\theta_s, J_s) \sim (2\varphi, Rv_c/2)$, i.e. a representation of the polar coordinates. Just after bar formation, a two-arm spiral rapidly emerges and winds up which, in Fig. 4.5, corresponds to the phase-space stripes outside the separatrix. Later, a crescent-shape region becomes apparent at the CR, which corresponds to the leaf-like resonant structure in the slow angle-action plane. Vaguely, we can see an overdensity librating and phase mixing inside the resonance. The bottom row of Fig. 4.16 shows the density of all orbits with $L = L_z$. By removing the restriction on J_r, a variety of eccentric orbits associated with different resonances (and having different libration/circulation periods) now visit the bar region, so we no longer see a sharp signal. However, by suppressing the particle noise by representing the density with basis functions (Hernquist & Ostriker, 1992) restricted to finite azimuthal degree ($l \leq 8$) and radial order ($n \leq 10$), we can clearly identify density wakes surrounding the bar. The behaviour of the wake is consistent with the total torque on the halo (Fig. 4.15): In the first few 100 Myrs (first three panels), a prominent density wake lags behind the bar, resulting in a large positive torque on the halo (negative torque on the bar). At around 1.5 Gyr, the wake moves to the bar front, hence receiving a net negative torque. Subsequently, the wake converges to a symmetric configuration around the bar, and the net torque diminishes.

4.6 Slowdown of the bar

The natural progression of this work will be a self-consistent slowdown model of the bar. However, the bar's moment of inertia is not a constant, the halo's self-gravity will amplify the torque, and the inflow of gas towards the nuclear disk provides an additional angular momentum term. Resolving these issues is beyond the scope of this thesis, and so must be deferred to future analysis. Instead, here we will discuss the effects of bar slowdown on the angular momentum balance using the bar's slowing rate directly measured from local stellar kinematics (Chiba et al., 2021) which agrees with N-body+SPH simulation of the bar in a live dark halo (Aumer & Schönrich, 2015).

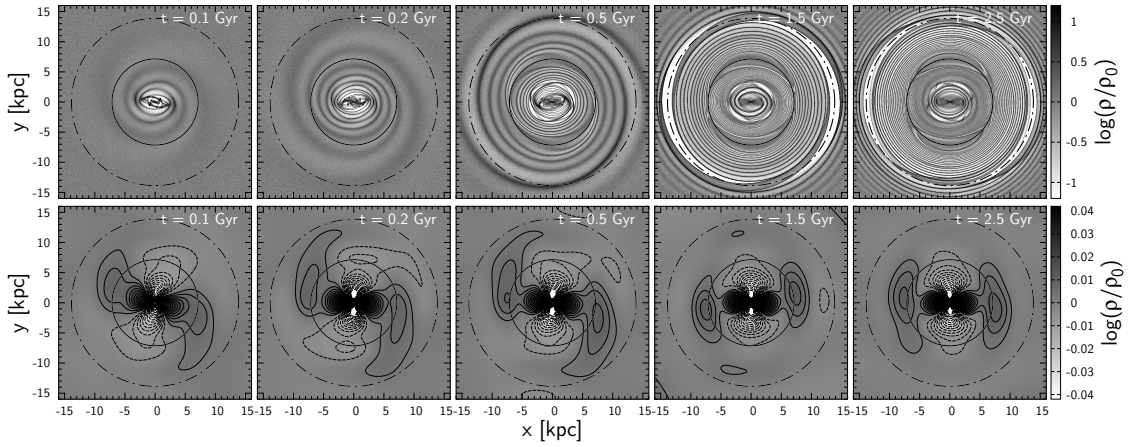

Fig. 4.16 Density wake in the dark matter halo at the galactic mid-plane ($L = L_z$) induced by a constantly rotating galactic bar (rotating anticlockwise). The bar lies horizontally along the x-axis, and we mark the radius of CR and OLR with solid and dot-dashed circles. Top row shows the density of initially circular orbits only ($J_r = 0$) and can thus be directly compared with the slow angle-action plane shown in Fig. 4.5. The bottom row shows the density of all orbits at the galactic mid-plane where we have extracted the dominant pattern by representing the density with basis functions (Hernquist & Ostriker, 1992) restricted to azimuthal degree $l \leq 8$ and radial order $n \leq 10$. A density wake lagging behind the bar is visible in the first few hundred Myrs in line with the large positive torque on the halo during that period (Fig. 4.15).

Figure 4.17 shows the phase space perturbed by a bar that slows with $\Omega_\mathrm{p} \propto 1/t$ from an initial value $\Omega_{\mathrm{p}0} = 81.8\,\mathrm{Gyr}^{-1}$ with rate $\eta \equiv -\dot{\Omega}_\mathrm{p}/\Omega_\mathrm{p}^2 = 0.004$[4]. The bar strength is fixed to $A = 0.02$. As the bar slows, the resonantly trapped orbits get dragged with the resonance towards larger J_s while they keep phase mixing internally. The dot-dashed curves show the separatrix evaluated in a 'time-frozen' Hamiltonian (when fixing the pattern speed) while the solid curves mark the approximate boundary of orbits that remain trapped in the moving resonance (Appendix 4.E). As described in Chiba et al. (2021), the deceleration tilts the potential of the resonance (4.68), making the effective trapped region shrink and shift towards positive θ_s. The latter effect could also be explained by the Euler force arising from the deceleration of the rotating frame of reference.

[4]A note on wording: This slowing rate implies $s \sim \eta/A = 0.2$ which is in the 'slow' regime ($s < 1$). However, Chiba et al. (2021) classified this model as a 'rapidly' decelerating bar in contrast to a yet slower model that evolves almost adiabatically.

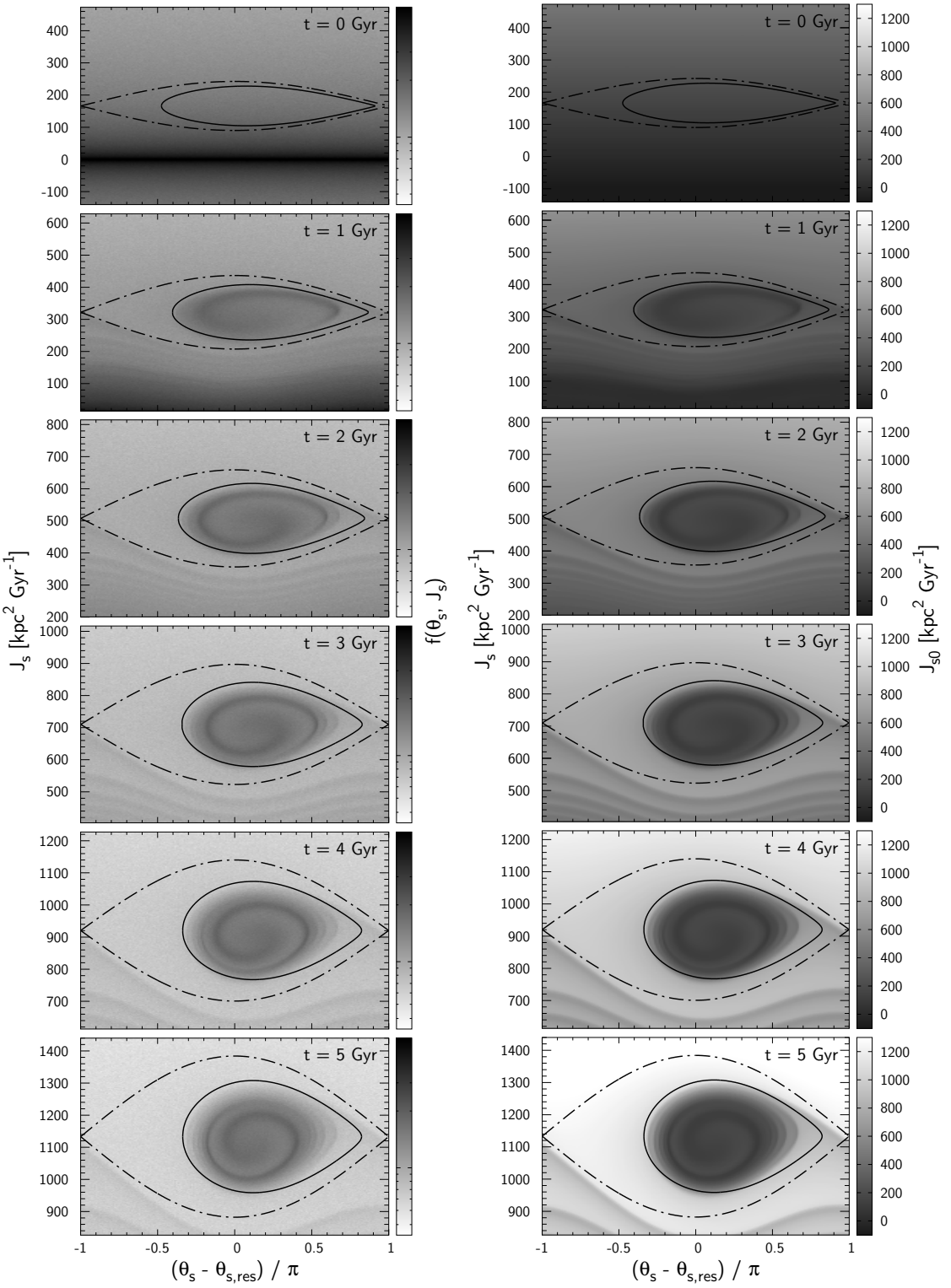

Fig. 4.17 Time evolution of the phase-space near the CR when the bar is slowing down. The left column shows the phase-space density in log scale, while the right column shows the initial J_s. The phase-space spiral continues to wind up as the resonance migrates upwards (note the increasing y axis from the top panel to the bottom). The bar slows down at rate $\eta = -\dot{\Omega}_\mathrm{p}/\Omega_\mathrm{p}^2 = 0.004$ starting from $\Omega_\mathrm{p} = 81.8\,\mathrm{Gyr}^{-1}$ and ends up being $\Omega_\mathrm{p} = 31.0\,\mathrm{Gyr}^{-1}$ after 5 Gyr.

4.6.1 Capture and escape from resonance

Resonance sweeping leaves a significant change in the distribution through capture and loss. When the resonance sweeps outwards, the untrapped orbits swept over by the upper separatrix (dot-dashed curves in Fig. 4.17) will temporarily get trapped, as adiabaticity is broken near the separatrix. Orbits that crossed the upper separatrix near $\theta_s - \theta_{res} = \pi$ may reach the adiabatic region (solid curves), where the libration action is conserved, and thus remain trapped and get dragged by the resonance. Other orbits will escape the resonance before completing one cycle of libration, proceeding to the lower circulating zone. Depending on the angle θ_s at which these uncaptured orbits enter the resonance, they will travel a different amount of distance in J_s: orbits crossing the separatrix near $\theta_s - \theta_{res} = -\pi$ will immediately escape the resonance, ending up at a relatively low J_s, while those that could almost but not quite reach the adiabatic region will be dragged a large distance in J_s before they get damped out of the resonance. Thus, after the passage of the resonance, orbits originally at the same action J_{s0} will spread over a wide range of J_s. These orbits then phase mix and form phase-space stripes in the lower circulating region.

As discussed in Chapter 3, the entire trapped volume (and the adiabatic region within) generally grows as the bar slows. Inside the adiabatic region, trapped orbits conserve their J_ℓ, so the newly captured orbits accrete on the surface of the adiabatic region. As a result, the resonance grows like a tree ring, where the J_s of origin increases from the core towards the surface.

Previous studies formalized the capturing and escaping processes in the adiabatic limit ($s \ll 1$) by the transition probability averaged over the libration/circulation angles (e.g. Henrard, 1982; Sridhar & Touma, 1996; Collett et al., 1997). However, to model the transient behaviour of dynamical friction, a phase dependent prescription for capture and loss is required. A straightforward way would be to numerically integrate the equations of motion for the averaged system with time-dependent parameters (Weinberg & Katz, 2007). Alternatively, one could return to the Eulerian approach (section 4.4) and fully address the non-linear terms of the CBE. This approach can in principle model the resonant structure with arbitrary time-dependence (e.g. bar growth), although it has the difficulty

that increasing numbers of higher-order modes will be required to model the fine structures developed by phase mixing.

4.6.2 Transfer of angular momentum by resonant dragging

In addition to the torque caused by phase mixing, the moving resonances give rise to another type of angular momentum transfer. The conservation of libration action ensures that the adiabatic region preserves the phase-space density at the time of capture. Since the resonances move towards higher angular momentum, this implies that the population on resonances is much denser than the surrounding phase space. When resonances move outward, the freed phase space below them will be filled with orbits jumping across the resonances, and just like lifting a heavy body in water, the halo gains net angular momentum which further slows the bar (i.e. positive feedback).

If we accelerate the bar instead, the resonances sweep inwards. As long as they are still denser than the surrounding phase space, the resonance frees angular momentum, further accelerating the bar (i.e. again, positive feedback). However, as the resonances proceed deep into the inner halo, the surrounding density rises and so the amount of freed angular momentum decreases up to even becoming negative when the resonances are underdense (i.e. negative feedback).

TW84 and Weinberg (1985) called these types of angular momentum exchange the 'dynamical feedback' and presented a formula to predict its amount, although they only figured in the torque due to orbits that jump across the resonance and separately discussed the effect of resonant dragging. They gave an insightful interpretation of dynamical feedback as a change in the moment of inertia of the bar: since dynamical feedback is to first order proportional to the change in pattern speed, ($\tau_{\rm feedback} = C\dot{\Omega}_{\rm p}$, where $C > 0$), the equation of motion for the bar becomes (Weinberg, 1985)

$$\dot{\Omega}_{\rm p} = \frac{\tau_{\rm friction} + \tau_{\rm feedback}}{I_{\rm b}} = \frac{\tau_{\rm friction}}{I_{\rm b} - C} \tag{4.40}$$

where the term $\tau_{\rm friction}$ represents dynamical friction and $I_{\rm b}$ is the bar's moment of inertia. This equation implies that dynamical feedback translates as a reduction in the moment of inertia. However we caution that (i) dynamical feedback is always delayed by an order

of the libration period, meaning that for a rapidly fluctuating torque caused by e.g. the bar-spiral interactions, the bar will react with its bared moment of inertia. (ii) C is not a constant and depends both on the pattern speed Ω_p as well as its derivative $\dot{\Omega}_\mathrm{p}$. In particular, C is a decreasing function of $\dot{\Omega}_\mathrm{p}$ (i.e. the faster the bar slows, the smaller the adiabatic/dragged region) which implies that dynamical feedback stabilizes the bar's slowing rate.

4.7 Summary

This work is a first attempt to push beyond the standard theory of dynamical friction between galactic bars (or in fact any galactic substructures) and dark matter haloes in the *slow regime*, i.e. for bars decelerating slowly enough to allow resonant trapping as observed in the Milky Way. In particular, we have:

- shown how the standard linear perturbation theory of dynamical friction breaks down in the slow regime due to the growth of non-linear responses near resonances,
- developed an improved analytical description for angular momentum transfer in the *slow limit* using the resonant angle-action coordinates and demonstrated numerically that the same mechanism applies generally to a growing or slowing bar,
- shown that dynamical friction oscillates with the libration period of the main resonances, which may drive a significant fluctuation in bar pattern speed at early times.

As first discussed in the seminal paper by TW84, the dynamic response to a perturbation qualitatively changes depending on the speed of resonance that sweeps the phase space. This is characterized by the parameter $s = |\mathrm{n}_\varphi \dot{\Omega}_\mathrm{p}/\omega_0^2|$ that measures the rate of change in pattern speed $\dot{\Omega}_\mathrm{p}$ with respect to the libration frequency ω_0; the regime is called *fast* when $s > 1$ and *slow* otherwise. While earlier simulations have reported bar evolution in the fast regime (e.g. Weinberg, 1985; Hernquist & Weinberg, 1992; Sellwood, 2006), recent observation of the Milky Way disk (Chiba et al., 2021) as well as N-body+hydrodynamic simulations of a realistically growing disk (Aumer & Schönrich, 2015) indicate that the

main bar resonances evolve in the slow regime, trapping a host of dark matter and disk stars in resonance. We note however that fast and slow regimes can coexist in different regions of phase space since ω_0 varies from resonance to resonance, and also within a single resonance (e.g. depending on the orbital inclination). Therefore, fast and slow regimes are both relevant in bar evolution and must be modelled accordingly to follow the secular evolution of the bar.

TW84 and W04 have shown that the bar evolutions in the fast limit ($s \gg 1$) can be well modelled by linear perturbation theory because the resonances will sweep past the orbits before any non-linearity can grow. In the slow limit ($s \to 0$), however, the linear assumption only holds for a fraction of the libration period (Fig. 4.1, Appendix 4.C). TW84 has provided a prescription for arbitrary s by Taylor approximation about the resonance although this approach cannot model the transient responses (phase mixing), which may last for several Gyrs.

We have developed a fully time-dependent theory of dynamical friction in the slow limit by modelling orbits near resonances with the resonant angle-action coordinates. In these new coordinates, the resonant motions become perfectly linear: trapped/untrapped orbits evolve linearly in their libration/circulation angles at constant rates.

The resonantly trapped orbits periodically exchange z-angular momentum with the bar as they slowly librate around the resonance. For instance, orbits trapped at the corotation resonance around the stable Lagrange points have increasing angular momentum while on the trailing side of the bar and are losing angular momentum while on the leading side. The net transfer of angular momentum to these trapped orbits is determined by their libration angle distribution: for a typical halo in equilibrium, the freshly trapped orbits are predominantly at lower angular momentum (libration angle near $\theta_\ell \sim \pi$). This phase imbalance initially leads to a net negative torque on the bar as this overdensity collectively librates up to higher angular momentum. However, after half a libration period, the overdensity starts librating back to lower angular momentum and can transfer angular momentum back to the galactic bar. Since libration periods increase towards the separatrix, this overdensity gradually winds up into a phase-space spiral inside the resonance and the net torque follows secular damped oscillations. The untrapped orbits circulating outside

the separatrix similarly exchange angular momentum with the bar as they phase mix, although they have a much shorter mixing time.

We have shown that due to the near-harmonic effective potential around the resonance centre, libration periods are quite similar across the trapped volume. This provides enough coherence to cause several oscillations in the torque. A straightforward prediction from this is that after bar formation, the pattern speed of the bar fluctuates with the typical libration frequencies of the main resonances. And indeed, while we are not aware of this having been noticed in previous literature, a closer inspection of previous N-body simulations shows these predicted bar pattern speed oscillations (e.g. Aumer & Schönrich, 2015, Fig.2). We note that these oscillations in bar pattern speed take place on an order of magnitude longer timescale ($> 1\,\mathrm{Gyr}$) than the short-term oscillations caused by alignments between bar and spiral patterns (Wu et al., 2016; Hilmi et al., 2020).

The resonant angle-action coordinates for each resonance are constructed by averaging the Hamiltonian over the fast angles. The averaged Hamiltonian is, however, not accurate when neighbouring resonances lie too close: overlap of resonances leads to the onset of chaos where orbits move from one resonance to another in a stochastic manner. In our current bar model, the limited regions of chaotic phase-space did not significantly affect the estimation of the total torque, although this may not be the case with a more realistic bar with additional higher order modes (e.g. octopole).

This thesis has shown qualitatively how dynamical friction may work in the slow regime. To obtain quantitative predictions, a self-consistent model is required. In particular, we must model (i) the growth of the bar, which changes its effective moment of inertia, (ii) the self-gravitational perturbation of the halo, which can amplify the torque on the bar by several factors (e.g. Weinberg, 1989; Chavanis, 2012; Dootson & Magorrian, 2022), and (iii) the angular momentum supply from the gas, which sheds angular momentum to the bar as it sinks into the inner bar-region (e.g. Regan & Teuben, 2004b; Berentzen et al., 2007; Athanassoula et al., 2013).

Finally, the phase-space spiral is also expected to form inside the resonances of the stellar disk. If we can identify this spiral pattern in the observational data, it will allow us to directly constrain the age of the Galactic bar.

Appendix

4.A Distribution function of Hernquist halo

The distribution function of an isotropic Hernquist halo normalized to 1 is (Hernquist, 1990)

$$f(E) = \frac{3\sin^{-1}\sqrt{\mathcal{E}} + \sqrt{\mathcal{E}(1-\mathcal{E})}(1-2\mathcal{E})(8\mathcal{E}^2 - 8\mathcal{E} - 3)}{8\sqrt{2}\pi^3 r_\mathrm{s}^3 v_g^3 (1-\mathcal{E})^{\frac{5}{2}}} \tag{4.41}$$

where $v_g = \sqrt{GM/r_\mathrm{s}}$, and $\mathcal{E} = -E/v_g^2$ is the dimensionless binding energy. We draw initial condition for the test particles by first sampling the energy from the differential energy distribution (Binney & Tremaine, 2008)

$$\mathcal{N}(E) = f(E)g(E) \tag{4.42}$$

where $g(E)$ is the density of states (i.e. phase-space volume per unit energy)

$$g(E) = \frac{2\sqrt{2}\pi^2 r_\mathrm{s}^3 v_g}{3\mathcal{E}^{\frac{5}{2}}}\left[3(8\mathcal{E}^2 - 4\mathcal{E} + 1)\cos^{-1}\sqrt{\mathcal{E}} - \sqrt{\mathcal{E}(1-\mathcal{E})}(4\mathcal{E}-1)(2\mathcal{E}+3)\right]. \tag{4.43}$$

We then choose the initial radius r at fixed E from the distribution

$$P(r) \propto \int \mathrm{d}^3\boldsymbol{x}\mathrm{d}^3\boldsymbol{v}\delta\left[\frac{1}{2}\boldsymbol{v}^2 + \Phi(\boldsymbol{x}) - E\right]\delta\left[|\boldsymbol{x}| - r\right] = (4\pi r)^2\sqrt{2\left[E - \Phi(r)\right]}. \tag{4.44}$$

With E and r, the initial speed $v = \sqrt{2\left[E - \Phi(r)\right]}$ is determined. Finally, we pick angles randomly over a sphere in position space (i.e. spherical) and in velocity space (i.e. isotropic). We confirmed that the density and anisotropy distribution of test particles constructed in this manner are unaltered after 10 Gyr of iteration without the bar.

4.B Fourier coefficients of bar potential

We follow the standard method of TW84, first expanding the bar's potential in spherical harmonics

$$\Phi_{\rm b}(r,\vartheta,\varphi,t) = \sum_{l=0}^{\infty}\sum_{m=-l}^{l} \Phi_{lm}(r) Y_{lm}\left(\vartheta, \varphi - \Omega_{\rm p} t\right). \tag{4.45}$$

For our bar model (4.2), only terms with $l = 2$ and $m = \pm 2$ are non-zero and their coefficients are

$$\Phi_{2,2}(r) = \Phi_{2,-2}(r) = \frac{\Phi_{\rm b}(r)}{2Y_{2,2}(\pi/2, 0)}, \tag{4.46}$$

where $\Phi_{\rm b}(r)$ is the radial profile of the bar potential (2.7). The Fourier coefficients $\hat{\Phi}_{\mathbf{n}}(\boldsymbol{J}, t)$ of the bar potential expanded in the angles $\boldsymbol{\theta} = (\theta_r, \theta_\psi, \theta_\varphi)$ can then be expressed as (TW84)

$$\begin{aligned}\hat{\Phi}_{\mathbf{n}}(\boldsymbol{J}, t) &= \int \frac{{\rm d}^3\boldsymbol{\theta}}{(2\pi)^3} \Phi_{\rm b}(r,\vartheta,\varphi,t) {\rm e}^{-i\mathbf{n}\cdot\boldsymbol{\theta}} \\ &= \sum_{l=0}^{\infty}\sum_{m=-l}^{l} i^{m-{\rm n}_\psi} \delta_m^{{\rm n}_\varphi} Y_l^{{\rm n}_\psi}\left(\frac{\pi}{2}, 0\right) d^l_{{\rm n}_\psi m}(\beta) W_{lm}^{{\rm n}_r {\rm n}_\psi}(\boldsymbol{J}) {\rm e}^{-im\Omega_{\rm p} t},\end{aligned} \tag{4.47}$$

where $d^l_{{\rm n}_\psi m}(\beta)$ is the Wigner's small d-matrix (e.g. Wigner, 1959)

$$d^l_{{\rm n}_\psi m}(\beta) = \sum_t (-1)^t \frac{\sqrt{(l+{\rm n}_\psi)!(l-{\rm n}_\psi)!(l+m)!(l-m)!}}{(l-m-t)!(l+{\rm n}_\psi-t)!t!(t+m-{\rm n}_\psi)!} \left(\cos\frac{\beta}{2}\right)^{2l+{\rm n}_\psi-m-2t} \left(\sin\frac{\beta}{2}\right)^{2t+m-{\rm n}_\psi}. \tag{4.48}$$

and

$$W_{lm}^{{\rm n}_r {\rm n}_\psi}(\boldsymbol{J}) \equiv \frac{1}{\pi}\int_0^\pi {\rm d}\theta_r \Phi_{lm}(r) \cos\left[{\rm n}_r\theta_r + {\rm n}_\psi(\theta_\psi - \psi)\right]. \tag{4.49}$$

Note that $\theta_\psi - \psi$ (the azimuthal deviation from the guiding centre) only depends on θ_r for a given $\boldsymbol{J}$, so the integral leaves no dependence on the angles. We may exert the $\delta_m^{{\rm n}_\varphi}$ in (4.47) and express the coefficients in the form of $\hat{\Phi}_{\mathbf{n}}(\boldsymbol{J}, t) = \hat{\Phi}_{\mathbf{n}}(\boldsymbol{J}) {\rm e}^{-i{\rm n}_\varphi\Omega_{\rm p} t}$ where

$$\hat{\Phi}_{\mathbf{n}}(\boldsymbol{J}) \equiv \sum_{l=0}^{\infty} i^{{\rm n}_\varphi - {\rm n}_\psi} Y_l^{{\rm n}_\psi}\left(\frac{\pi}{2}, 0\right) d^l_{{\rm n}_\psi {\rm n}_\varphi}(\beta) W_{l{\rm n}_\varphi}^{{\rm n}_r {\rm n}_\psi}(\boldsymbol{J}). \tag{4.50}$$

The Fourier coefficients of the bar potential expanded in the slow-fast angles $\boldsymbol{\theta}' = (\theta_{\mathrm{f}_1}, \theta_{\mathrm{f}_2}, \theta_{\mathrm{s}})$ at resonance $\boldsymbol{N}$ are

$$\begin{aligned}
\hat{\Psi}_{\boldsymbol{k}}(\boldsymbol{J}') &= \int \frac{\mathrm{d}^3\boldsymbol{\theta}'}{(2\pi)^3} \Phi_{\mathrm{b}}(r, \vartheta, \varphi, t) \mathrm{e}^{-i\boldsymbol{k}\cdot\boldsymbol{\theta}'} \\
&= \int \frac{\mathrm{d}^3\boldsymbol{\theta}'}{(2\pi)^3} \left[\sum_{\mathbf{n}} \hat{\Phi}_{\mathbf{n}}(\boldsymbol{J}) \mathrm{e}^{i(\mathbf{n}\cdot\boldsymbol{\theta} - \mathrm{n}_\varphi \Omega_{\mathrm{p}} t)} \right] \mathrm{e}^{-i\boldsymbol{k}\cdot\boldsymbol{\theta}'} \\
&= \sum_{\mathbf{n}} \hat{\Phi}_{\mathbf{n}}(\boldsymbol{J}) \int \frac{\mathrm{d}^3\boldsymbol{\theta}'}{(2\pi)^3} \mathrm{e}^{i\left[\left(\mathrm{n}_r - N_r \frac{\mathrm{n}_\varphi}{N_\varphi} - k_{\mathrm{f}_1}\right)\theta_{\mathrm{f}_1} + \left(\mathrm{n}_\psi - N_\psi \frac{\mathrm{n}_\varphi}{N_\varphi} - k_{\mathrm{f}_2}\right)\theta_{\mathrm{f}_2} + \left(\frac{\mathrm{n}_\varphi}{N_\varphi} - k_{\mathrm{s}}\right)\theta_{\mathrm{s}}\right]},
\end{aligned} \tag{4.51}$$

where the last line follows from the relation $(\theta_r, \theta_\psi, \theta_\varphi) = (\theta_{\mathrm{f}_1}, \theta_{\mathrm{f}_2}, (\theta_{\mathrm{s}} - N_r\theta_{\mathrm{f}_1} - N_\psi\theta_{\mathrm{f}_2})/N_\varphi + \Omega_{\mathrm{p}} t)$. Since n_φ is restricted to $m = \pm 2$, we have for resonances with $N_\varphi = 2$

$$\begin{aligned}
\hat{\Psi}_{\boldsymbol{k}}(\boldsymbol{J}') &= \sum_{\mathbf{n}} \hat{\Phi}_{\mathbf{n}}(\boldsymbol{J}) \int \frac{\mathrm{d}^3\boldsymbol{\theta}'}{(2\pi)^3} \mathrm{e}^{i\left[\left(\mathrm{n}_r \mp N_r - k_{\mathrm{f}_1}\right)\theta_{\mathrm{f}_1} + \left(\mathrm{n}_\psi \mp N_\psi - k_{\mathrm{f}_2}\right)\theta_{\mathrm{f}_2} + (\pm 1 - k_{\mathrm{s}})\theta_{\mathrm{s}}\right]} \\
&= \sum_{\mathbf{n}} \hat{\Phi}_{\mathbf{n}}(\boldsymbol{J}) \delta_{\mathrm{n}_r, k_{\mathrm{f}_1} \pm N_r} \delta_{\mathrm{n}_\psi, k_{\mathrm{f}_2} \pm N_\psi} \delta_{k_{\mathrm{s}}, \pm 1} \\
&= \hat{\Phi}_{(k_{\mathrm{f}_1} \pm N_r, k_{\mathrm{f}_2} \pm N_\psi, \pm N_\varphi)}(\boldsymbol{J}) \delta_{k_{\mathrm{s}}, \pm 1}.
\end{aligned} \tag{4.52}$$

Therefore, the resonant term $\Psi(\boldsymbol{J}') \equiv 2\left|\hat{\Psi}_{(0,0,1)}(\boldsymbol{J}')\right|$ in the averaged Hamiltonian (4.20) is

$$\Psi(\boldsymbol{J}') = 2\left| \sum_{l=0}^{\infty} i^{N_\varphi - N_\psi} Y_l^{N_\psi}\left(\frac{\pi}{2}, 0\right) d^l_{N_\psi N_\varphi}(\beta) W^{N_r N_\psi}_{l N_\varphi}(\boldsymbol{J}) \right|. \tag{4.53}$$

4.C Linear response

As discussed in TW84, the linear response remains valid so long as the bar's pattern speed changes sufficiently rapidly (the fast limit, $s \gg 1$). In the slow regime ($s < 1$), however, the error of linear approximation increases due to the growth of non-linearity near resonances. In section 4.4, we have demonstrated this in the slow limit ($s \to 0$), showing that linear theory fails to predict the torque beyond few hundred Myrs. Here we take a closer look at this issue by directly observing the distribution function in the slow angle-action plane. The Fourier coefficients of the linear response (4.11) to a constantly rotating perturbation

is

$$\begin{aligned}\hat{f}_{\mathbf{n}}(\boldsymbol{J},t) &= i\mathbf{n}\cdot\frac{\partial f_0}{\partial \boldsymbol{J}}\int_0^t \mathrm{d}t' \mathrm{e}^{-i\mathbf{n}\cdot\boldsymbol{\Omega}(t-t')}\left[\hat{\Phi}_{\mathbf{n}}(\boldsymbol{J})\mathrm{e}^{-\mathrm{n}_\varphi\Omega_\mathrm{p}t'}\right]\\ &= i\mathbf{n}\cdot\frac{\partial f_0}{\partial \boldsymbol{J}}\hat{\Phi}_{\mathbf{n}}(\boldsymbol{J})\mathrm{e}^{-i\mathbf{n}\cdot\boldsymbol{\Omega}t}\left[\int_0^t \mathrm{d}t' \mathrm{e}^{i\left(\mathbf{n}\cdot\boldsymbol{\Omega}-\mathrm{n}_\varphi\Omega_\mathrm{p}\right)t'}\right]\\ &= \mathbf{n}\cdot\frac{\partial f_0}{\partial \boldsymbol{J}}\hat{\Phi}_{\mathbf{n}}(\boldsymbol{J})\frac{\mathrm{e}^{-i\mathrm{n}_\varphi\Omega_\mathrm{p}t}-\mathrm{e}^{-i\mathbf{n}\cdot\boldsymbol{\Omega}t}}{\mathbf{n}\cdot\boldsymbol{\Omega}-\mathrm{n}_\varphi\Omega_\mathrm{p}}.\end{aligned} \tag{4.54}$$

The total linear response is then

$$f_1(\boldsymbol{\theta},\boldsymbol{J},t) = \sum_{\mathbf{n}}\hat{f}_{\mathbf{n}}(\boldsymbol{J},t)\mathrm{e}^{i\mathbf{n}\cdot\boldsymbol{\theta}} = \sum_{\mathbf{n}}\mathbf{n}\cdot\frac{\partial f_0}{\partial \boldsymbol{J}}\hat{\Phi}_{\mathbf{n}}(\boldsymbol{J})\frac{\mathrm{e}^{i\left(\mathbf{n}\cdot\boldsymbol{\theta}-\mathrm{n}_\varphi\Omega_\mathrm{p}t\right)}-\mathrm{e}^{i(\mathbf{n}\cdot\boldsymbol{\theta}-\mathbf{n}\cdot\boldsymbol{\Omega}t)}}{\mathbf{n}\cdot\boldsymbol{\Omega}-\mathrm{n}_\varphi\Omega_\mathrm{p}}. \tag{4.55}$$

Note that this equation contains the resonant frequency at the denominator but it does not diverge at the resonance because the numerator also vanishes there. From the condition that the perturbed potential is real $\hat{\Phi}_{-\mathbf{n}}(\boldsymbol{J},t) = \hat{\Phi}^*_{\mathbf{n}}(\boldsymbol{J},t)$, one can express f_1 as

$$\begin{aligned}f_1(\boldsymbol{\theta},\boldsymbol{J},t) &= \sum_{\mathbf{n}}\mathbf{n}\cdot\frac{\partial f_0}{\partial \boldsymbol{J}}\left|\hat{\Phi}_{\mathbf{n}}(\boldsymbol{J})\right|\frac{\cos\left(\theta_\mathrm{s}-\theta_{\mathrm{s,res}}\right)-\cos\left(\theta_\mathrm{s}-\theta_{\mathrm{s,res}}-\Omega_s t\right)}{\Omega_s}\\ &= -\sum_{\mathbf{n}}\mathbf{n}\cdot\frac{\partial f_0}{\partial \boldsymbol{J}}\left|\hat{\Phi}_{\mathbf{n}}(\boldsymbol{J})\right|\sin\left(\theta_\mathrm{s}-\theta_{\mathrm{s,res}}-\Omega_s t/2\right)\frac{\sin\left(\Omega_s t/2\right)}{\Omega_s/2},\end{aligned} \tag{4.56}$$

where $\theta_\mathrm{s} = \mathbf{n}\cdot\boldsymbol{\theta} - \mathrm{n}_\varphi\Omega_\mathrm{p}t$ and $\Omega_s = \mathbf{n}\cdot\boldsymbol{\Omega} - \mathrm{n}_\varphi\Omega_\mathrm{p}$. A similar equation is presented in Weinberg & Katz (2007). At the resonance $\Omega_s \to 0$, the term $\sin\left(\Omega_s t/2\right)/(\Omega_s/2)$ becomes t, implying linear growth of perturbation f_1 in time. For linear theory to hold, f_1 must remain sufficiently smaller than the variation of the background distribution Δf_0 across the resonance $\Delta J_\mathrm{s} \sim J_0 = \sqrt{-\Psi/G}$ (4.23). This requires

$$1 \gg \frac{f_1}{\Delta f_0} \sim \frac{\Psi}{\Delta J_\mathrm{s}}t \sim \sqrt{-\Psi G}t = \omega_0 t. \tag{4.57}$$

Hence the timescale at which linear theory is valid in the slow limit is set by the libration period $\omega_0^{-1} \gg t$.

Figure 4.18 compares the simulated phase flow near the corotation resonance (left) with linear theory (middle) and the resonant angle-action theory (right) described in section 4.5. Here, the libration period at the core of the resonance is $T_\ell = 2\pi/\omega_0 \sim 1.2\,\mathrm{Gyr}$. For the top five plots, the time since bar formation increases in steps of 0.25 Gyr, while the bottom plot shows the result after 10 Gyr. The linear response oscillates sinusoidally in θ_s with phase velocities that vanish towards the resonance, as described by the term $\sin\left(\theta_\mathrm{s}-\theta_{\mathrm{s,res}}-\Omega_s t/2\right)$ in (4.56). For the first few hundred Myrs (top two rows), this

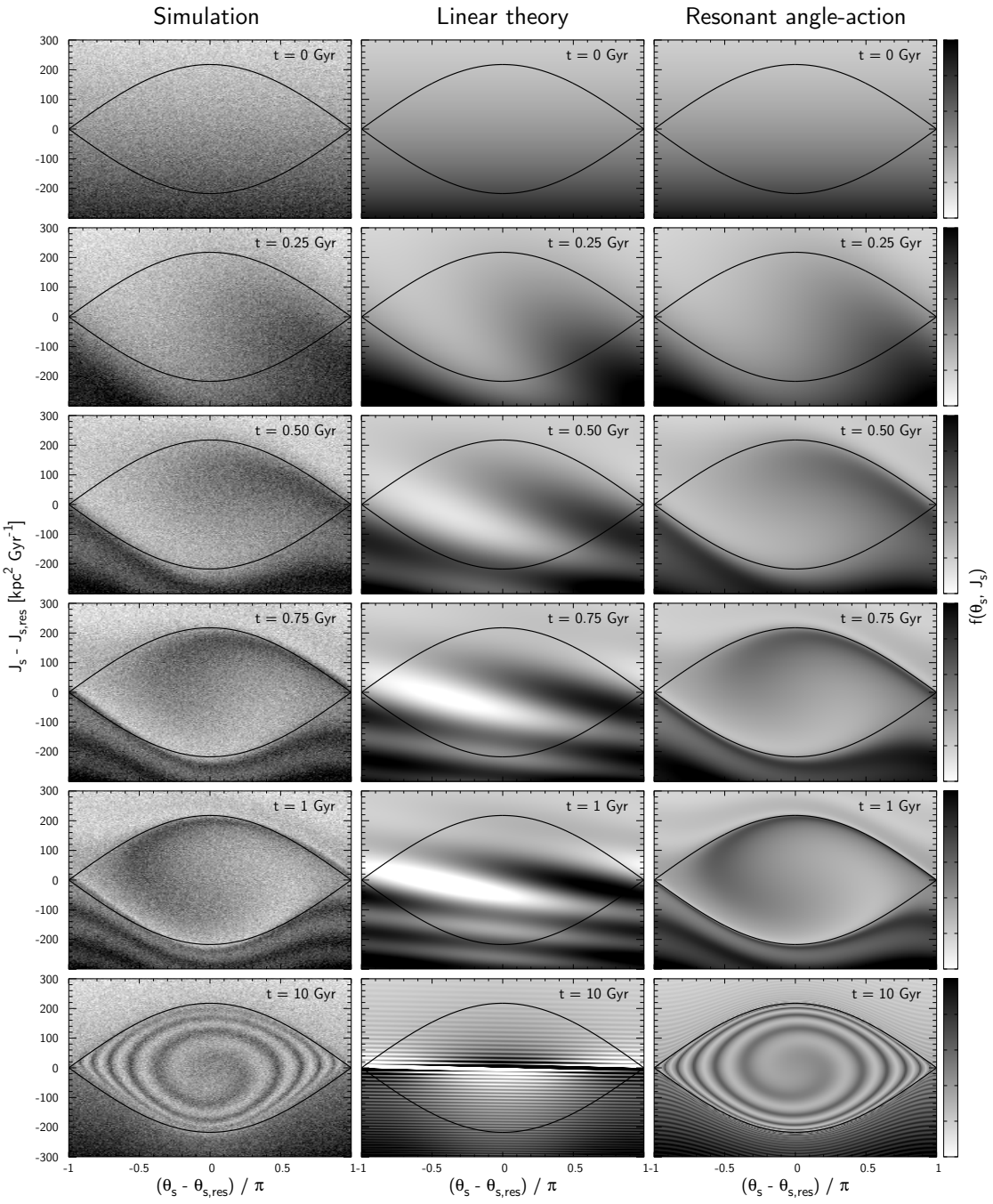

Fig. 4.18 Time evolution of the phase space density near the corotation resonance at $(J_{f_1}, J_{f_2}) = (10, 0)\,\mathrm{kpc}^2\,\mathrm{Gyr}^{-1}$. Comparison between simulation (left), linear perturbation theory (middle) and resonant angle-action theory (right). Linear theory properly predicts the phase flow for the first few hundred Myrs but fails to predict the subsequent behaviour.

shearing motion results in a change in distribution similar to that caused by the motion of libration and circulation. However, errors in linear theory become prominent beyond $t \gtrsim 0.2T_\ell$.

Despite the growing error in linear theory, past works (e.g. TW84; LBK72) have commonly assumed that the perturbation was switched on in the distant past which is equivalent to taking $t \to \infty$. As noted in Weinberg & Katz (2007), in this time-asymptotic limit, the function $\sin(\Omega_s t/2)/(\Omega_s/2)$ in (4.56) approaches a delta function $\pi\delta(\Omega_s/2)$[5], i.e. the wavelength of the linear response in frequency (or action) space gets narrower and narrower with time, and eventually an integration over phase space will only leave contribution from the perfectly resonant orbits. This is the prediction of the LBK formula (4.14). This time-asymptotic limit not only ignores transient phenomena relevant in real galaxies, but also leads to qualitatively wrong conclusions: in the limit $t \to \infty$, LBK predicts that contribution from non-resonant orbits vanish by phase mixing and only the perfectly resonant orbits give rise to a *non-zero* torque, whereas in truth, the resonant orbits would also phase mix within the trapped zone resulting in a *zero* torque as shown in Fig. 4.1.

4.D Elliptic integrals

The complete elliptic integral of the first K and second E kinds are

$$K(k) = \int_0^{\frac{\pi}{2}} \frac{\mathrm{d}\theta}{\sqrt{1-k^2\sin^2\theta}}, \quad E(k) = \int_0^{\frac{\pi}{2}} \mathrm{d}\theta\sqrt{1-k^2\sin^2\theta}. \tag{4.59}$$

The incomplete elliptic integral of the first kind $F(\phi|k)$ is

$$u = F(\phi|k) \equiv \int_0^{\phi} \frac{\mathrm{d}\theta}{\sqrt{1-k^2\sin^2\theta}}. \tag{4.60}$$

and the Jacobi elliptic functions are defined via the inverse of $F(\phi|k)$:

$$\phi = F^{-1}(u|k), \quad \mathrm{sn}(u|k) \equiv \sin\phi, \quad \mathrm{cn}(u|k) \equiv \cos\phi, \quad \mathrm{dn}(u|k) \equiv \sqrt{1-k^2\sin^2\phi}. \tag{4.61}$$

[5] In the sense that,

$$\lim_{t\to\infty} \int \mathrm{d}^3\boldsymbol{J}\, g(\boldsymbol{J}) \frac{\sin(\Omega_s t/2)}{\Omega_s/2} = g(\boldsymbol{J})\pi\delta(\Omega_s/2) \tag{4.58}$$

The derivatives of the Jacobi elliptic functions are

$$\frac{\mathrm{d}}{\mathrm{d}u}\mathrm{sn}(u|k) = \mathrm{cn}(u|k)\mathrm{dn}(u|k), \quad \frac{\mathrm{d}}{\mathrm{d}u}\mathrm{cn}(u|k) = -\mathrm{sn}(u|k)\mathrm{dn}(u|k),$$
$$\frac{\mathrm{d}}{\mathrm{d}u}\mathrm{dn}(u|k) = -k^2\mathrm{sn}(u|k)\mathrm{cn}(u|k). \tag{4.62}$$

4.E Orbit subject to a slowing bar

We model an orbit trapped and dragged by a slowing bar using the Hamiltonian (4.20) with a time-dependent pattern speed $\Omega_\mathrm{p}(t)$,

$$\bar{H}(\theta_\mathrm{s}, \boldsymbol{J}', t) = H_0(\boldsymbol{J}') - N_\varphi \Omega_\mathrm{p}(t) J_\mathrm{s} + \Psi(\boldsymbol{J}') \cos\left(\theta_\mathrm{s} - \theta_\mathrm{s,res}\right). \tag{4.63}$$

As before, we Taylor expand around $J_\mathrm{s} = J_\mathrm{s,res}$ which satisfies the resonance condition at $t = t_\mathrm{res}$:

$$\bar{H}(\theta_\mathrm{s}, \boldsymbol{J}', t) \simeq \left[H_0(\boldsymbol{J}') - N_\varphi \Omega_\mathrm{p}(t) J_\mathrm{s}\right]_{J_\mathrm{s,res}} + \left[\frac{\partial H_0}{\partial J_\mathrm{s}} - N_\varphi \Omega_\mathrm{p}(t)\right]_{J_\mathrm{s,res}} \Delta$$
$$+ \frac{1}{2} G(\boldsymbol{J}_\mathrm{f}, J_\mathrm{s,res})\Delta^2 + \Psi(\boldsymbol{J}_\mathrm{f}, J_\mathrm{s,res}) \cos\theta, \tag{4.64}$$

where we wrote $\Delta \equiv J_\mathrm{s} - J_\mathrm{s,res}$, $\theta \equiv \theta_\mathrm{s} - \theta_\mathrm{s,res}$ and $G \equiv \frac{\partial^2 H_0}{\partial J_\mathrm{s}^2}$ for convenience. Removing the first bracket term, which does not affect the slow dynamics, and substituting $\frac{\partial H_0}{\partial J_\mathrm{s}}\big|_{J_\mathrm{s,res}} = \boldsymbol{N} \cdot \boldsymbol{\Omega}(\boldsymbol{J}_\mathrm{f}, J_\mathrm{s,res}) = N_\varphi \Omega_\mathrm{p}(t_\mathrm{res})$ in the second bracket term yields (Weinberg, 1994)

$$\bar{H}(\theta_\mathrm{s}, J_\mathrm{s}, t) = -N_\varphi \left[\Omega_\mathrm{p}(t) - \Omega_\mathrm{p}(t_\mathrm{res})\right] \Delta + \frac{1}{2} G\Delta^2 + \Psi \cos\theta. \tag{4.65}$$

From the Hamilton's equations of motion:

$$\dot{\theta} = -N_\varphi \left[\Omega_\mathrm{p}(t) - \Omega_\mathrm{p}(t_\mathrm{res})\right] + G\Delta \quad \text{and} \quad \dot{\Delta} = \Psi \sin\theta, \tag{4.66}$$

we obtain

$$\ddot{\theta} + \omega_0^2 (\sin\theta - s) = 0, \tag{4.67}$$

where $\omega_0^2 \equiv -G\Psi$, and $s = -N_\varphi \dot{\Omega}_\mathrm{p}/\omega_0^2$ is the speed parameter. If we assume that $\dot{\Omega}_\mathrm{p}$ vary little during the typical libration period $2\pi/\omega_0$, s can be assumed constant and we obtain the following energy integral:

$$E_\mathrm{p} = \frac{1}{2}\dot{\theta}^2 + V(\theta) \quad \text{where} \quad V(\theta) = \omega_0^2 (-\cos\theta - s\theta). \tag{4.68}$$

Trapped orbits are confined in the potential well of $V(\theta)$ which is linearly tilted due to the second term (see Fig.4 of Chiba et al., 2021). The crest of the potential is at $\theta_{\rm sep} = \sin^{-1}(s)$ $(\pi/2 \leq \theta_{\rm sep} \leq \pi)$ and the minimum energy $E_{\rm p}$ required to reach the crest is

$$E_{\rm p,sep} = \omega_0^2 \left(-\cos\theta_{\rm sep} - s\theta_{\rm sep}\right). \tag{4.69}$$

Orbit with $E_{\rm p} = E_{\rm p,sep}$ approximately marks the boundary of phase space that remains trapped in resonance. Hence, by a slight abuse of language, we will refer to the orbit $E_{\rm p} = E_{\rm p,sep}$ as the 'separatrix'. Inserting (4.69) and (4.66) to (4.68) yields an equation for the separatrix:

$$\Delta_{\pm} = \frac{N_\varphi \left[\Omega_{\rm p}(t) - \Omega_{\rm p}(t_{\rm res})\right]}{G} \pm \frac{\omega_0}{G}\sqrt{2\left[\cos\theta - \cos\theta_{\rm sep} + s\left(\theta - \theta_{\rm sep}\right)\right]}. \tag{4.70}$$

The first term describes the drift of the resonance and the second term describes the shape of the separatrix. Since the first term is time dependent, the separatrix is not closed in phase space. However, in the slow limit $s \ll 1$ the distance the resonance travels in a typical libration period is smaller than the size of the resonance, so we may mark the approximate area of trapped phase space by neglecting the first term. This is drawn in Fig. 4.17. In comparison to the separatrix of the time-frozen Hamiltonian (dot-dashed black), the separatrix of the time-dependent Hamiltonian (solid black) is contracted and shifted towards θ, describing the trapped boundary of the simulation remarkably well. The first term in fact breaks/opens the separatrix and thus allows orbits to enter or escape the trapped region.

Setting $s = 0$ in equation (4.70), we recover the equation for the separatrix of a standard pendulum Hamiltonian (e.g. Lichtenberg & Lieberman, 1992):

$$\Delta_{\pm} = \pm\frac{2\omega_0}{G}\cos\frac{\theta}{2}. \tag{4.71}$$

CHAPTER 5

Conclusions

5.1 Overview

In this thesis, we have provided the first evidence for the deceleration of the Galactic bar from both the kinematics and chemistry of Solar neighbourhood stars. The discovery of the bar's slowdown offers a novel dynamical evidence for the existence of dark matter that must have taken up the energy and angular momentum from the bar by dynamical friction. This has far-reaching consequences: (i) The deceleration of the bar requires the inertial mass of dark matter, and is thus in strong tension with alternative theories of gravity. (ii) More importantly, the measured bar's slowing rate encodes the kinematic state of dark matter as well as its nature, hence paving a new path to probe the fundamental properties of dark matter beyond just mapping its spatial distribution.

In Chapter 2, we modelled the local stellar kinematics under the impact of a decelerating Galactic bar. We first explained the theory of resonant dragging using secular perturbation theory and showed that the direction of dragging in action space is determined by the resonant vector $\boldsymbol{N}$ as well as the sign of the parameter $G = \partial^2 H_0 / \partial J_s^2$. We further showed that the resonantly dragged phase-space shrinks as the bar slows down more rapidly, implying that the bar's slowing rate is an important parameter in shaping the kinematics of the stellar disk. These theoretical predictions are subsequently corroborated using test-particle simulations. We showed that the sweeping resonances capture and drag orbits from the inner disk, which naturally resolves the issue of reproducing the Hercules stream with the bar's corotation resonance. The Hercules stream's asymmetricity in radial velocity

and its variation in azimuth are both in favour of a slowing slow bar model. Finally, we fit our model to the *Gaia* data and provided the first estimate on the bar's slowing rate $\dot{\Omega}_{\rm p} = -4.5 \pm 1.4\,{\rm km\,s^{-1}\,kpc^{-1}\,Gyr^{-1}}$.

In Chapter 3, we devised a new method to decode the evolutionary history of the bar. From the analysis on the adiabatic invariants of the trapped orbits, we realized that the resonant phase-space evolves analogously to a tree: just as a tree grows from its surface, keeping its internal ring pattern intact, so the resonance captures new stars by expanding its surface (separatrix) while conserving the internal phase-space density. The bar's evolutionary history is thus *recorded* due to the non-adiabatic evolution of stars (resonant capture) and subsequently *preserved* by their adiabatic evolution (resonant drag). If the bar has been slowing down, this tree-ring structure yields a straightforward prediction: the sweeping resonances will capture stars sequentially from the inner disk and should thus exhibit an increase in metallicity towards the resonant centre. We showed that the bar's corotation resonance bears this exact trend. The data shows that the bar has slowed down at least 24% since its formation, which is already in 2σ tension with modified gravity theories. We further used the metallicity ordering to measure the current bar pattern speed $\Omega_{\rm p} = 35.5 \pm 0.8\,{\rm km\,s^{-1}\,kpc^{-1}}$ which is in excellent agreement with the latest made-to-measure models of the bar/bulge region (Clarke & Gerhard, 2021).

In Chapter 4, we turned to developing a theory of dynamical friction on the bar in the realistic nonlinear regime where resonant trapping dominates the bar-halo interaction. Conventionally, dynamical friction was described using linear theory, which is only valid in the fast limit (i.e. rapidly slowing bars). In the slow/nonlinear regime, dark matter become trapped in resonances and exchange angular momentum with the bar while they librate around the resonance. We showed that the net dynamical friction results from the imbalance in the halo's libration angle: just after bar formation, there are initially more orbits trapped on the lower angular momentum side. As these orbits phase mix inside the resonance, they give rise to an oscillating friction that damps over secular timescales, similarly to the non-linear Landau damping in plasma systems. We conjectured that this mechanism could be responsible for the long-term fluctuation of bar pattern speeds observed in N-body simulations. We showed that, in the slow limit (i.e. no bar slowdown),

dynamical friction is well modelled using the resonant angle-action coordinates. In the future, it will be our task to extend the theory to the general slow regime as well as to quantify the self-gravitational amplification by collective effects.

5.2 Outlook

The barred Galaxy model employed in this thesis was designed to be as simple as possible to gain a clear understanding on the underlying dynamics. There are thus many aspects of the Galaxy that we have not addressed in this thesis. We will mention a few of these here that we have already noted in the main text.

The most important process ignored in our model is the scattering of stars by transient spiral arms and giant molecular clouds (Sellwood & Binney, 2002). Scattering diffuses stars in action space and thus weakens the resonant structures of the galactic bar. This implies that our measurement on the bar's slowing rate, which is determined by the size and density of the bar's corotation resonance, has generally been overestimated: the loss of trapped orbits by diffusion must be offset by making the bar slowdown slower. Similarly, due to stellar diffusion, the current metallicity ordering in J_ℓ inside the corotation can only set a lower limit on the distance travelled by the resonance. Quantifying secular diffusion is thus an inevitable step towards improving our estimates on the bar's evolution parameters.

The interpretation of the metallicity dependence on J_ℓ also requires a more subtle treatment as the radial metallicity profile of the stellar disk is not strictly linear and, more importantly, flattens with stellar age[1] (e.g. Schönrich & McMillan, 2017; Vickers et al., 2021). This implies that the metallicity gradient in J_ℓ may correspondingly flatten towards the centre of the resonance, where we might even observe an inverse metallicity gradient depending on the age of the bar.

In our current work, we have restricted the stellar samples to those with small vertical energies and analysed them with a two dimensional disk model. This enabled us to map the actions of the in-plane motions straightforwardly but also eased the interpretation of

[1] Note that the age dependence on metallicity is different from the age dependence on the radial metallicity gradient. The former is observed as the [M/H] – J_R correlation which we have removed in our analysis, while the latter, required to interpret the [M/H] – J_ℓ correlation, is not addressed in this thesis.

the result. To apply our tree-ring analysis to stars out of the plane, we need to additionally model their vertical motion and its correlation with age and metallicity (e.g. Beane et al., 2018). These correlations are heavily impacted by stellar migration (Schönrich & Binney, 2009) and are also coupled with the radial motion near the vertical Lindblad resonances (Debattista et al., 2017). These three dimensional resonant structures are best modelled using the torus machinery and its perturbative extension developed by Binney (2016, 2018).

Finally, the Galactic disk is by no means an isolated system: it can exchange energy with its environment (e.g. satellite galaxies), and gain mass by accretion or mergers. Fossil relic of past satellite interactions are found in the Galaxy as remnant stellar streams (e.g. Laporte et al., 2020) or as incomplete phase mixing in the vertical motion of the stellar disk (Antoja et al., 2018). It is unclear how and to what extent these satellite interactions impact the tree-ring structure of the bar's resonance. While satellite interactions cannot have entirely destroyed the tree-ring structure (as the data manifests a monotonic metallicity variation in J_ℓ), they have likely distorted or left measurable scars on the rings. This implies that detecting an imperfect tree-ring pattern in the future may vice versa provide information about the past merging history.

These future studies will be facilitated by the upcoming *Gaia Data Release* 3, which will extend the stellar samples with 6D phase-space measurements by roughly a factor of 5, and will also provide the first stellar parameters, including age and metallicity. These data will allow us to cut deeper into the core of the bar's corotation resonance as well as to investigate the age/metallicity dependence on the libration angle, thus identifying, if any, the predicted phase-spiral inside the resonance. Efforts are underway to model this rich kinematic and chemical data, combining all pieces of galaxy evolution mentioned above.

We hope that this thesis has opened up a new avenue to probe the nature of dark matter. Particularly exciting is the prospect of using the measured bar's slowdown rate to test models of dark matter beyond the standard CDM. For example, fuzzy/ultralight dark matter, which has recently become popular for its potential to resolve the small-scale crisis of CDM, is expected to cause weaker dynamical friction because small density wakes cannot form due to the Heisenberg's uncertainty principle. It will be our major task in the future to explore how rapidly bars decelerate in these alternative dark matter models.

References

Aguerri J. A. L., Debattista V. P., Corsini E. M., 2003, MNRAS, 338, 465
Aguerri J. A. L., Méndez-Abreu J., Corsini E. M., 2009, A&A, 495, 491
Aguerri J. A. L., et al., 2015, A&A, 576, A102
Antoja T., et al., 2014, A&A, 563, A60
Antoja T., et al., 2017, A&A, 601, A59
Antoja T., et al., 2018, Nature, 561, 360
Arnol'd V. I., 1963, Russian Mathematical Surveys, 18, 9
Asano T., Fujii M. S., Baba J., Bédorf J., Sellentin E., Portegies Zwart S., 2020, MNRAS, 499, 2416
Athanassoula E., 1992, MNRAS, 259, 345
Athanassoula E., 1996, in Buta R., Crocker D. A., Elmegreen B. G., eds, Astronomical Society of the Pacific Conference Series Vol. 91, IAU Colloq. 157: Barred Galaxies. p. 309
Athanassoula E., 2003, MNRAS, 341, 1179
Athanassoula E., 2007, MNRAS, 377, 1569
Athanassoula E., 2014a, MNRAS, 438, L81
Athanassoula E., 2014b, MNRAS, 438, L81
Athanassoula E., Machado R. E. G., Rodionov S. A., 2013, MNRAS, 429, 1949
Aumer M., Schönrich R., 2015, MNRAS, 454, 3166
Babcock H. W., 1939, Lick Observatory Bulletin, 498, 41
Banik U., van den Bosch F. C., 2021, arXiv e-prints, p. arXiv:2103.05004
Barazza F. D., Jogee S., Marinova I., 2008, ApJ, 675, 1194
Barros D. A., Pérez-Villegas A., Lépine J. R. D., Michtchenko T. A., Vieira R. S. S., 2020, ApJ, 888, 75
Batcheldor D., Robinson A., Axon D. J., Perlman E. S., Merritt D., 2010, ApJ, 717, L6
Beane A., Ness M. K., Bedell M., 2018, ApJ, 867, 31
Bekenstein J. D., 2004, Phys. Rev. D, 70, 083509
Berentzen I., Shlosman I., Martinez-Valpuesta I., Heller C. H., 2007, ApJ, 666, 189
Binney J., 2016, MNRAS, 462, 2792
Binney J., 2018, MNRAS, 474, 2706
Binney J., 2020a, MNRAS, 495, 886
Binney J., 2020b, MNRAS, 495, 895
Binney J., Schönrich R., 2018, MNRAS, 481, 1501
Binney J., Tremaine S., 2008, Galactic Dynamics: Second Edition. Princeton University Press
Binney J., Gerhard O. E., Stark A. A., Bally J., Uchida K. I., 1991, MNRAS, 252, 210
Bland-Hawthorn J., Tepper-García T., 2021, MNRAS, 504, 3168
Blitz L., Spergel D. N., 1991, ApJ, 379, 631
Bontekoe T. R., van Albada T. S., 1987, MNRAS, 224, 349
Bosma A., 1978, PhD thesis, University of Groningen, Netherlands
Bovy J., Hogg D. W., 2010, ApJ, 717, 617

Bovy J., Leung H. W., Hunt J. A. S., Mackereth J. T., García-Hernández D. A., Roman-Lopes A., 2019, MNRAS, 490, 4740
Bressan A., Marigo P., Girardi L., Salasnich B., Dal Cero C., Rubele S., Nanni A., 2012, MNRAS, 427, 127
Brizard A. J., 2013, Commun. Nonlinear Sci. Numer. Simul., 18, 511
Brownstein J. R., Moffat J. W., 2007, MNRAS, 382, 29
Buta R., Combes F., 1996, Fundamentals Cosmic Phys., 17, 95
Buta R. J., et al., 2015, ApJS, 217, 32
Carrera R., et al., 2019, A&A, 623, A80
Casagrande L., Schönrich R., Asplund M., Cassisi S., Ramírez I., Meléndez J., Bensby T., Feltzing S., 2011, A&A, 530, A138
Ceverino D., Klypin A., 2007, MNRAS, 379, 1155
Chandrasekhar S., 1943, ApJ, 97, 255
Chavanis P.-H., 2012, Physica A Statistical Mechanics and its Applications, 391, 3680
Chiba R., Schönrich R., 2021, MNRAS, 505, 2412–2426
Chiba R., Schönrich R., 2022, MNRAS,
Chiba R., Friske J. K. S., Schönrich R., 2021, MNRAS, 500, 4710
Chirikov B. V., 1979, Phys. Rep., 52, 263
Ciotti L., Binney J., 2004, MNRAS, 351, 285
Clarke J., Gerhard O., 2021, arXiv e-prints, p. arXiv:2107.10875
Clarke J. P., Wegg C., Gerhard O., Smith L. C., Lucas P. W., Wylie S. M., 2019, MNRAS, 489, 3519
Clowe D., Bradač M., Gonzalez A. H., Markevitch M., Randall S. W., Jones C., Zaritsky D., 2006, ApJ, 648, L109
Cole D. R., Binney J., 2017, MNRAS, 465, 798
Collett J. L., Dutta S. N., Evans N. W., 1997, MNRAS, 285, 49
Collier A., Madigan A.-M., 2021, ApJ, 915, 23
Collier A., Shlosman I., Heller C., 2018, MNRAS, 476, 1331
Combes F., 2014, A&A, 571, A82
Contopoulos G., 1979, A&A, 71, 221
Contopoulos G., 1980, A&A, 81, 198
Contopoulos G., Grosbol P., 1989, A&ARv, 1, 261
Cropper M., et al., 2018, A&A, 616, A5
Cuomo V., Aguerri J. A. L., Corsini E. M., Debattista V. P., 2020, A&A, 641, A111
D'Onghia E., L. Aguerri J. A., 2020, ApJ, 890, 117
Debattista V. P., Sellwood J. A., 1998, ApJ, 493, L5
Debattista V. P., Sellwood J. A., 2000, ApJ, 543, 704
Debattista V. P., Ness M., Gonzalez O. A., Freeman K., Zoccali M., Minniti D., 2017, MNRAS, 469, 1587
Dehnen W., 1999a, AJ, 118, 1201
Dehnen W., 1999b, ApJ, 524, L35
Dehnen W., 2000, AJ, 119, 800
Destri C., de Vega H. J., Sanchez N. G., 2013, New Astron., 22, 39
Dierickx M. I. P., Loeb A., 2017, ApJ, 847, 42
Dootson D., Magorrian J., 2022, to be submitted
Earn D. J. D., Lynden-Bell D., 1996, MNRAS, 278, 395
Eskridge P. B., et al., 2000, AJ, 119, 536
Famaey B., McGaugh S., 2013, in Journal of Physics Conference Series. p. 012001 (arXiv:1301.0623), doi:10.1088/1742-6596/437/1/012001
Fragkoudi F., et al., 2019, MNRAS, 488, 3324

Frankel N., et al., 2022, arXiv e-prints, p. arXiv:2201.08406
Friske J. K. S., Schönrich R., 2019, MNRAS, 490, 5414
Fux R., 2001, A&A, 373, 511
Gaia Collaboration et al., 2018, A&A, 616, A1
Ghafourian N., Roshan M., Abbassi S., 2020, ApJ, 895, 13
Goodman J., 2000, New Astron., 5, 103
Gravity Collaboration et al., 2019, A&A, 625, L10
Grenon M., 1972, in Cayrel de Strobel G., Delplace A. M., eds, IAU Colloq. 17: Age des Etoiles. Kluwer Academic Publishers, p. 55
Grenon M., 1999, in Spite M., ed., Galaxy Evolution: Connecting the Distant Universe with the Local Fossil Record. Kluwer Academic Publishers, p. 331
Halle A., Di Matteo P., Haywood M., Combes F., 2018, A&A, 616, A86
Hehl F. W., Mashhoon B., 2009, Physics Letters B, 673, 279
Henrard J., 1982, Celestial Mechanics, 27, 3
Hernquist L., 1990, ApJ, 356, 359
Hernquist L., Ostriker J. P., 1992, ApJ, 386, 375
Hernquist L., Weinberg M. D., 1992, ApJ, 400, 80
Hilmi T., et al., 2020, MNRAS, 497, 933
Hohl F., 1971, ApJ, 168, 343
Hu W., Barkana R., Gruzinov A., 2000, Phys. Rev. Lett., 85, 1158
Hui L., Ostriker J. P., Tremaine S., Witten E., 2017, Phys. Rev. D, 95, 043541
Hunt J. A. S., Bovy J., 2018, MNRAS, 477, 3945
Hunt J. A. S., Hong J., Bovy J., Kawata D., Grand R. J. J., 2018, MNRAS, 481, 3794
Hunt J. A. S., Bub M. W., Bovy J., Mackereth J. T., Trick W. H., Kawata D., 2019, MNRAS, 490, 1026
Hunt J. A. S., Stelea I. A., Johnston K. V., Gandhi S. S., Laporte C. F. P., Bédorf J., 2021, MNRAS, 508, 1459
Iocco F., Pato M., Bertone G., Jetzer P., 2011, J. Cosmology Astropart. Phys., 2011, 029
Jiang I.-G., Binney J., 2000, MNRAS, 314, 468
Joshi Y. C., 2007, MNRAS, 378, 768
Kaasalainen M., 1994, MNRAS, 268, 1041
Kalnajs A. J., 1972, ApJ, 175, 63
Kalnajs A. J., 1991, in Sundelius B., ed., Dynamics of Disc Galaxies. Göteborgs University and Chalmers University of Technology, p. 323
Katz D., et al., 2019, A&A, 622, A205
Kawata D., Baba J., Ciucă I., Cropper M., Grand R. J. J., Hunt J. A. S., Seabroke G., 2018, MNRAS, 479, L108
Khanna S., et al., 2019, MNRAS, 489, 4962
Kushniruk I., Bensby T., Feltzing S., Sahlholdt C. L., Feuillet D., Casagrande L., 2020, A&A, 638, A154
Lancaster L., Giovanetti C., Mocz P., Kahn Y., Lisanti M., Spergel D. N., 2020, J. Cosmology Astropart. Phys., 2020, 001
Laporte C. F. P., Belokurov V., Koposov S. E., Smith M. C., Hill V., 2020, MNRAS, 492, L61
Leaman R., 2012, AJ, 144, 183
Lichtenberg A., Lieberman M., 1992, Regular and Chaotic Dynamics. Springer-Verlag
Little B., Carlberg R. G., 1991, MNRAS, 251, 227
Long R. J., Mao S., Shen J., Wang Y., 2013, MNRAS, 428, 3478
Long S., Shlosman I., Heller C., 2014, ApJ, 783, L18
Luck R. E., 2018, AJ, 156, 171

Lynden-Bell D., 1979, MNRAS, 187, 101
Lynden-Bell D., Kalnajs A. J., 1972, MNRAS, 157, 1
Malhotra R., 1998, in Lazzaro D., Vieira Martins R., Ferraz-Mello S., Fernandez J., eds, Astronomical Society of the Pacific Conference Series Vol. 149, Solar System Formation and Evolution. p. 37
Malmberg J. H., Wharton C. B., 1967, Phys. Rev. Lett., 19, 775
Marinova I., Jogee S., 2007, ApJ, 659, 1176
Marrodán Undagoitia T., Rauch L., 2016, Journal of Physics G Nuclear Physics, 43, 013001
Martinez-Valpuesta I., Shlosman I., Heller C., 2006, ApJ, 637, 214
McMillan P. J., 2017a, MNRAS, 465, 76
McMillan P. J., 2017b, MNRAS, 465, 76
Milgrom M., 1983, ApJ, 270, 365
Minchev I., Quillen A. C., Williams M., Freeman K. C., Nordhaus J., Siebert A., Bienaymé O., 2009, MNRAS, 396, L56
Minchev I., Boily C., Siebert A., Bienayme O., 2010, MNRAS, 407, 2122
Moffat J. W., 2006, J. Cosmology Astropart. Phys., 2006, 004
Monari G., Famaey B., Siebert A., Duchateau A., Lorscheider T., Bienaymé O., 2017a, MNRAS, 465, 1443
Monari G., Famaey B., Fouvry J.-B., Binney J., 2017b, MNRAS, 471, 4314
Monari G., Famaey B., Siebert A., Wegg C., Gerhard O., 2019a, A&A, 626, A41
Monari G., Famaey B., Siebert A., Bienaymé O., Ibata R., Wegg C., Gerhard O., 2019b, A&A, 632, A107
Mühlbauer G., Dehnen W., 2003, A&A, 401, 975
Nakada Y., Onaka T., Yamamura I., Deguchi S., Hashimoto O., Izumiura H., Sekiguchi K., 1991, Nature, 353, 140
Netopil M., Paunzen E., Heiter U., Soubiran C., 2016, A&A, 585, A150
Nipoti C., Ciotti L., Binney J., Londrillo P., 2008, MNRAS, 386, 2194
Noguchi M., 1987, MNRAS, 228, 635
O'Neil T., 1965, Physics of Fluids, 8, 2255
O'Neill J. K., Dubinski J., 2003, MNRAS, 346, 251
Patsis P. A., Skokos C., Athanassoula E., 2003, MNRAS, 346, 1031
Pérez-Villegas A., Portail M., Wegg C., Gerhard O., 2017, ApJ, 840, L2
Pérez I., Aguerri J. A. L., Méndez-Abreu J., 2012, A&A, 540, A103
Petersen M. S., Weinberg M. D., Katz N., 2016, MNRAS, 463, 1952
Planck Collaboration et al., 2020, A&A, 641, A6
Portail M., Gerhard O., Wegg C., Ness M., 2017, MNRAS, 465, 1621
Read J. I., Moore B., 2005, MNRAS, 361, 971
Regan M. W., Teuben P. J., 2004a, ApJ, 600, 595
Regan M. W., Teuben P. J., 2004b, ApJ, 600, 595
Reid M. J., Brunthaler A., 2020, ApJ, 892, 39
Reid M. J., et al., 2019, ApJ, 885, 131
Roberts M. S., Whitehurst R. N., 1975, ApJ, 201, 327
Rodriguez-Fernandez N. J., Combes F., 2008, A&A, 489, 115
Roshan M., Ghafourian N., Kashfi T., Banik I., Haslbauer M., Cuomo V., Famaey B., Kroupa P., 2021, MNRAS, 508, 926
Rubin V. C., Ford W. Kent J., 1970, ApJ, 159, 379
Saha K., Naab T., 2013, MNRAS, 434, 1287
Sanders J. L., Smith L., Evans N. W., 2019, MNRAS, 488, 4552
Sartoretti P., et al., 2018, A&A, 616, A6
Schönrich R., 2012, MNRAS, 427, 274

Schönrich R., Binney J., 2009, MNRAS, 396, 203
Schönrich R., McMillan P. J., 2017, MNRAS, 467, 1154
Schönrich R., Binney J., Dehnen W., 2010, MNRAS, 403, 1829
Schönrich R., McMillan P., Eyer L., 2019, MNRAS, 487, 3568
Schwarz M. P., 1984, MNRAS, 209, 93
Sellwood J. A., 2006, ApJ, 637, 567
Sellwood J. A., 2010, MNRAS, 409, 145
Sellwood J. A., 2014, Reviews of Modern Physics, 86, 1
Sellwood J. A., 2016, ApJ, 819, 92
Sellwood J. A., Binney J. J., 2002, MNRAS, 336, 785
Sellwood J. A., Carlberg R. G., 2014, ApJ, 785, 137
Sellwood J. A., Carlberg R. G., 2019, MNRAS, 489, 116
Sellwood J. A., Wilkinson A., 1993, Reports on Progress in Physics, 56, 173
Sellwood J. A., Trick W. H., Carlberg R. G., Coronado J., Rix H.-W., 2019, MNRAS, 484, 3154
Sormani M. C., Binney J., Magorrian J., 2015a, MNRAS, 449, 2421
Sormani M. C., Binney J., Magorrian J., 2015b, MNRAS, 454, 1818
Spagna A., Lattanzi M. G., Re Fiorentin P., Smart R. L., 2010, A&A, 510, L4
Springel V., et al., 2005, Nature, 435, 629
Sridhar S., 2019, ApJ, 884, 3
Sridhar S., Touma J., 1996, MNRAS, 279, 1263
Stanek K. Z., Mateo M., Udalski A., Szymanski M., Kaluzny J., Kubiak M., 1994, ApJ, 429, L73
Tiret O., Combes F., 2007, A&A, 464, 517
Toomre A., 1981, in Fall S. M., Lynden-Bell D., eds, Structure and Evolution of Normal Galaxies. pp 111–136
Tremaine S., Weinberg M. D., 1984, MNRAS, 209, 729
Tremaine S. D., Ostriker J. P., Spitzer L. J., 1975, ApJ, 196, 407
Trick W. H., Fragkoudi F., Hunt J. A. S., Mackereth J. T., White S. D. M., 2021, MNRAS, 500, 2645
Vickers J. J., Shen J., Li Z.-Y., 2021, ApJ, 922, 189
Vikhlinin A., Kravtsov A., Forman W., Jones C., Markevitch M., Murray S. S., Van Speybroeck L., 2006, ApJ, 640, 691
Villa-Vargas J., Shlosman I., Heller C., 2009, ApJ, 707, 218
Wegg C., Gerhard O., Portail M., 2015, MNRAS, 450, 4050
Weiland J. L., et al., 1994, ApJ, 425, L81
Weiler M., 2018, A&A, 617, A138
Weinberg M. D., 1985, MNRAS, 213, 451
Weinberg M. D., 1989, MNRAS, 239, 549
Weinberg M. D., 1992, ApJ, 384, 81
Weinberg M. D., 1994, ApJ, 420, 597
Weinberg M. D., 2004, arXiv e-prints, pp astro–ph/0404169
Weinberg M. D., Katz N., 2007, MNRAS, 375, 425
White S. D. M., 1983, ApJ, 274, 53
Wigner E. P., 1959, Group Theory and Its Application to the Quantum Mechanics of Atomic Spectra. Academic Press
Wisdom J., 2004, AJ, 128, 484
Wu Y.-T., Pfenniger D., Taam R. E., 2016, ApJ, 830, 111
Yoshida H., 1993, Celestial Mechanics and Dynamical Astronomy, 56, 27
Zwicky F., 1937, ApJ, 86, 217

de Vaucouleurs G., 1964, The Galaxy and the Magellanic Clouds, Proceedings of the International Astronomical Union Symposium no. 20, 20, 195
dell'Antonio I. P., Tyson J. A., 1996, ApJ, 473, L17